ETH *zürich*

Felix Bachmair

CVD Diamond Sensors In Detectors For High Energy Physics

DISS. ETH NO. 23725

ETH zürich

CVD Diamond Sensors In Detectors For High Energy Physics

a thesis submitted to attain the degree of

Doctor of Sciences of ETH Zürich

(Dr. sc. ETH Zürich)

presented by

Felix Bachmair

Dipl. Physiker, RWTH Aachen

born on Sept. 26th, 1984 in Münster, Germany
accepted on the recommendation of

Prof. Dr. Rainer Wallny   examiner
Prof. Dr. William Trischuk   co-examiner

Abstract

At the end of the next decade an upgrade of the Large Hadron Collider (LHC) to High Luminosity LHC (HL-LHC) is planned which requires the development of new radiation tolerant sensor technology. Diamond is an interesting material for use as a particle detector in high radiation environments. The large band gap (5.47 eV) and the large displacement energy suggest that diamond is a radiation tolerant detector material. In this Thesis the capability of Chemical Vapor Deposition (CVD) diamond as such a sensor technology is investigated. The radiation damage constant for 800 MeV protons is measured using single crystalline CVD (scCVD) and polycrystalline CVD (pCVD) diamonds irradiated to particle fluences up to $12 \times 10^{15} \, \mathrm{p/cm^2}$. In addition the signal response of a pCVD diamond detector after an irradiation to $12 \times 10^{15} \, \mathrm{p/cm^2}$ is investigated to determine if such a detector can be operated efficiently in the expected HL-LHC environment. By using electrodes embedded in the bulk material (3D detector geometry) it is possible to reduce the drift distances of charge carriers in a detector material. This results in an increased signal response for materials with a limited charge carrier lifetime, for example irradiated sensors. The results of a scCVD and a pCVD diamond detector using the 3D geometry are presented. Furthermore the sensitivity of irradiated diamond detectors to particle flux is determined for particle fluxes up to $10 \, \mathrm{MHz/cm^2}$.

Zusammenfassung

In der zweiten Hälfte des nächsten Jahrzehnts ist ein Aufrüstung vom Large Hadron Collider (LHC) Beschleuniger zum High Luminosity LHC (HL-LHC) Beschleuniger geplant. Für diese Aufrüstung ist es notwendig neue stahlenharte Sensormaterialien zu entwickeln. Diamant ist ein vielversprechendes Material für den Einsatz als Teilchendetektor in strahlenbelasteten Umgebungen. Die grosse Bandlücke und die hohe Verschiebungsenergie deuten darauf hin, dass Diamant ein strahlungshartes Detektormaterial ist. In dieser Doktorarbeit wird das Potenzial von Chemical Vapor Deposition (CVD) Diamanten als solche Sensortechnologie untersucht. Die Strahlenhärte von Diamant gegenüber 800 MeV Protonen wird quantifiziert. Dafür wurden einkristalline und polykristalline CVD Diamanten mit Teilchenfluenzen von bis zu $12 \times 10^{15} \, \mathrm{p/cm^2}$ bestrahlt. Mithilfe des polykristallinen CVD Diamanten der mit $12 \times 10^{15} \, \mathrm{p/cm^2}$ bestrahlt wurde, wird untersucht ob die Signale nach nach so einer Bestrahlung hoch genug sind, so dass der Detektor noch effizent betrieben werden kann. In dem man die Elektroden im Sensormaterial plaziert (3D Detektorgeometrie) ist es möglich die Driftdistanzen von freien Ladungsträgern zu verringern. Dies ermöglicht es höhere Signale in Materialien mit vielen Störstellen zu messen. Jedes bestrahlte Sensormaterial ist solch ein Störstellen dominiertes Material. Die Ergebnisse für einen einkristallinen und einem polykristallinen CVD Diamantdetektor, welche die 3D Detektorgeometrie nutzen, werden präsentiert. Des weiteren wird die Sensitivität von bestrahlten Diamantdetektoren gegenüber Teilchenfluenz bis zu $10 \, \mathrm{MHz/cm^2}$ untersucht.

Contents

1. Introduction

The turn on of the Large Hadron Collider (LHC) in 2009 started a new era in particle physics opening energy regimes that have never been reached with particle accelerators before. With the latest energy ramp up to a centre-of-mass (c.o.m.) energy of 13 TeV the LHC has almost reached its design energy of 14 TeV. From the initial conception of building a proton-proton collider in the tunnel of the Large Electron-Positron Collider (LEP) experiment in 1984 [1], the development and construction until stable operation took more than 25 years.

The aim of the LHC is to continue to push the understanding of the fundamental structure of the universe. The Standard Model (SM) of particle physics describes all known elementary particles and their electromagnetic, weak, and strong interactions. The elementary particles are classified in six leptons (e, ν_e, μ, ν_μ, τ, ν_τ), six quarks (u, d, c, s, t, b), four gauge bosons (g, γ, Z, W) and the Higgs boson. In summer 2012, the collaborations of the two experiments, ATLAS and CMS, announced the discovery of a new particle with a mass around 125 GeV. This particle is compatible with the long sought-after Higgs boson [2, 3], which was predicted more than 50 years ago [4, 5]. With this discovery the missing piece of the SM was found, but the search for new phenomena and particles continues as many problems of particle physics do not have simple answers with the present description of the SM. Different theories to extend the SM, like SUperSYmmetry (SUSY), have been developed, from which many predict new particles in the TeV energy range. Therefore, particle physicists hope to find evidence of new particles and phenomena in the coming years of LHC operation.

All of the processes from extensions of the SM mentioned above are very rare. In order to observe rare processes, high luminosities are required. The high luminosities required imply many overlapping events, perhaps as many as 200, for each trigger. By tracing back the trajectories of different particles the various collisions can be reconstructed and disentangled. This reconstruction requires precision tracking which can only be obtained by placing position sensitive tracking detectors as close to the Interaction Point (IP) as possible.

In the current LHC experiments the innermost detectors are placed at a distance of less than 5 cm away of the IP (A Toroidal LHC ApparatuS (ATLAS)-IBL at 3.3 cm, Compact Muon Solenoid (CMS) 1st layer at 4.4 cm). During their operation in the LHC these detectors will receive high radiation levels. These levels are usually given in a 1 MeV

neutron equivalent particle doses (Non Ionizing Energy Loss (NIEL)) and will reach $10^{15}\,\mathrm{n_{eq}/cm^2}$ at the end of operation.

Already now the development of the next generation of particle accelerators has started for which new technologies need to be explored. In the mid 2020s the next major upgrade of LHC, called High Luminosity LHC (HL-LHC), will be installed. With this upgrade the collision rates will increase significantly, creating a very harsh radiation environment for the experiments. The total number of particle collisions will increase by approximately one order of magnitude (from $\sim$500/fb to $\sim$3000/fb) and the expected particle flux will increase by a factor of five to ten.

At radiation levels of more than $1-2\times10^{16}\,\mathrm{n_{eq}/cm^2}$ the radiation tolerance of the detectors, especially of the sensors, becomes a major aspect in the design. The current tracking detectors use silicon sensors, a well tested and well understood material. At the expected particle fluences the state of the art silicon sensor will not be able to operate. The incident particles will damage the crystalline structure and change the material properties. Even with cooling the leakage currents of these sensors will make it difficult to detect the particles with high efficiency. Therefore new radiation tolerant sensor technologies are needed.

Similar to silicon, diamond can be operated as an ionization chamber, which can be used to measure the deposited energy of an incident particle. With its large band-gap ($E_{gap} = 5.5\,\mathrm{eV}$ at $T = 302\,\mathrm{K}$) and its high binding energy, diamond has ideal material properties which indicate that it is a radiation tolerant sensor material. The fast charge collection, the high thermal conductivity, the low dielectric constant and the ability to work at room temperature without drawing leakage current are also properties which are very appealing for a sensor material of a tracking detector. As it is possible to artificially grow diamonds by Chemical Vapor Deposition (CVD), diamond becomes one potential sensor technology for the innermost layers where the radiation levels are the highest. In this thesis the performance of CVD diamond sensors for their application in high luminosity experiments is investigated within the framework of the RD42 collaboration at CERN. One possible use of CVD diamond sensors is in pixelated tracking detectors in the inner-most tracking layers of HL-LHC experiments.

1.1. The Large Hadron Collider

The LHC [6] is a circular proton-proton particle collider at the European Organization for Nuclear Research (CERN) [7] in Geneva, Switzerland. It was designed to produce centre-of-mass energies of up to $14\,\mathrm{TeV}$ and instantaneous luminosities of $1\times10^{34}/(\mathrm{cm^2\,s})$. The collider was built into a tunnel with a circumference of $27\,\mathrm{km}$ at a depth from $50\,\mathrm{m}$ to $175\,\mathrm{m}$ and crosses the border of Switzerland and France. The tunnel contains two rings (beamlines) with four points of intersection. Protons circulate in opposite

directions in the two rings such that they are brought into collision at the Interaction Points (IPs). At these points the collisions are observed by four big particle experiments: ATLAS, CMS, Large Hadron Collider beauty (LHCb) and A Large Ion Collider Experiment (ALICE). The LHCb experiment is specialized on physics related to *b*-hadrons, like CP violation (violation of the charge conjugation parity symmetry [8]). ALICE is optimized for studying quark gluon plasma in heavy ion collisions, e.g. $Pb - Pb$. The two large general purpose experiments ATLAS and CMS focus on proton-proton collisions to find new physics beyond the SM and to study electroweak symmetry breaking mechanisms.

Since 2015 the LHC has operated at a centre-of-mass energy of 13 TeV. In several steps, the protons are pre-accelerated to an energy of 450 GeV and then injected into the LHC where they are further accelerated to their final energy of 6.5 TeV. An overview of the whole accelerator complex of CERN is shown in Figure 1.1.

When the protons reach their final energy they have 99.999 999 0 % of the speed of light. 1232 superconducting dipole magnets, each having a magnetic field of up to 8.33 T, keep the protons on their circular path. Proton beams in each of the two rings are bunched where each bunch contains $\sim 1.5 \times 10^{11}$ protons before collisions. A beam has up to 2808 bunches that are spaced in such a way that a collision could happen every 25 ns. In the first operation from 2010 to 2013, called Run 1, the LHC operated at centre-of-mass energies of 7 TeV and 8 TeV and a bunch spacing of 50 ns (2010: 150 ns).
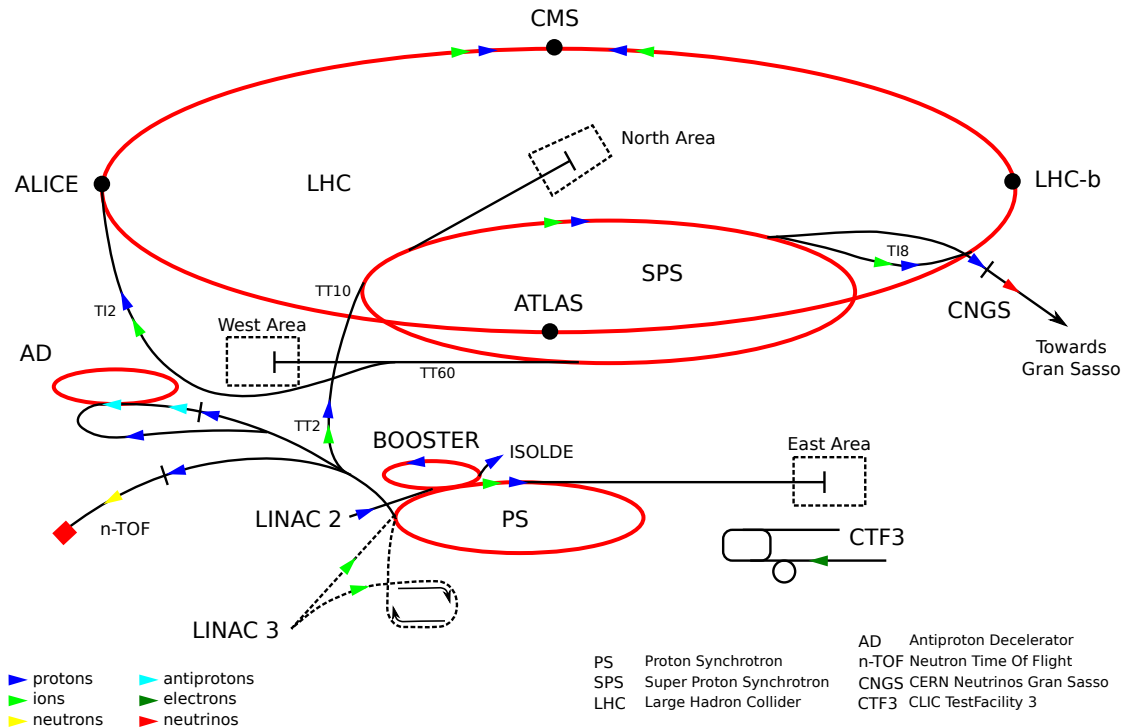

Figure 1.1.: An overview of the full accelerator complex at CERN [9].

1. Introduction

As only a small fraction of the protons in the bunches actually collide at the IPs, the LHC sustains collisions in stable operation for up to 35 h. During such a fill the collision rate reduces with time and at some point the beams are extracted from the circular collider and are absorbed in a beam dump block.

To describe the ability of a particle accelerator to produce a given number of interactions per unit time the instantaneous luminosity is used. For a circular collider with a bunched beam structure the luminosity can be approximated by

$$\mathscr{L} = f \frac{n_1 n_2}{4\pi \cdot \sigma_x \cdot \sigma_y} \,, \tag{1.1}$$

where f is the collision frequency, n_1 and n_2 are the number of particles in each bunch and σ_x and σ_y are the transverse beam sizes in horizontal and vertical directions [10]. The integrated luminosity $\mathcal{L}$ is used to describe the delivered and recorded number of collisions of a particle physics experiment and is calculated by the integral of the instantaneous luminosity $\mathscr{L}$ with respect to the time:

$$\mathcal{L} = \int \mathscr{L} \mathrm{d}t \,. \tag{1.2}$$

The number N of events of a specific process is derived from the integrated luminosity and the production cross section σ_p:

$$N_{\text{event}} = \mathcal{L} \cdot \sigma_p \,. \tag{1.3}$$

As the cross section describes an effective area the unit of luminosity is an inverse area. The cross section, σ_p, is usually expressed in units of barn (b). One barn is defined as an area of $1 \times 10^{-28} \, \mathrm{m}^2$. For ease of use the integrated luminosity is therefore usually given in b^{-1}. The total cross section of proton-proton collision at the LHC is more than ten orders of magnitude higher than the production cross section of a Higgs particle ($\sim 10^8$ nb versus $\sim 10^{-2}$ nb). This is shown in Figure 1.2, which also shows the production cross section of several other SM processes. The luminosity determines the total number of events for a process with a given cross section. A higher luminosity increases the sensitivity to interesting physics processes with small cross sections. To measure rare processes with high precision or to detect physics processes beyond the SM, it is required to reach high integrated luminosities and therefore to also work at the highest instantaneous luminosities possible. This results in high probabilities of multiple collisions within one bunch crossing. The number of events per bunch crossing is called pile-up (μ). For the experiments it is very challenging to disentangle the different collisions by reconstruction of the different vertices of the collisions. The precise measurement of the luminosity is of crucial importance, as the uncertainty of the luminosity measurement directly translates to the uncertainty of the measured cross sections.
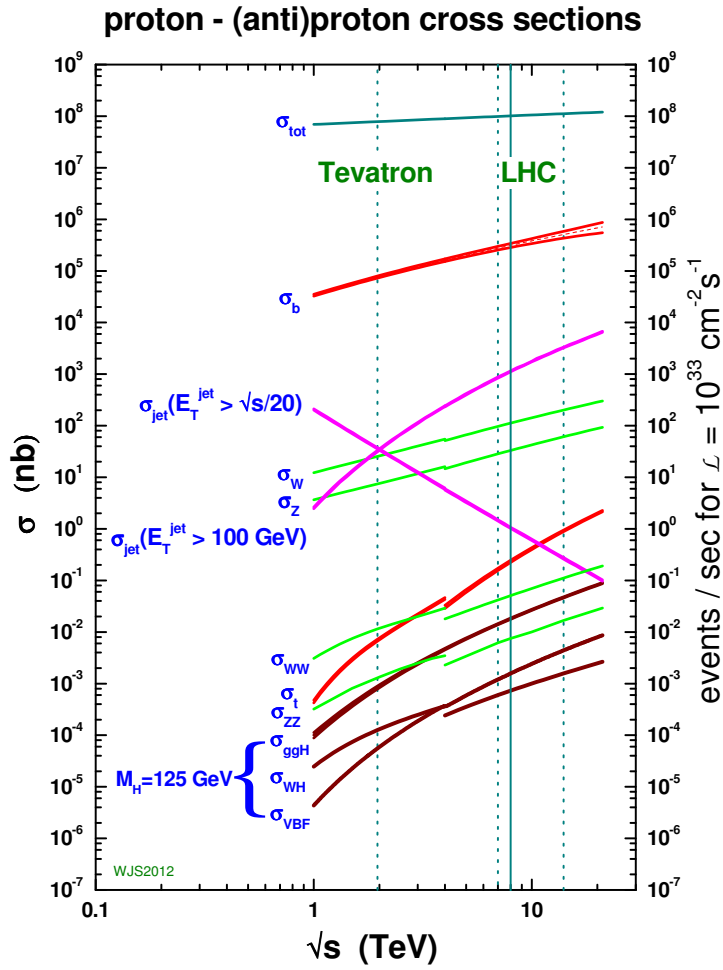
Figure 1.2.: Standard Model production cross sections at hadron colliders as a function of centre-of-mass energy [11].

1.2. From LHC to High Luminosity LHC

From 2008 until early 2013 the LHC was operating at centre-of-mass energies of 7 TeV and 8 TeV. After this run the LHC accelerator complex shut down for a two year maintenance period. During this time the magnet system was revised to stabilize operation at the design energy. In addition, the bunch crossing interval was reduced to 25 ns. During this shutdown the experiments upgraded their detectors to reach the same performance at higher energies and collision rates. Additional upgrades of detectors are planed during the shut downs in the coming years.

In order to further increase its discovery potential, the LHC will need a major upgrade after 2025. The High Luminosity LHC project will increase the luminosity beyond the original design values of LHC. With this increased luminosity it will be possible to precisely study new particles observed in the LHC, such as the Higgs boson, and will also enable the observation of rare processes that are below the sensitivity levels of the LHC.

An operation schedule for the LHC/HL-LHC including the expected machine parameters is shown in Table 1.1 and illustrated in Figure 1.3. During its expected time of operation of twelve years it is planed to reach a total integrated luminosity of $\mathcal{L} = 3000/\text{fb}$ [12], which requires an increase of the instantaneous luminosity to $\mathscr{L} = 5 \times 10^{34}/(\text{cm}^2\,\text{s})$. At this luminosity 140 to 200 pp-collisions per bunch crossing are expected.

This upgrade will not only necessitate changes to the accelerator complex, but will also have major impacts on the experiments. The experiments must be capable of maintaining or even improving their performance at a five to ten times higher pile-up level and in a much harsher radiation environment. Thus, upgrades of all detector systems are planned. In particular the tracking detectors will need major upgrades as these detectors are the closest to the IP and will be exposed to the highest particle rates. In order to be ready to

Name	Start [yr]	int. Lum. $\mathcal{L}$ [1/fb]	inst. Lum. $\mathscr{L}$ [1/(cm^2 s)]	Bunch Spacing [ns]	Energy $\sqrt{s}$ [TeV]	exp. particle flux at $r = 5\,\text{cm}$ [n$_{\text{eq}}$/cm^2]
LHC						
Run 1	2010	25	6×10^{33}	50	7 - 8	$\sim 1 \times 10^{14}$
Run 2	2015	75	1×10^{34}	25	13 - 14	$\sim 2 \times 10^{14}$
Run 3	2020	350	2×10^{34}	25	14	$\sim 1 \times 10^{15}$
HL-LHC						
	2025	3000	5×10^{34}	25	14	$\sim 2 \times 10^{16}$

Table 1.1.: Overview of the delivered/expected integrated and instantaneous Luminosities of LHC and HL-LHC and the expected durations of each run phase.
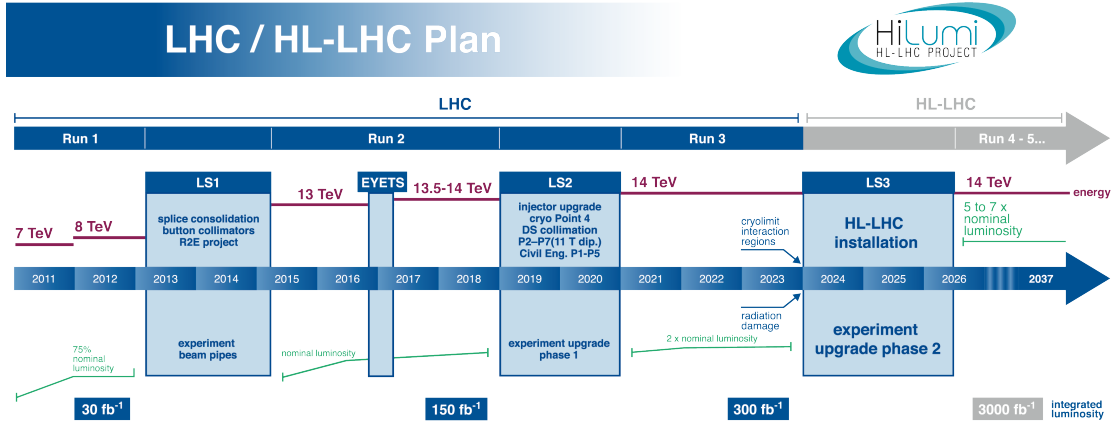
Figure 1.3.: LHC/HL-LHC road map [13].

install the upgraded detectors in time, the development of the new detectors has already started and first design reports have been published [14, 15].

In the inner most layers of the pixel detector the predicted particle fluences after an integrated luminosity of 3000/fb are simulated to be $1 - 2 \times 10^{16}\,\mathrm{n_{eq}/cm^2}$ (NIEL) and $5 - 10\,\mathrm{MGy}$ (Total Ionizing Dose (TID)). The NIEL describes the damage in the sensor, while the TID quantifies the damage in the electronics. Due to radiation damage in the sensor material the signal response of the detectors decreases with increasing radiation dose. This is explained in detail in Chapter 2.2.3. These levels of radiation damage are a factor of ten above the expected lifetime of the inner most detectors of the current experiments, which are designed for particle fluences of $1.5 \times 10^{15}\,\mathrm{n_{eq}/cm^2}$, corresponding to 250/fb [16]. In addition, higher granularity will be needed in order to separate particle tracks at the expected pile-up levels, the bandwidth of the readout electronics must be increased and the tracker most-likely needs to be included in the trigger decision of the experiments. A redesign of the readout electronics is required as the readout electronics must be capable of working with the small signals expected at these high radiation levels, of operating with high efficiencies at the the expected hit rate of $1\,\mathrm{GHz/cm^2}$ to $3\,\mathrm{GHz/cm^2}$ in the inner most layers and of operating after the expected radiation levels.

1.3. Diamond Detectors In Current High Energy Experiments

The safe operation of many high energy particle experiments relies on fast, radiation-tolerant Beam Condition Monitor (BCM) systems to protect the experiment from destruction by the the beam, i.e. adverse beam conditions. This requires detecting abnormal particle fluxes and sending a signal to the beam interlock system to dump the beams.

In order to minimize the time until the beam is dumped, the corresponding detectors need to be placed in the forward regions of the detectors close to the beam pipe. In these regions space is usually limited which makes it difficult to install a cooled detector system. Detectors made out of diamond are an ideal candidate for this especially harsh environment. Due to the large band gap and the high displacement energy, diamond sensors can withstand high particle fluences, have fast signal responses and can be operated with minimum services, e.g. no cooling is required.

In 2002 the first diamond sensors were used for radiation monitoring in the BaBar experiment at the Stanford Linear Accelerator Center (SLAC). Since then, diamond sensors have become a key technology for real-time radiation monitoring and protection. Many high-energy experiments including Belle, CDF and all LHC experiments [17–20], use BCM systems based on CVD diamond sensors. Diamond sensors are also used in the beam loss monitor system of the LHC accelerator complex [21]. In different locations in the LHC tunnel polycrystalline CVD (pCVD) diamond detectors are installed, performing a bunch-by-bunch beam loss analysis.

Figure 1.4 shows the active area of various diamond detector systems that have been operated over the last 15 years. With each new experiment the area of diamond detectors increased. In the following section the detector systems based on diamond sensors used in CMS and ATLAS are presented.

1.3.1. Detectors with Diamond Sensors in CMS

The BCM system of CMS consists of several detectors of which some are based on diamonds. The BCM1F [23] is a fast beam monitoring system and BCM1L/BCM2L [24] is used as a beam abort system .
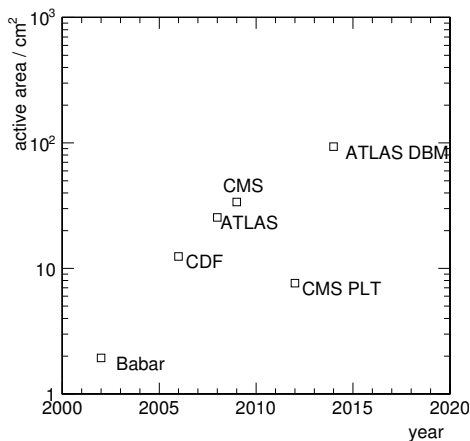
Figure 1.4.: Active area of various diamond detector systems that have been operated over the last 15 years [22, edited].

The BCM1F is designed to provide real time diagnostics of the beam conditions by monitoring the flux and timing of the particles originating from the proton-proton interactions and machine induced background particles. In addition, it provides online, bunch-by-bunch instantaneous luminosity measurements [25]. Its readout is able to resolve the sub-bunch structure of the beam. The BCM1F consists of 24 single crystalline CVD (scCVD) $5 \times 5\,\text{mm}^2$ sized diamonds, each with a thickness of $500\,\mu\text{m}$. Fast electronics are used for the readout. By using a two pad metalization on the diamond sensor the hit probability on each readout channel is reduced.

The beam abort systems BCM1L and BCM2L consist of $1 \times 1\,\text{cm}^2$ sized pCVD diamond detectors which are used to protect the silicon tracker from catastrophic beam loss events. The integrated signal response during a given time window is monitored to detect beam losses. This system is important as an active protection of the CMS detector.

The Pixel-Luminosity-Telescope (PLT) was designed to provide a bunch-by-bunch measurement of the luminosity for the CMS experiment. During the LHC Run 1 in 2012 diamond pixel telescopes were employed in the pilot run of the PLT [26, 27]. Four diamond telescopes were installed. Each telescope consisted of three pixelated scCVD diamond detectors with an area of $4.5 \times 4.5\,\text{mm}^2$ and a pixel size of $150 \times 150\,\mu\text{m}^2$. For comparison one additional telescope using silicon sensors was installed. The full assembly was placed $14.5\,\text{m}$ away from the collision point.

In Figure 1.5 the setup of the PLT pilot run is shown. The scCVD diamond sensors were bump bonded to the CMS pixel ReadOut Chip (ROC), shown Figure 1.5 (a). The size of the diamond sensor was only one fourth of the ROC. The full assembly before installation in the CMS experiment is shown in Figure 1.5 (b) .

Particles crossing the detectors of the PLT fall into three different categories: particles from proton-proton collisions at the IP, particles moving parallel to the beam pipe axis (beam halo), and random scattering events at any angle. By reconstructing the particle track with the three pixelated sensors each particle crossing can be associated with one of the categories. The luminosity can then be measured by counting the number of interactions coming from the IP. In addition the PLT was designed to provide measurements of the location of the actual IP and of the amount of beam halo.

During the PLT pilot run issues with the scCVD PLT diamond sensors were observed. The pulse height of the sensors decreased with increasing incident particle flux, after the diamond sensors had received a relatively low fluence of $10^{13}\,\text{hadrons/cm}^2$. When the particle flux was increased from $400\,\text{Hz/cm}^2$ to $16\,\text{MHz/cm}^2$, the pulse height of these scCVD sensors decreased by $50\,\%$ [27]. This behavior has prompted a study in several high rate beam tests that were carried out in the framework of this thesis and that is further described in Chapter 5.

These problems led to a delay of the PLT project and it was not guaranteed that the installation deadline of a diamond-based PLT could be met. Therefore the CMS collaboration decided to install a silicon based PLT. This required the design of a full cooling system [29].

1 Si pixel telescope

4 diamond pixel telescopes
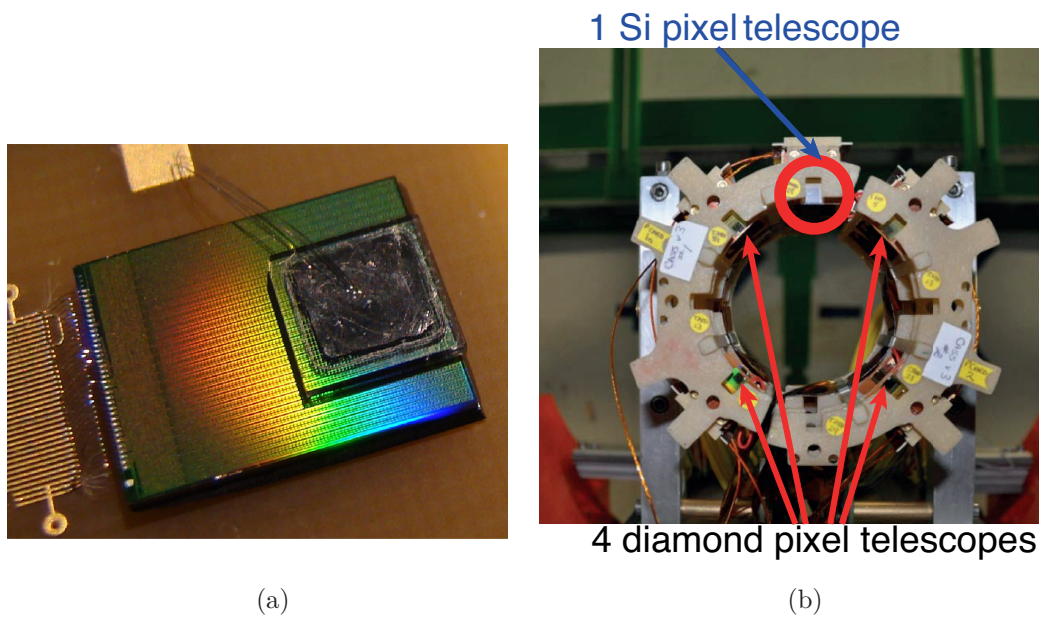
(a)   (b)

Figure 1.5.: The setup of the PLT pilot run. Figure (a) shows a single scCVD diamond sensor bump bonded to the CMS readout chip. The full setup before installation consisting out of five three-plane telescopes is shown in Figure (b). Four telescopes used diamond sensors, one telescope was based on silicon [28, edited].

1.3.2. Detectors with Diamond Sensors in ATLAS

The ATLAS experiment uses a BCM detector system based on pCVD diamond pad detectors. It consists of eight detector modules organized in two sets of four modules on each side of the IP. With these detectors precise Time Of Flight (TOF) measurements of the particles can be performed. Each BCM detector contains two $1 \times 1\,\mathrm{cm}^2$ pCVD diamond sensors. In Figure 1.6, one detector module and the installed detector system around the beam line is shown. In addition to beam condition monitoring, the BCM provides valuable complementary luminosity monitoring information which is used for direct feedback to the LHC operation and to measure the bunch-by-bunch luminosity variations.

With increasing instantaneous luminosity the ATLAS BCM will start saturating at instantaneous luminosities above $\mathscr{L} = 10^{34}/(\mathrm{cm}^2\,\mathrm{s})$ [31]. In order to further provide a precise bunch-by-bunch luminosity measurement the ATLAS Diamond Beam Monitor (DBM) was designed as an upgrade of the ATLAS BCM. The ATLAS DBM has a similar design as the CMS PLT and was designed to measure the bunch-by-bunch luminosity with much better segmentation and with a precision of $1\,\%$. Instead of reading out the signals from a diamond pad detector, the diamond pixel sensors are bump bonded to a pixelated ROC (FE-I4 [32]), producing diamond pixel detectors with fine segmentation. In addition, ATLAS DBM was designed to monitor the beam spot on a bunch-by-bunch base and to distinguish collisions from beam halo. Therefore it consist of telescopes with three planes to allow particle tracking. In total, the DBM consists of four three layer pixel telescopes on each side of the interaction point. Each pixel detector has a sensor size of approximately $18 \times 21\,\mathrm{mm}^2$ and a pixel size of $50 \times 250\,\mathrm{\mu m}^2$. Six of these telescopes use pCVD diamond sensors with a thickness of $\sim500\,\mathrm{\mu m}$. The DBM has been included in the central data taking since the beginning of 2015.
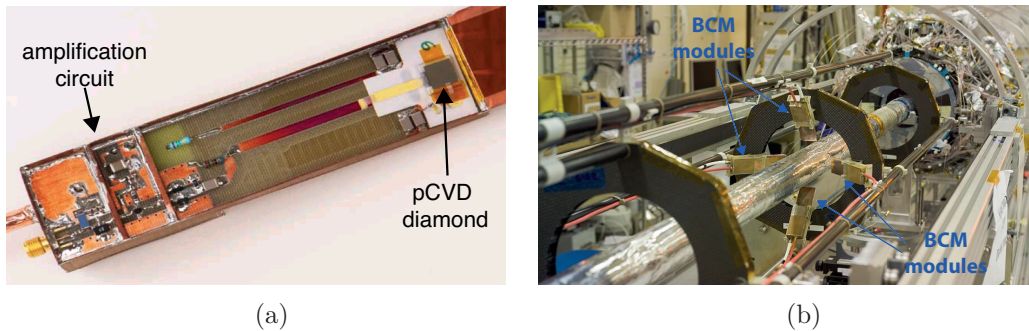

| (a) | (b) |

Figure 1.6.: The ATLAS BCM detector system. In Figure (a) one detector module, consisting out of the sensor and an amplification circuit, is shown. The final installation of these modules around the beam line can be seen in Figure (b) [30].
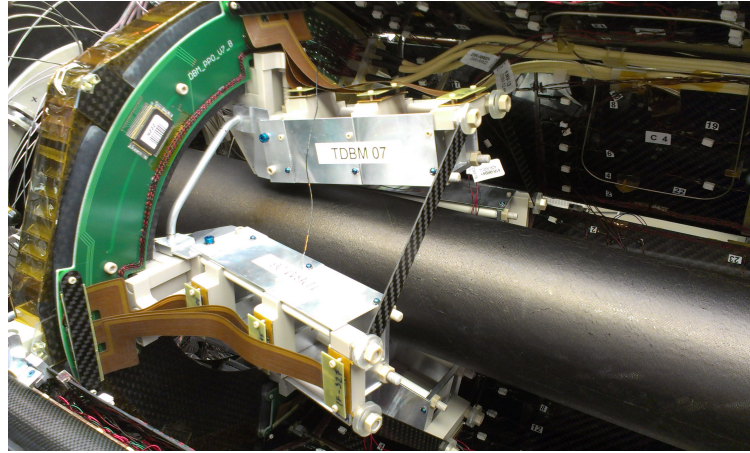
Figure 1.7.: Two DBM telescopes as installed around the ATLAS beam pipe [31].

1.4. The Scope of this Thesis

In this thesis CVD diamond as a sensor material for high energy physics is investigated. A special focus is put on its application as pixelated tracking detectors of HL-LHC experiments. After a discussion of the properties of CVD diamonds, the manufacturing process by CVD and the mechanism of signal creation in diamond material is discussed. The results of three major aspects for CVD diamond as a sensor material in high energy particle experiments are presented in this thesis:

- The large band gap and large displacement energy of diamond make it an attractive material for the expected radiation environments at HL-LHC. In Chapter 3 the analysis of the radiation tolerance of diamonds irradiated with 800 MeV protons up to 12.6×10^{15} p/cm^2 is presented.

- Due to its large band gap, the average number of electron-hole pairs created per path length by a Minimal Ionizing Particle (MIP) in diamond is smaller than in silicon (36 e/µm vs. 80 e/µm). For sensors with a limited Mean Free Path (MFP), like irradiated sensors, this effect is further enhanced, as only a part of the created charge is measured. With the introduction of a 3D geometry the drift distances of the charge carriers can be reduced and therefore the signal response increased. In Chapter 4 a method to produce diamond detectors with a 3D geometry is presented. With the first 3D scCVD diamond detector the proof-of-principle of this detector layout is made and with the results of the first 3D pCVD diamond detector the capability of the 3D diamond detector concept for detectors with a limited MFP is explored.

- The signal dependence on incident particle flux observed during the pilot run of the PLT provoked a major effort to understand this effect. In several beam tests, irradiated pad and pixel diamond sensors were studied as a function of the incident particle flux. First results were published in 2014 for rates up to $300\,\mathrm{kHz/cm^2}$ [33]. In order to validate the results over a wider range of particle fluxes, a new beam test setup was developed in this thesis which is introduced in Chapter 5. The first results of the beam test campaigns that have been performed in August and October 2015 using the new setup are presented. Measurements at particle fluxes up to $10\,\mathrm{MHz/cm^2}$ were performed.

The results of this thesis are summarized in Chapter 6 and a short outlook on the next steps in the development towards a pixelated diamond detector for the inner-most tracking layers of HL-LHC experiments is given.

2. Theory

In order to detect the presence of a particle, an interaction of the particle with the detector material is mandatory. In this interaction the particle deposits energy in the detector material. Different processes lead to either a full deposition of the particle energy (absorption) or a fractional deposition of the particle energy. This chapter introduces the mechanisms of the energy deposition, focusing on particle detection with solid-state detectors, especially diamond detectors.

In Section 2.1 the basic principles of particle detection are described. After the theory of interaction of different particle species with matter, the structure of a modern high energy particle experiment is discussed. In Section 2.2 the main principles of solid state particle detectors are introduced. The deposited energy mainly ionizes the atoms of the detector material. These free charge carriers (electrons and holes) move towards electrodes if an electric field is applied and the induced electric current is used for detection of the particle. All other non-ionizing interactions damage the detector material. With increasing damage of the detector material the signal of an incident particle decreases. The basic mechanisms of radiation damage in solid-state detectors are discussed, followed by an overview of CVD diamonds, as one special solid state detector in Section 2.3. After discussing the properties and the production of CVD diamonds, the principles of particle detectors with a diamond detector are explained. The construction of a diamond detector consists of several steps. A short summary of the state-of-the-art production method is presented.

2.1. Basic Principles of Particle Detection

Highly energetic particles interact with matter in different ways. A quick introduction to the physics of the different types of interactions is given. The main focus lies on the interactions of charged particles which are relevant for the application in tracking detectors for high energy particle physics experiments and the measurements presented in this thesis.

2. Theory

2.1.1. Interaction of Particles with Matter

The processes resulting in energy loss of incident particles are different for charged particles, like electrons and charged hadrons, for neutral hadrons, like neutrons, and for photons. While neutral particles can only interact discreetly, charged particles mainly interact with the electrons and protons of the nucleus via the long-range Coulomb force and via elastic scattering with the atomic electrons (Rutherford scattering). In these electromagnetic processes the charged particle continuously deposits energy in the detector material. The main process of energy loss is elastic scattering. Thus the process of energy loss for charged particles in matter is a stochastic process of multiple collisions of the particle with the atoms of the matter. This section is split into the interaction of heavy charged particles, of electrons and positrons, of photons and of neutrons, followed by a discussion about fluctuations in energy loss and multiple scattering of the particles.

2.1.1.1. Heavy Charged Particles

For all charged particles, except electrons, with a mass M, a speed $v = \beta \cdot c$ and a charge z, the mean energy loss $\mathrm{d}E$ per unit length $\mathrm{d}x$ can be described by the Bethe-Bloch equation [10]

$$-\left\langle \frac{\mathrm{d}E}{\mathrm{d}x} \right\rangle = Kz^2 \frac{Z}{A} \frac{1}{\beta^2} \left[\frac{1}{2} \ln \frac{2m_e c^2 \beta^2 \gamma^2 W_{\max}}{I^2} - \beta^2 - \frac{\delta(\gamma\beta)}{2} \right] , \qquad (2.1)$$

where $K = 4\pi N_A r_e m_e c^2 \sim 0.307\,\mathrm{MeV\,cm^2/mol}$ is a constant, Z the atomic number and A the atomic mass of the absorber, $W_{\max}$ the maximum energy transfer in a single collision and I the mean excitation energy. The relativistic quantities γ and β can be expressed by

$$\gamma = \frac{1}{\sqrt{\beta}} = \frac{E}{Mc^2} . \qquad (2.2)$$

The dimensions of this formula are $\mathrm{MeV\,cm^2/g}$. The relativistic *density-effect* $\delta(\gamma\beta)$ corrects for the transverse extension of electric field at relativistic velocities. This formula describes the mean energy loss per length for moderately relativistic particles in a region of $0.1 \lesssim \beta\gamma \lesssim 1000$ and for intermediate Z materials.

In Figure 2.1 the mean rate of energy loss for positive muons in copper is shown. One can split it the energy loss into three different regions, depending on $\beta\gamma$:

- At a $(\beta\gamma)$ in the range of 0.1 to 1 the β^{-2} dependency results in a steep decrease. After $\gamma \sim 1$, the $\log \beta^2$ term is only increasing slowly.
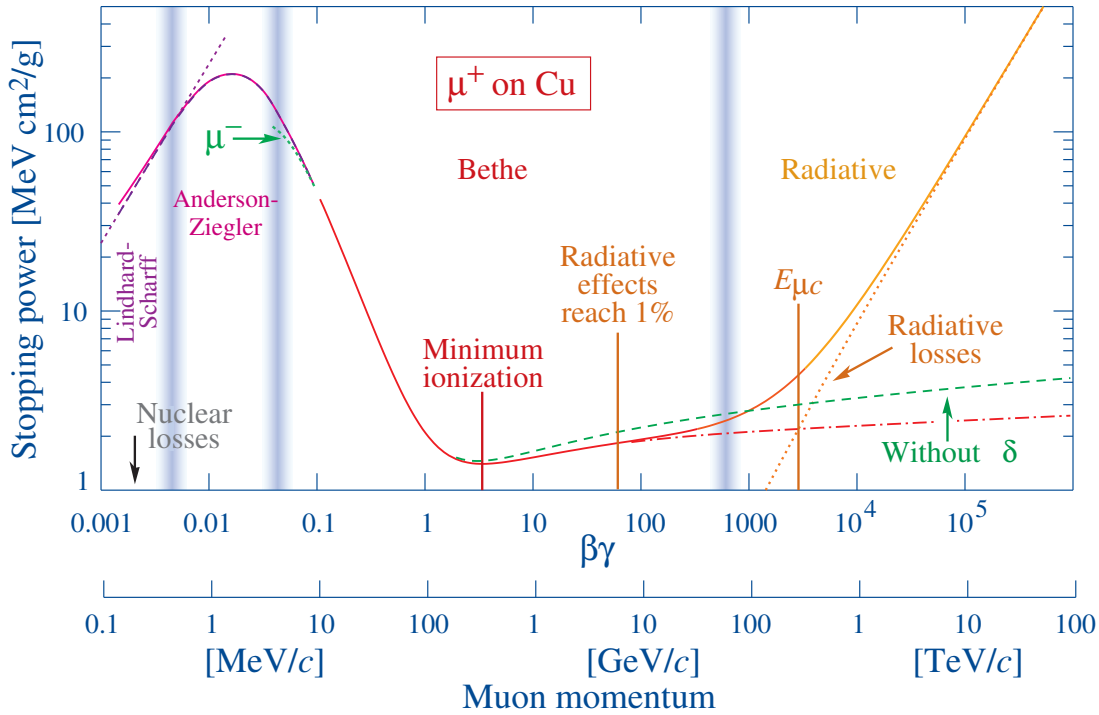
Figure 2.1.: Stopping power $(= \left\langle -\frac{\mathrm{d}E}{\mathrm{d}x} \right\rangle)$ for positive muons in copper as a function of $\beta\gamma = p/Mc$ over nine orders of magnitude in momentum (12 orders of magnitude in kinetic energy).Solid curves indicate the total stopping power. Vertical bands indicate boundaries between different approximations. The short dotted lines labeled "μ^-" illustrate the "Barkas effect", the dependence of stopping power on projectile charge at very low energies [34]. $\frac{\mathrm{d}E}{\mathrm{d}x}$ in the radiative region is not simply a function of β [10].

- For higher momenta β is approaching 1 and $\frac{1}{\beta^2}$ is almost constant, resulting in an increasing $\beta\gamma$. The logarithmic term becomes the dominant factor, so the Equation 2.1 becomes proportional to $\ln\beta\gamma$.

- In between these two regions a minimum at around $\beta\gamma \sim 3-4$ is reached. Particles whose mean energy loss rate through matter is close to this minimum, are called Minimal Ionizing Particles (MIPs). In particular the energy of most relativistic particles can be considered to be close to the energy loss of a MIP.

The minimum energy loss for a MIP depends on the detector material and varies between $\sim 1\,\text{MeV}\,\text{cm}^2/\text{g}$ for lead (Pb) and $\sim 4\,\text{MeV}\,\text{cm}^2/\text{g}$ for liquid H_2. For elements with an atomic number Z larger than 6 a linear dependence of the stopping power for a MIP with Z can be observed and is shown in Figure 2.2. The Equation 2.1 is valid down to $\beta\gamma$ of ≈ 0.1, but can be extended to smaller momenta by various phenomenological corrections (Anderson-Ziegler [35]). At very low momenta a theory with a linear dependency of the stopping power with β has been developed by Lindhard-Scharff [36]. At high energies radiative processes become more important than ionization. For muons and pions this limit is reached at energies of several hundred GeV, for protons and other hadrons this limit is much higher. At these energies further corrections need to be applied.

2.1.1.2. Electrons and Positrons

The Bethe-Bloch formula needs to be modified for electrons and positrons as they have the same mass as the electrons of the detector material. Therefore, the collision happens between two particles with the same mass. This results in the possibility of large
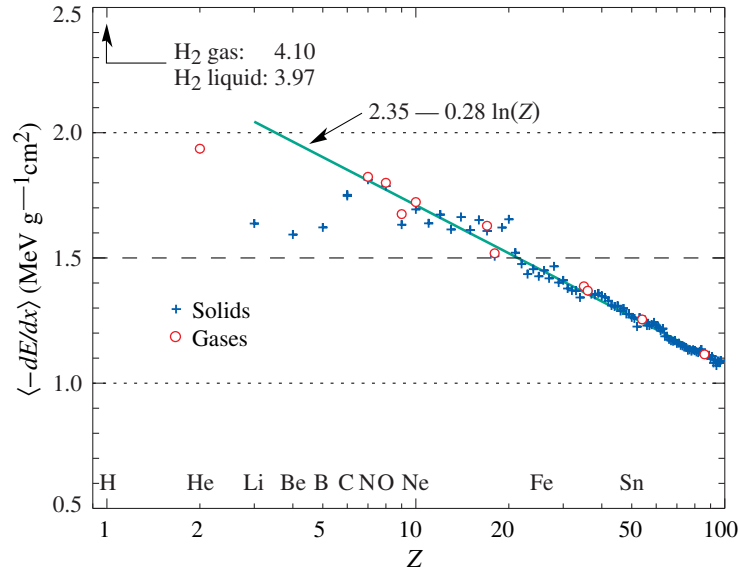

Figure 2.2.: Stopping power at minimum ionization for the chemical elements [10]. The straight line is fitted for $Z > 6$.

energy transfers and large angle multiple scattering. In electron-electron scattering incident and target electron are indistinguishable. At low energies electrons and positrons lose their energy primarily by ionization, but additional process like Møller scattering, Bhabbha scattering, $e^+ - e^-$ annihilation contribute. The energy loss via scattering can be described by a modified version of the Bethe-Bloch formula (Møller [37]):

$$-\left\langle\frac{\mathrm{d}E}{\mathrm{d}x}\right\rangle_{el.} = \frac{1}{2}K\frac{Z}{A}\frac{1}{\beta^2}\left[\ln\frac{m_e\beta^2c^2\gamma^2\left\{m_ec^2(\gamma-1)\right\}}{2I^2} + F(\gamma)\right] \tag{2.3}$$

where I is the mean excitation energy of the matter and $F(\gamma)$ is a correction term. The logarithmic term can be compared with the logarithmic term in the Bethe Bloch Equation 2.1. The mean energy transfer $W_{max} = m_ec^2(\gamma-1)/2$ is only half of the energy transfer in the Bethe-Bloch equation, since the scattering particles are identical.

The energy loss for positrons and electrons is not identical, as positrons are distinguishable from electrons. This results in a different correction term and is described by the Bhabha scattering [10].

Bremsstrahlung At energies of the order of a few MeV Bremsstrahlung becomes the important interaction process for electrons and position. Bremsstrahlung is the electromagnetic radiation of photons when a charged particle is accelerated in the field of a nucleus. It can be described by

$$\frac{\mathrm{d}E}{\mathrm{d}x} = 4\alpha N_A\frac{z^2Z^2}{A}\left(\frac{1}{4\pi\varepsilon_0}\frac{e^2}{mc^2}\right)E\ln\frac{183}{Z^{\frac{1}{3}}}. \tag{2.4}$$

Since the energy loss is proportional to $\frac{1}{m^2}$, it is only an important factor for light particles, particularly for electrons and positrons. In case of electrons, Equation 2.4 can be rewritten in terms of radiation lengths X_0:

$$-\frac{\mathrm{d}E}{\mathrm{d}x} = \frac{E}{X_0}. \tag{2.5}$$

Here the radiation length X_0 is approximated by

$$X_0 = \frac{A}{4\alpha N_A Z^2 r_e^2 \ln\left(183Z^{-1/3}\right)} \tag{2.6}$$

where Z and A are the atomic number and the atomic weight of the absorber, respectively [10]. This differential equation has the following solution:

$$E(x) = E_0\exp\left(-x/X_0\right). \tag{2.7}$$

Thus, an electron crossing a thickness X_0 will lose on average $^1/_e$ of its energy.

2. Theory

Another important interaction process is the energy loss due to ionization. While the process of energy loss by Bremsstrahlung is almost proportional to energy, the loss due to ionization has only a logarithmically dependence on the energy. At some energy Bremsstrahlung becomes the dominant effect for energy loss and defines a critical energy E_c. There are two different approximations for this critical energy depending on the phase of the material. An overview of the different contributions to the mean energy loss of electrons and positrons can be seen in Figure 2.3.
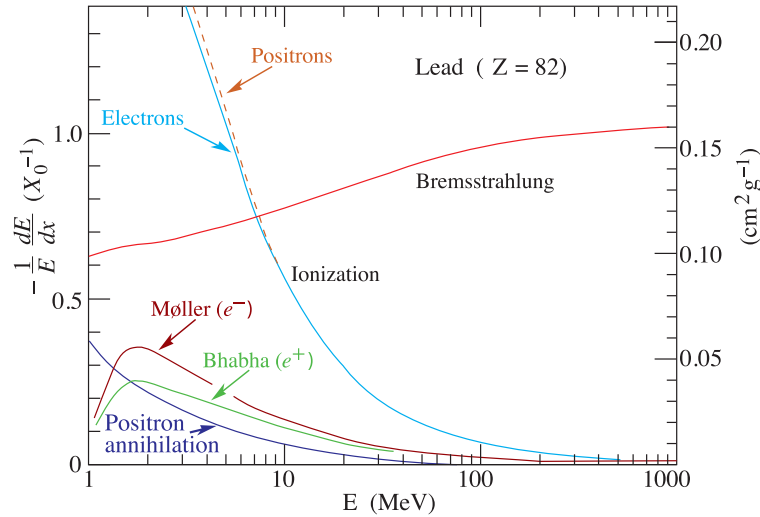
Figure 2.3.: Fractional energy loss per radiation length in lead as a function of electron or positron energy [10].

2.1.1.3. Photons

The interaction of photons with matter is different from the interaction of charged particles. Instead of inelastic collisions the following interactions of photons contribute most:

Photoelectric Effect Photon absorption by interaction with an electron in an atom.

Compton Scattering Photon scattering from an atomic electron, which recoils and carries off a fraction of the photon's energy.

Pair Production Creation of an electron position pair.

20

Depending on the energy of the incoming photon which contribution of the three effects is largest changes. For energies $E_\gamma < 100\,\text{keV}$ the predominant interaction is the absorption via the photoelectric effect. In the middle energy regime with $100\,\text{keV} < E_\gamma < 2\,\text{MeV}$ Compton scattering dominates. At energies above twice the rest mass of an electron $E_\gamma > 1.02\,\text{MeV}$ pair production becomes possible and is the dominant interaction for energies above $E_\gamma > 2\,\text{MeV}$. The absorption coefficient for a photon in lead is shown in Figure 2.4.
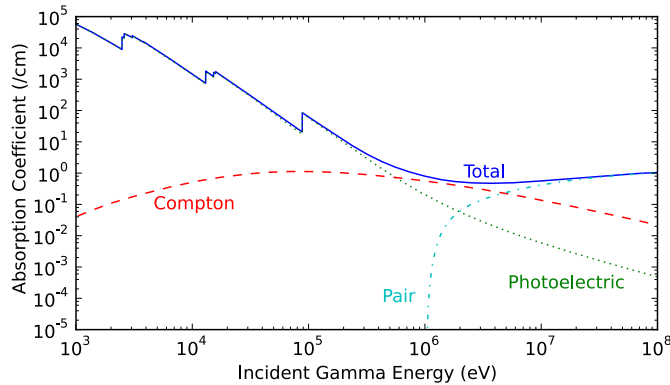
Figure 2.4.: Absorption coefficient for a photon in lead. In the low energy range the photoelectric effect is the main contribution, while at high energies pair production gets dominant. In the middle energy range Compton scattering is the most probable interaction [38].

2.1.1.4. Neutrons

In comparison to all other neutral hadrons, neutrons have a long life-time of $\tau_n = 880.3 \pm 1.1\,\text{s}$ [10], therefore neutrons can transverse particle detectors without decaying. Like photons, neutrons are uncharged particles. Thus they are not subject to electromagnetic interactions with the orbital electrons of the nuclei. Their main interaction is due to the strong force with the nuclei. Due to the short range of the strong force, the probability for interaction is very small.

Strong interactions with the atomic nuclei are described by several mechanisms, e.g. Elastic scattering with the nuclei or inelastic scattering [39]. The total cross section σ_{tot} is given by the sum of the cross section of each mechanism.

2.1.1.5. Landau Fluctuations

As the actual energy loss ΔE of a particle is a statistical process, large fluctuations in the energy loss for different particles can occur. In a material with a thickness Δx the actual energy loss ΔE is a sum of many small contributions δE_n. The number of contributions and their size can vary, resulting in large fluctuations. The first description of these fluctuations was given by Landau for thin layers of matter [40], resulting in an asymmetric probability density function, which is called Landau(-Vavilov) distribution. Further corrections were included later [41].

The Landau distribution for a thin absorber is shown in Figure 2.5. Due to its asymmetry, the most-probable energy loss of the distribution is lower than the mean energy loss. It is a skewed distribution with a long tail to high energy transfers. Measurements with solid-state detectors show that the most probable energy loss agrees rather well with the prediction of the theory, while the width of the distribution is broader than expected from a pure Landau distribution [42]. A convolution of the Landau distribution with a Gaussian distribution with a width σ can correct for this difference, it results in a broader distribution with a peak value slightly increased compared to a pure Landau distribution.

2.1.1.6. Multiple scattering

Charged particles traversing a medium are deflected by many small-angle scatter events due to Coulomb scattering from a nuclei. Due to the central limit theorem a Gaussian displacement distribution will be created [43, 44]. An approximation of the width of the
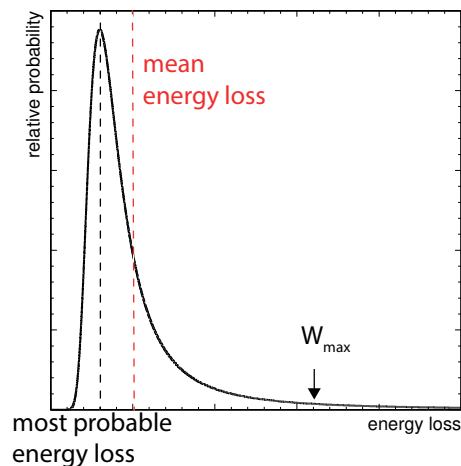

Figure 2.5.: Landau distribution for a thin absorber. The mean and the most probable energy loss do not agree with each other.

Gaussian distribution for a material with a thickness x/X_0,given in units of radiation lengths, can be calculated by [45]

$$\Theta_0 = \frac{13.6\,\text{MeV}}{\beta cp} Z \sqrt{x/X_0}\left[1 + 0.038\ln x/X_0\right] \tag{2.8}$$

where $p, \beta c$ and z are the momentum, velocity and charge number of the incident particle.

2.1.2. The Principle of Big Particle Physics Experiments

Big particle physics experiments, like the four big LHC experiments ATLAS, CMS, ALICE and LHCb, have usually onion like structures to measure the properties of long living charge particles ($e^{\pm}, \mu^{\pm}, \pi^{\pm}, k^{\pm}, p, \bar{p}$) and neutral particles, like photons and neutrons. By measuring the trajectories of the decay products of particles with short lifetimes lifetimes (like c, b, τ with lifetimes τ of a few 10^{-12} s) it is possible to identify and measure these particles. This requires precise measurement of the particle track in particular close to the IP. Weak interacting particles, like neutrinos, can be identified by a precise measurement of the missing transverse energy $\not{E}_T$.

One example for a full experiment in shown in Figure 2.6, the CMS experiment. Typical high energy particle physics experiments have strong magnets to bend charged particles. In the case of the CMS experiment a solenoid magnet with a magnetic field of 4 T is used. The inner most layer of such an experiment is the Tracker, nowadays usually consisting of a pixel vertex detector and a strip Tracker, precisely measuring the tracks of charged particles. The electromagnetic calorimeter is optimized for a precise measurement of the energy of particles primarily interacting via the electromagnetic interaction, like $e^{\pm}$ or γ, while the hadronic calorimeter is designed for measuring the energies of particles interacting by the strong force, i.e. hadrons. As high energetic muons are not absorbed when passing through the experiment, dedicated muon detectors are placed in the outer most region of the experiment. The muon detectors are a huge tracking system, in combination with the inner track they measure the track and the momentum of the muon.

Example tracks for muons, electrons, charged and neutral hadrons and photons are shown in Figure 2.6. The Tracker can reconstruct the track of high-energy muons, electrons and charged hadrons, while neutrons, neutrinos and most photons usually pass the detector without any interaction. Electrons and photons are stopped in the electromagnetic calorimeter, while charged and neutral hadrons are usually stopped in the hadronic calorimeter. This indicates that the different particles can be identified by the signatures they leave in the different detectors.

Key:
— Muon
— Electron
— Charged Hadron (e.g. Pion)
--- Neutral Hadron (e.g. Neutron)
···· Photon

Transverse slice through CMS

Silicon Tracker

Electromagnetic Calorimeter

Hadron Calorimeter

Superconducting Solenoid

Iron return yoke interspersed with Muon chambers
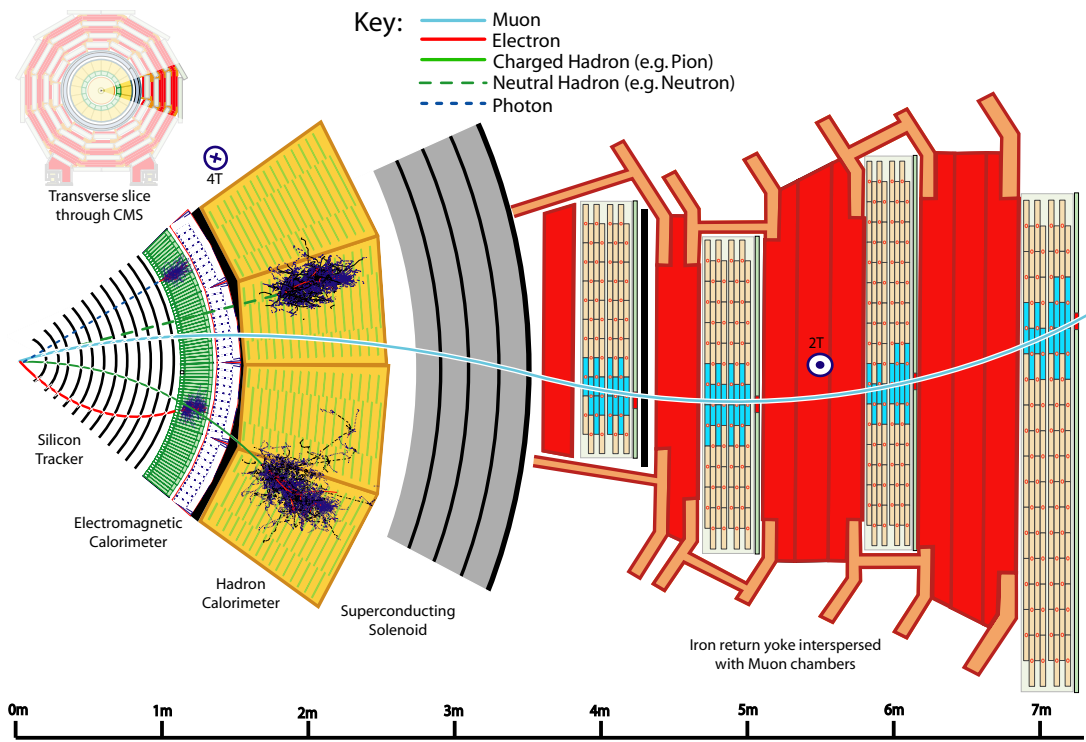
0m   1m   2m   3m   4m   5m   6m   7m

Figure 2.6.: Slice through the CMS detector [46]. The tracks of a muon, an electron, a charged hadron, a neutral hadron and a photon are shown. Neutral particles (neutral hadrons and photons) are only detected in the calorimeters, indicated with dashed lines.

2.1.2.1. Momentum measurement

An important property of each particle is its momentum. A particle with a charge q, mass m and a speed $\vec{v}$ is bent in a magnetic field $\vec{B}$ by the Lorentz force:

$$\vec{F} = \dot{\vec{p}} = q\left(\vec{v} \times \vec{B}\right) \quad \Longrightarrow \quad \dot{\vec{v}} = \frac{q}{\gamma m}\left(\vec{v} \times \vec{B}\right) . \tag{2.9}$$

By measuring the curvature of the track with several position-sensitive detectors, the momentum can be deduced. The momentum resolution depends on the length of the measured track L, the strength of the magnetic field B and the spatial resolution of each position-sensitive detector σ. For N ($N > 10$) equidistant measurements the momentum resolution can be described by the Gluckstern formula [10, 47]:

$$\left.\frac{\sigma(p_T)}{p_T}\right|_{meas} = \frac{\sigma(x) \cdot p_T}{0.3 \cdot BL^2} \cdot \sqrt{\frac{720}{(N+4)}} \propto p \cdot \frac{\sigma}{B \cdot L^2} \tag{2.10}$$

In addition, the multiple scattering, described in Section 2.1.1.6, degrades the resolution. This contribution can be described by [37]

$$\left.\frac{\sigma(p_T)}{p_T}\right|_{MS} = 0.045 \cdot \frac{1}{B\sqrt{LX_0}} \propto \frac{1}{B\sqrt{LX_0}} . \tag{2.11}$$

This term is only depending on the properties of the Tracker and is not momentum dependent. For the total momentum resolution an additional term depending of θ the angle of track with respect to the magnetic field needs to be added [48]. The transverse momentum can be expressed by

$$p_T = p \cdot \sin(\theta) , \tag{2.12}$$

and therefore

$$\left(\frac{\sigma_p}{p}\right)^2 = \left(\frac{\sigma_{p_T}}{p_T}\right)^2 + \left(\frac{\sigma_{\sin(\theta)}}{\sin(\theta)}\right)^2 \tag{2.13}$$

This results in a total uncertainty of

$$\left(\frac{\sigma(p)}{p}\right)^2 = A \cdot \left(\frac{p_t}{B \cdot L^2}\right)^2 + C \cdot \left(\frac{1}{B\sqrt{LX_0}}\right)^2 + D \cdot \left(\frac{\sigma_\theta}{\tan\theta}\right)^2 \tag{2.14}$$

One can see that for high energetic particles the momentum resolution is linear with the momentum of the particle. The nominal momentum resolution of the CMS experiment is typically $0.7\,\%$ ($5.0\,\%$) at $1\,\mathrm{GeV}/c$ ($1000\,\mathrm{GeV}/c$) in the central region and the impact parameter resolution for high-momentum tracks is typically $10\,\mathrm{\mu m}$ [49].

2.1.2.2. Vertexing/Tracker

In order to precisely measure the momentum and to identify short-live particles by their decay products it is important to precisely measure the trajectories of the particles. This implies the first measurement point be as close as possible to the IP. As multiple scattering reduces the precision of the measurement it is also necessary to reduce the material of the detector as much as possible.

Trackers consist of multiple layers of tracking detectors for a precise reconstruction. Most Trackers are split into a pixel detector and a (silicon) strip Tracker due to the high particle fluxes in environments, such as the one at LHC, and the $1/r^2$ dependency of the particle flux on the distance r. With its high hit density and its high collision frequency the LHC environment also causes high radiation doses. As described later in Section 2.2.3 the sensors get damaged by this radiation dose and the electrical currents through the sensors increase. In order to be capable to operate the silicon detectors after radiation damage, it is necessary to cool the detector systems, as lower temperatures decrease the leakage currents.

Pixel detector   The pixel detector system is the detector closest to the IP, which requires a high granularity as the particle fluxes are the highest. Strip detectors would not work at these particle fluxes as the hit multiplicity results in an ambiguous track reconstruction. By using pixelated detectors this problem is solved on cost of a higher number of readout channels. The pixel detector is subdivided into the barrel pixel and the forward pixel sections, each consisting of several layers of pixel detectors. A sketch of the current CMS pixel detector system is shown in Figure 2.7. The three layers of barrel pixel detectors are placed around the beam pipe (colored in blue) and two forward pixel discs of pixel detectors are placed on each side of the barrel (orange). A comparison of the ATLAS, the CMS and the planned upgraded CMS pixel detector is shown in Table 2.1. The installation of the upgraded CMS pixel detector is scheduled in the winter shutdown 2016/2017 of the LHC. The active area of the CMS pixel detector will increase from approximately $1.06\,\text{m}^2$ [50] to $1.94\,\text{m}^2$ [51].

Strip Tracker   Taking into account the decrease of density of traversing particles with increasing radius, the active area of each readout channel can be adjusted for different radial positions to keep the occupancy below a certain level. With increasing radius it is possible to switch from pixel detectors to strip detectors. Strip detectors have less readout channels and their technology is simpler than of pixel detectors, such that the cost to cover a given area is significantly lower for strip detectors than for pixel detectors. Therefore it is possible to built bigger detectors with larger active area. The CMS strip Tracker, for example, consists of ten layers of silicon strip detectors with a total active area of $\sim\!210\,\text{m}^2$ and $9.8\,\text{M}$ readout channels.

	ATLAS	CMS	CMS upgrade
number of barrel layers	3+1	3	4
number of end disks	2×3	2×2	2×3
number of channels	$80\,\text{M} + 12\,\text{M}$	$66\,\text{M}$	$124\,\text{M}$
pixel size [µm $\times$ µm]	$50 \times 400,\ 50 \times 250$	100×150	100×150
Barrel radii [cm	3.27, 8.9, 12.3	4.4, 7.3, 10.2	3.0, 6.8, 10.9, 16.0
in-time threshold [e]	3700	3500	<2000
pixel charge readout	ToT	analog	digitized(8 bit)
cooling	C_3F_8, CO_2	C_6F_{14}	CO_2

Table 2.1.: Comparison of the ATLAS (including Insertable B-Layer (IBL)), the CMS and the planned upgraded CMS pixel detector [52–56]. The charge in the ATLAS pixel detector is measured using a Time-over-Threshold (ToT) technique.
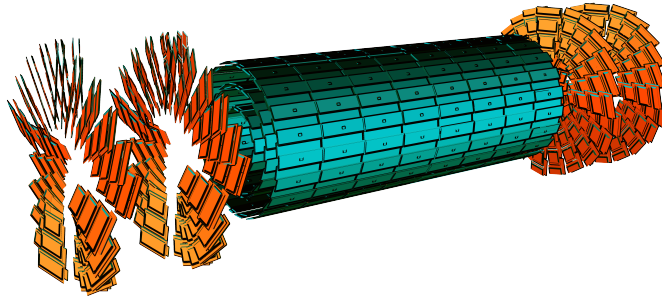
Figure 2.7.: The current CMS pixel detector [57]. The three layers of barrel pixel detector are highlighted in blue, while the two forward pixel discs on each side of the barrel are highlighted in orange.

2.1.2.3. Energy measurement

The energy of particles is measured by the energy loss of the particle in the detector. As described in 2.1.1 the interaction of heavy charged particles is different than for electrons. In order to take into account of these differences the calorimeter system is split into an electromagnetic calorimeter and a hadronic calorimeter. The energy of the particle is transfered to new, lower energetic particles, initiating a particle cascade (particle shower). Important parameters for a calorimeter are the linearity of the energy measurement, the uniformity for different particles and the precision (resolution) of the energy measurement. The resolution of the energy measurement is usually described by a stochastic and a constant term [58]:

$$\frac{\Delta E}{E} = c_1/\sqrt{E} + c_2 \,, \tag{2.15}$$

where c_1 and c_2 are constants depending on the specific calorimeter.

Electromagnetic calorimeter Particle showers created by electrons, positrons or photons are called electromagnetic showers (as only electromagnetic interactions are involved). The basic processes for shower creation are Bremsstrahlung and pair production. In a simplified model a cascade of electron-positron pairs and photons is created. While the energy of the particle is $E > E_c$ the particles do not lose any energy by ionization and excitation. If the energy is below the critical energy $E < E_c$ the particles lose their energy only by ionization and excitation. The number of particles in the shower increases until a critical energy E_c is reached. Particles with an energy $E < E_c$ loss their energy by ionization and excitations and stop within the calorimeter. The shower development is governed by the radiation length X_0. After a distance X_0 an electron remains with an $1/e$ of its primary energy and in average a photon produces an e^+/e^- pair every $9/7X_0$. By measuring the location of the shower maximum and the longitudinal/transversal shower distribution it is possible to precisely measure the energy of the particle.

There are two main types of electromagnetic calorimeters: sampling calorimeters and homogeneous calorimeters. In homogeneous calorimeters the detector material serves as the absorber and as the active detection medium. It could be made out of on high-density scintillation materials (BGO,CeF$_3$,...), based on Cherenkov light (lead glass,...) or on ionization signals (liquid nobel gases). Such a calorimeter provides a very good energy resolution due to its homogeneity, but this kind of calorimeters are usually expensive. In a sampling calorimeter layers of absorber material and active detection material are combined in a sandwich like structure. A high density material like iron or lead are used as an absorber. The active material could be based on any detection technique like scintillators, silicon detectors or gas detectors. Since the absorber material can be freely chosen sampling calorimeters can be built very compactly and thus are usually

cheaper than a homogeneous calorimeters. As only a part of the energy is deposited in the actual active layers sampling calorimeters usually have a poorer energy resolution than homogeneous calorimeters.

Hadronic calorimeter The energy loss of hadrons is more complex than the energy loss of electrons as it also involves the strong interactions. In collisions with the atomic nuclei secondary particles are produced. Nuclear reactions form hadronic cascades and particles with an electromagnetic decay, like π or η, initiate electromagnetic showers. In addition a part of the energy is absorbed by nuclear binding and recoil. This results in energy losses which are not usually detected by the calorimeter. Therefore hadronic showers are more complex than electromagnetic showers and simulations (Monte Carlo (MC)) are needed to understand the process. As the hadronic interaction length is larger than the electromagnetic radiation length, the calorimeter needs to be bigger to fully stop the hadron inside the calorimeter. Therefore hadronic calorimeters are larger and more massive than electromagnetic calorimeters. As these hadronic showers contain invisible components, the use of homogeneous calorimeters in unnecessary and thus hadronic calorimeters are usually realized as sampling calorimeters. As hadrons also interact with the electromagnetic calorimeter, it is necessary to combine the measurements of both calorimeters to get a good measurement of the hadron energy.

2.1.2.4. Muon system

Because muons interacts very little with matter, they travel through several meters of dense material before they stop. Therefore, muon chambers, tracking devices specialized for detecting muons, are usually placed in the outer most regions of the experiment. By tracking its hit position through the multiple layers of muon chambers and combining these measurements with the position measurements performed with the Tracker, a precise reconstruction of the particle track can be achieved. The momentum of the muon can be measured with this particle track. Due the position of the muon chambers, muons are likely the only particles which create a signal in these detectors. Therefore signals in the muon system can be precisely identified as caused by muons.

2.1.2.5. Beam Condition Monitors and Luminosity Measurements

Beam Condition Monitor (BCM) systems are built to monitor background levels and issue beam-abort requests when beam losses start to risk damaging the inner detectors. These systems are usually placed close around the beam pipe on each side of the IP. In these regions usually no cooling infrastructure is provided, as putting a cooling infrastructure in this region would add a lot of extra material close to the IP that can get activated and produce showers. High particle fluxes are expected in these forward regions and

therefore radiation hard detectors are needed. At the positions of the BCM systems of ATLAS and CMS radiation levels reaching 10^{16} p/cm^2 during their time of operation are expected, which cannot be withstood by conventional silicon sensors. As presented already in Section 1.3 all LHC experiments therefore use BCM systems using diamond sensors.

There are mainly two different implementations of BCM systems. On the one hand there are systems using fast electronics which distinguish beam collisions from beam halo. This implementation is used in the ATLAS BCM and in the BCM1F of CMS. A second method is a simplified readout using integrated signal response in the detector and calculating the mean particle flux during the integration time. This technique is used by the ATLAS BLM and the CMS BCM1L/BCM2L.

As the luminosity is one of the most important parameters, it is important to precisely measure the luminosity. Since the number of particles produced by the collisions is proportional to the luminosity, one approach for luminosity measurement is the counting of such particles. To reach a precise measurement it is required to distinguish particles from the IP from non-collision beam background and beam halo. The BCM systems using fast electronics can be used for such a measurement and the concept is illustrated in Figure 2.8.

If the measured particles are produced at the IP, they reach the BCM detectors simultaneously. Particles due to beam losses or beam halo transverse the experiment parallel to the beam without interaction. This results in a time difference between both detectors of $\tau = \frac{2 \cdot l}{c}$, where l is the distance of the detectors to the IP and c is the speed of light. With an optimized distance of $l \sim 1.88$ m the time difference is approximately 12.5 ns for relativistic particles. This corresponds to half a LHC clock cycle and therefore in-time coincidences can be easily distinguish from out-of-time coincidences. By measuring both rates the BCM system can provide collision and loss rates in parallel. These measurements can then be used to estimate the luminosity. These systems are therefore used
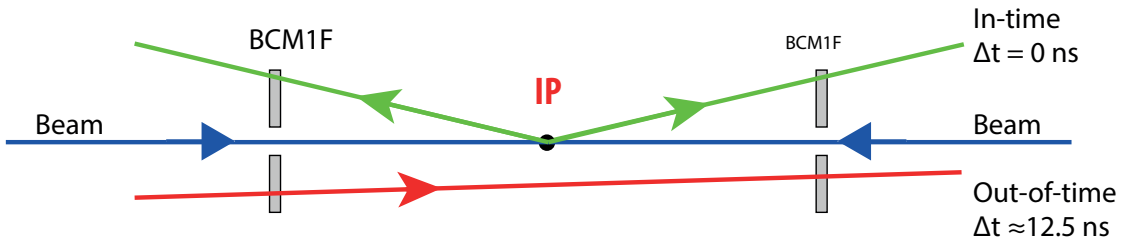
Figure 2.8.: Illustration of the BCM concept [59, edited]. Particles from beam halo (red) create coincidences with a time difference of 12.5 ns, while particles (green) from the interaction point reaches the detector at the same time.

for online luminosity measurements. Direct feedback is provided from these BCM systems to LHC operations to optimize the beam overlap and to optimize the collision rate. With the bunch-by-bunch measurements it is also possible to compute the emittance of the beam [60].

The concept of measuring the in-time and out-of-time coincidence only works as long as the particle densities in the detectors are small. To further improve the luminosity measurement ATLAS and CMS have recently installed new detectors dedicated for luminosity measurements, which are also counting particles coming from the IP. In order to distinguish particle tracks coming from the IP from particle tracks coming from beam halo or other sources, particle tracking telescopes with pixelated sensors were used. In both detectors, the CMS PLT and the ATLAS DBM, each telescope consists of three layers of pixel detectors. The principle of these telescopes is sketched in Figure 2.9. By separating horizontal tracks caused by non-collision backgrounds from those pointing to the IP the luminosity, the non-collision beam and cavern backgrounds can be estimated. In both systems coincidence rates, requiring a hit in all three sensors, are used for the estimation of the luminosity. The full pixel hit information is read out at a lower rate and is used to measure systematic effects and to measure the position of the beamspot.
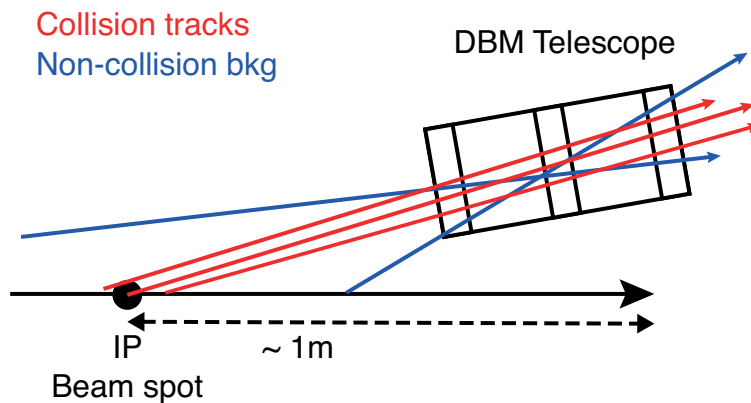
Figure 2.9.: Principle of track discrimination between tracks originating from the IP or other [61, edited].

2.2. Principle of Operation of Solid-State Particle Detectors

Solid state particle detectors are essentially ionization chambers that use solids as the sensor material. The energy absorbed from a incident charge particle (or the photon) creates free charge carriers (electron and hole pairs) in the sensor volume. These charge carriers drift towards the electrodes due to an applied electric field, inducing an electrical current on the readout electrodes, which are connected to an external amplification circuit. The pulse of the electrical signal is then shaped with a pulse shaping circuit and usually digitized with an Analog to Digital Converter (ADC). This basic principle of a solid-state detector is shown in Figure 2.10.
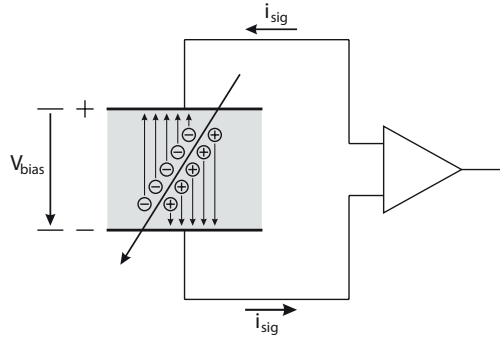
Figure 2.10.: Principle of a semiconductor detector [62]. Due to an electric field the free charge carries drift towards the electrodes inducing an electric current in the amplifier circuit.

2.2.1. The Sensor Material

The incident particle deposits a certain amount of energy E in the sensor material, as described in Section 2.1.1.1. From this energy loss only the part ε due to ionizing energy loss $E_I = \varepsilon \cdot E$ can be converted into an electrical signal Q_S.

$$Q_S = \frac{\varepsilon \cdot E}{E_I} e \qquad (2.16)$$

where E is the deposited energy of the incident particle and E_I is the ionization energy which is required to form a charge pair. In solid state detectors the ionization energy E_I is proportional to the band gap of the sensor material. This means that higher band gap materials produces less signal charge [62]. Since the signal charge Q_S is proportional to the deposited energy E the signal increase with the thickness of the sensor material for charged particles. The detection of photons requires thick sensor materials in order to reach high probabilities for an interaction in the sensor.

The charge carriers created are free to move through the sensor material. By applying an electric field the charge carriers are accelerated towards the electrodes. While moving through the medium they scatter off atoms of the medium. This results in a constant drift velocity depending on the applied electric field. The carrier velocity is given by

$$v(E) = \frac{\mu_x \cdot \vec{E}(x)}{1 + \frac{\mu_x \cdot E(x)}{v_{S_x}}} \,, \tag{2.17}$$

where μ_x is the electron or hole mobility of the semiconductor and v_{S_x} are the saturation velocities [63]. Due to scattering the mobility at large electric fields is proportional with $1/E$ causing the speed to saturate. In order to reach fast and efficient charge collection, the applied electric fields have to be large enough to get velocity saturation.

As the expected signal currents are only of the order of micro amperes, a good noise performance is needed. An important contribution to the noise of the detector is the leakage current in the sensor. Therefore the leakage current should be small compared to the signal current. In combination with the high electric field this requires sensor materials with a high resistivity. As the resistivity depends exponentially on the band gap, materials with high band gaps have lower leakage current, but simultaneously smaller signal charges. Diamond is an excellent insulator, such that the leakage currents are very small, but due to its ionization energy E_I of about $13\,\text{eV}$ the signals are small. The ionization energy of pure silicon is only $3.6\,\text{eV}$. With its resistivity of $\sim 10^4\,\Omega\,\text{cm}$, the leakage currents are too high to use pure silicon as a sensor material.

Doping   By intentionally introducing a dilute concentration of impurities the electrical properties of a semiconductor can be modified. This process is called *doping*. In a material with an atomic number Z a *n-type* doping uses a material with an atomic number of $Z + 1$. This creates an extra energy level (the donor level) close to the conduction band. The electrons can be thermally excited to the conduction band and are available as free charge carriers. If the doping material has an atomic number of $Z - 1$ an additional hole energy level (the acceptor level) just above the valence band is created. Electrons of adjacent atoms can be excited to "fill" the hole left by this atom. Thus the unfilled hole can move within the material and acts like a positive carrier. Combining a *p-type* and a *n-type* forms a *pn-junction*. Due to the gradients of the electron and hole density, charge carries migrate by diffusion creating charge buildup at the interface. This charge buildup causes an electric field directed against the diffusion direction. In the equilibrium of thermal diffusion with the created electric field a depleted region and a potential difference between the p- and n-sides, the "built-in" potential V_{bi}, are created. This effect is shown in Figure 2.11. When applying a reverse bias to the *pn-junction* the depletion region can be artificially increased to the width w_d [62]:

$$w_d = \sqrt{2\varepsilon \frac{(V_{bi} + V_b)}{e} \left(\frac{1}{n_A} + \frac{1}{n_D} \right)} \tag{2.18}$$
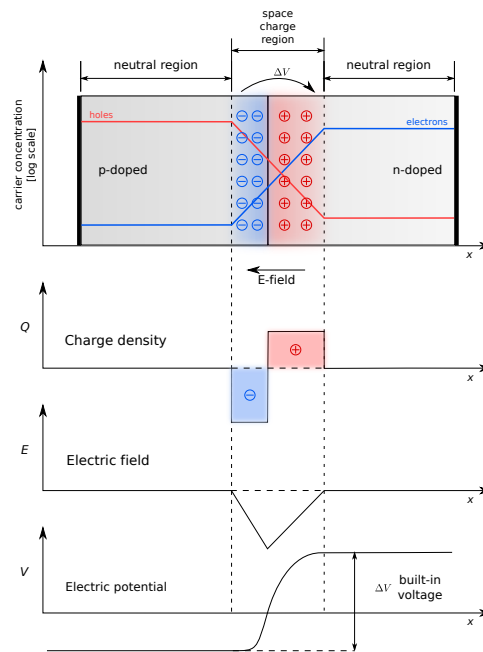
Figure 2.11.: A p-n junction in thermal equilibrium with zero-bias voltage applied [64]. Under the junction, plots for the charge density, the electric field, and the voltage are reported.

where n_A and n_D are the doping concentrations of the donor and the acceptor doping. A detector in which the depletion region w_d is as big as the detector thickness d is called *fully depleted*.

As high-quality single crystals of silicon can be grown economically and the process of doping is well understood, most solid state detectors are based on silicon sensors. However, due to the large displacement energy (Section 2.3) and the low leakage current, diamond is a very promising alternative.

2.2.2. The Readout Electronics

The readout electronics are a very important component in a detector system. In the first step the electrical signal from the sensor is acquired, followed by the signal shaping to optimize the response of the system. In the last step the signal must be digitized and stored for further analysis. The performance of a detector system strongly depends on the noise performance of the system. In order to reach high efficiencies a clear separation of the signal from the noise is required. This separation is usually expressed by the Signal-to-Noise Ratio (SNR) and is defined by the Most Probable (MP) signal S_{MP} for a MIP and the width of the measured noise distribution σ_{noise} .

$$\text{SNR} = \frac{S_{MP}}{\sigma_{noise}} \tag{2.19}$$

For nearly all particle detector applications the measurement of the charge amplitude, the hit detection time and the hit position are of importance. Further properties, like radiation hardness, power consumption, robustness and cost, usually have to be included for setup optimization. A typical detector front-end circuit is shown in Figure 2.12. A bias circuit including a bias resistor R_b and a stabilizing capacitance C_b ensures the biasing of the sensor, which is represented by the capacitance C_d. Due to the leakage currents of the sensor most amplifiers use AC coupling to decouple the sensor from amplifier and therefore reduce power consumption, heat and noise. This charge coupling is done with a capacitance C_c. The signal is amplified in a preamplifier with a given gain, before the signal is shaped by the pulse shaper. In the pulse shaper the signal response to different frequencies are chosen to optimize the SNR. In this optimization the required shaping times have to be taken into account to accommodate the signal rates.
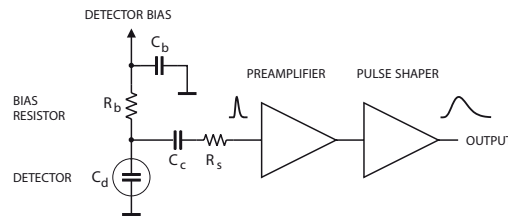
Figure 2.12.: Typical detector front-end circuit for a solid-state particle detector [62].

The limits on detection efficiency and energy resolution are introduced by the interaction of the sensor and the electronics. The sensor can be viewed as a feedback loop of the electronics. The gain of the amplification circuit can be controlled very precisely, but the electronic noise which is superimposed on the signal can alter the signal amplitude. Typical noise is randomly distributed in time and amplitude. The noise performance is usually described by the Equivalent Noise Charge (ENC). The Equivalent Noise Charge (ENC) is the number of electrons one would have to collect in the sensor in order to create a signal equivalent to the noise of the system. Four of the most important noise contributions are

1. the leakage current in the sensor

2. the detector capacitance

3. thermal noise within the bias circuit (parallel resistor)

4. thermal noise due to the resistance of the connection between sensor and amplifier input (series resistor)

The leakage current of the semiconductor detector is caused by thermally generated electron holes pairs within the depletion region. These charges are separated by the electric field and generate the leakage current. The fluctuations of this current are a source of noise and are one component of the "shot noise" (also called *Poisson noise*). In order to minimize this noise contribution, the detector should have small leakage current and/or the integration time needs to be minimized.

In a charge sensitive amplifier the noise of the system depends linearly on the detector capacity C_d. This contribution can be written as

$$\text{ENC}_{C_d} = a + b \cdot C_d \,, \tag{2.20}$$

with the two amplifier parameters a and b. For detectors in which a and b are comparable in size, the noise can be strongly reduced by decreasing the detector capacity. This can be achieved by using a material with a higher dielectric constant or by limiting the area of the connected sensor channel.

Any resistors in the circuit exhibit noise due to thermal velocity fluctuations of the charge carriers, this results in two noise contributions, one due to series and one due to parallel resistors. The component due to the parallel bias resistor can be decreased by increasing the bias resistor. The component due to series resistors can be decreased by reducing the resistance of the connections. Therefore all connections need to be as short as possible.

While shot noise and thermal noise have a "white" frequency distribution, which means they have a constant power spectral density, the trapping and de-trapping process in resistors introduces a $1/f$ spectral noise distribution. All noise contributions are assumed
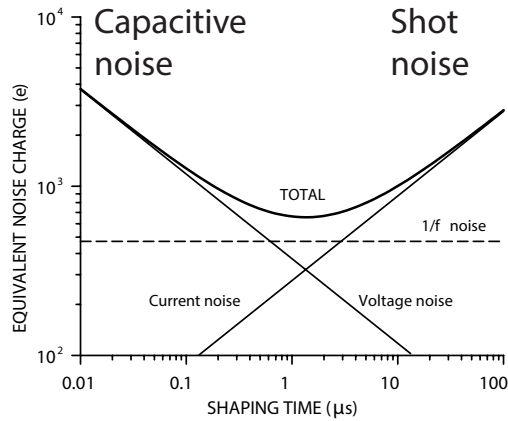
Figure 2.13.: Equivalent Noise Charge (ENC) vs. shaping time of a typical detector system [62, edited]. For small shaping times the noise due to the detector capacity is the dominant component.

to be random and uncorrelated, such that they add in quadrature. The total noise of a system at the output of the pulse shaper is given by integrating over the whole frequency spectrum of the detector system. In Figure 2.13 the ENC as a function of the shaping time is shown. For each detector system the ENC can be optimized by changing the shaping time. It can be observed that at the required shaping times in LHC experiments the detector capacity is usually the dominant component in the noise performance of a typical detector system.

2.2.3. Radiation Damage

The detection of particles requires the interaction of the particle with the detector material. The ionizing energy loss of the particle by interaction with the electrons of the detector material is used for particle detection and usually does not affect the structure of the material. However the interactions with the nuclei may cause permanent changes (defects) in the detector material. Both, the sensor material and the readout electronics, can be damaged due to the incident radiation. One can distinguish between two types of radiation damage.

Damage inside the detector bulk material is called *bulk damage*. Atoms in the material are dislocated from their original position in the lattice. This damage is primarily caused by massive particles and is usually described with the theory of Non Ionizing Energy Loss (NIEL).

The second damage is introduced in the surface layers and is called *surface damage*. Ionizing radiations in oxides create charge carriers which can be trapped for long times. This surface damage can affect the detector capacity, the internal electric field, the breakdown behavior and other structures of the material. As readout electronics use transistors and other surface structures the surface damage is the only relevant contribution for damage

in silicon based readout electronics. It is usually quantified by the Total Ionizing Dose (TID).

The focus in this thesis is the radiation damage in diamond as a sensor material, and therefore the bulk damage is explained in greater detail in the following sections.

2.2.3.1. Bulk damage

A traversing particles can introduce defects in the semiconductor lattice via interactions with the atomic bodies. A displaced atom produces an empty space in the lattice (Vacancy) and in another place an atom in an inter lattice space (Interstitial). If the strong force is responsible for the interaction, atoms might transform into another type. This atoms then act as a dopant. Figure 2.14 shows examples for these defects and in addition more complex damaging structures. The type and the rate of such defects depend on the energy and the type of the penetrating particle. Defects create additional energy levels which can modify the properties of the material. A change of the effective doping concentration changes the depletion voltage of the sensor. Additional deep energy levels can increase the probability of trapping of charge carriers and reduce the signal response of the detector. Energy levels in the middle of the band gap may increase the probability to thermally excite electrons or holes in the conduction band. This result in an increase of the leakage current. All these mechanisms result in a decrease of the Signal-to-Noise Ratio (SNR) with radiation.

Damage through displacement depends on energy and momentum transfer to the lattice atoms. Several experiments showed that the damage in the bulk is proportional to the
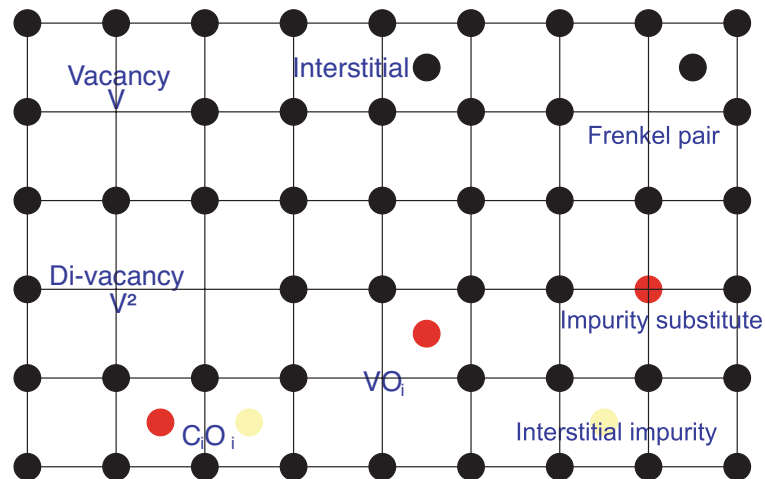
Figure 2.14.: Different kinds of atomic displacement due to interaction with a traversing particle [65]. These displacements create new levels in the energetic scheme of the semiconductor.

displacement damage cross section D. Based on these measurements the "NIEL-scaling hypothesis" was developed which assumes that the radiation damage is linear proportional to the Non Ionizing Energy Loss (NIEL) of the penetrating particles (radiation) and this energy loss is again linear proportional to the energy used to dislocate lattice atoms (displacement energy). With this hypothesis it is possible to calculate or simulate the damage function for any particle as a function of the energy. Examples for the NIEL in diamond and silicon for different particle species and energies are shown in Figure 2.15. While the damage cross section is usually given in units of [MeV mb], NIEL is quantified in units of [keV cm^2/g]. With this hypothesis it is possible to scale the damage of any particle with an energy E to the equivalent damage of neutrons with an energy of $E = 1\,\text{MeV}$. The damage is than described by the hardness factor $\kappa = \frac{D(E)}{D(1\,\text{MeV}\,n)}$ and radiation levels are expressed by the 1 MeV neutron equivalent fluence $\Phi_{eq} = \kappa \cdot \Phi$. Instead of stating explicitly the scaling to 1 MeV neutrons, usually the unit [n$_{eq}$/cm^2] is used. To describe the damage the mass and the energy of the particle needs to be known. Usually a damage constant is specified for a specific particle and energy.

2.2.3.2. Leakage current

The leakage current induced by irradiation increases linearly with fluence [67]:

$$\frac{\Delta I_{leak}}{V} = \alpha \cdot \Phi_{eq} \tag{2.21}$$

α is a current related damage rate and V is the sensitive sensor volume V. In Figure 2.16 the leakage current for different silicon sensors as a function of the 1 MeV neutron equivalent fluence is shown. This increasing leakage current strongly decreases the SNR and
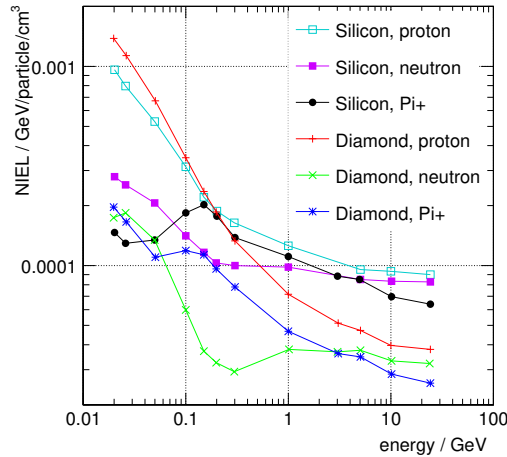
Figure 2.15.: NIEL simulations for diamond (red, green, blue data) and silicon (cyan, magenta, black data) exposed to protons, neutrons, and pions [66, edited].
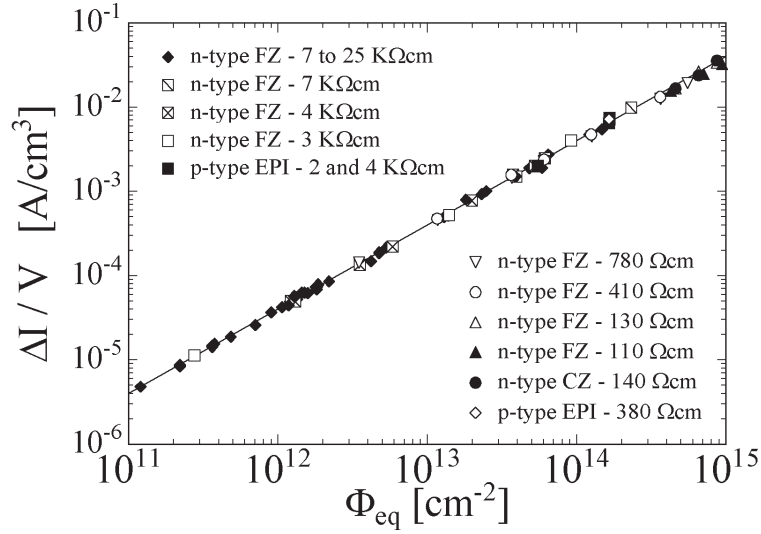
Figure 2.16.: Leakage current of different types of silicon as a function of fluence [67].

an irradiated silicon detector could not be operated at room temperature already after small amounts of radiation. The leakage current is strongly temperature dependent [62] and is given by

$$I \propto T^2 \, e^{-\frac{E_g}{2k_B T}} \, , \tag{2.22}$$

where T is the operating temperature, E_g the band gap and k_B the Boltzmann constant. For this reason silicon detectors need to be operated below room temperature after irradiation. By reducing the temperature to $-10\,°\mathrm{C}$ the leakage current can be reduced by a factor 15.

2.2.3.3. Annealing

The position of defects is not fixed in the lattice, but defects are mobile depending on the temperature. Therefore it can occur that different defects recombine (called beneficial annealing) or form immovable, stable (secondary) defects in the lattice (reverse annealing). The beneficial annealing results in a reduction of the leakage current, but after some time the effect inverts, secondary defects develop and worsen the radiation damage with time. Due to the two different time constants and their dependence on temperature, it is important to find a compromise to benefit from annealing. In order to not suffer from inverse annealing, irradiated detectors remain cooled down even in periods of non-operation.

2.2.3.4. Trapping Probability of Charge Carriers in Irradiated Sensors

With increasing radiation levels the trapping of the drifting charge carries becomes a limiting factor for the radiation hardness of a sensor. For silicon detectors this effect becomes important during the operation of HL-LHC. The probability for trapping can be described by the Mean Free Path (MFP) $\lambda_{e/h}$ for electrons and holes in the sensor material. The MFP depends on the velocity $v_{e/h}$ of the charge carriers and their life time $\tau_{e/h}$. To describe the damage due to radiation a simplified model is used, which assumes that the number of defects in the material is proportional to the neutron equivalent fluence Φ:

$$N_{Defects} = N_{0,Defects} + k \cdot \Phi \tag{2.23}$$

where k is a constant describing the generated number of defects per particle. Since the $N_{Defects}$ and the charge carrier life time $\tau_{e/h}$ are inversely proportional, the MFP as a function of fluence can be described by

$$\frac{1}{\lambda_{e/h}} = \frac{1}{\lambda_{0,e/h}} + k_{mfp,e/h} \cdot \Phi_{eq} \tag{2.24}$$

with $k_{mfp,e/h}$ the damage constant and $\lambda_{0,e/h}$ the MFP before radiation [68].

2.2.4. Detector Geometries

With the segmentation of the electrodes of the sensor material it is possible to build position-sensitive particle detectors. This requires the individual readout of each electrode in order to extract the position of crossing particle. A particle crossing the detector with an angle deposits its charge on several electrodes. With an evaluation of the charge ratios in adjacent electrodes the resolution of this track can be improved. Figure 2.17 shows the main principle of a segmented detector.
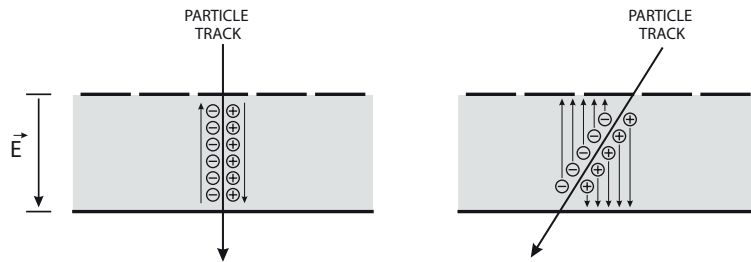
Figure 2.17.: Segmented particle detector providing position information. Angled particle tracks can deposit charge in several electrodes [62].

2.2.4.1. Pad Geometry

The pad geometry, or detector diode, is the most simple geometry. Single pads on top and bottom of the surface are the electrodes of the detector. The detector is read out with one single channel. For a better isolation of the diode from the edges of the sensor material guard rings are often placed around the pad electrodes. Figure 2.18 shows a typical silicon pad detector with a guard ring around. The setup is similar to a parallel
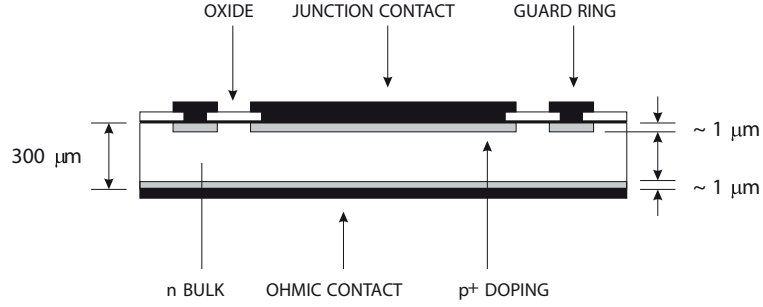
Figure 2.18.: A typical silicon pad detector [62]. An oxide layer layers (SiO_2) protects the silicon surface. A guard ring isolates the diode from the edges of the chip.

plate capacitor, which makes it easy to calculate the electric field E and the capacitance C:

$$E = \frac{V}{d}, \qquad C = \varepsilon \frac{A}{d} \tag{2.25}$$

where V is the applied bias voltage, d the thickness and A the area. With a pad detector only the particle crossing time through the sensor and the deposited energy can be measured, no additional position information can be extracted.

2.2.4.2. Strip Geometry

The segmenting of one electrode into several strips provides a measurement of a one dimensional position. A two-dimensional position can be extracted by subdividing the second electrode into strips, which are orthogonal to the ones from the first electrode, these detectors are called Double Sided Strip Detectors (DSSDs). A single sided and a double sided strip detector are sketched in Figure 2.19. Even though the electrodes are segmented, strip detectors remain almost as efficient as pad detectors as only the electric field close to the surface is changed. The position resolution σ_P of such a detector is mainly determined by the strip pitch p. The "digital" resolution of such a detector is given by $\sigma_P = p/\sqrt{12}$ [62]. This position resolution can be improved due to transverse diffusion of the charge carriers. By evaluating the charge distribution of several adjacent
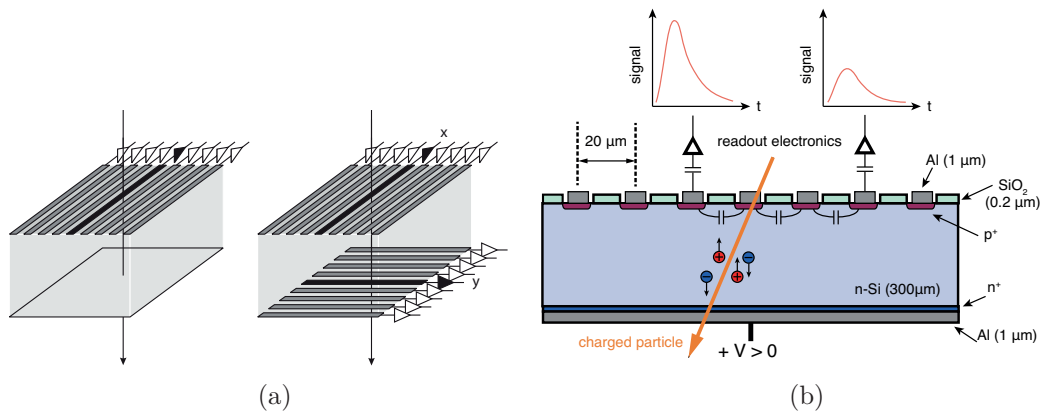
Figure 2.19.: Figure (a): Sketch of a single sided and a double sided strip detector [62]. Figure   (b): Principle of a silicon strip detector with two intermediate strip [69, edited]

strips the position resolution can be reduced below the digital resolution. The effect of charge interpolation can be even further improved by introducing intermediate strips that are not connected to separate readout channels. The signal current induced on the intermediate electrodes is transfered to the readout strip by capacitive coupling. For high SNR it is possible to benefit from the intermediate strips and the resolution can be improved without adding additional readout channels.

The principle of DSSD is capable to measure the two dimensional position of a particle track. However this method reaches its limit if the hit density becomes to high. If more than one particle hit the strip detector the measured position is no longer unambiguous. In Figure 2.20 (a) an example for two particles traversing the detector is shown. In addition to the two true hit positions two "ghost" hits appear. Due to such ghosts hits the reconstruction of particle hits becomes more complicated. The probability for ghost
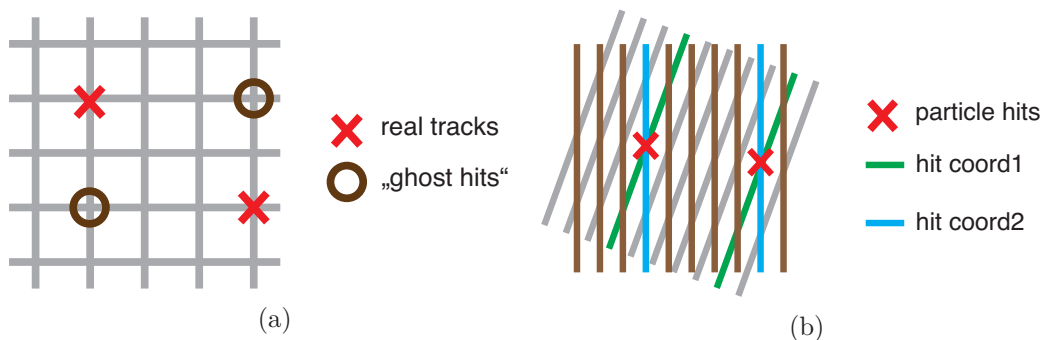
Figure 2.20.: Ghost hits in double sided strip sensor result in ambiguities in the hit position. By using a stereo angle smaller than 90 deg, the probability for ghost hits can be reduced on an expense of resolution in coordinate.

hits can be reduced on an expense of resolution in the second coordinate by using stereo angles smaller than 90 deg. Such a configuration is sketched in Figure 2.20 (b).

2.2.4.3. Pixel Geometry

In order to be capable to measure accurate, unambiguous two dimensional position information with a small amount of material at high particle fluxes, the pixel geometry is used. In pixel detectors the electrode is segmented in two dimensions as a chess board. Each single pixel has its own amplifier and read out circuit, resulting in a fine granularity. Pixel sizes of 30 µm to 100 µm are practically possible today, depending on the complexity of readout electronics. Special Application Specific Integrated Circuit (ASIC) readout chips must be developed, which contain the amplifier circuits as well as the readout control and bias circuits.

Two different pixel detector technologies are used. In Hybrid Active Pixel Sensors (HAPS) the pixelated sensor is directly bump-bonded (also called "flip-chip-bonded") to a readout ASIC. In the Monolithic Active Pixel Sensors (MAPS) design the amplifier electronics of each pixel are integrated in the sensor material.

In the two big LHC experiments ATLAS and CMS the HAPS technology is used. The amplifier and the readout electronics for each pixel are part of the readout ASIC, often called ROC. The pixel size is limited by the size of the readout electronics needed for each pixel. Several processes for flip-chip-bonding exist. Different bump materials, like indium, lead tin in combination with a Under Bump Metallization (UBM), like Au, Ti, Ni, are used. The process of flip-chip-bonding is shown in Figure 2.21. After putting the bump material a reflow process (heating up the bump bonds in a controlled environment) is used to form the bumps due to surface tension. In the last step ROC and sensor are flip-chipped by aligning and pressing them together. To ensure the connection of each readout cell often another reflow step is performed.

Typical pixel sizes in HAPS detectors are 50 µm to 100 µm in each direction. By using small pixel sizes low detector capacitance and low leakage current per pixel can be reached. This decreases the noise and therefore improves the SNR of each channel. The current ROCs of CMS and ATLAS reaches noise levels below 200 e [53]. The large number of readout channels results in large data volumes. In order to reduce the data volumes of the pixel detectors usually a zero-suppressed readout is used. Only signals above a certain threshold are readout. In order to reach similar efficiencies within the full detector, each pixel threshold needs to be tuned. The thresholds which can be reached for the current pixel ROCs are usually between 1000 e and 4000 e. As every readout channel needs its own amplifier, a pixel detector has a large power consumption per area which complicates the cooling. As the bump bonding is a complicated and expensive technology, the costs of a hybrid pixel detectors per active area is much higher than for a strip detector.
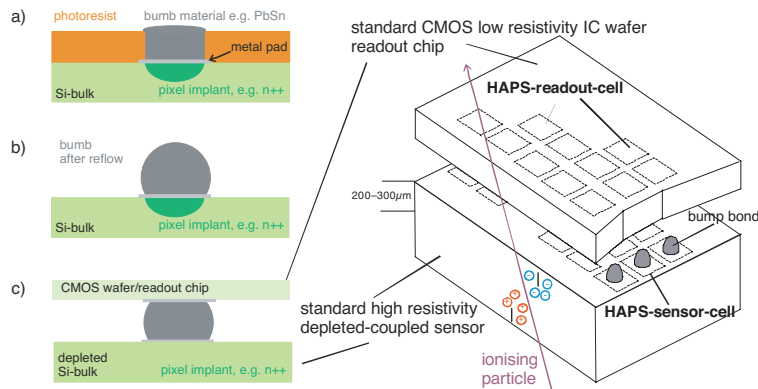
Figure 2.21.: Schematics of a HAPS detector [65]. The pixellated sensor is connected to a ROC by a two-dimensional array of solder bumps. On the left the process of bump formation is sketched. The metal for the solder bump is placed in the holes of the photoresist (a). After removing the photoresist the metal is heated to form the bumps in the so called "reflow" process (b). In the last step (c) the sensor and the ROC are pressed together to connect the sensor channel with the readout channel.

2.2.4.4. 3D Geometry

To decrease the collection distance and the collections times the idea of three-dimensional (3D) sensor geometries was introduced by Parker et al. [70]. Figure 2.22 shows the design's key feature: the orientation of the electrodes. Instead of being on the surface as in the case for planar sensors, 3D sensor electrodes are electrodes transversely drilled/micro-machined in the bulk of the sensor material. This has a major effect on the length of the charge carriers drift distances: While in the planar geometry the drift distance is given by the thickness of the sensor material, the drift distance in the 3D geometry is depended on the electrode distance. This distance can be varied and optimized for the specific application.
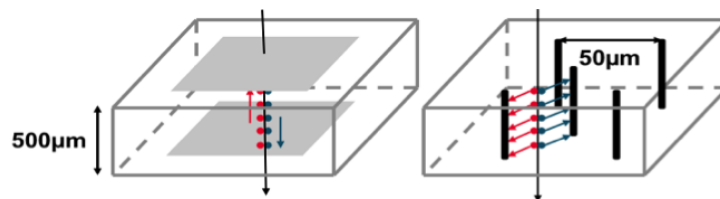
Figure 2.22.: Comparison of planar geometry with 3D geometry. With the 3D geometry shorter drift distances can be accomplished.

The advantages of this structure include short collection distances, fast collection times and low depletion voltages, depending on the electrode diameter and pitch chosen. Since

the drift distances of the charge carriers is reduced the probability of trapping in a radiated sensor is reduced, so the radiation tolerance is increased. The electric field configuration in 3D detectors is more complex than in planar detectors. By positioning the electrodes in different arrangement it is possible to change the electric field configuration for the detector. The most common arrangements are quadratic and hexagonal arrangements of the bias electrodes with a readout electrode in the middle. The electric field configuration for a quadratic cell is shown in Figure 2.23. The electric field close to the electrodes is increased and regions with low electric field can be found in between electrodes. Due to the smaller drift distances and the change of the electric field configuration much smaller depletion voltages and fast collections times can be achieved.

For silicon sensors the electrodes need to consist of $p - type$ and $n - type$ material. Additional steps, like Deep-Reactive Ion Etching (RIE) are required to implant the dopant into the bulk material. Therefore the production of 3D silicon sensors is a more complex technology than the production of planar silicon sensors and the construction of 3D silicon detectors is very challenging and expensive.
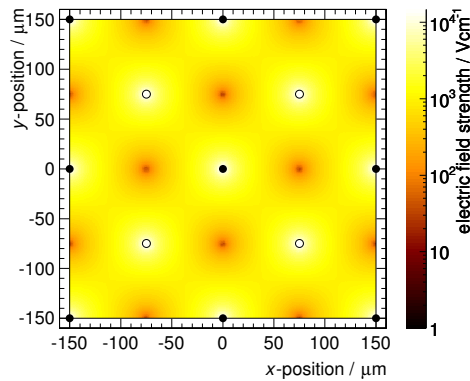
Figure 2.23.: Electric field configuration in a 3D sensor with quadratic cells. Each cell has a size of $150 \times 150 \, \mu m^2$. The bias electrodes are indicated with a filled circle, while the readout electrodes are highlighted with an empty circle.

2.3. CVD Diamonds

In this section the general properties of diamond are discussed. This discussion concentrates on properties which have influences on diamonds as a sensor material and compares them with the one of silicon as the standard semiconductor material.

Diamond is well known for its optical and mechanical properties. It is an allotrope of carbon where the atoms are arranged in a face-centered cubic (fcc) crystal structure. This structure is also called diamond lattice. In Figure 2.24 the composition of the diamond lattice is shown for a single unit cell.
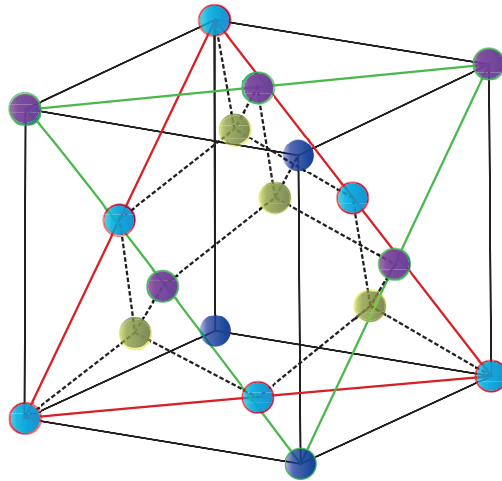
Figure 2.24.: Unit cell of the diamond cubic crystal structure [71, edited].

Diamonds can be found in nature but can also be produced in an artificial process in laboratories and in industry. Diamond is based on carbon atoms which have an atomic number of $Z = 6$ and a weight of 12.011 u. Two stable isotopes of carbon exist in nature, ^{12}C (99.9 %) and ^{13}C (1.1 %). In Figure 2.25 (a) the phase diagram of carbon is shown. As can be seen in the Figure, carbon can form many different allotropes due to its valency. Diamond and graphite are the most common ones, but in the last century many other allotropes, like graphene [72], carbon nano-tubes [73], fullerene [74] and amorphous carbon, were discovered. The structure of different carbon allotropes can be seen in Figure 2.25 (b). Due to the strong variation of its material properties, a lot of research is ongoing in the field of alltropes of carbon.
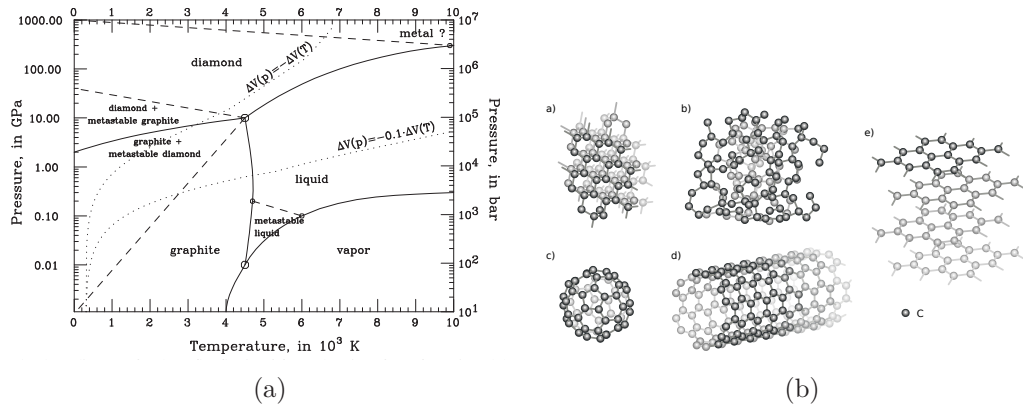
Figure 2.25.: Phase diagram of carbon [75] and different allotropes of carbon (a) diamond, b) amorphous carbon, c) fullerene, a C60 bucky-ball, d) single walled carbon nanotube and e) graphite) [76].

In the periodic table carbon is located between boron ($_5B$) and nitrogen ($_7N$). It is the first element in the fourth group, which also includes the semiconductors silicon ($_{14}Si$) and germanium ($_{32}Ge$).

2.3.1. Properties of Diamond

The crystallization of carbon atoms into a diamond lattice is a fcc lattice structure, with bounds over the tetrahedral sp^3 hybrid. At each lattice point two atoms are positioned relative to this point at $[0, 0, 0]$ and $[\frac{1}{4}, \frac{1}{4}, \frac{1}{4}]$ in terms of fractions of the diamond lattice constant $a = 3.567$ Å. The closest distance between two carbon atoms is $d = 1.545$ Å. Per unit cell 8 atoms are placed. This lattice arrangement is typical for elements of the *IV* group in the periodic table (e.g. silicon, germanium, tin). It has an atomic density of 1.76×10^{23} atoms/cm^3, which is the highest atomic density of all matter on earth. It is an optical isotropic crystal, which can be from optically transparent to optically translucent. Carbon atoms in a diamond lattice are strongly bound, their cohesive energies per bound are 3.62 eV/bound and 7.24 eV/bound [77]. Each carbon atom has four neighbors joined to it with covalent bonds. It is the hardest material in nature with a Mohs hardness of 10. Its hardness depends on the orientation of the crystal and varies between the strongest and the weakest plane by a factor of 100 [78]. This fact is used to be able to polish diamonds with diamond powder. In Table 2.2 an overview of several properties of diamond are compared with the ones of silicon. Compared to the displacement energy of silicon atoms ($13 - 20$eV), the displacement energy of carbon atoms in the diamond lattice is relatively high with 43 eV due to the strong covalent bonds. The conductivity of intrinsic diamond at room temperature is close to zero and therefore diamond is often referred to as an insulator. Many electrical properties are

described by the physics of semiconductors, why it is classified as a wide band gap semiconductor with a band gap of 5.47 eV. This is relatively high compared to silicon ($E_{gap} = 1.1$ eV) and germanium ($E_{gap} = 0.76$ eV). All three band gaps are indirect band gaps requiring a phonon for excitation of an electron in the conduction band in order to conserve momentum. The direct band gap in diamond is $E_{gap,direct} = 7.3$ eV. Electron and hole mobilities in diamond are higher than in silicon. The energy required to create an electron hole pair is ∼13 eV, which is much higher than the energy of 3.61 eV in silicon. Therefore the signal induced by an ionizing particle is smaller (36 e/µm vs. 89 e/µm).

Both natural and synthetic diamonds always possess characteristic imperfections, arising from the circumstances of their crystal growth. In addtion imperfections can be arise due to irradiation with particles. One can distinguishes between point, line, planar and bulk defects [79]. A point defect (or Zero-dimensional defect) is a defect around one single lattice point, such as vacancies, irregular placed atoms or substitutions with different atoms. The most common impurities in diamond are nitrogen N, boron B and hydrogen H. This impurities happen in the growth process. Point defects can also be caused by radiation. Line defects (or One-dimensional defects) are planes where a crystal plane stops within a crystal [80]. A grain boundary is the interface between two grains, or crystallites [81]. They exists on the plane where two different orientated orientated grains meet. Grain boundaries are defects in the crystal structure, and tend to decrease the electrical and thermal conductivity of the material. They are planar defects. (Two-dimensional defects) [82]. Bulk damage are three-dimensional defects such as cracks, inclusions or pores [83]. If this microscopic regions get bigger the properties of the diamond can change significantly. Bulk defects which extend through the whole thickness decrease the breakdown field dramatically, which makes it unusable for detectors. Bulk defects can also be created artificially by a laser [84]. This can be used to build 3D detectors based on diamond material, described in Chapter 4.

2.3.2. Chemical Vapor Deposition

Synthetic diamonds are commonly produced with a High-Pressure High-Temperature (HPHT) and a CVD crystal formation process. The HPHT process is orientated on the natural production process. To recreate the process that takes place deep inside the Earth's crust, high temperatures and high pressures are used to form synthetic diamond from graphite. The needed temperatures are in the order of 1500 °C to 2000 °C, the pressure must exceed 5 GPa. The first artificial diamonds were produced with this technique in the 1950's [99]. This diamonds usually have high nitrogen impurities and many crystal defects. Thus, these are not suitable for detector applications.

CVD diamond growth was first postulated in 1955, but only in the 1980s this method reached significant growth rates. In the CVD process diamond grows from a hydrocarbon gas mixture. Its advantages are the ability to grow large area diamonds and the better control of the impurities within the diamond, thus the quality of the synthetic diamond.

Property		Silicon		Diamond	
Proton number		14	[10]	6	[10]
Atomic number	[u]	28.0855(3)	[10]	12.010(7)	[10]
Mass density ρ	[g/cm^3]	2.329	[10]	3.520	[10]
Lattice constant	[angstrom]	5.430 95	[85]	3.567	[85]
Melting point	[K]	1687	[86]	4713	[86]
indirect Band gap	[eV]	1.12	[87]	5.46 to 5.6	[87]
Rel. dielectric constant		5.7	[88]	11.9	[89]
Resistivity	[Ω cm]	2.3×10^5	[90]	10^{16}	[91]
Breakdown field	[V/cm]	$\approx 3 \times 10^5$	[87]	10^6 to 10^7	[87]
e mobility μ_e	[cm^2/(V s)]	$\leq$1400	[87]	$\leq$2200	[87]
h mobility μ_h	[cm^2/(V s)]	$\leq$450	[87]	$\leq$1800	[87]
e saturation velocity	[10^7 cm/s]	0.86	[92]	9.6	[93]
h saturation velocity	[10^7 cm/s]	0.8	[92]	1.4	[93]
Thermal conductivity	[W/(K cm)]	1.3	[87]	6 to 20	[87]
Energy to create eh-pair	[eV]	3.6	[94]	13	[95]
Radiation length X_0	[cm]	9.370	[10]	12.13	[10]
no. of eh-pairs/MIP	[e/µm]	80	[94]	36	[96]
Displacement energy	[eV]	$13 - 20$	[97]	$37 - 47$	[98]

Table 2.2.: Material properties of diamond and silicon. Properties, which depend on the temperature, are given for room temperature and atmospheric pressure.

CVD diamond growth occurs at a relatively low pressures of $1\,\text{kPa}$ to $27\,\text{kPa}$. In this method a chemical reactions is occurring in a gas phase above a solid surface, the seed, which causes deposition onto that surface. This gas is usually a mixture of hydrogen and methane. For this reaction energy is needed which can be provided, for example, by thermal energy (hot filament) or by a plasma (AC, DC, microwave,..). For the growth of high quality CVD diamonds mostly plasma CVD reactors are used. The schematics of such a plasma-assisted CVD reactor can be seen in Figure 2.26 (a). With a microwave generator the plasma is generated in the reaction chamber. The gas mixture is provided externally and the substrate (seed) is cooled.

(a)

(b)
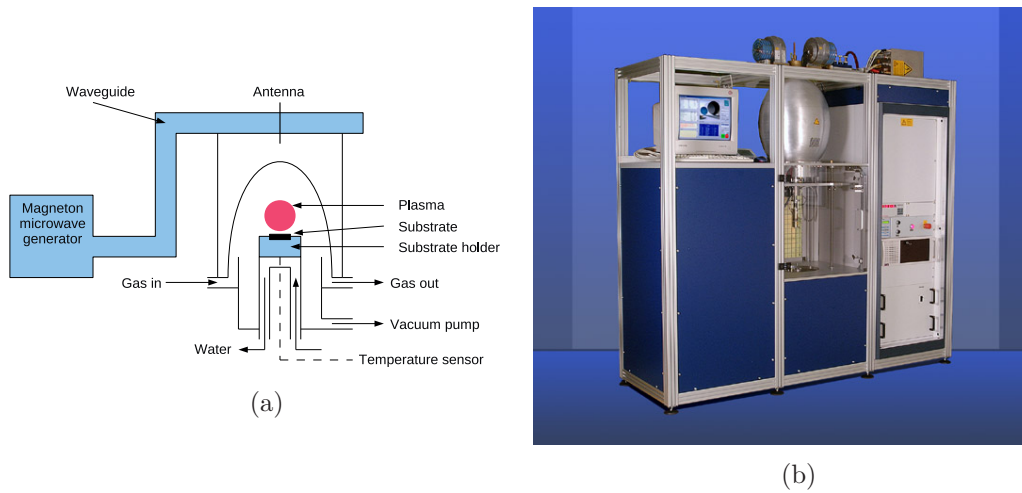
Figure 2.26.: Schematic view and real picture of a Microwave-assisted CVD reactor [82, 100, 101].

With the choice of the seed the quality and the properties of the resulting diamond might change. One distinguishes between two different substrate types, the *homo-epitaxial* substrates and *hetero-epitaxial* substrates. In the homo-epitaxial growth a substrate with a diamond like crystal structure is used. For electronic grade diamonds usually the homo-epitaxial growth technique is used. Two types of homo-epitaxial grown diamonds exist: single crystalline CVD (scCVD) and polycrystalline CVD (pCVD) diamonds. The most scCVD diamonds are grown on surface-treated HPHT diamond, while for pCVD diamonds diamond powder is used as substrate. By using a diamond powder for the growth of pCVD diamond material, the diamond consist of many grains. During the growth single grains become bigger, while other disappear. Therefore with increasing thickness of the pCVD diamond the sizes of the single grains increase, but the grain structure never disappears completely. In Figure 2.27 shows the schematic view of the pCVD crystalline grain structure.
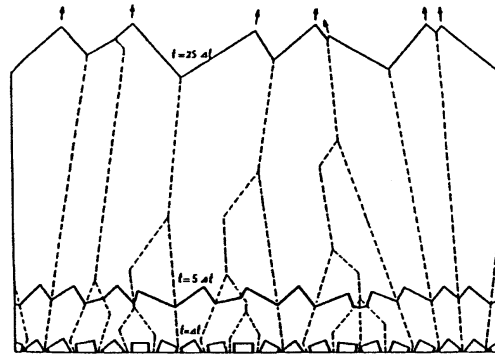
Figure 2.27.: Sketch of pCVD diamond film growth from isolated, randomly oriented crystals shown at the bottom of the Figure [102]. The dashed lines indicate the grain boundaries. The solid lines show the surface of the film at selected times. With increasing thickness the grain size increases.

The standard model of growing CVD diamonds is illustrated in Figure 2.28 and consist of three main steps

1. The breakup of hydrogen molecules to atomic hydrogen by the plasma.
2. The diamond nucleation.
3. The diamond growth.

In this process a high concentration of H_2 gas molecules is assumed. With the energy of the plasma these molecules are dissociated to single hydrogen atoms(H). Therefore the diamond growth surface is surrounded with these reactive atoms. The removal of impurities, such as polymers, by etching non-diamond materials from the surface. Due to the fact that hydrogen etches the sp^2 bounded graphite much faster than the sp^3 bounded diamond it can reduce the graphite layers. The hydrogen atoms are used to split up the methane compounds to single carbon atoms by

$$CH_4 + H \rightarrow CH_3 + H_2$$
$$\ldots$$
$$CH + H \rightarrow C + H_2$$
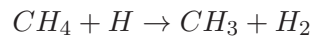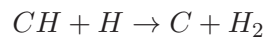
and to remove the hydrogen of the hydrogen-terminated surface by forming H_2. More details about the growth of CVD diamonds can be found in [104, 105].
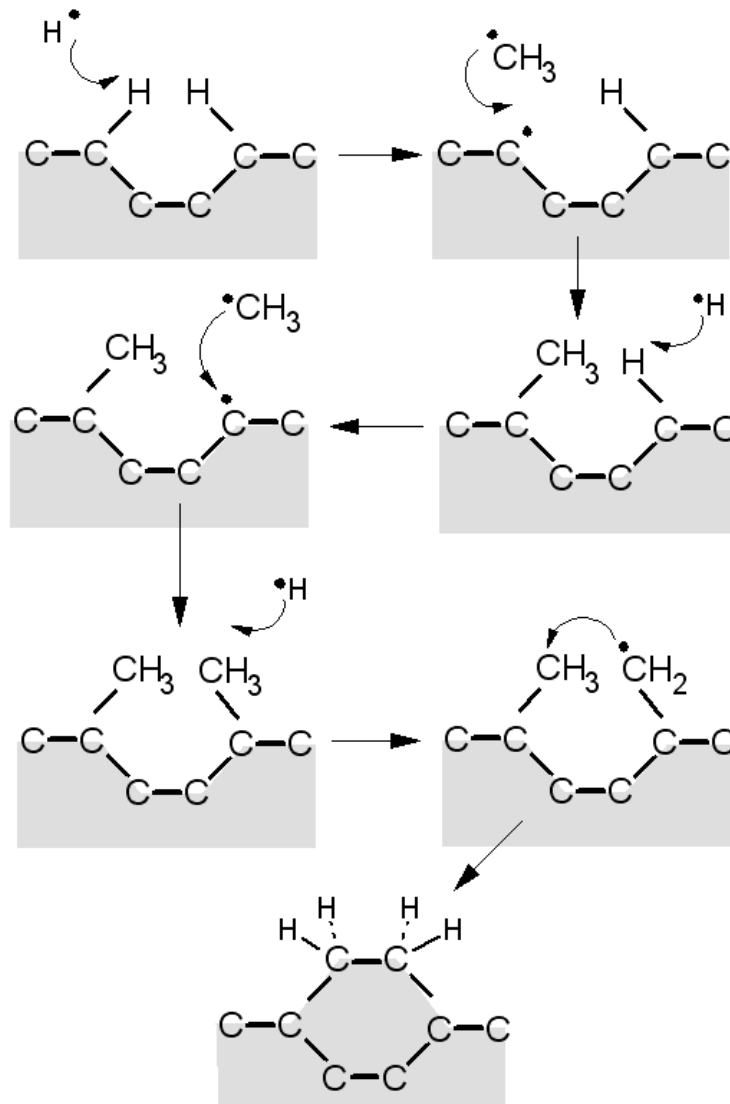
Figure 2.28.: Schematic diagram of simplified CVD diamond growth process [103].

2.3.3. Signal Creation in Diamond Detectors

Due to its high carrier mobility diamond can work as as a simple solid-state ionization chamber, as described in Section 2.2. To operate it as an ionization chamber a voltage V_B is applied across the diamond.

Figure 2.29 shows the schematic layout of a diamond particle detector. The electrodes consist usually out of Chromium or Titanium, deposited for example by sputtering. The electrode material is then covered by a layer of gold for passivation and to allow connections by wire or bump bonding. Before the deposition of the electrodes the diamond surfaces are mechanically polished and plasma etched to smooth the surface, and then cleaned. Details about the preparation of the diamond for metalization can be found in Section 2.3.4. Typical diamond sensor material has a thickness of about 500 µm.
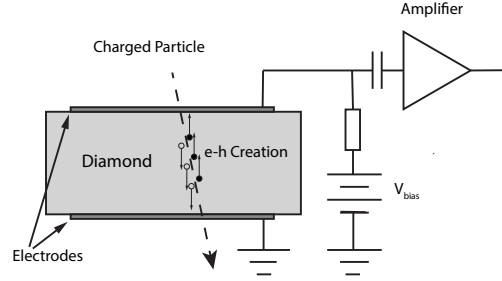
Figure 2.29.: Schematic layout of a diamond particle detector [106, edited].

Due to the high breakdown field, it is possible to operate the detector with electric fields as high as 2 V/µm and more. This results in bias voltages of $V_B = 1000\,\text{V}$ for a diamond with a thickness of $t = 500\,\text{µm}$. When a charged particle traverses the diamond, the atoms in the crystal lattice sites are ionized, promoting electrons into the conduction band and leaving holes in the valence band. The average energy to produce an electron/hole pair is 13 eV [95]. With the Bethe Bloch Formula, described in Section 2.1.1.1, the average number of electrons and holes produced by a MIP in 1 µm diamond material can be calculated to be $q_0 = 36\,\text{e/µm}$ [95]. These charge carriers drift within the electric field across the diamond and induce the signal.

The signal response of a CVD diamond detector is usually quantified by the Charge Collection Distance (CCD). A traversing particle produces $Q_0 = t \cdot q_0$ ionization charges within the bulk material. As explained in Section 2.2.3.1, this charge can be reduced by charge traps during the drift through the detector. A charge Q_m is measured with the front-end electronics. This charge can be expressed in the thickness of an detector without any charge losses.

$$CCD = Q_m/q_0 \qquad (2.26)$$

This corresponds to the average drift distance of an electron or hole under the influence of the electric field. The Charge Collection Distance (CCD) together with the sample thickness t describe the quality of a CVD diamond.

As shown in Figure 2.27 pCVD has a grain structure, which results in a less homogeneous material compared to scCVD diamond material. scCVD diamond sensors can have CCDs as big as their thickness, collecting all charges produced. pCVD diamond sensors have CCDs below their thickness. This is mainly caused by charge traps inside the bulk material induced by the grain boundaries. Current state-of-the-art pCVD diamond sensors have CCDs of 300 μm and more [107]. The grain boundaries in pCVD sensor material also cause a non-uniform signal response within the sensor. This results in a wider spread of signal amplitudes. As the grain size in pCVD diamond material increases with thickness, high quality pCVD diamond sensors are produced by growing a thick pCVD diamond wafer ($\sim 1 - 1.5$mm) and thinning it down to the final thickness of $\sim$500 μm. The material is primary removed from the substrate side. In Figure 2.30 the signal response of a scCVD and a pCVD diamond detector are shown. The wider signal response of the pCVD diamond detector compared to that of the scCVD detector can be observed. The Most Probable Value (MPV) was extracted by fitting the top of the distribution with a Gaussian. In addition a fit of a Landau distribution is performed. A good indicator for the width of the distribution is the ratio of the Full Width Half Maximum (FWHM) over the MPV. It was found that for unirradiated scCVD diamonds this ratio is approximately 0.3 and for unirradiated pCVD diamond approximately one [108]. The corresponding ratio for silicon is approximately 0.6.
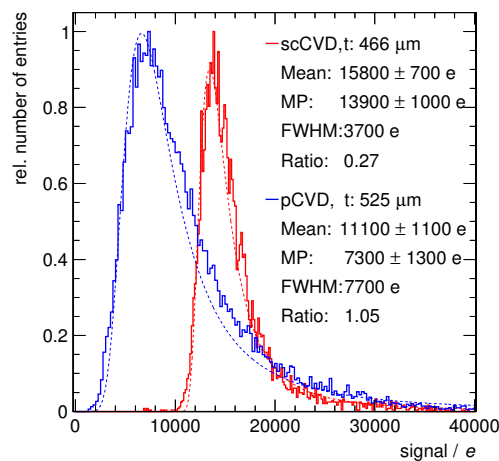
Figure 2.30.: Comparison of the signal response of a 440 μm thick scCVD and a 525 μm thick pCVD diamond.

2. Theory

Since the higher drift speed of the charge carriers reduces the drift time, the CCD can be increased by increasing the electric field. The drift velocity v of the charge carriers in Equation 2.17 is given by

$$v = \frac{\mu_0 E}{1 + \frac{\mu_0 E}{v_S}} \, , \tag{2.27}$$

where μ_0 is the low field mobility of the charge carrier (electrons or holes) and v_S is their saturation velocity. At high fields, the drift velocity saturates. Hence the CCD saturates as well. Unirradiated scCVD diamonds, which have been grown nearly defect free, do not have any grain structure and therefore little or no charge trapping. This results in a CCD similar or equal to its thickness, often called full-charge-collecting. These diamonds already show full charge collection at low electric bias fields.

In Figure 2.31 the CCD as a function of the bias voltage is shown for a pCVD and a scCVD diamond. The scCVD diamond shown in the Figure reaches full charge collection between 100 V and 200 V, corresponding to an electric field of less than 0.43 V/µm. The CCD of the pCVD diamond is continuously increasing with increasing bias voltage. At a bias voltage of ±1000 V a CCD of 300 µm is reached.

The CCD of a diamond detector is the quantity which can be measured with the signal response of the detector, but the underlying process, describing the charge collection, is based on the Mean Free Path (MFP) $\lambda_{e/h}$ of electrons and holes. The presented model of
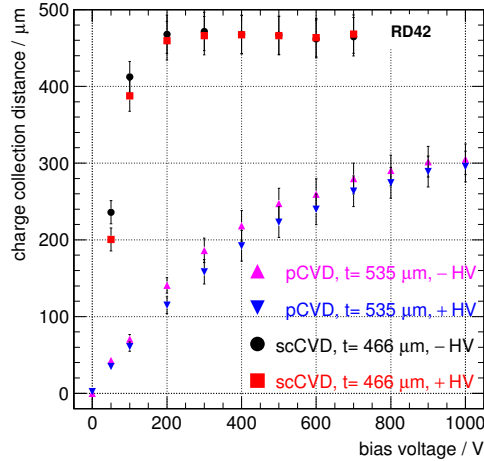
Figure 2.31.: Charge collection distance as a function of bias voltage for a pCVD diamond with a thickness $t = 535$ µm and a scCVD diamond with a thickness $t = 466$ µm.

radiation damage, described in Section 2.2.3, uses the MFP. The conversion function of MFP $\lambda_{e/h}$ to CCD d_{ccd} for a diamond pad detector with a thickness t is given by [109]

$$d_{ccd} = \lambda_e \cdot \left[1 - \frac{\lambda_e}{t} \cdot \left(1 - \exp^{-\frac{t}{\lambda_e}} \right) \right] + \lambda_h \cdot \left[1 - \frac{\lambda_h}{t} \cdot \left(1 - \exp^{-\frac{t}{\lambda_h}} \right) \right] . \tag{2.28}$$

and shown in Figure 2.32. For both, the MFP and the CCD, a representation relative to the thickness t is used. For this representation the MFP is the sum of the MFP of electrons λ_e and holes λ_h. The ratio of the two MFPs λ_e/λ_h is fixed to the ratio of the saturation velocities $v_{S,e}/v_{S,h} = 1.47$. It can be observed that for a relative CCD close to one the relative MFP approaches to infinity.

2.3.3.1. Pumping

It was observed that the signal response of diamond detectors improves by irradiation of the detector by a small amount of radiation. This effect is called "pumping". In Figure 2.33 the effect of pumping is shown for a pCVD diamond. During this measurement the diamond was exposed by a ^{90}Sr source. It can be seen that the CCD increased by more than $40\,\%$ after an exposure of more than $3\,$h. The pumping process is not completely understood, but it is believed that the increased signal response is due to a filling of deep traps in the diamond bulk material. Primary free charge carriers are trapped and neutralize these deep traps. As these traps are filled, the life time of the free charge carriers increases and therefore the signal response increases. With (UV-)light
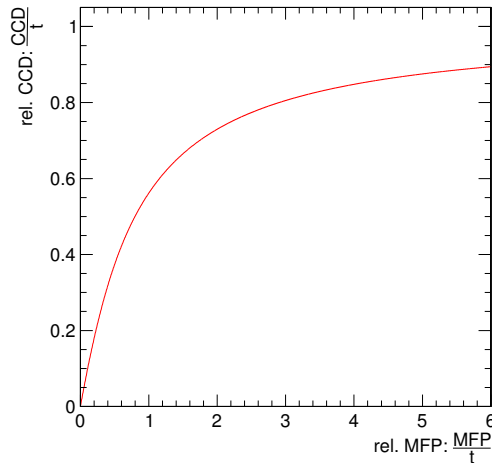
Figure 2.32.: The relative CCD as a function of relative MFP. The CCD and the MFP are given relative to the thickness t of the detector. The MFP is the sum of the MFP of electrons λ_e and holes λ_h. The ratio of the two MFPs is fixed to 1.47.
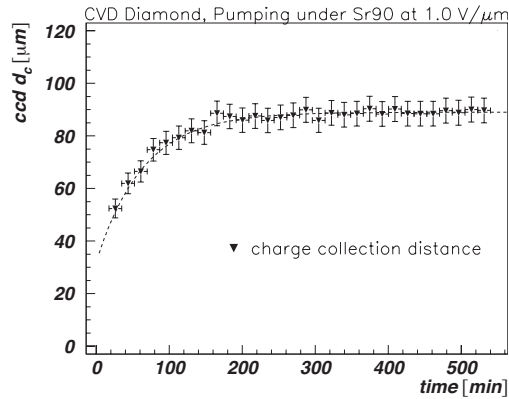
Figure 2.33.: CCD as a function of a time during the exposure to a ^{90}Sr source [110]. The CCD increased by more than $40\,\%$ after an exposure of more than $3\,$h.

it is possible to release the trapped charges again and therefore the diamond can be reset in the umpumped state. In order to pump a CVD diamond a particle fluence of $10^{10}\,$MIP/cm^2 is sufficient [111] and remains in this state for several months if it is not exposed to light.

2.3.4. Cleaning and Metalization of CVD Diamonds

To build a diamond detector the surface of the diamond sensor material needs to be metalized to form the electrodes. This metalization is the most crucial step in the construction of a diamond detector. A good mechanical and a good electrical connection with the sensor material is required. Two different contacts between semiconductors and metals exist, ohmic contacts and Schottky contacts. It was found that an ohmic contact is preferred for the use of precision, radiation hard diamond detectors [112]. Chromium, titanium and other transition metals that form carbides tend to produce ohmic contacts to diamond. By metallizing the diamond with titanium, chromium and other transition metals tend to create ohmic contacts with the diamond sensor material. This ohmic contact requires the formation of carbide binding between the metal and the diamond. An additional metal layer is used as passivation against corrosion. By using gold it is possible to directly connect bond-wires.

The presented method uses a Cr/Au metalization in which Cr is the adhesive layer. In order to rather create binding of chromium with carbon instead of oxygen, metalization techniques with high energy transfers are preferred as $C - O$ bindings result in a lower energy state than the $C - Cr$ bindings. The metalization is performed by sputtering and the corresponding thicknesses are $500\,$Å Cr and $2000\,$Å Au. To guarantee the formation of the carbide bindings, the sensors are annealed at $400\,°$C for $4\,$min in a N_2 atmosphere after metalization.

It was found that the cleaning of the diamond before the metalization has a big influence on the quality of the connection. It was found that a termination of the diamond with oxygen instead of hydrogen has positive effects on the quality of the connection. The following recipe was developed within the RD42 collaboration and was used for all samples shown in this thesis:

Removal of gold using boiling gold etch for ∼5 min.

Removal of chrome using boiling chrome etch for ∼5 min.

Removal of carbides using boiling Chrome Oxide solution in H_2SO_4 (sulphuric acid) for $5 - 10$min.

Removal of residues two to three repetitions

- boiling aquaregia ($3 \times HCl : 1 \times HNO_3$) for 5 min

- boiling $3 \times H_2SO_4 : 2 \times HNO_3$ for 5 min

- boiling piranha ($5 \times H_2SO_4 : 1 \times H_2O_2$) for 5 min

Oxygen termination 50 W O_2 plasma etching for $2 - 10$min.

In between the steps the diamond is rinsed with deionized water. During the irradiation campaign of this work, described in Chapter 3, it was found that a short RIE of the surface can further improve the quality of the connection. With a duration of 15 min on each side the process removes a total of 0.1 μm to 0.3 μm from each side. Since 2014 this step is included in the recommend cleaning procedure.

3. Radiation Tolerance Studies of CVD Diamond Detectors

The high radiation environment at the inner-most tracking layers of HL-LHC experiments requires the development of radiation tolerant sensor materials which can be operated after receiving particle fluences of more than $10^{16}\,\mathrm{n_{eq}/cm^2}$ [113]. With its large band gap and its high binding energy, diamond has ideal material properties for such a radiation tolerant sensor material.

In order to validate the expected radiation tolerance, the RD42 collaboration studied the signal response of the CVD diamond after irradiation with different particle species and energies. The results for neutron, pion and proton irradiations were already published [111, 114–117]. In these campaigns scCVD diamonds were irradiated to several $10^{15}/\mathrm{cm^2}$ and pCVD diamonds to fluence levels as high as $20 \times 10^{15}\,\mathrm{p/cm^2}$. In these measurements it was observed that the damage constant for pCVD and scCVD material are similar and that the spatial resolution of pCVD diamond sensors improves with proton irradiation at least up to $2.2 \times 10^{15}\,\mathrm{p/cm^2}$ [108] .

During the course of this thesis an additional radiation campaign was performed using $800\,\mathrm{MeV}$ protons from the Los Alamos Neutron Science Center (LANSCE) irradiation facility [118]. One scCVD diamond was irradiated in four steps to radiation levels of $7.8 \times 10^{15}\,\mathrm{p/cm^2}$ and three pCVDs were irradiated up to $12 \times 10^{15}\,\mathrm{p/cm^2}$. These diamonds were characterized in several beam tests before and after irradiation and their signal response was measured.

In this chapter the results of these measurements are presented. The hypothesis that the damage constants for pCVD and scCVD diamond material are similar was tested and the damage constant for $800\,\mathrm{MeV}$ proton irradiation was measured. Measurements using scCVD diamond were used to check whether the spatial resolution in scCVD diamond improves with radiation, as measured for pCVD diamonds. At the end of this chapter the measurements of the pCVD diamond irradiated to $12 \times 10^{15}\mathrm{p/cm^2}$ are used to evaluate the capability of pCVD diamond as a sensor material for particle tracking detectors after a radiation level which is comparable with expected fluence at the innermost layer of HL-LHC experiments.

3.1. Beam Test

The beam tests described in this chapter were performed at *CERN* using protons in the H6 north area from the Super Proton Synchrotron (SPS) [119]. The H6 beam line is a secondary particle beam that can provide hadrons, electrons or muons with energies between 10 GeV to 205 GeV [119]. The primary proton beam with a momentum of 450 GeV is extracted from the SPS and directed onto a beryllium target to produce three secondary beams in the ECN3, H8 and H6 beam lines. The optimization of the beam tuning is performed by the user. This requires adjusting several dipole and quadrupole magnets, as well as collimators, along the 500 m long beam line from the primary interaction target to the testing area.

As the SPS beam is extracted to many different beam-lines and experiments, it has a supercycle which is adjusted to the number of beam lines and experiments used. The most common supercycle duration is 40 s to 45 s, when all experiments are operating. The beam extraction to the H6 beam line in each supercycle results in a $4 - 10$ s long extraction, in which the intensity is constant. One beam extraction is called a spill. The duration of each supercycle and also the beam delivery time may change during the test-beam period and so must be monitored.

3.2. Setup

The beam tests were performed in the H6 beam line at *CERN* using the "Strasbourg"-telescope [120, 121]. This telescope consists of eight high resolution silicon strip detector reference planes, $4x$ and $4y$ on an aluminum frame. Each plane is made up of a single sensor. Each silicon sensor has a size of 12.8 mm × 12.8 mm with a thickness of 300 μm. Up to two Devices Under Test (DUTs) with strip geometry can be tested with the setup. Four reference planes, $2x$ and $2y$, are placed in front and four reference planes are placed in the back of the DUTs. Figure 3.1 shows a schematic view of the telescope.
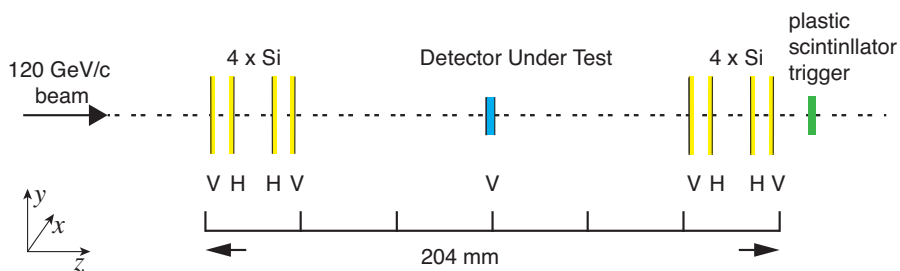
Figure 3.1.: Schematic view of the eight plane "Strasbourg" telescope used to identify candidate tracks which pass through the DUT. The planes are identified as V for vertical strips (providing a measurement of the x-coordinate) and H for horizontal strips (providing a measurement of the y-coordinate). The telescope readout was triggered by a signal in a $7 \times 7 \, \mathrm{mm}^2$ scintillation counter.

The silicon detectors were single sided p-on-n strip sensors with a readout strip pitch of $50\,\mu\text{m}$. Two different kind of sensors were used. Along the direction of the beam the two front pairs used sensors with one intermediate strip, resulting in an effective pitch width of $25\,\mu\text{m}$. Behind the DUTs the sensors had two intermediate strips with an effective pitch width of $16.6\,\mu\text{m}$. The strips of the planes were placed in the order $x - y - y - x$ in the front as well as in the back. A fast plastic scintillator with a size of $7 \times 7\,\text{mm}^2$ was placed in the back of the telescope. Two PhotoMultiplier Tubes (PMTs) detected the scintillation light and the coincidence of their signal response to a traversing charged particle triggered the readout of the telescope and the DUTs.

The signals of each silicon strip were amplified with a *VA* charge sensitive readout amplifier, produced by IDEAS[122]. It is based on the Viking chip and contains 128 low-noise charge-sensitive preamplifiers with a $CR - RC$-shaper, sample and hold, analog memory and multiplexed readout to one output. The *VA* peaking time was adjusted to be $1\,\mu\text{s}$. To read out the 256 strips of each reference plane two *VA* readout chips were connected serially together. For the readout of the DUTs *VA2.2* readout chips with 128 readout channels were used. The peaking time was adjusted to be $2\,\mu\text{s}$. This results in an ENC of $60\,\text{e} + 11\,\text{e/pF} \times C_d$ for a input capacity C_d. The *VA* / *VA2.2* readout chips were connected to repeater cards, which contained level converters for logic signals, buffer amplifier for analog output signal, and adjustable bias supply for the *VA* chip. By adjusting the supply voltages of the *VA* chip the gain of the amplifier can be adjusted slightly.

The analog signals from the amplifier were digitized with the Strip Detector Read-out System (SDR) based on an VME-based SIROCCO ADC[123]. The signals of the silicon reference planes were digitized with a precision of $8\,\text{bits}$, while the signals of the DUTs were digitized with $12\,\text{bits}$. The channel acquisition readout rate for the silicon reference planes was set to $1\,\text{MHz}$, resulting in a readout time of $128\,\mu\text{s}$ for each reference plane. To reduce the overall readout time, the $4x - y$ pairs were read out together in parallel in $512\,\mu\text{s}$. Each DUT was readout with a separate digitizer. The channel acquisition readout rate was set to $500\,\text{kHz}$, resulting in a readout time of $256\,\mu\text{s}$ per DUT.

The readout system consisted of two different kinds of Versa Module Eurocard-bus (VME) modules: The SDR-Flash and SDR-Seq module. In addition, a separate card SDR-Trig was used for generating triggers. The SDR-Flash is the ADC-converter with two channels per VME module. It uses an AD1671 12 bit converter chip which contains an on-board, high performance sample and-hold amplifier [124]. The sampling point of the ADC must be adjusted to fit to the multiplexed signals from the *VA* readout chip. The SDR-Seq generated the control signals for the readout amplifiers and drives the SDR-Flash. It handled the external triggers and initiated the readout sequence by generating a VME interrupt signal. The SDR-Trig card was used for the generation of the trigger. It provides four fast discriminators and an arbitrary logic unit. It can generate a hold signal within $20\,\text{ns}$ and a trigger for the SDR-Seq module.

3.3. Analysis Method

The analysis of the beam test data was based on the methods developed in [125]. For easier data handling the raw data files were transformed into a *ROOT* tree [126]. The first step of the analysis was the estimation of the pedestal offset for each channel, followed by creating hit clusters. After selecting events for further analysis, the telescope reference and the DUT planes were aligned with an iterative alignment procedure using the first 10 % of the data. The data used for alignment was not used in the final analysis step. In the final step of the analysis the pulse height and residuals of the DUT were extracted using both, a clustered and a transparent analysis. With each step a new *ROOT* tree was created adding information which can be easily accessed. For each run a separate configuration file was used to store all parameters of the analysis.

3.3.1. Pedestal Calculation and Subtraction

As described in Section 3.2 each *VA* channel has its own amplification circuit but the analog output levels are digitized with a single digitizer for each plane. Since the *VA* does not provide zero-suppression, it was important to find a good estimate for each channel pedestal. Each digitized (raw-)signals from the SIROCCO ADC can be associated with a certain event n and a channel ch of one plane, called $r_{n,ch}$. The (raw-)signals consists of different parts. The real physical charge $q_{n,ch}^{phys}$ is the amplified signal induced in the detector by the passage of a charged particle. For each event there exists a pedestal signal of the channel amplifier $p_{n,ch}$ and a common mode shift c_n for the readout chain. In addition there are random charge $q_{n,ch}^{rnd}$ which include the errors due to digitization. The signal after digitization is measured in ADC units and is given by:

$$r_{n,ch} = q_{n,ch}^{phys} + p_{n,ch} + c_n + q_{n,ch}^{rnd}. \tag{3.1}$$

The above mentioned Common Mode Noise (CMN), although rare, has been observed in other detector systems [62, 65, 127, 128]. The effect manifests itself as a common baseline shift during on all channels. For analog readout it is critical to be able to identify and correct for baseline shifts [62]. This effect has often a slow (order of hertz) component. Due to the serialized readout of each detector it was necessary to correct for this effect in this setup.

For each channel a separate pedestal offset and a pedestal width σ_{noise}^{ch} was calculated. To estimate both values a "sliding window" method was used. The sliding window consisted of the N last channels and N was typically chosen to be 512. For each channel and each event all signals responses within the last N events, which were smaller than $3 \times \sigma_{noise}^{ch}$ were averaged to determine an estimate for the pedestal for this channel in this event. This method uses the fact that events with particles crossings in the detector are sparse (1 to 3 channels per plane per event), which means that the ratio of events,

which have a physical charge $q_{n,ch}^{phys} > 3 \times \sigma_{noise}$, is small. The common mode noise was estimated for each event and each detector plane individually by calculating the average of the pedestal subtracted signals.

The noise of each individual channel was determined after pedestal correction by mesuring the width of the pedestal distribution. In Figure 3.2 (a) the average pedestal and average noise for each channel for plane $D2Y$ are plotted. The pedestal mean is in the range between 70 ADC and 90 ADC for channels 0 to 127, and between 30 ADC and 60 ADC for channels 128 to 255. This is a result of supplying common current and voltage to two separate *VA* chips. Both *VA* readout chips show similar noise performance.

In Figure 3.2 (b) the difference between the raw signal $r_{n,ch}$ and the pedestal $p_{n,ch}$ is shown for all events and all channels in the third vertical silicon plane (D2Y). This distributions has a Gaussian shape with a mean of 0 ADC and a width of 0.9 ADC. As signals of the silicon reference planes were digitized with a lower resolution compared to that of the DUTs, it was found that the common mode correction in these planes did not reduce the noise of the detectors and therefore this correction was only applied for the DUTs [129]. In the following sections the pedestal subtracted common mode corrected raw signal of a channel is called *signal*.

(a)   (b)
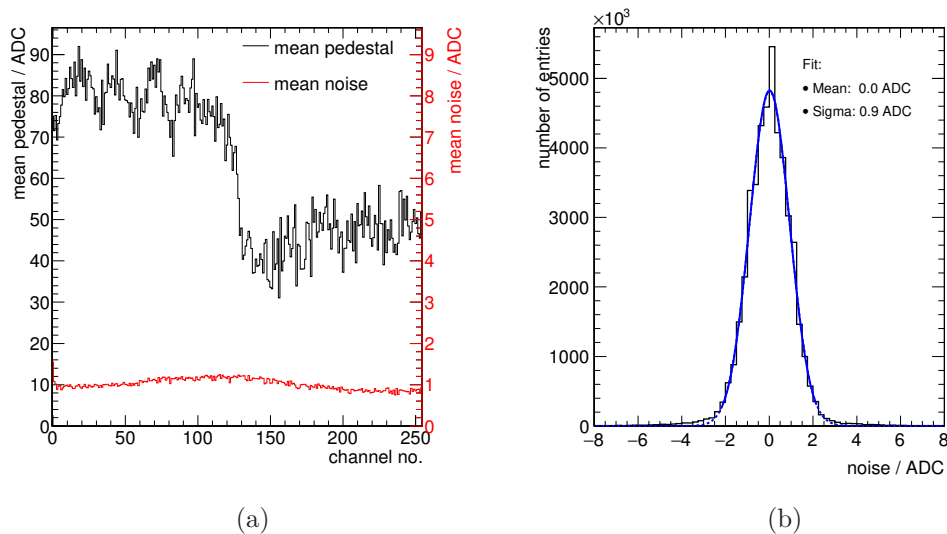
Figure 3.2.: Figure   (a): The average pedestal and average noise for each channel of detector plane $D2Y$. The step in the pedestal value at channel 127 can be associated with the use of two *VA* readout chips with a serial readout and a common power.

Figure (b): Noise (raw signal - pedestal) distribution for all channels this detector

.

3.3.2. Clustering

Whenever a charged particle traverses a detector plane, the particle produces electron hole pairs and their motion in the electric field of the sensor induces a charge on the strips, as described in Section 2.2. This charge can be spread over multiple channels of the detector. A clustering algorithm was used to search for clusters of "hits" by searching for signals within a channel and those adjacent to it, and combining them into a cluster. In the first step the algorithm looks for a seed, defined as a channel whose SNR exceeds the seed threshold t_s. This seed channel is the starting point to build the cluster. In the next step adjacent channels are added to the cluster if they exceed the hit threshold t_h.
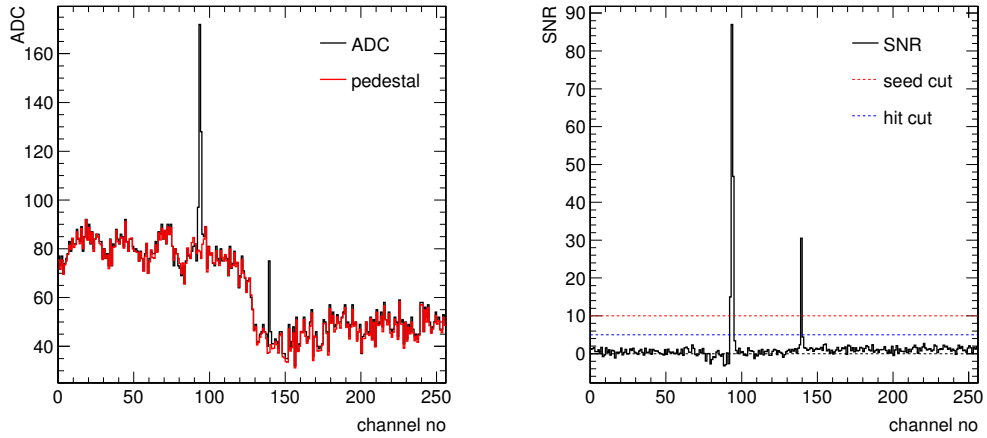
(a) Event in ADC space. (b) Event in SNR space.

Figure 3.3.: Figure (a): Signal per channel distribution for one event in detector plane *D2Y* in ADC space. The measured signals are drawn in black, while the pedestal values for this event are drawn in red.
Figure (b): in the Signal-to-Noise Ratio space. With the clustering algorithm two clusters are built. Around channel 95 and 140 the seed threshold t_s is exceeded, resulting in two clusters with cluster size three and one.

Figure 3.3 shows an example charge per channel distribution for one event. On the left, one can see the raw-signal distribution in black and the pedestal in red, while the right figure shows the SNR for every channel along with indicators of both the seed threshold t_s and the hit threshold t_h. Both hits in channel 95 and 140 exceed the higher seed threshold and therefore two clusters were formed by the clustering algorithm. The first cluster consists of several channels while the second one has a cluster size of one. Although both peaks are clear in the raw spectrum in Figure 3.3 (a), they become clearer once the pedestal variation is remove in the SNR plot of Figure 3.3 (b).

(a) Number of clusters. (b) Cluster size.
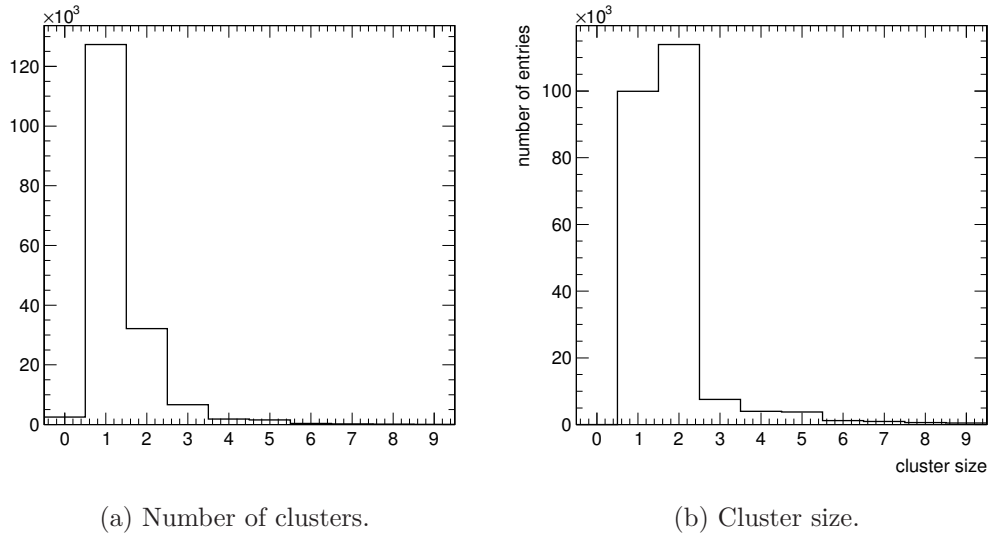
Figure 3.4.: Number of clusters and the cluster size in detector $D2Y$ for run 17 000.

In Figure 3.4 (b) the distribution of cluster sizes in one detector is shown. One can see that most clusters consist of one or two channels, indicating events with and without charge-sharing. The number of clusters formed depends strongly on the beam profile and the flux. In order to reduce hit ambiguities due to multiple particle crossings in one event, the beam parameters were tuned in each beam test campaign such that most events contain only one particle track, leaving one cluster per detector in the silicon telescope. The number of clusters in one detector is shown in Figure 3.4 (a). The majority (73 %) of events have one cluster, in 22 % of the events two clusters were formed. A small fraction of the events (1.5 %) did not contain any cluster at all. This represents the inefficiency due to the combination of the trigger and the plane efficiency with the seed and hit threshold used.

3.3.2.1. Charge of the cluster

The charge of a cluster is defined as the sum of signals for all channels exceeding the hit threshold. In the following this charge will be called *pulse height* for the clusters.
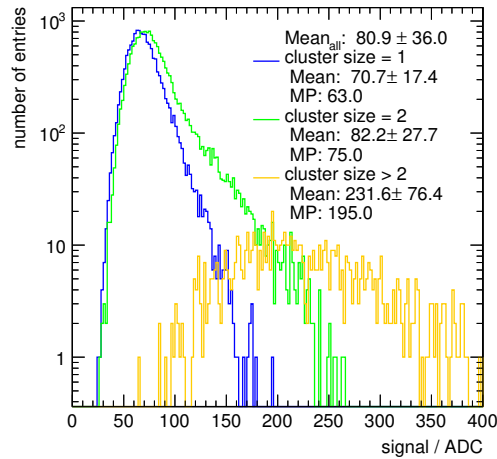
Figure 3.5.: Pulse height distribution for different cluster sizes. Only clusters with cluster size one and two are used for the further analysis.

Figure 3.5 shows the pulse height distribution for cluster sizes one, two and greater than two. The distribution can be described with a convolution of a Landau and a Gaussian distribution. One can see that the average and the MPV of the pulse height for a cluster size of two is larger than that for a cluster size of one. The mean of all cluster sizes is 80.9 ADC. The distribution of the pulse height for clusters with a cluster size larger than two has a most probable of 195 ADC and a mean of 231.6 ADC much larger than cluster sizes one and two. The same effect was also seen before [125]. As these clusters could be caused by nuclear interaction in the detector plane or by delta rays, only events with cluster size of one or two were used in further analysis.

3.3.2.2. Position of the cluster

The goal of a position sensitive detector is to measure where a particle crosses the detector plane. In a strip detector the hit position is deduced from the collected charge of the readout channels. Various methods are available to find the position which has the smallest measurement error. The predicted hit position within one detector plane is calculated by using a reconstruction of the particle track with the other planes of the beam telescope. The residual is defined as the difference between the predicted and the measured hit position. In the following paragraphs different algorithms for measuring the hit position are presented. The comparison of the algorithms can be performed by using the residual distribution. In general, the narrower the residual distribution the more precise the measurement. In what follows, the readout pitch of the detector is referred as P. In the final analysis the two methods *Highest Two Centroid* and *Charge Weighted* are only used as cross checks and are not discussed in much detail.

Maximum Hit Position/Digital Hit Position   The "digital hit position" is defined as the position of strip with the highest signal. In an ideal detector without any noise the residual distribution is a flat top distribution in an interval $-P/2$ to $+P/2$. The standard deviation σ_{dig} of this distribution is given by [62]

$$\sigma_{\mathrm{dig}} = \frac{P}{\sqrt{12}} \approx 0.287 \cdot P\,. \tag{3.2}$$

For a strip detector with a readout pitch of $50\,\mu\mathrm{m}$ a digital resolution of $14.4\,\mu\mathrm{m}$ is expected. Due to random noise in the detector and uncertainties on the predicted hit position this distribution will be smeared with a Gaussian.
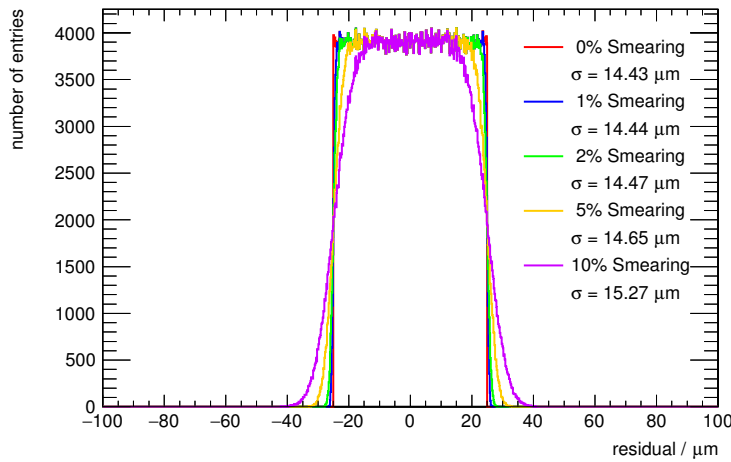
Figure 3.6.: Residual distribution for the digital position, showing a simulation in which Gaussian smearing of the position by $1\,\%$, $2\,\%$, $5\,\%$ and $10\,\%$ was added. The primary effect of Gaussian smearing shows up at the edges of the distribution.

Figure 3.6 shows simulation data where the measured position was smeared with Gaussians of different widths. The primary effect of the Gaussian smearing can be observed in the edges of the distributions. With larger smearing the standard deviation of $\sigma_{\mathrm{dig,noise}}$ increases.

Figure 3.7 shows a residual distribution for a real detector. A fit using a flat top distribution convoluted with a Gaussian was performed and is shown. The smearing due to noise and the uncertainty on the predicted hit position are clearly visible at the edges of the distribution.

Charge Weighted Hit Position   In addition to the information of the highest signal strip position, the adjacent readout channels can be used to get a more precise prediction of the hit position. The "Charge Weighted Hit Position" is calculated by using the signal information of all channels of the cluster as a weighting parameter.
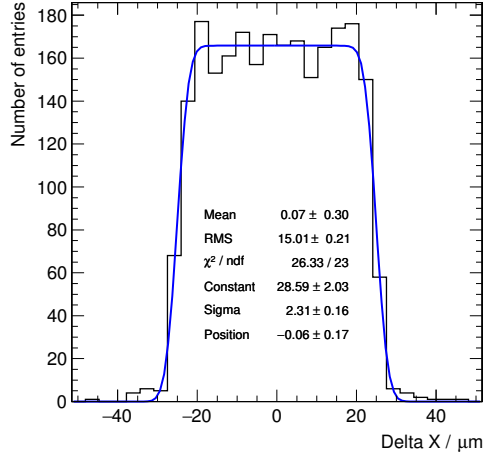
Figure 3.7.: Digital residual distribution for a diamond detector.

Highest Two Centroid Hit Position   A slight modification of the "Charge Weighted Hit Position" is the "Highest Two Centroid Hit Position" algorithm. In this case not all hits of a cluster are used for calculating a charge weighted position but only the two highest strips are used. For a clustered analysis this result in the same position has the "Charge Weighted Hit Position" as long as the cluster size is below three. In the transparent analysis, described in section 3.3.6, a difference between both methods might be observed.

Eta Corrected Hit Position   A cluster of two strips can be described by its charge Q_{cl} and the charge share between both strips η. The variable η is defined by [130]

$$\eta = \frac{S_R}{S_R + S_L} = \frac{S_R}{Q_{cl}} \, , \tag{3.3}$$

where $S_{R(L)}$ is the signal of the right (left) strip in the cluster. In this thesis the left strip is defined to be the strip with the smaller channel number.

As shown in Figure 2.19 (b), the signal induced on intermediate strips is transfered to the readout strips by capacitive coupling. Therefore the signal response on the readout strips depends on the number of intermediate strips. Figure 3.8 shows the signal measured in the left strip vs the signal of the right strip, as defined in equation 3.3, for a detector with one intermediate strip and for a detector with two intermediate strips. In both detectors the distributions show an anti-correlation. The distribution is not flat but has three peaks in the case of one intermediate strip and four peaks in the case of two intermediate strips.

In Figure 3.9 the distribution of the variable η is shown for these two detectors under uniform illumination. Both distributions show peaks at η close to zero and η close to
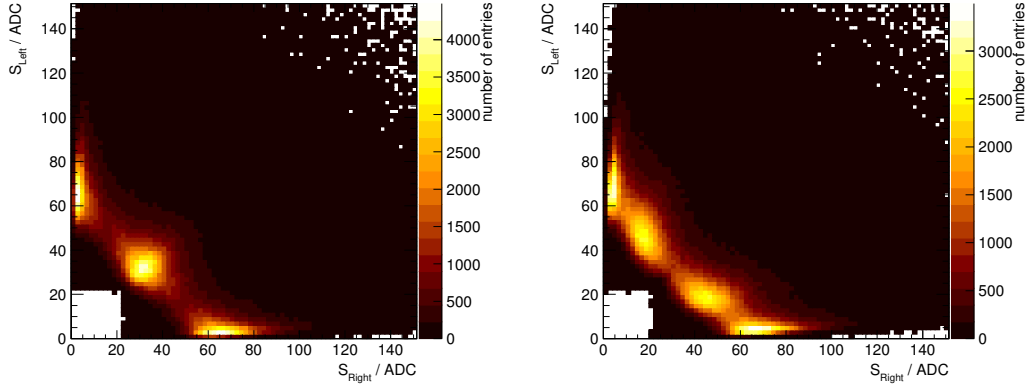
(a) One Intermediate Strip.

(b) Two Intermediate Strip.

Figure 3.8.: Signal charges on the left strip versus the signal charge of the right strip for detectors with one and two intermediate strips.
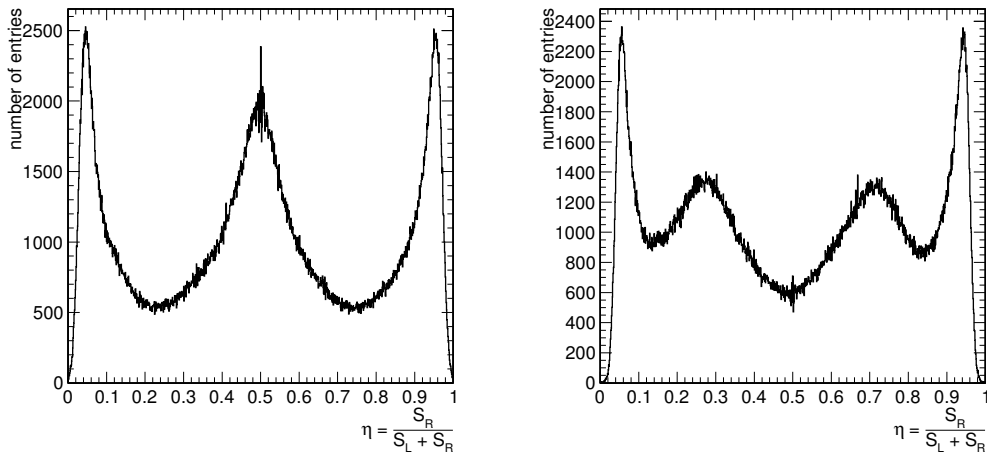
(a) One Intermediate Strip.

(b) Two Intermediate Strip.

Figure 3.9.: Eta distribution for detectors with one and two intermediate strips

one. In the case of one intermediate strip one additional peak at $\eta \sim 0.5$ exists, while in the case of two intermediate strips there are two additional peaks at $\eta \sim 0.3$ and $\eta \sim 0.7$, corresponding to the relative positions of the intermediate strips. This indicates that charge division in the detector is far from being linear which is expected for uniform illumination. This non-linearity can be explained by the width of the diffusion cloud, which depends on detector parameters as the thickness, the resistivity and the applied voltage and by the different response of the charge coupled intermediate strips. If a particle hits the detector in between two strips, charge division will be effective. But when a particle crosses the detector close ($\lesssim 10\,\mu\text{m}$) to a strip frontier, almost all charge will be collected by this strip.

The "eta correction algorithm" [131] assumes that the particles crossing the detector are uniformly distributed. A new weighting function $f(\eta)$ based on the measured eta distribution is defined by

$$f(\eta_0) = \frac{1}{N} \int_0^{\eta_0} \frac{\mathrm{d}n}{\mathrm{d}\eta} \mathrm{d}\eta \qquad (3.4)$$

where N is the normalization constant

$$N = \int_0^1 \frac{\mathrm{d}n}{\mathrm{d}\eta} \mathrm{d}\eta \,. \qquad (3.5)$$

The function $f(\eta)$ defines the integral of the η distribution normalized with the total number of events in this distribution. With this function the "Eta Corrected Hit Position" is defined as

$$X_{etacor} = x_L + P \cdot f(\eta) = x_L + \frac{P}{N} \int_0^{\eta_0} \frac{\mathrm{d}N}{\mathrm{d}\eta} \mathrm{d}\eta \,. \qquad (3.6)$$

In Figure 3.10 the eta integral for detectors with one and two intermediate strips are shown. Due to noise fluctuations the probability to have a $\eta < 0.04$ or larger than 0.96 is very small. In these regions $f(\eta_0)$ is close to zero or one. Due to the intermediate strips it is possible to deduce the charge sharing between the readout strips. This should result in an improved precision determination. The comparison of the distribution for one and two intermediate strips show that by adding the second intermediate strip the function $f(\eta)$ becomes more linear.

The effect of the residual distributions can be seen in Figure 3.11, which shows the residual distributions for detectors with one and two intermediate strips. It can be seen that the eta algorithm provides a more precise measurement of hit position. The width of the Gaussian fits are $2.8\,\mu\text{m}$. It was found that this algorithm results in the best resolution when the particle tracks crosses the detector at small angle. Therefore it is used for the alignment of the reference detectors.

(a) One intermediate strip.

(b) Two intermediate strips.
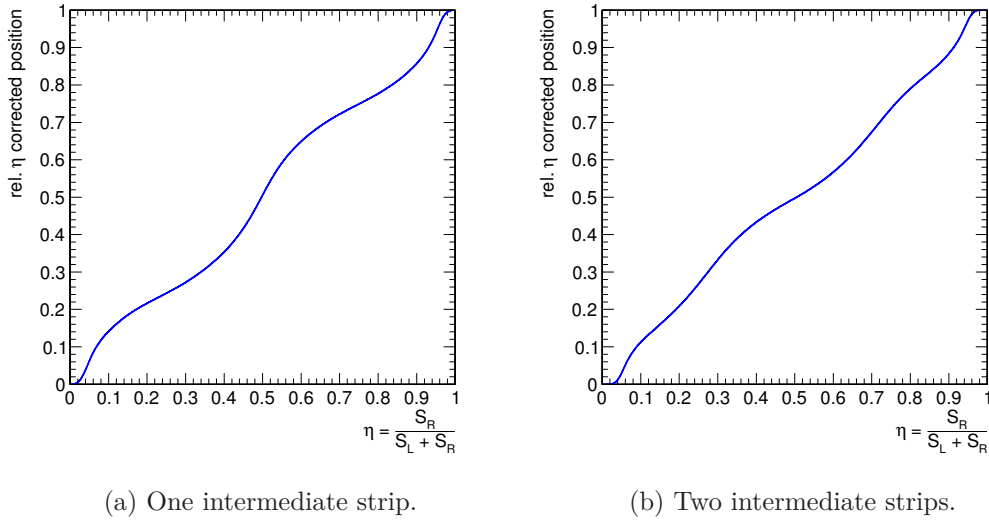
Figure 3.10.: Eta integrals for detectors with one and two intermediate strips

(a) One Intermediate Strip.

(b) Two Intermediate Strip.
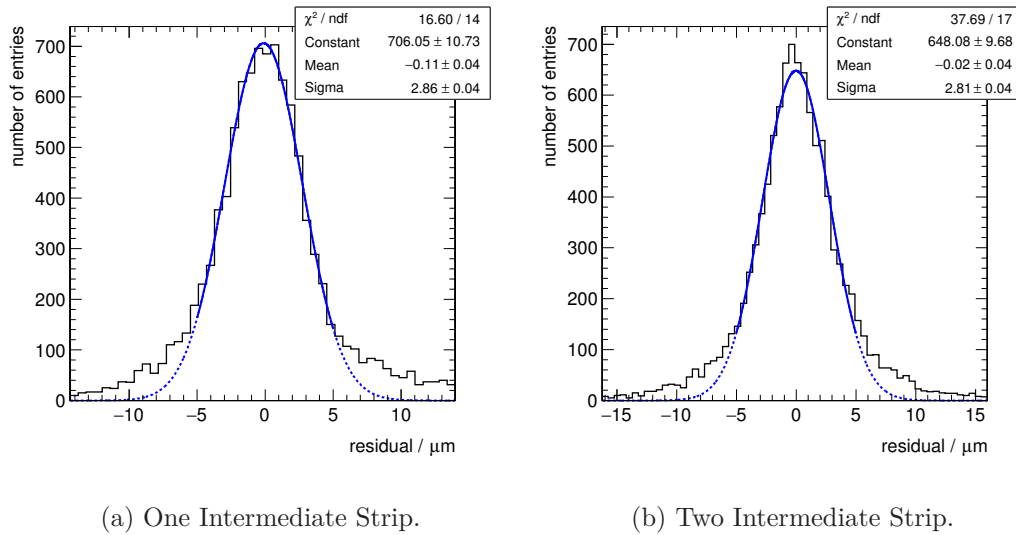
Figure 3.11.: Residual distributions after eta correction for detectors with one and two intermediate strips.

Comparison of the different algorithms In Figure 3.12 the residual distributions for the different algorithms are shown for an unirradiated scCVD diamond. The distribution for the "maximum position" algorithm was fitted with a square function convoluted with a Gaussian. The width of the Gaussian was measured to be 4 µm. This width was used as an estimate for the telescope resolution. The Root Mean Square (RMS), the RMS$_{cor}$ after unfolding a telescope resolution of 4 µm and the FWHM of the distributions for the

73
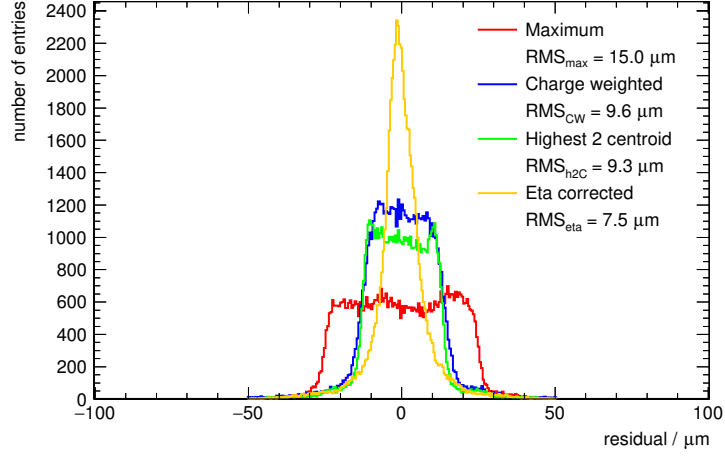
Figure 3.12.: Residual distributions using the different algorithms for position measurement.

	RMS	RMS$_{cor}$	FWHM
Method	[µm]	[µm]	[µm]
Maximum	15.01	14.46	49.63
Charge weighted	9.57	8.69	26.75
Highest 2 centroid	9.29	8.39	26.63
Eta corrected	7.48	6.32	9.69

Table 3.1.: Comparison of the residuals using different algorithms for position measurement. A 4 µm telescope resolution was unfolded for the corrected RMS$_{cor}$.

different algorithms are summarized in Table 3.1. The distribution using the maximum hit position is the broadest with a RMS of 15.0 µm before and RMS$_{cor}$ of 14.5 µm after unfolding. This RMS$_{cor}$ is close to the expected digital resolution of 14.43 µm. The performance of the charge weighted and the highest two centroid algorithms is very similar, the RMS and the FWHM are essentially the same. This is caused by the fact the charge sharing is usually occurring only between two strips.As expected, the narrowest distribution is produced by the eta corrected hit position. A RMS of 7.5 µm was measured before unfolding and 6.32 µm after unfolding. A comparison of the FWHMs demonstrate the precision of the "Eta Corrected Hit Position" algorithm. The "Maximum Hit Position" algorithm results in a FWHM of 49.6 µm, close to the pitch width of 50 µm. With the charge weighted and the highest two centroid hit position algorithms FWHMs of 26.8 µm and 26.6 were achieved, while with the eta corrected hit position algorithm the FWHM is only 9.7 µm.

3.3.3. Asymmetric Eta Distributions - Feed-Across-Correction

During operation of the beam telescope in several beam test campaigns an asymmetric eta distribution was observed and is most likely caused by a change of the readout speed of the telescope. These asymmetries have been observed from other groups using high speed serial readout electronics [132–134].

In Figure 3.13 examples for a symmetric and an asymmetric eta distribution are shown. While the eta distribution from a run during the August 2012 beam test is symmetric, a clear asymmetry can be observed in the eta distribution of the run in the October 2015 beam test.

The observed asymmetry in the eta distribution was not expected for a detector arranged orthogonally to the incident beam. The "eta corrected position" algorithm uses this distribution to improve the position calculation. For runs with an asymmetric eta distribution it was observed that the residual distribution is not centered at zero. In Figure 3.14 the residual distribution for both runs is shown. The "eta corrected position" algorithm was used to measure the hit position in the DUT. It can be seen that the residual distribution in the August 2012 run is centered at zero, while the residual distribution in the October 2012 run has a clear offset.

A method to correct this effect was developed. In the following section this method is described and the influence of this algorithm on the pulse height and the residual distribution was studied.

As described in Section 3.2 the readout of the strip detectors is done with a *VA* amplifier circuit followed by an SIROCCO digitizer. An integrated multiplexer in the *VA* readout chip is used to dispatch all 128 analog signals to one output in a sequential readout mode. This sequential readout mode requires an adjustment of the sample time with respect
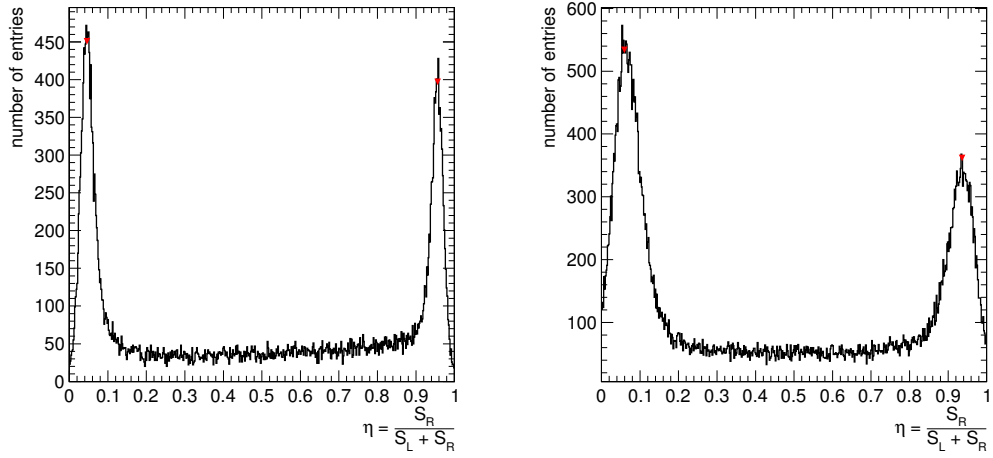
(a) Eta distribution in the August 2012 beam test.

(b) Eta distribution in the October 2015 beam test.

Figure 3.13.: Eta distribution the same detector in two different beam tests. In Figure (a) a symmetric eta distribution is observed, while in Figure (b) the distribution is asymmetric.
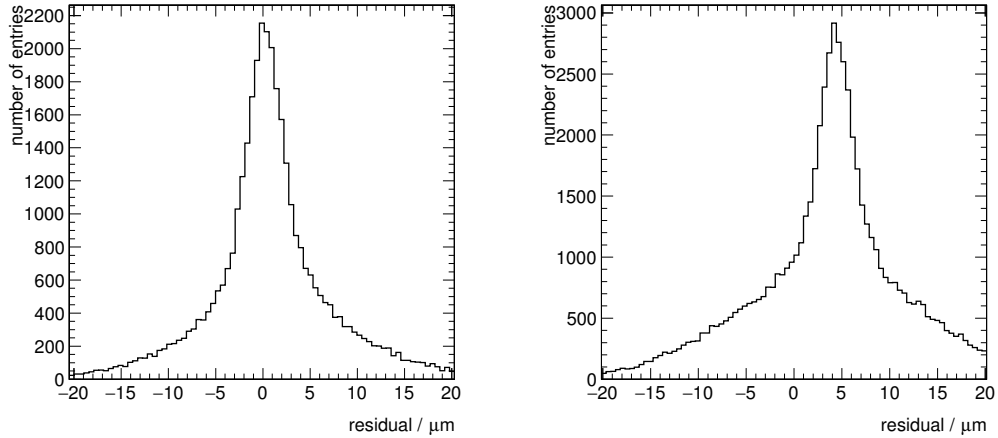
(a) Residual distribution in the August 2012 beam test.

(b) Residual distribution in the October 2015 beam test.

Figure 3.14.: Residual distribution of the same detector in two different beam tests. The "eta corrected position" is used for calculation. In Figure (a) the residual is centered at zero, while in Figure (b) residual has an offset.
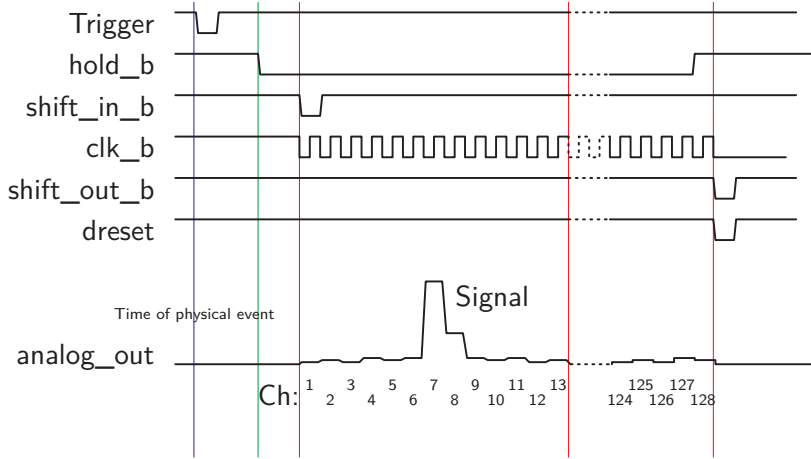
Figure 3.15.: Timing diagram of the *VA* readout chip.

to trigger time. In Figure 3.15 the timing diagram of the *VA* circuit is shown. After the trigger the signal on each DUT channel is integrated for $2\,\mu s$. If the timing is correct the falling edge of the Sample/Hold signal *hold_b* holds the signal of the *VA* readout channel at the peak. Immediately after this a sequential read-out can be performed by activating the output bit-register using *shift_in_b* and *clk_b*. Each falling edge of the *clk* signal switches the output of the *VA* chip in the next channel. The logic part of the chip can be reset either by applying a reset signal *dreset* or, by setting the signal/hold signal back to high, initiating the digital reset signal. The read-out sequence starts with issuing a hold signal *hold_b*, which will open the sampling switches such that each channel holds the signal at the time the hold was issued (green line). The chip is clocked and an ADC sampling performed, and this is repeated until all channels have been sampled.

The change of the eta distribution was studied over several beam test campaigns and the following observations were made. The strength of the asymmetry was constant during each individual beam test, but varied between beam tests. It was observed that the asymmetry is such that the peak close to zero is larger than the peak at one. By the definition of eta η it can be concluded that the probability for the left signal being higher than the right signal is increased. This means that the left signal is the larger signal of the two. This observation leads to the assumption that this asymmetry is caused by electronic feed across between adjacent strips. Such a feed across in the readout system used can occur by non-optimum settings of the SIROCCO sampling time. Since the input resistance of the SDR-Flash is non-zero, a RC-time constant defines the form of the signal for a voltage step V_{step}:

$$V_{\mathrm{cap}} = V_{\mathrm{step}} \left(1 - \exp\left(-\frac{t}{RC}\right) \right) + V_0 \,, \tag{3.7}$$

where RC is the corresponding RC time constant. The time t is the difference between the moment the multiplexer of the *VA2.2* switches to the next channel and the moment when the ADC digitizes the signal.

For a given RC and a given time t the error on the digitization is given by:

$$V_{\text{error}} = V_{\text{step}} \exp\left(-\frac{t}{RC}\right). \tag{3.8}$$

Since the relative sampling time and the RC constant τ should not change within an run, a correction factor α can expressed by

$$\alpha = \exp\frac{t}{\tau}. \tag{3.9}$$

Based on this theory, a method called *Feed-Across-Correction* was developed to correct for this effect. Since neither the RC constant nor the relative sampling time t are known this method is data driven and the correction is applied for each detector individually. Assuming a two channel detector with "real" pedestals of P_0 and P_1 and signals S_0 and S_1 the measured voltage $V_1(\tau, t)$ of channel 1 can be described by:

$$V_1(\tau, t) = V_1(\alpha) = S_1 + P_1 + (S_0 + P_0 - (S_1 + P_1)) \cdot \exp\frac{t}{\tau} \tag{3.10}$$

$$= S_1 + P_1 + (S_0 + P_0 - (S_1 + P_1)) \cdot \alpha \tag{3.11}$$

$$= S_1 + (S_0 - S_1) \cdot \alpha + P_1 + (P_0 - +P_1) \cdot \alpha \tag{3.12}$$

$$= S_1 + (S_0 - S_1) \cdot \alpha + P_1(\alpha) \tag{3.13}$$

$$V_1(\alpha) - P_1(\alpha) = S_1 + (S_0 - S_1) \cdot \alpha \tag{3.14}$$

$$S_{1,measured}(\alpha) = S_1 + (S_0 - S_1) \cdot \alpha \tag{3.15}$$

For a given correction factor α and a given cluster a corrected cluster can be extracted by adding/subtracting a certain amount α to the next readout channel. In the first step the correction factor α is found in an iterative method using the cluster information of the first 40 000 events. This correction factor is then applied to the full data set. After finding the corrections α_i for all detectors, these corrections were used to create a corrected raw data file, which applied the corrections on the raw ADC data. For this new data file all analysis steps were performed in order to extract the calculate the corrected pedestal values.

In Figure 3.16 the results for one DUT in the October 2012 beam test are shown. The black distribution corresponds to the η distribution, while in blue the mirrored distribution $1 - \eta$ is shown. In 19 steps a correction factor $\alpha = -1.2\,\%$ was calculated. After this correction the eta distribution becomes more symmetric. In Figure 3.17 (a) the residual distribution before and after correction are shown. While the original distribution, shown in black, peaks at a residual of $12\,\mu\text{m}$, the corrected distribution is centered at
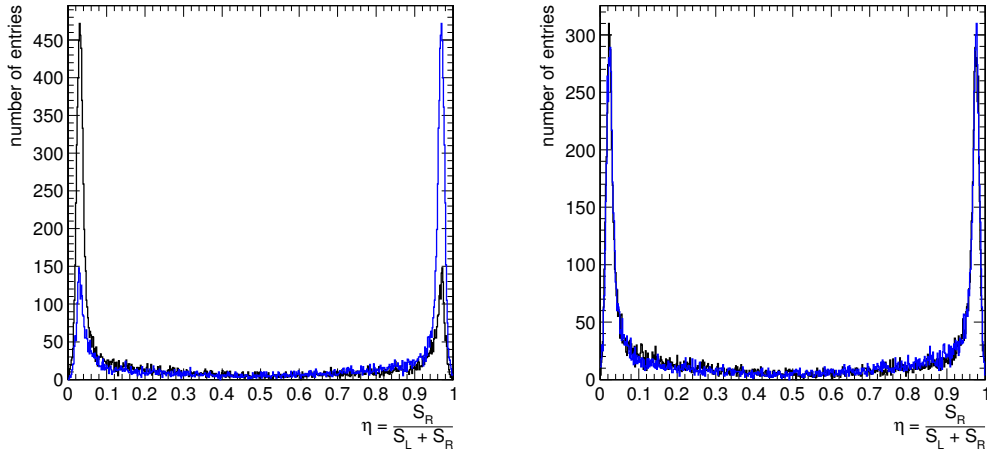
(a) Original eta distribution of Run 16302. The black distribution is the distribution of η, in blue the mirrored distribution $1-\eta$ is shown to enhance the asymmetry.

(b) Eta distribution after applying a correction factor of $\alpha = -1.2\,\%$. The black distribution shows η while the blue distribution shows $1 - \eta$.

Figure 3.16.: Results of the eta correction algorithm. Figure (a)) shows the original distribution, while Figure (b)) shows the corrected distribution with a correction factor $\alpha = -1.2\,\%$.
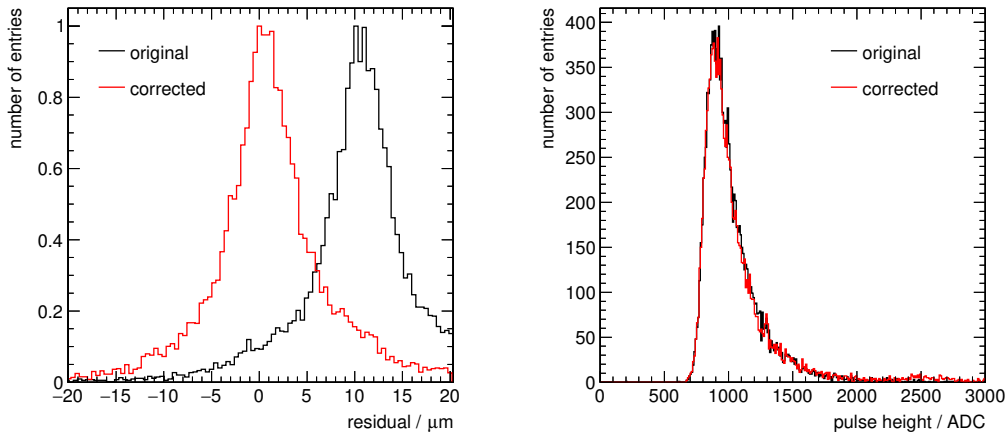
(a) Residual distributions.

(b) Pulse height distributions.

Figure 3.17.: Residual and pulse height distribution before and after the asymmetric eta correction.
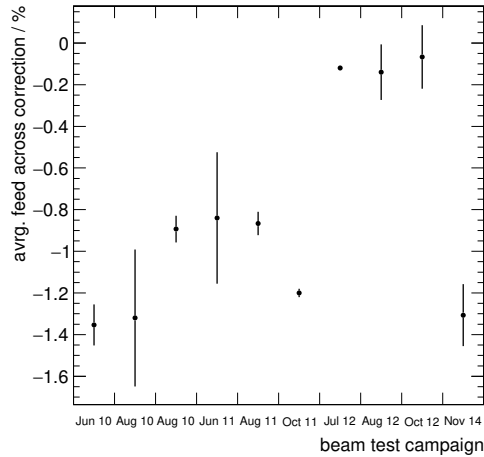
Figure 3.18.: Average feed across correction for all diamonds of the 800 MeV irradiation campaign as function of beam test.

zero. The observed change in the residual distribution suggest that this method corrects for the underlying effect.

In Figure 3.18 the feed across correction for the diamond is shown for multiple beam test campaigns. It can be observed that the strength of the feed across correction changed between beam tests. Only during the beam tests in the year 2012 the feed across correction was close to zero indicating that the timing was close to the optimum.

An important factor is the influence of the feed across correction on the pulse height. In Figure 3.17 (b) the pulse height distribution before and after correction are shown. No differences in the shape of the two distributions can be observed. The mean pulse height has increased by from 1025 ADC to 1056 ADC. The influence on the collected charge was studied over several beam test campaigns in which different feed across corrections were measured. In Figure 3.19 the fraction of the mean pulse height difference after correction over the mean pulse height before correction is shown. The distribution is very narrow indicating that this correction affects the pulse height by less than 1 %.
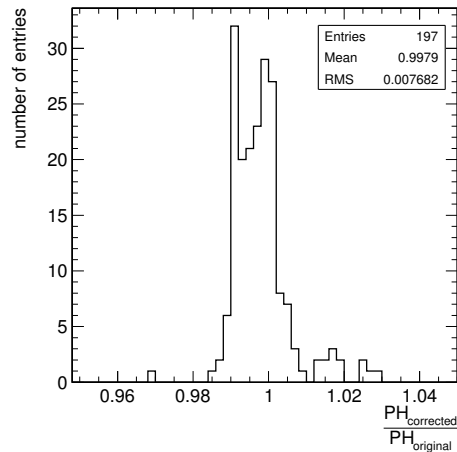
Figure 3.19.: The influence of the Feed-Across-Correction on the collected charge.

From all 197 analyzed runs $96\,\%$ the difference between both means is less than $2\,\%$. This shows that the algorithm can fix the observed offset in the residual distribution, but does not influence the pulse height. Therefore this algorithm was applied for each run.

3.3.4. Detector Alignment

Since the telescope consists of eight detector planes which are separate in the sense that they can be replaced individually, the relative position of each of the detectors must be known very precisely. Due to packaging and measurement uncertainties the absolute position of each detector was not measured with a sub-millimeter precision.

For this reason particle tracks were used to find the precise detector alignment. Each detector plane was aligned with respect to the global telescope coordinate system, shown in Figure 3.1. The position of the detector plane in z direction was fixed. The alignment was performed using an iterative procedure. The alignment procedure consisted of rotations around the beam axis and translations in the x and the y-direction with respect to a global telescope frame. The residual distribution of the DUT, using the "maximum hit position" algorithm, was used to estimate the telescope precision at the DUT. The distribution was fitted with a square function convoluted with a Gaussian. The width of the Gaussian was used as an estimate for the telescope resolution. After the alignment procedure this method results in an error on the predicted hit position at the DUT between $2\,\mu$m and $4\,\mu$m.
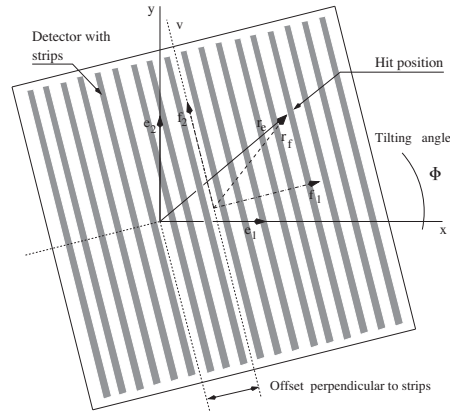
Figure 3.20.: Coordinate system of telescope and detector. The rotation and translation of the detector coordinate system relative to the telescope detector system can be described by an offset x_{off} and an angle Φ_{off}.

3.3.5. Event Selection

For the final analysis step only events were selected which fulfill certain selection criteria. In order to have single particle tracks and avoid hit ambiguities, only events were selected which contain one and only one cluster in each reference detector This selection simplifies all reconstruction steps and typically results in a loss of 25 %. Clusters with saturated channels were rejected. Noisy channels were masked and events with noisy channels in a channel were rejected. Events, which passed these criteria, are called *valid tracks*. Since the DUTs were usually much smaller than the scintillator trigger area, a selection based on the average hit position in all silicon planes was used to remove events passing the telescope outside the active area of the DUT. The positions of the DUTs was found by requiring at least one cluster in the DUT and plotting the average reference hit position.

In Figure 3.22 the average hit position within the reference planes is shown for events with one and only one cluster in each reference plane. By additionally requiring exactly one cluster in the DUT, the shadow of the DUT can be found. This is shown in Figure 3.21 (b). One can see the approximate position of the DUT and noise hits in the active area of the scintillator. The red boxes in both figures indicates the fiducial region in which events were used for the further analysis.
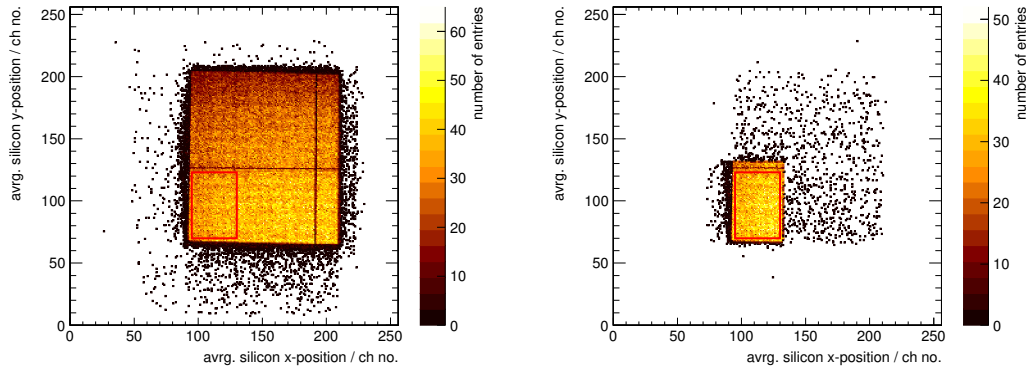
(a) One and only one cluster in each refer-
ence plane.

(b) One and only one cluster in each refer-
ence plane and in the DUT.

Figure 3.21.: Average hit position within the silicon reference planes. In Figure (a) one
and only one cluster in each reference plane is required, while in Figure
(b) exactly one additional cluster in the DUT is required.
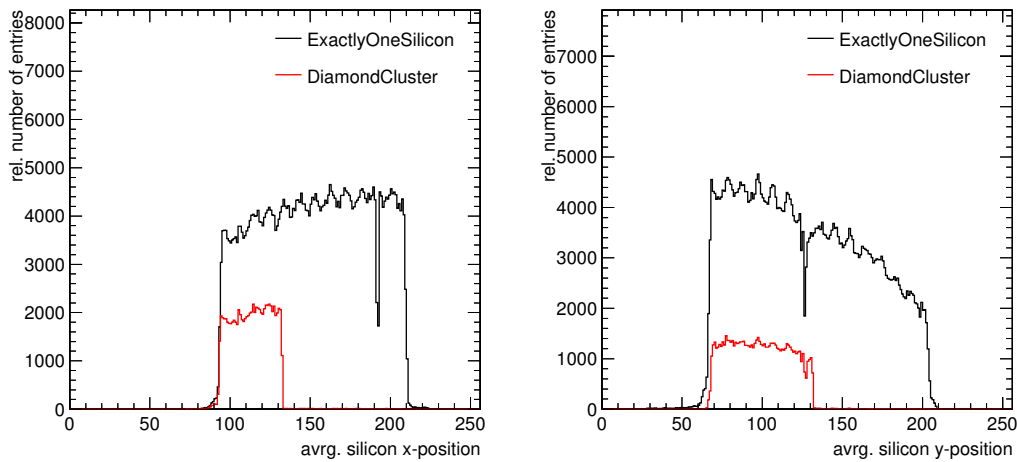
(a) x-Projection.

(b) y-Projection.

Figure 3.22.: Average hit position within the silicon reference planes for events with one
and only one cluster in each reference detector (black) and for events with
one and only one cluster in each reference detector and the DUT (red). The
reduction by requiring additional exactly one cluster in the DUT can be
explained by the small size of the DUT in comparison of the trigger area.

The corresponding projections in the x and in the y-direction are shown in Figure 3.22
(a) and 3.22 (b). The projections for events with exactly one cluster in each reference
detector are shown in black, the projections for requiring in addition exactly one cluster
in the DUT are shown in red. Due to the small size of the DUT in comparison to the

scintillator trigger area many events are removed by requiring a track in the fiducial regions of the DUT. With the black distribution, in which one cluster in each reference plane is required, the actual beam profile can be measured. In the x-direction the distribution is falling with increasing x, while in th y-direction the distribution is flat in the region from channel 50 to 110 and then falls steep. Two inefficient channels due to a broken or noisy strip can be observed in the two dimensional distribution as one vertical and one horizontal line, and as dips in the projections. Over the region of the DUT, shown in red, the beam profile is essentially flat.

For the alignment of the reference telescope events with exactly one valid cluster in each reference detector were selected. From these events the events with exactly one cluster in the DUT were used for the alignment of the DUT.

In the final analysis step, the "transparent analysis" (see Section 3.3.6), the signal response of the DUT was studied without requiring a cluster in the DUT. In addition to requiring exactly one valid cluster in each silicon reference detector, the reconstructed track needed to have a predicted hit position in the fiducial region of the DUT and the goodness of the track fit, described by the χ^2, needed to be below a fixed threshold. Reconstructed tracks which fulfill these criteria are called valid tracks.

3.3.6. Transparent Analysis

The "transparent analysis" is the final analysis in which the signal response of the DUT is studied without the requirement of a cluster in the DUT. By requiring a valid track the hit position is predicted to be in the fiducial region of the DUT. A transparent cluster is built around this predicted hit position. With these clusters it is possible to study the charge response in a region around the predicted hit position. One transparent cluster contains the signal responses of the N closest strip channels around this position. Since no threshold is applied this cluster contains noise fluctuations as well as real signals. The number of channels N included in the transparent cluster can be varied to study the resolution and the charge response without any threshold in a given region around the predicted hit position.

Figure 3.23 shows an example how such a transparent cluster is constructed. With the cluster hit positions in the reference planes $R0$, $R1$, $R2$ and $R3$ the position of the crossing particle in the DUT is predicted. The height of the signal for each channel of the DUT is diagrammed by the height of the bar. The order in which the channels are added to the transparent cluster is indicated above. The corresponding hit and seed threshold are displayed as a blue and green dashed line. In this example the biggest pulse height is in the 2nd channel. The 1st and 4th channel have a signal response above the hit threshold, while all others would not be included in a standard cluster. The 3rd and 8th channel show negative signal responses.
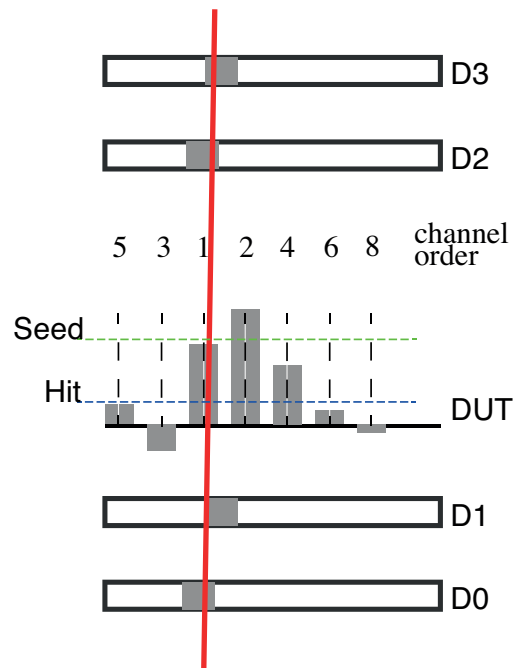
Figure 3.23.: Building transparent cluster the particle track, reconstructed by the detectors D0,D1,D2 and D3 is sketched with a red line. The DUT is in the middle, showing the ordering of the channels by the closeness of the predicted hit position.

Two different methods were used to quantify the signal response of a transparent cluster with cluster size N: The sum of the signals of all N channels ("N out of N"), the sum of the highest and the highest adjacent signal "2 out of N". For the "2 out of N" signal definition the "eta corrected hit position" was calculated. The pulse height distributions for both signal definitions was created during the transparent analysis. The distributions for the "N out of N" signal definition were mainly used as a cross check, while the distributions using the "2 out of N" signal definition were used to define the signal response of the detector. This definition was also used for the comparison of the resolution of the detector. It was also possible to measure the hit recognition efficiency as a function of the cluster threshold t_c. While in a clustered analysis the efficiency ε_{t_S} depended on the cluster seed cut, with this method the threshold t_c for which the detector is fully efficient was found. The threshold was applied on the signal of the whole transparent cluster and on the highest signal within the cluster.

3.4. Measurement of the Damage Constant

As discussed in Section 2.2.3 the MFP $\lambda_{e/h}$ of the sensor material is reduced due to the damage by incident particles. In the model presented the trapping probability increases with increasing fluence and can be described by the formula:

$$\lambda_{e/h}(\Phi_{eq}) = \frac{1}{\frac{1}{\lambda_0} + k_{mfp}\Phi_{eq}} \tag{3.16}$$

where $\lambda_{e/h}(\Phi_{eq})$ is the MFP after being penetrated by a particle fluence Φ_{eq}. λ_0 describes the initial MFP and the damage is represented by the damage constant k_{mfp} .

In the beam tests the collected charge of a DUT can be measured. The collected charge can be converted into the corresponding CCD by using the average number of produced charge carriers per micrometer thickness. The CCD denotes the average distance the electron-hole pair drift apart under the influence of the applied external electric field. In combination with the thickness t of the diamond it is possible to extract the MFP of the material. With measurements of the MFP at several radiation fluences it is possible to extract the damage constant for the penetrating particle species.

3.4.1. Charge Collection Distance to Mean Free Path

The transformation from MFP to CCD for a pad detector [68] with a thickness t is given by formula 2.28:

$$d_{ccd} = \lambda_e \cdot \left[1 - \frac{\lambda_e}{t} \cdot \left(1 - \exp^{-\frac{t}{\lambda_e}}\right)\right] + \lambda_h \cdot \left[1 - \frac{\lambda_h}{t} \cdot \left(1 - \exp^{-\frac{t}{\lambda_h}}\right)\right]$$

This formula depends on the MFPs λ_e and λ_h of electrons and holes and the thickness t of the diamond. It is valid for pad geometries, but is used as a approximation for detectors with a strip geometry.

The MFP depends on the velocity of the charge carriers and the average time until the carrier gets trapped. As the electron and hole mobilities are different [93] ($v_e = 9.6 \times 10^6$ cm/s and $v_h = 14.1 \times 10^6$ cm/s), the ratio of MFPs is approximated by the ratio of the two mobilities, assuming that the trapping probability for electrons and holes are the same. For all results a ratio of $R = \frac{\lambda_h}{\lambda_e} = 1.47$ is assumed. The influence of this ratio is discussed later in this section.

Figure 3.24 shows the relation of MFP and CCD for the scCVD diamond *SINGLE A* with a thickness $t = 466$ µm. With a MFP of 6000 µm 95 % of the produced charge is collected. There exists no analytic form to describe the inverse of this function. For this reason the conversion from CCD to MFP is done by numeric conversion using the *ROOT* framework. As this function is non linear, the error on the CCD measurement needs to be converted into an error on the MFP.

3.4.2. Extraction of Damage Constant

The linearized form of the damage function, in Equation 3.16 is used to measure the damage constant:

$$\frac{1}{\lambda_{e/h}(\Phi_{eq})} = \frac{1}{\lambda_0} + k_{mfp} \cdot \Phi_{eq} \,. \tag{3.17}$$

By plotting $\frac{1}{\lambda}$ versus the fluence Φ_{eq} this linear relation can be directly fitted. As every diamond can have a different constant λ_0, depending on its initial properties, the data
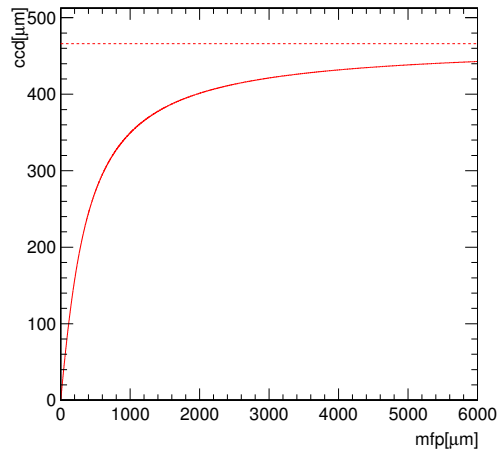
Figure 3.24.: Conversion function of MFP into CCD for the 466 µm thick scCVD diamond.

were fitted for each diamond separately. The measured slope corresponds to the damage constant of that specific sample and the offset is a measure for its initial properties λ_0 and can be translated into an equivalent radiation Φ_0. A weighted mean of these damage constants was calculated to extract the final damage constant for one radiation campaign.

3.4.3. Errors

The errors on the fluences were given by the radiation facilities, and are typically 10% of the respective radiation fluence. For diamonds which have been irradiated multiple times the errors were propagated.

The accuracy of the charge measurement with the beam test telescope was estimated to be 5%. For this estimation the reproducibility of measurements with the same diamonds over multiple years was studied, as well as comparisons of measurements with the beam telescope. The results for positive and negative bias polarity were averaged and the difference of both measurements is associated to an additional error, called *polarity error*. Both, the accuracy error and the polarity error, were added in quadrature.

The Gaussian error of the CCD were converted into an error on the MFP. As there is no analytic function, different methods were compared with each other to estimate the error on the MFP. For several CCDs d_{ccd} and errors σ_{ccd} toy MCs with 1×10^4 events were performed. It was observed that due to the shape of the conversion factor the error on the MFP is asymmetric. The comparison of the different methods showed that a simple method, using the positive and negative difference between $\lambda_{e/h}(d_{ccd})$ and $\lambda_{e/h}(d_{ccd} \pm \sigma_{ccd})$ is a good estimate for the error as soon as the MFP limited. For sensor with a CCD close to its thickness the MFP was estimated to be $10000 \, {}^{+\,40000}_{-\,6500} \, \mu m$, corresponding to a CCD of 97% of the maximum thickness.

For combining the damage constants to the final value, the errors of each fit were used to weight the different constants. This resulted in the final value including an uncertainty. The ratio of the MFPs of electrons and holes was varied up and down to see the influence of this on the damage constant. The spread when varying the ratio by 50% was taken as a systematic error.

3.5. 800 MeV Irradiation

The samples were irradiated in the blue room of the LANSCE irradiation facility [118] in multiple steps in order to be able to measure the radiation damage as a function of dose. The dose of the various irradiations was provided by the facility and was measured with a precision of roughly 10 % by the procedure described below. Aluminum foils were placed directly in front of each sample (or behind as space allowed) in the 800 MeV proton beam and used as dosimeters. In the interaction of the aluminum with the proton beam p, the element ^{22}Na was produced. The ^{22}Na decays via $\beta^+ \sim 90.32$ % of the time and via electron capture 9.62 % of the time to excited ^{22}Ne. The half-life of ^{22}Na is 2.602 years. The excited ^{22}Ne quickly de-excites by emitting a gamma ray of energy 1274.5 keV. The gamma energy spectrum was acquired at a distance of 11 cm with an ORTEC GEM45P4-76-SMP gamma ray detector system [135] and an ORTEC DSPEC-50 Multi Channel Analyzer (MCA) [136]. With a mixed gamma standard point source containing 11 different radionuclides an energy calibration with a quadratic fit and an efficiency calibration, using a 6-term polynomial fit, were performed. After calibration the activity at a particular energy was measured and the total activity of the foil was extracted. In the last step the total activity was used to calculate the incident proton fluence.

The estimated uncertainty in the measurement of the production cross-section of ^{22}Na is about 2.6 %. A typical aluminum foil was weighed to ± 0.1 mg precision, and its contribution to the uncertainty in the measurement was less than 1 %. The counting uncertainty was highly dependent on the amount of time the aluminum foil was measured by the gamma ray spectrometer. It can very between 10 % when counting for 10 min and 2 % to 3 % when counting for 12 h or longer. The dimensions of the foil were measured to the precision of ± 0.001 cm and contribute uncertainty to the measurement of about 0.5 %. The uncertainty due to the uncertainty of the measurement of counting time was less than 0.1 %. This results in a total uncertainty of about 10 % for each radiation dose. The error on the total radiation is calculated by adding the errors of each radiation dose in quadrature.

3.6. Test Procedure

In the following section the test procedure for each diamond is described. Since the *VA2.2* readout chip is not radiation hard the diamonds were irradiated without readout electronics and had to be (re-)connected for each beam test.

3.6.1. Device Preparation for Radiation

After removing the *VA2.2* readout electronics, the metalization on the diamond was removed by chemical cleaning, as described in Section 2.3.4. This avoided activation of the metalization and simplified the shipping procedure. Two diamonds were tested in multi step irradiation which required the removal of the metalization from an irradiated sample. In order to avoid annealing of the sample due to high temperatures during the chemical cleaning, the cleaning method was slightly adjusted. More details about the adjustments can be found in Appendix A.4.

3.6.2. Device Preparation for Beam Test

To test each diamond in the beam test a strip pattern was fabricated on each sample. The same strip mask was used for both scCVD and pCVD diamonds. The contact electrodes for all devices tested were made out of Cr/Au, in which Cr is working as the adhesive layer. The thicknesses of the metals were chosen to be 500 Å for Cr and 2000 Å for Au. The bias side was fabricated with a single pad. The readout side was fabricated with 25 µm wide strips with a 25 µm gap between strips producing a device with 50 µm pitch. The strip pattern was enclosed with a guard ring to minimize edge currents from being picked up by the individual electronic channels. After metalization of both sides the device were annealed at 400 °C for 4 min in an N$_2$ atmosphere to provide a good contact of the metalization with the diamond. The bias electrode was glued with conductive epoxy to a ceramic hybrid containing a bias pad and bias circuit to power the device. The ceramic hybrid was mounted next to a printed circuit board which housed the IDEAS *VA2.2* readout chip so that each readout strip could be directly wire bonded from the diamond strip to one *VA2.2* readout channel. Figure 3.25 shows a picture of the scCVD diamond sensor *SINGLE A* mounted on a ceramic printed circuit board and wire bonded to the *VA2.2* readout electronics.
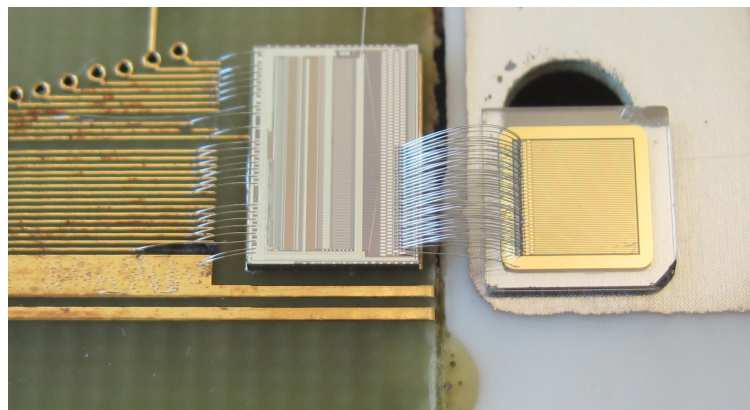
Figure 3.25.: Photograph of the scCVD diamond strip detector *SINGLE A* (on the right) mounted on a ceramic hybrid and wire bonded to *VA2.2* readout electronics (in the middle).

3.6.2.1. Initial Source Tests

All diamonds were initially measured using source tests. As a new *VA2.2* readout chip was used for each beam test, the detectors were calibrated in the lab. The lab calibration was performed at Ohio State University (OSU) with a 37 MBq ^{90}Sr source using the same readout electronics used in the test beam. The gain and noise of every channel was measured and adjusted. After the gain calibration the signal response of the diamond detector was studied as a function of bias voltage. At bias voltages of ±500 V and ±1000 V extended measurements with a duration of 4 h to 8 h were performed. A comparison of the signal response in the original (unpumped) and the pumped state was made. Depending on the radiation dose, each diamond was pumped for 4 h to 8 h. During these tests the current of the device was monitored. The maximum bias voltage that each device could withstand was measured for positive and negative polarity. Diamonds were selected for the irradiation studies if they held ±1000 V with less than 2 nA of leakage current and had less than 20 % difference in the CCD for positive and negative bias voltages.

3.6.3. Beam Tests

As described in Section 3.2, all diamonds were tested with the *Strasbourg Telescope* in the H6 beam line at CERN using 120 GeV protons.

(a) *X* direction.
(b) *Y* direction.
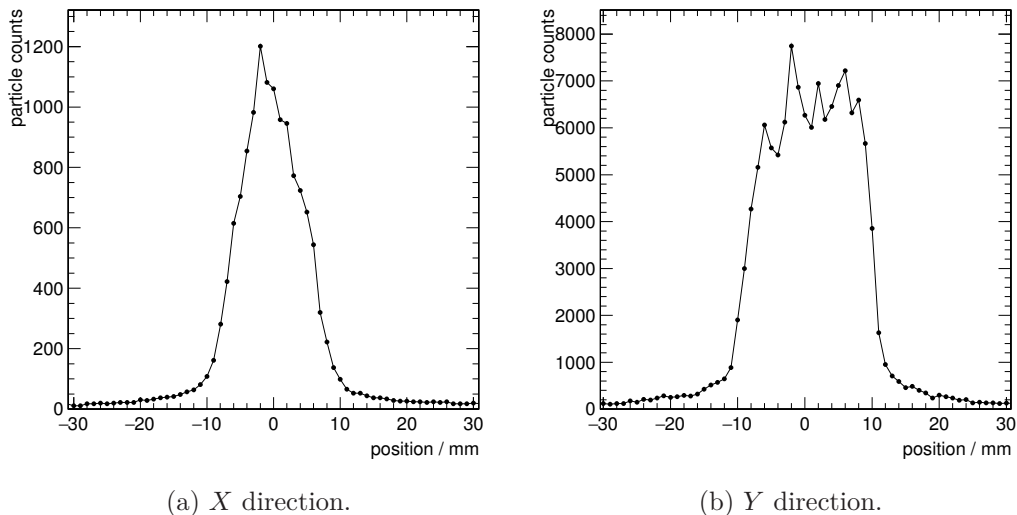
Figure 3.26.: Beam Profiles of the May 2016 beam test.

91

3.6.3.1. Beam Profile

The beam line is equipped with multiple wire chambers to measure the beam profile during operation. During each beam test the beam settings were optimized in such that the profiles look similar to the ones shown in Figure 3.26. The measurements of the beam profile were performed with a wire chamber located directly behind the beam telescope. The beam profile in X direction has a mean of $-0.48\,$mm and a sigma of $4.82\,$mm, while the profile in Y direction is broader with a mean of $1.04\,$mm and a sigma of $7.18\,$mm. The FWHMs of the distributions are $11\,$mm, respectively $17\,$mm. The intensity of the beam was optimized such that preferentially one single track was recorded during each trigger. This resulted in a data taking rate of 3000 to 3600 triggers per spill.

3.6.3.2. Data-Taking Protocol

Each diamond was tested at both polarities at two different voltages. Usually the low voltage runs were taken at a bias voltage of $\pm 500\,$V, corresponding to an electric field of $\pm 1\,$V/µm. The high voltage runs were typically taken at $\pm 1000\,$V to $\pm 1100\,$V, corresponding to an electric field of approximately $\pm 2\,$V/µm.

A typical run low voltage run had $400\,000$ triggers and took about $2\,$h, while a high voltage run had $1\,000\,000$ triggers and took about $\sim 5\,$h.

The test of each diamond started with the positive polarity and was followed by the negative polarity. In order to bring the detector into a stable state which it would be in during data taking at any high luminosity collider experiment, each diamond was "pumped" (see Section 2.3.3.1) with two beta sources. First the diamond was pumped with a $\sim 54\,$MBq ^{90}Sr source on the bench before it was transported to the setup. In order to guarantee a fully pumped diamond even in case if there is a small light leak the diamond was pumped again for additional $20\,$min with a $\sim 23\,$MBq^{90}Sr source at the test side. The full data taking protocol consisted of

- $4\,$h pumping before the first test with a $\sim 54\,$MBq ^{90}Sr source
- $20\,$min pumping with a $\sim 23\,$MBq ^{90}Sr source
- data taking at positive low voltage, $400\,000$ events ($\sim 2\,$h)
- $20\,$min pumping with a $\sim 23\,$MBq ^{90}Sr source
- data taking at positive high voltage, $1\,000\,000$ events ($\sim 5\,$h)
- $4\,$h pumping before the first test witha $\sim 54\,$MBq ^{90}Sr source
- $20\,$min pumping with a $\sim 23\,$MBq ^{90}Sr source
- data taking at negative low voltage, $400\,000$ events ($\sim 2\,$h)
- $20\,$min pumping with a $\sim 23\,$MBq ^{90}Sr source
- data taking at negative high voltage, $1\,000\,000$ events ($\sim 5\,$h)

3.6.4. Calibration

The signal response of the diamond was measured in ADC units. A calibration was required in order to obtain the calibration constant that converts it into an electric charge. The calibration constant C_{setup} is defined as the number of ADC counts per $100\,e$. The calibration constants for each beam test was provided by OSU. Various methods were used in order to find the calibration constant.

For each repeater card and each beam test campaign a separate calibration constant was measured. Four different methods for determine the calibration constant are presented in this section. For certain beam test campaigns, depending on the tested diamonds, not all methods could be performed. If multiple methods were performed, the different results were used to perform a consistency check.

Calibration with scCVD diamond The most accurate calibration method uses an unirradiated scCVD diamond as a reference detector. These calibration scCVD diamonds were measured with a source in the lab and determined to be collecting full charge. The full charge collection Q_{full} is given by the thickness t and the average signal $\langle Q_S \rangle = 36\,e/\mu m$ created by a MIP in $1\,\mu m$ diamond.

$$Q_{full} = t \cdot \langle Q_S \rangle \tag{3.18}$$

Therefore the calibration constant can be extracted by the mean M of the measured pulse height distribution.

$$C_{setup} = \frac{M}{Q_{full}} . \tag{3.19}$$

This calibration method was the primary method used and required a beam test of an unirradiated scCVD diamond. It was used in 14 of the 24 data sets analyzed. The errors on the measurement of the charge collection and on the thickness was propagated, resulting in an error on the calibration constant.

Calibration with noise measurement This method involves measuring the noise in the lab N_{lab} before the beam test and obtaining the ratio of the noise in the DUT to that of a detector previously measured N_{prev} in a test beam. The ADC to e calibration was then determined by the previous calibration C_{prev} by

$$C_{setup} = C_{prev} \times N_{lab}/N_{prev} \tag{3.20}$$

Calibration with *VA2.2* calibration mode   The *VA2.2* readout chip provides a calibration mode. During the initial source testing a calibration of each channel was performed individually. An external test input was connected to the input of the amplifier circuit of one channel. Via the test input a voltage step ΔV was put on a precision capacitor C.

A $1.80\,\mathrm{pF}$ capacitor with a $1\,\%$ tolerance was used for this purpose. The voltage step injected a charge $Q = \Delta V \cdot C$ and the signal response of the amplifier circuit were measured for several voltage steps. By correlating the signal response and the input charge it was possible to measure the slope which corresponds the the calibration constant.

Noise Consistency Check   As discussed in Section 3.2 the *VA2.2* readout chip has an ENC of $60e^- + 11e^-/\mathrm{pF} \cdot C_d$. All tests DUTs have similar sizes of $5 \times 5\,\mathrm{mm}^2$. Therefore length of the readout strips was relatively short. This results in similar input capacities for all DUTs.

For each DUT the noise of each channel was measured before and after common mode correction during each run. In Figure 3.27 the measured noise before and after common mode correction is shown for 24 runs. The average raw noise for all channels was observed to be between $91.5\,\mathrm{e}$ and $139.9\,\mathrm{e}$ with a RMS of $13\,\mathrm{e}$. By applying the common mode correction the noise could be reduced. The common mode corrected noise ranged from

(a) Raw noise.   (b) Common mode corrected noise.
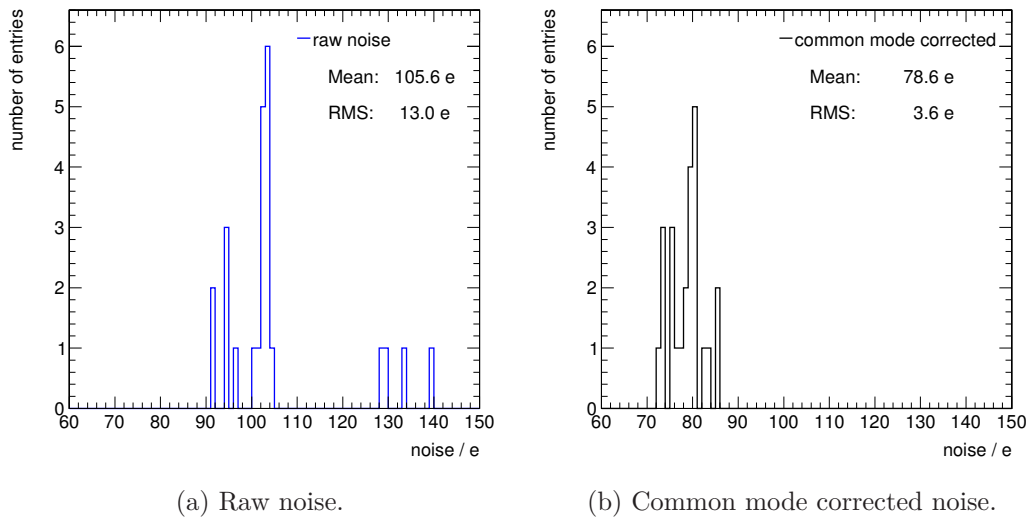
Figure 3.27.: Raw and common mode corrected noise observed in 24 data sets. By applying the common mode correction the both the mean and the RMS were reduced. The raw noise distribution has a mean of $105.6\,\mathrm{e}$ and a RMS of 13e, while the common mode corrected noise distribution has a mean of $78.6\,\mathrm{e}$ and a RMS of $3.6\,\mathrm{e}$.

72.2 e to 85.9 e with a mean of 78.4 e and RMS of 3.8 e. The measurement of the common mode corrected noise was therefore used as a consistency check for the calibration. The common mode corrected noise was required to agree within $\pm 10\,\%$ with the average.

3.7. Tested Diamonds

In order to compare the radiation tolerance of scCVD and pCVD diamonds a selection of scCVD and pCVD diamond samples with various properties (size, thickness, charge collection distance) were irradiated with 800 MeV protons. The different diamonds are described in the following. One scCVD and three pCVD diamonds were irradiated to doses up to 12.6×10^{15} protons/cm^2. Table 3.2 shows the diamonds used in this study and the doses of 800 MeV protons they received. The scCVD diamond *SINGLE A* was irradiated in five steps up to a dose of 7.82×10^{15} protons/cm^2 and is therefore the diamond with the most data points. The three pCVD diamonds were irradiated in one and two steps. These diamonds had CCDs of 218 µm, 227 µm and 227 µm, which corresponded to state of the art pCVD diamond material at the time they were tested.

Diamond	Type	Thickness [µm]	Size [mm^2]	CCD [µm]	Doses [10^{15} p/cm^2]
SINGLE A	scCVD	466	5×5	466 / 466	0
					0.78 ± 0.09
					2.39 ± 0.18
					3.05 ± 0.19
					7.82 ± 0.51
POLY A	pCVD	516	10×10	230 / 227	0
					$12.6 \ \pm 1.3$
POLY B	pCVD	510	10×10	218 / 223	0
					3.50 ± 0.35
POLY C	pCVD	466	10×10	227 / 241	0
					5.50 ± 0.55
					10.30 ± 0.73

Table 3.2.: Properties of diamonds irradiated with 800 MeV protons and the doses they received. The two CCDs for each diamond are measured at positive and negative polarity in the unirradiated state.

3.8. Results

In this section the results of the beam test campaigns are presented. In the scCVD diamond a time dependency on pulse height was observed which was studied in order

to understand the underlying cause. It is followed by the measurement of the damage constant for 800 MeV proton irradiation. A study of the change of resolution with in increasing fluence was performed for the scCVD diamond. The chapter closes with a study of the signal response and the position resolution of the pCVD diamond after an irradiation to 12×10^{15} p/cm^2.

3.8.1. Pulse Height Stability Studies

As described in Section 3.6.1 the metalization on the diamond was removed before irradiation to reduce the activation of the sample. The scCVD diamond *SINGLE A* was one of the first diamonds which was irradiated in multiple steps in order to measure multiple points on the damage curve. This meant removing the metalization of an irradiated diamond. In order to avoid systematic uncertainties introduced by annealing of the diamond sample, see Section 2.2.3.3, the cleaning method for the irradiated sample was adapted to prevent unnecessary heating of the sensor. Therefore the duration of the single steps was reduced and certain steps were skipped. In the Table in Appendix A.4 the full history of the diamond can be found. After each irradiation a new metalization was applied and the diamond was wire bonded to the *VA2.2* readout chip and tested in a beam test. In Figure 3.28 the signal response during one run is shown. An unexepected dependencey of the signal response on the event number can be observed. In the following the procedure to study this dependency is described and the results are shown.

The analysis of the time dependence of the signal response uses the event number as an indicator for the time, as the trigger time stamp was not recorded. For this study
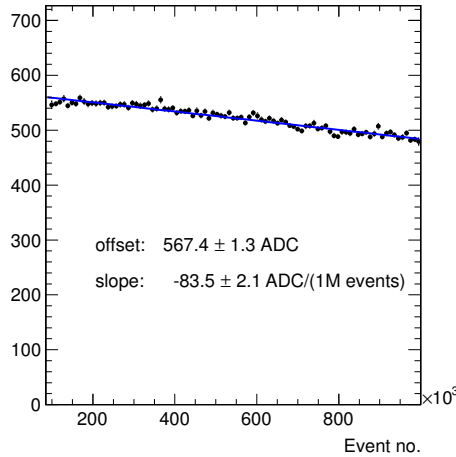
Figure 3.28.: Average pulse height as a function of event number for the scCVD diamond *SINGLE A* after the 3$^{\mathrm{rd}}$ irradiation, corresponding to a total fluence of $3.05 \pm 0.19 \times 10^{15}$ p/cm^2.

each run was divided into subsets of 10 000 events, corresponding to approximately three spills, each containing ∼3000 to 3500 events. Each subset contained 300 to 700 events, depending on the beam test campaign. For each subset the average pulse height was calculated. The profile of the average pulse height response for each 10 000 was then plotted as a function of event number. The first 100 000 events were removed from this analysis as these events were used for alignment and therefore were not included in the final dataset.

In Figure 3.29 the corresponding plots for the unirradiated diamond as well as the measurements performed after the first, the second and the third irradiation are shown. In the measurement performed for the unirradiated scCVD diamond, shown in Figure 3.29 (a),no pulse height dependence can be observed. A linear fit results in a slight positive slope of 10.7 ± 8.7 ADC/1M events which is compatible with a flat distribution within less than two sigma. The goodness of the linear fit ($102/90 = 1.13$) is similar to the goodness of a constant fit ($106/91 = 1.16$). Therefore it can be concluded that the pulse height is stable during the full run for the unirradiated scCVD diamond sensor.

The reproducibility error was estimated by dividing it into two runs of the same length and using two runs performed in two different beam tests. The mean slope of these two measurements was compared with the slope of a fit of the full data set. This resulted in a sigma of 6.6 ADC/1M events. After the fourth irradiation the diamond was tested in two different beam tests without changing the metalization. The two runs were compared with each other using the same amount of events, i.e. 1M events. This results in an additional component of 0.9 ADC/1M events. Both errors are added in quadrature and the resulting reproducibility error is 6.7 ADC/1M events. Another component on the reproducibility error are variations of the slope due to different pulse heights. This component could not be studied as only one unirradiated diamond was tested. Therefore the reproducibility error of 6.7 ADC/1M events can be considered as a lower limit on this error.

The results of the linear fit for all four tests are summarized in Table 3.3. It can be observed that after the first irradiation the pulse height of the detector is decreasing with increasing event number. With a linear fit a baseline slope of -40.0 ± 10.2 ADC/1M events was found. This effect was amplified with the 2nd and 3rd irradiation. After the third radiation a slope of -83.5 ± 7.0 ADC/1M events and an interpolated pulse height at the beginning of the run of 567.4 ADC was observed. The mean pulse height for all events used for the transparent analysis is 522.6 ADC. Resulting in a difference of 45 ADC, which corresponds to reduction by 10%.

This pulse height decrease during a run was not observed before and could not be easily understood. The main difference between this diamond and other diamonds was the number of irradiation steps. It was one of the first diamond samples which was irradiated in multiple steps. This decrease got more pronounced after each irradiation step and it was concluded that the reduced cleaning procedure might be a possible cause.
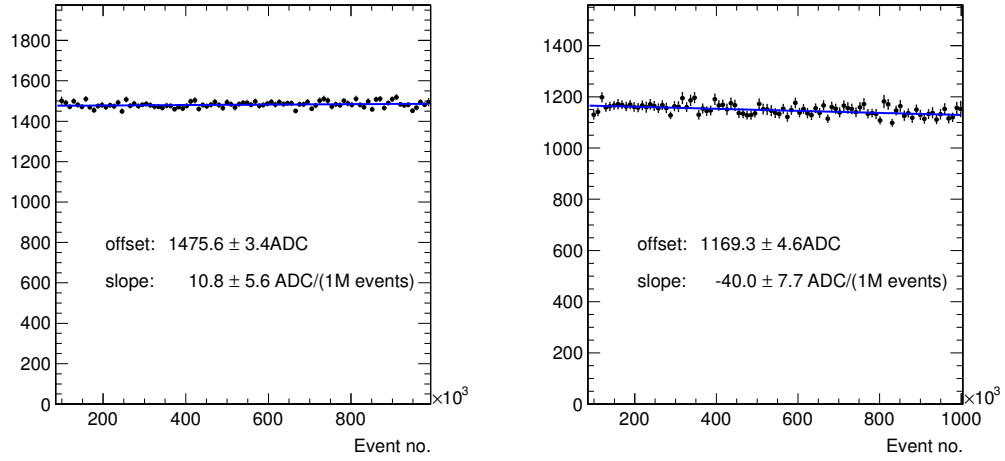
(a) Without irradiation, corresponding to a total fluence of 0×10^{15} p/cm^2.

(b) After the 1st irradiation, corresponding to a total fluence of $0.775 \pm 0.074 \times 10^{15}$ p/cm^2.
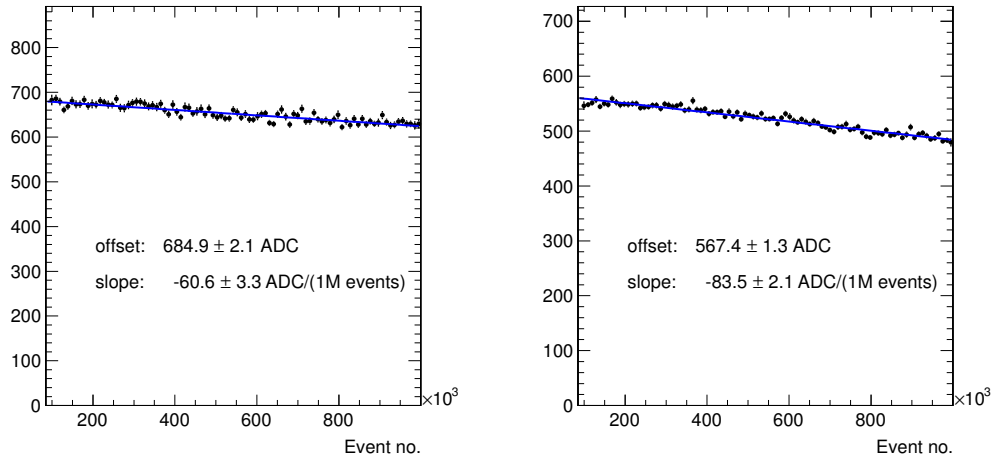
(c) After the 2nd irradiation, corresponding to a total fluence of $2.39 \pm 0.18 \times 10^{15}$ p/cm^2.

(d) After the 3rd irradiation, corresponding to a total fluence of $3.05 \pm 0.19 \times 10^{15}$ p/cm^2.

Figure 3.29.: Average pulse height as a function of event number for the scCVD diamond *SINGLE A*. The diamond was cleaned with the simple cleaning method.

Run No.	Irr. Step	Mean PH [ADC]	Offset [ADC]	rel. PH difference [%]	Slope p1 [ADC/1M ev.]	total error [ADC/1M ev.]	Sign. $\frac{p1}{\sigma_{p1}}$	Goodness of Fit χ^2/NDF
16001	0	1482.5	1476.0 ± 3.4	-0.4	$+10.8 \pm 5.6$	8.7	1.2	102.0/ 90
16303	1	1159.6	1169.0 ± 4.6	0.8	-40.0 ± 7.7	10.2	4.0	78.5/ 90
17101	2	652.2	684.9 ± 2.1	4.7	-60.6 ± 3.4	7.5	8.2	99.0/ 90
17208	3	522.6	567.4 ± 1.3	7.9	-83.5 ± 2.1	7.0	12.1	104.5/ 90
18003	4	273.9	280.3 ± 0.6	2.3	-6.6 ± 0.5	6.7	1.0	183.6/187
	4	277.3	281.3 ± 0.9	1.4	-8.3 ± 1.5	6.9	1.2	75.1/ 90
	4	270.5	276.0 ± 2.2	2.0	-3.8 ± 1.4	6.8	0.6	93.4/ 90
19109	4	284.1	287.3 ± 0.8	1.1	-6.6 ± 1.3	6.8	1.0	96.2/ 90

Table 3.3.: Pulse height dependence of each run at a bias of $+1000\,\text{V}$. The cleaning method was switched for the fourth irradiation (before run 18003). The total error was calculated by adding the fit error on the slope and the reproducibility error in quadrature.

During the preparation of the sample after the third irradiation to a total dose of $3.05 \times 10^{15} \, \text{p/cm}^2$ the metalization of the detector failed. The metal did not stick on the diamond which is an indicator that residuals were left on the diamond surface. Even though additional cleaning steps were performed after this failure, the pulse height dependence on event number increased, indicating that the additional cleaning steps did not solve the problem.

After the fourth irradiation step it was decided to use RIE as an extra cleaning step. With a duration of 15 min on each side a total of 0.1 μm to 0.3 μm diamond material was remove from each side. The results of the two following beam test campaigns are shown in Figure 3.30. It can be seen that the pulse height dependence is strongly reduced by more than one order of magnitude. The pulse height decreased by $6.6 \pm 6.7 \, \text{ADC/1M}$ events, which is consistent with a measurement without any dependence. While the extracted offset resulted in pulse height of 287.3 ADC, a mean pulse height of 284.1 ADC was measured in run 19109. This corresponds to a 1 % effect, which can be neglected in comparison to the other uncertainties of the measurement.

The same analysis was performed for the pCVD diamonds. The results are summarized in Table 3.4. It can be seen that the relative error is much smaller and the offset is compatible with the mean pulse heights. The measured differences between the mean pulse height and the offset extracted from the fit are used as an additional error on the CCD measurement of the scCVD *SINGLE A*.

(a) Tested in Nov 2014.   (b) Tested in Oct 2015
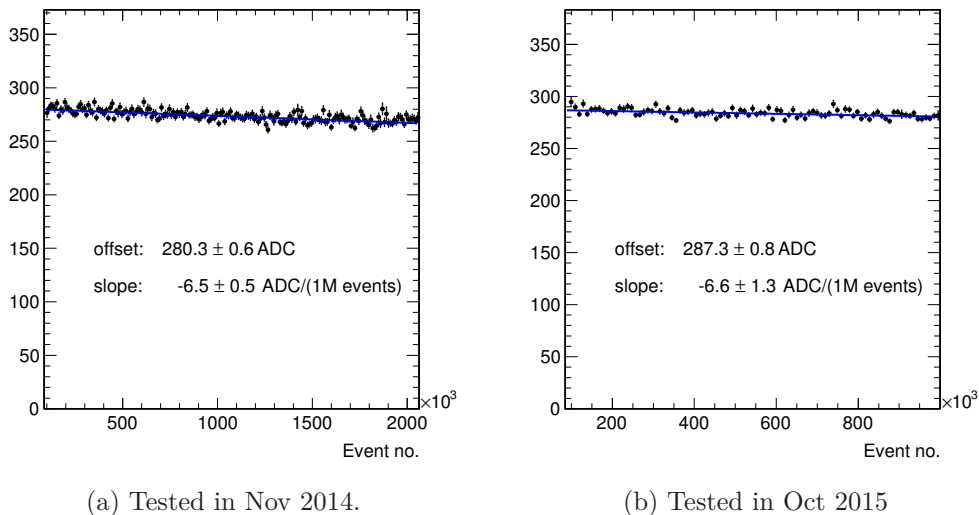
Figure 3.30.: Average pulse height as a function of event number for the scCVD diamond *SINGLE A* after the 4th irradiation, corresponding to a total fluence of $7.82 \pm 0.51 \, \text{p/cm}^2$. The diamond was cleaned using RIE.

Diamond	Run	Mean PH [ADC]	Offset [ADC]	Slope [ADC/1M ev.]	tot. Error	rel. Error [%]
POLY A	15 005	139.8	139.7 ± 0.6	-0.4 ± 1.0	6.7	-0.1
POLY B	16 009	378.2	383.8 ± 2.8	-23.6 ± 5.7	8.7	1.5
POLY C	15 005	242.5	240.3 ± 1.2	$+3.4 \pm 2.0$	6.9	-0.9
	16 009	160.1	163.6 ± 1.2	-8.9 ± 2.4	7.0	2.1

Table 3.4.: Pulse height dependence of each run at a bias of $+1000\,\text{V}$ for all pCVD diamonds.

3.8.1.1. Conclusion

In order to test diamonds with multiple radiation levels, a removal of the metalization was required before each radiation. It was decided to use a modified cleaning method which reduced the heating of the diamond and therefore prevent annealing of the diamond after irradiation. A pulse height decrease during each run was observed after the first radiation step, which got more enhanced with the second and third irradiation. Due to this observation and due to the problems during the metalization of the sample, an additional cleaning step using RIE was included in the procedure for the preparation of the sample after the fourth irradiation. With this method the pulse height decrease during the run was consistent with zero. This suggests that the observed decrease was caused by surface effects and is not a diamond bulk effect. In order to avoid such behavior in the future the use of RIE to clean the diamond is recommended. In order to improve the measurement it is necessary to reduce the reproducibility error. This could be achieved by testing the same diamond multiple times during one beam test and within multiple beam tests without changing the metalization and the readout electronics.

3.8.2. Damage Constant for 800 MeV Protons

The CCD of each diamond was extracted from the mean pulse height of each run, measured in ADC and then converted into electrons with the corresponding calibration constant. In Table 3.5 an overview of all tested diamonds is given, including the beam test campaigns, total integrated fluences, the calibration constants and the measured noise. The pCVD diamonds were not tested in a beam test campaign before the radiation. Therefore the initial CCD was only measured on the calibrated source setup. The CCDs were measured at electric fields of $\sim 1\,\text{V/µm}$ and $\sim 2\,\text{V/µm}$, corresponding to a bias voltage of $500\,\text{V}$ and $1000\,\text{V}$ for a diamond with a thickness of $500\,\text{µm}$. The data at the lower electric field was used for consistency checks and the data taken at an electric field of $\sim 2\,\text{V/µm}$ were used for the final analysis. For runs which showed decreasing signal response during run the average signal response was taken as the mean signal response,

Diamond	Fluence [p/cm^2]	Beam Test	Calib. Constant [ADC/100 e]	measured Noise [e]
Single A	0 ± 0	Jun 2011	8.72 ± 0.12	81.0 /82.2
	0.78 ± 0.07	Oct 2011	7.80 ± 0.12	72.5 /73.3
	2.39 ± 0.18	Aug 2012	7.80 ± 0.12	80.6 /80.0
	3.05 ± 0.19	Oct 2012	7.60 ± 0.12	82.4 /85.5
	7.82 ± 0.51	Nov 2014	7.80 ± 0.12	75.6 /76.4
	7.82 ± 0.51	Oct 2015	7.80 ± 0.12	77.7 /85.9
Poly A	0.00 ± 0.00	–	–	–
	12.60 ± 1.30	Jun 2010	7.60 ± 0.12	79.2 /79.2
Poly B	0.00 ± 0.00	–	–	–
	3.50 ± 0.35	Aug 2010	8.72 ± 0.12	73.8 /75.2
Poly C	0.00 ± 0.00	–	–	–
	5.50 ± 0.55	Jun 2010	7.60 ± 0.12	79.6 /80.0
	10.30 ± 0.73	Jun 2011	8.72 ± 0.12	73.6 /75.2

Table 3.5.: Overview of all diamonds irradiated with 800 MeV protons. The total fluence in the different beam test campaigns as well as the calibration constants and the measured noises for positive and negative bias voltage are given.

the spread of between the initial signal response and the signal response at the end of the run was taken as an additional error and was added in quadrature to the reproducibility error and the polarity error.

From the beam test data the CCD at each radiation dose was measured for the positive and the negative bias polarity. Both results were averaged to the result for one irradiation level. The results of the two polarities agree with each other for the pCVD diamonds, while a difference was measured for the scCVD diamond. In order to understand this difference the data point at the highest fluence was retaken in a different beam test. The results of both beam tests are in agreement with each other. This difference is associated with a systematic error and is discussed later in this section. In Table 3.6 the measured CCDs of the diamonds are summarized including the corresponding errors.

In Figure 3.31 the linearized data including the corresponding fits are shown. The fit of the scCVD sample crosses the x axis close to the origin, while the fits of the pCVD sample cross the y axis at ∼3/mm. The slopes are similar for pCVD and scCVD diamonds. This can also be seen in Table 3.7, in which the results of all fits are summarized. All damage constants agree with each other within the errors. The error of the scCVD diamond is the smallest as the fit is performed with the most data points.

The damage constants of all samples are depicted in Figure 3.32. All constants appear consistent with each other, indicating a common mechanism of radiation damage. The

Diamond	Fluence $[10^{15}\,\mathrm{p/cm^2}]$	CCD [µm]	Error [µm]	Spread [µm]	Slope Error [µm]
Single A	0.00 ± 0.00	466.0	20.0	0.0	1.9
	0.78 ± 0.07	396.2	19.0	16.0	3.2
	2.39 ± 0.18	227.7	12.0	7.0	10.7
	3.05 ± 0.19	184.2	10.0	9.0	14.5
	7.82 ± 0.51	88.8	13.5	9.0	2.0
	7.82 ± 0.51	91.1	13.5	9.0	1.0
Poly A	0.00 ± 0.00			$-$	
	12.60 ± 1.30	51.75	5.5	0.8	0.1
Poly B	0.00 ± 0.00			$-$	
	3.50 ± 0.35	121.85	8.0	2.75	1.8
Poly C	0.00 ± 0.00			$-$	
	5.50 ± 0.55	93.67	6.0	4.78	0.8
	10.30 ± 0.73	51.45	7.5	0.75	1.1

Table 3.6.: Measured CCDs and errors for all runs used for the measurement of the damage constant.
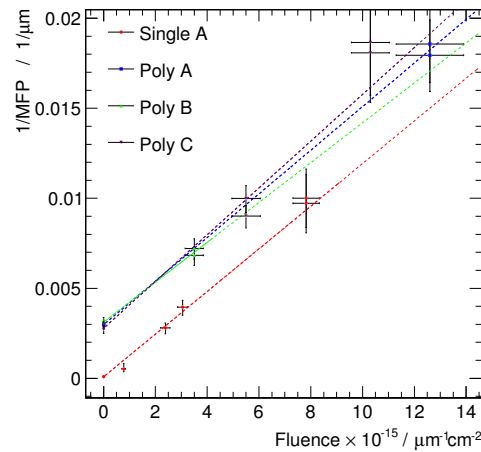
Figure 3.31.: The inverse of the MFP as a function of fluence, including the linear fits, for the three pCVD diamonds and the scCVD diamond which are irradiated with 800 MeV protons.

Diamond	λ_0 [1/mm]	k_{mfp} $[\cdot 10^{-18}/(\mu m\,cm^2)]$
Single A	0.08 ± 0.06	1.18 ± 0.10
Poly A	2.98 ± 0.13	1.21 ± 0.15
Poly B	3.12 ± 0.14	1.11 ± 0.14
Poly C	2.78 ± 0.12	1.30 ± 0.12
All pCVDs	$--$	1.22 ± 0.08
Result	$--$	1.20 ± 0.06

Table 3.7.: Extracted offset and damage constant of the linearized fit for each diamond.
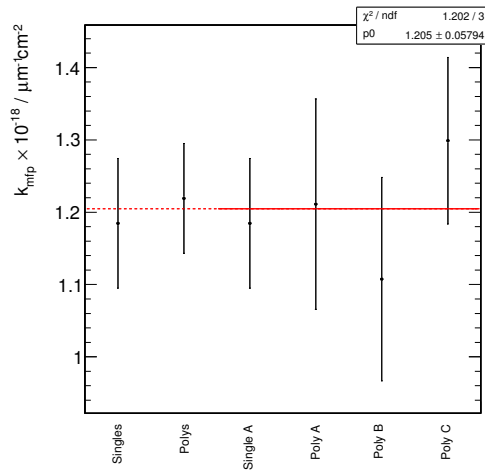
Figure 3.32.: Damage constants for all four samples, separate damage constants for sc-CVD and pCVD diamonds and the the fit of the combined damage constant.

resulting k_{MFP} for 800 MeV proton irradiation is then extracted by averaging the damage constants of all samples to be $1.21 \pm 0.06 \times 10^{18}/(\mu m \, cm^2)$. A separate fit of the pCVD samples resulted in a damage constant of $k_{MFP}^{pCVD} = 1.22 \pm 0.08 \times 10^{-18}/(\mu m \, cm^2)$.

As the ratio of MFPs of electrons and holes is not known exactly, the ratio was varied to study the influence of this variable. In Figure 3.33 the extracted damage constant for different MFP ratios is shown. It can be seen that the highest damage occurs at a ratio of approximately one. At the ratio of 1.47 the damage constant is close to this value. In Table 3.8 the resulting damage constants for different ratios are summarized. These differences are associated with a systematic uncertainty $\sigma_{syst,MFP}$. The variation when varying the ratio by 50 % is taken as the error, resulting in an error of $\sigma_{syst,MFP} = {}^{+\,0.01}_{-\,0.05}$.

As the measured CCDs of the scCVD diamond at different polarities have a difference of up to 10 %. A possible reason for this difference could be differences in gain for positive and negative polarity. Thee influence of this difference was studied by only using the measurements of positive or negative polarity. This differences can be associated to an additional systematic uncertainty $\sigma_{syst,Polarity}$, resulting in $\sigma_{syst,Polarity} = {}^{+\,0.01}_{-\,0.02}$ on the combined result.

The final result for the damage constant is therefore the

$$k_{MFP} = 1.20 \pm 0.06(stat.) \, {}^{+\,0.01}_{-\,0.05}(syst_{MFP}.) \, {}^{+\,0.03}_{-\,0.05}(syst_{Polarity}) \cdot 10^{-18}/(\mu m \, cm^2) \,. \tag{3.21}$$
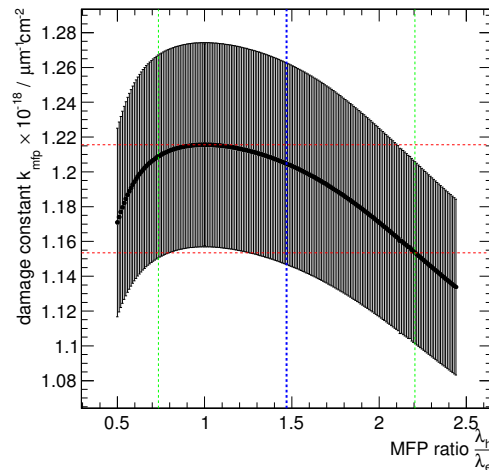
Figure 3.33.: Influence of the variation of the MFP ratio on the resulting damage constant. The blue line marks the standard ratio of 1.47. The vertical green dotted lines indicate the band the variation the ratio by 50 %. The horizontal red dotted lines indicate the maximum and the minimum damage constant in this band.

Ratio λ_h/λ_e	k_{mfp} $[\cdot 10^{-18}/(\mu\mathrm{m\,cm}^2)]$
$1.47-66\% = 0.50$	1.17 ± 0.05
$1.47-50\% = 0.74$	1.21 ± 0.06
$1.47-32\% = 1.00$	1.22 ± 0.06
$1.47-10\% = 1.32$	1.21 ± 0.06
$1.47\pm\ 0\% = 1.47$	1.20 ± 0.06
$1.47+10\% = 1.62$	1.12 ± 0.06
$1.47+32\% = 1.94$	1.18 ± 0.06
$1.47+50\% = 2.21$	1.15 ± 0.05
$1.47+66\% = 2.44$	1.13 ± 0.05

Table 3.8.: Damage constant when varying the ratio of the MFPs of holes over electrons. This results in a systematic error of $\sigma_{syst.,MFP} = {}^{+\,0.02}_{-\,0.05} \cdot 10^{-18}/(\mu\mathrm{m\,cm}^2)$.

The MFP as a function of integrated particle fluence is shown in Figure 3.34 with one-sigma bands indicated. All results conform to Equation 2.24 to better than 2 sigma, demonstrating validity of the assumption of a common radiation damage mechanism in scCVD and pCVD diamonds.

(a) Linear.   (b) Logarithmic.
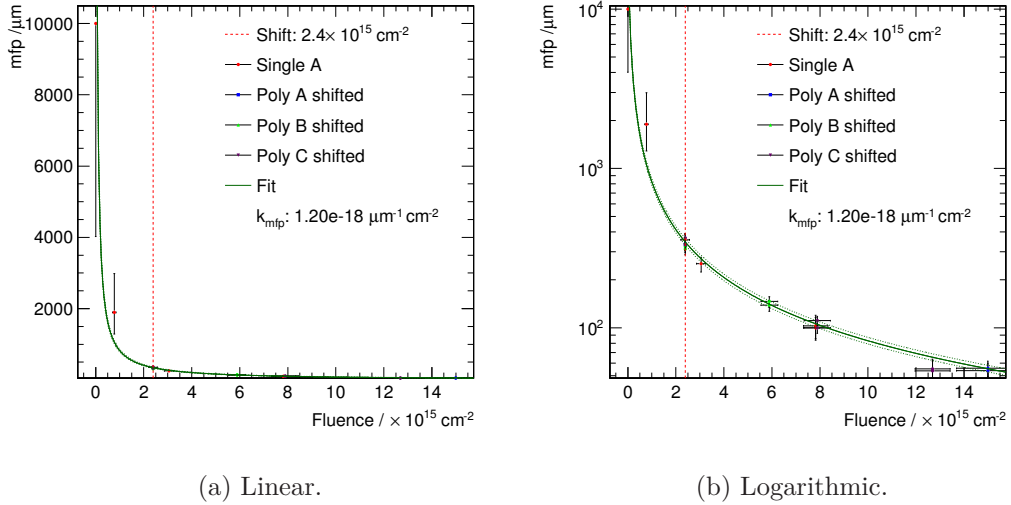
Figure 3.34.: Damage Curve for 800 MeV protons in logarithmic scale 3.34 (b) and normal scale 3.34 (a). The one sigma band of the fit is indicated with the dotted line.

3.8.3. Study of the Position Resolution on a scCVD Diamond

An important factor for vertex detectors is the intrinsic position resolution of the detector. For a given readout pitch the resolution of the detector can be improved if charge sharing between the readout channels occurs. To study the resolution of the diamond detectors the residual distribution was examined. It was observed that the resolution of pCVD diamond strip detectors improves with proton and pion irradiation [137]. In this section the influence of proton radiation on the resolution is studied for scCVD diamond. The scCVD diamond *SINGLE A* was used for this study.

3.8.3.1. Procedure

The residual was defined as the difference of the predicted hit position by the beam telescope and the measured hit position by the detector. The method to extract the resolution of the diamond detector is illustrated with a irradiated scCVD diamond sample using the Feed-Across-Corrected data. The measured hit position was calculated using an eta corrected method. In Figure 3.9 the eta distribution is shown. The distribution is symmetric with two peaks at $\eta \approx 0.06$ and $eta \approx 0.94$. These peaks correspond to events with a neglectable amount of charge sharing. In between 0.2 to 0.8 the distribution is flat indicating a proportional charge sharing with respect to the hit position. Using the integrated distribution of eta the eta corrected hit position can be calculated.

(a)   (b)
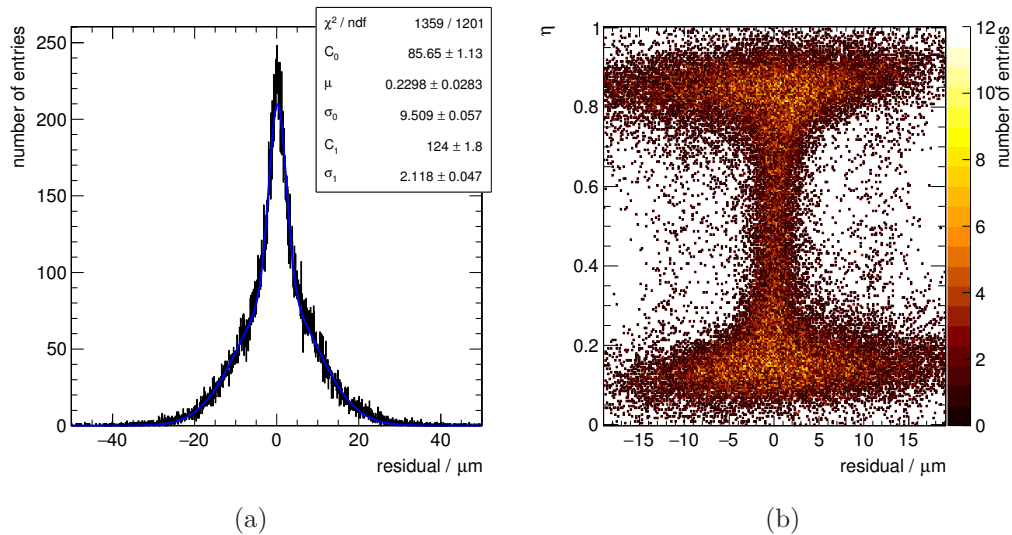
Figure 3.35.: (a): The residual distribution for an irradiated scCVD using the eta corrected hit position. The data is fitted with two Gaussians sharing one mean.
(b): The residual distribution as a function of measured eta.

In Figure 3.35 (a) the corresponding residual distribution is shown. The distribution has a mean of 0.3 µm and a sigma of 9.1 µm. The distribution was fitted with two Gaussians sharing the same mean. This fit describes the data fairly well. The narrow Gaussian has a sigma of 2.1 µm and the wide Gaussian has a sigma of 9.5 µm. The two contributions can be associated with different regions in the eta spectrum. In Figure 3.35 (b) the residual distribution as a function of eta is shown. It can be seen that events with eta values between 0.2 to 0.8 result in a narrow distribution, while all other events contribute to the wide Gaussian distribution. This indicates that there is a region within the readout pitch in which the position resolution can be strongly improved due to charge sharing. In order to find this region, the relative predicted hit channel was calculated. This position was defined by the relative distance to the next readout strip. The eta distribution as a function of the relative predicted hit channel, shown in Figure 3.36 (a), indicates that actual charge sharing only occurs in the outer 10 % to 20 % of the readout strip. This means that the narrow distribution should be produced by events which crossed the detector 5 µm to 10 µm around the middle of two readout strips. This can be confirmed by Figure 3.36 (b). This figure shows the residual distribution as a function of the relative predicted hit channel. In the outer 10 % the charge sharing improves the resolution, resulting in the narrow Gaussian distributions. In the region in between the residual is widely spread. The diagonal line is produced by events for which no eta value can be calculated and therefore a single channel is used to estimate the hit position.
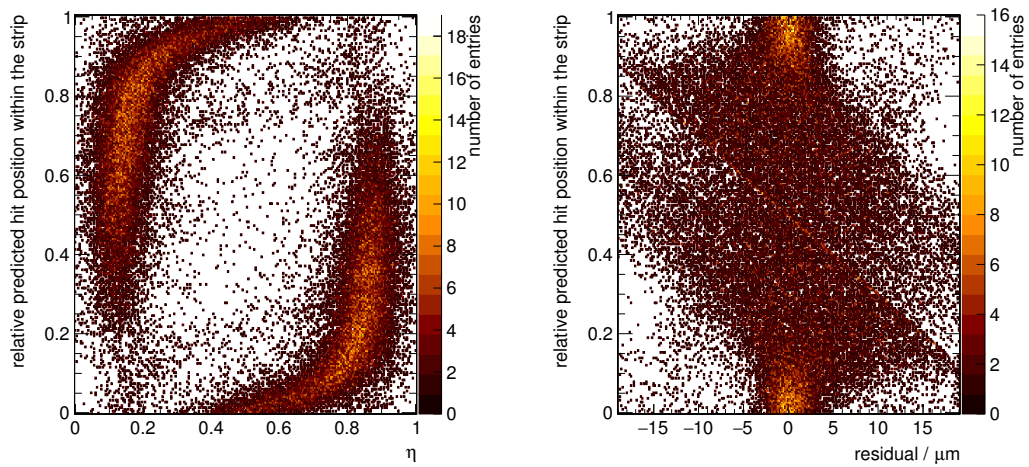
(a) Relative predicted hit position versus eta.

(b) Residual distribution versus relative predicted hit position.

Figure 3.36.: Relative predicted hit position versus eta and versus the measured residual for a transparent cluster using two out of 10 channels.

3.8.3.2. Results

The residual distributions for positive and negative polarity are plotted in Figure 3.37. All distributions are scaled in such a way that the most probable value is one. It can be seen that all distributions peak around zero. The shape of the distributions is similar, a narrow peak is on top of a wide distribution. It can be seen that not all distributions are fully centered at zero. This indicates that in certain runs the feed across correction could not fully resolve the asymmetry of the readout. Therefore a slight asymmetry in the eta distribution could be observed. For positive polarity the two residual distributions of the lowest fluences are wider than the other distributions, indicating a slight improvement. This effect cannot be seen for the negative polarity.

Three different methods were used to extract the width of the residual distribution. The simple method used a fit of a single Gaussian distribution. This fit is built of three parameters a constant C, the peak center μ_G and the standard deviation σ_G. In the FWHM method the FWHM is extracted from the distribution and the sigma is calculated by using the relationship between FWHM and standard deviation $\sigma_{FWHM} = \frac{FWHM}{2\sqrt{2\ln 2}} \approx \frac{FWHM}{2.355}$. The third method describes the shape of the residual distribution by a two Gaussian distributions which have the same center position. This results in a total of five parameters, two constants C_1 and C_2, one peak center position μ_{DG} and two standard deviations σ_{DG1} and σ_{DG2}. The two standard deviations are sorted in such a way that σ_{DG1} is the larger one $(\sigma_{DG1}) > \sigma_{DG2})$. Additionally the mean and the 'RMS' of the distribution are extracted from the histogram as another measure.

In Table 3.9 the results for these methods a summarized and illustrated in Figure 3.38. For positive polarity a slight trend to better resolutions can be seen for fluences up to $2.39 \times 10^{15}\,\mathrm{p/cm^2}$. The point at $3.05 \times 10^{15}\,\mathrm{p/cm^2}$ has a residual distribution as the

(a) Positive polarity.   (b) Negative Polarity.
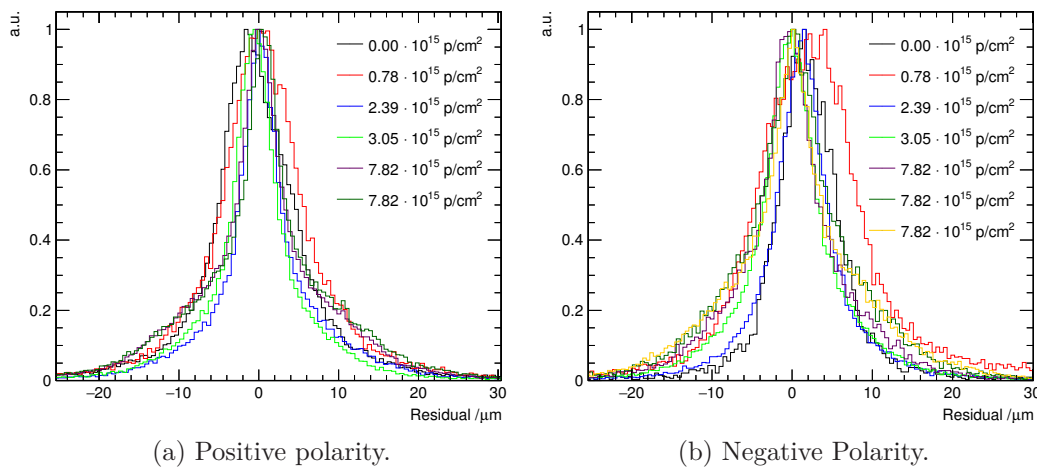
Figure 3.37.: Residual distribution after feed-a-cross correction for positive and negative polarity. The electric field is $\pm 2\,\mathrm{V/\mu m}$.

Fluence [10^{15} p/cm^2]	Voltage [V]	Mean [µm]	RMS [µm]	σ_{FWHM} [µm]	σ_G [µm]	σ_{DG1} [µm]	σ_{DG2} [µm]
0.00	+1000	−0.34	8.76	4.43	4.71	8.61	3.59
0.78	+1050	+0.48	9.30	4.30	5.04	8.82	3.63
2.39	+1050	+0.77	7.96	2.24	2.96	8.58	2.42
3.05	+1050	−0.42	7.47	2.44	2.96	7.48	2.25
7.82	+1100	+0.15	8.77	2.47	3.39	9.53	2.19
7.82	+1100	+0.62	9.22	2.28	3.26	9.77	1.95

(a) Positive polarity.

Fluence [10^{15} p/cm^2]	Voltage [V]	Mean [µm]	RMS [µm]	σ_{FWHM} [µm]	σ_G [µm]	σ_{DG1} [µm]	σ_{DG2} [µm]
0.00	−1000	+1.94	+6.95	3.35	3.37	14.76	3.03
0.78	−1050	+2.57	+10.52	5.99	5.87	9.25	4.58
2.39	−1050	+1.33	+6.95	2.78	3.28	6.52	2.44
3.05	−1050	+0.01	+7.49	2.88	3.62	7.58	2.55
7.82	−1050	−0.16	+7.74	2.85	3.93	8.22	2.45
7.82	−1100	+0.38	+8.54	3.73	5.05	9.17	2.85
7.82	−1100	+0.31	+9.12	2.87	4.27	9.51	2.12

(b) Negative polarity.

Table 3.9.: Extracted width of the residual distribution using three different methods: A double Gaussian fit ($\sigma_{DG1}, \sigma_{DG2}$), the FWHM ($\sigma_{FWHM}$) and a single Gaussian fit(σ_G).

(a) Positive polarity.

(b) Negative Polarity.
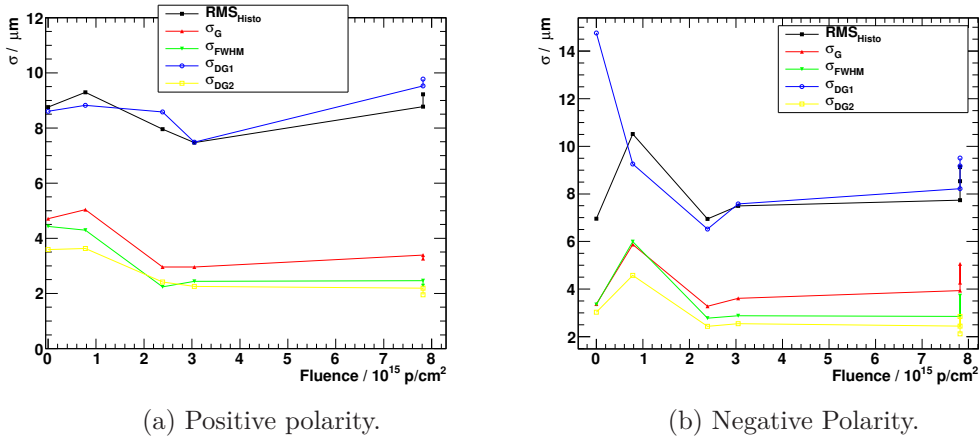
Figure 3.38.: The extracted width of the residual distributions as a function of irradiation using different methods to estimate the width.

lower point showing that the resolution stays constant at this fluence. This trend can be seen in all fitting methods. With further irradiation the RMS and the wide Gaussian are increasing. This effect is expected. A higher irradiated diamond creates a smaller signal response and therefore the SNR is decreasing. In a wider range of eta noise fluctuation gets prominent and therefore the region in which the eta correction improves the position calculation gets smaller and the other region gets wider. With increasing fluence it is expected that the sigma of the wide gaussian will converge asymptotically the digital resolution of $14.43\,\mu m$.

3.8.3.3. Conclusion

The results published for pCVD diamonds showed an improvement of resolution for fluences up to $3 \times 10^{15}\,p/cm^2$. A similar improvement of resolution was observed for the measurements performed with the scCVD diamond at positive bias polarity. The resolution improved up to $3.2 \times 10^{15}\,p/cm^2$. The measurement at $7.8 \times 10^{15}\,p/cm^2$ did not show any further improvement. The improvement of resolution for fluences up to $3.2 \times 10^{15}\,p/cm^2$ is not obvious for the measurements at negative bias polarities. Compared to the measurement for the unirradiated scCVD diamond and compared to the measurement after an irradiation to $2.4 \times 10^{15}\,p/cm^2$, the residual distribution is wider for the measurements at $0.78\,p/cm^2$. Measurements with additional scCVD diamonds may help to clarify the behavior at negative bias polarity. Additional measurements of pCVD diamonds irradiated to fluences above $3 \times 10^{15}\,p/cm^2$ can show if the resolution further improves for pCVD diamonds or if a similar behavior as for scCVD diamonds can be observed and the resolution stays constant for fluences above $3 \times 10^{15}\,p/cm^2$.

3.8.4. Capability of pCVD Diamonds for Tracking Detectors at HL-LHC

The pCVD diamond sample *POLY-A* was irradiated to 1.2×10^{16} p/cm^2, which corresponds to the fluence in the inner most layer of a HL-LHC experiment after the total integrated luminosity of 3000/fb. Therefore the measurements at this fluence can be used to study the capability of pCVD diamond sensors for tracking detectors in the inner most layers of HL-LHC. During the first tests of this diamond sensor it was state of the art diamond material with a CCD of 229 µm, but within the last years the quality of pCVD diamond material has significantly improved. Recently first pCVD diamonds with initial CCD of 350 µm have been measured. In this section the signal response of a pCVD sample after such a radiation is studied. As this measurements were performed with a threshold free readout, the efficiency of the sensor can be studied.

In Figure 3.39 the pulse height distribution for the pCVD diamond after irradiation is shown using a transparent analysis. The pulse height is defined as the sum of the highest and the highest adjacent signal in the transparent cluster with ten channels (2 out of 10). The mean of the distribution is 1870 e and its MPV is 1690 e. The noise after common mode correction was measured to be 79.2 e. Therefore the detector still has a SNR of 23.7 using the mean and 21.3 using the MPV. These measurements were performed using a strip readout and a 2 µs shaping time. In order to estimate the performance in a pixel detector at HL-LHC, the noise of the current pixel detectors can be used instead. With the CMS readout chip a noise of 155 e was measured [138] and with the readout chip of the ATLAS IBL a noise of ~120 e was measured [139] when a silicon sensor is bump bonded to the ROC. Therefore the SNR of such a detector can be estimate to be above 10 after such a radiation level.
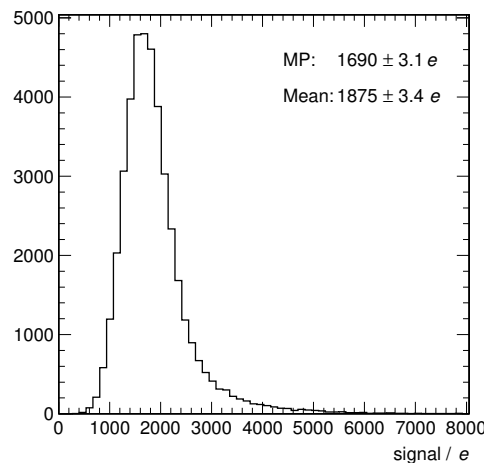
Figure 3.39.: The "2 out of 10" pulse height for the pCVD sample *POLY A* after an irradiation of 1.2×10^{16} p/cm^2.

(a)

(b)
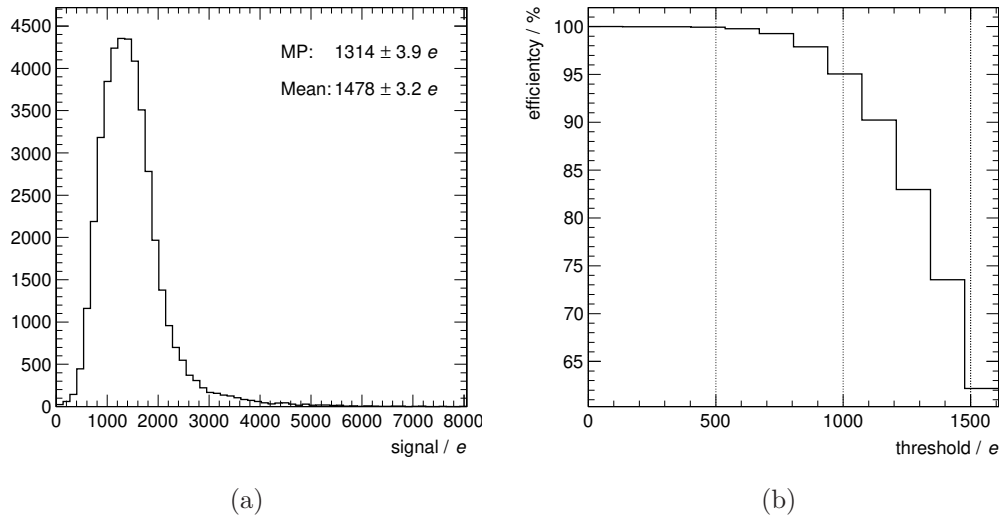
Figure 3.40.: Pulse height and efficiency of the highest signal in a transparent cluster for the pCVD sample *POLY A* after an irradiation of $1.2 \times 10^{16} \, \mathrm{p/cm}^2$.

An important factor for the operation in the HL-LHC environment is the operation with a zero suppressed readout. Thus it is important to study the response and efficiency when requiring a minimum signal height on the channel with the highest signal. In Figure 3.40 (a) the pulse height of the highest signal channel in the transparent cluster is shown. The MPV of 1310 e corresponds to a SNR of 16.5 and its mean of 1480 e to a SNR of 18.7. This SNR indicates that such a detector is capable of working after such a high radiation dose. In Figure 3.40 (b) the efficiency as a function of threshold is shown. With this detector the efficiency for a threshold of 500 e is $98.0\,^{+\,2.4}_{-\,0.4}\%$ and at a threshold of 1000 e approximately 95 %.

In order to build a tracking detector which reaches high efficiencies required at HL-LHC after the expected radiation levels, the signal response of the sensor material needs to be further increased and the thresholds of the ROCs needs to decrease. With the conversion function from MFP to CCD and the damage function it is possible to estimate the signal increase when using current state of the art pCVD. By increasing the CCD from ∼230 µm to 350 µm the signal response after such a radiation level increases by approximately 10 %, corresponding to 200 e.

As discussed in Section 2.2.4, the spatial resolution of tracking detectors can improve as soon as charge sharing between electrodes occur and the information of multiple readout channels is used to extract the position. In Figure 3.41 the residual distribution for this diamond is shown. The measurement is fitted with a sum of two Gaussian distributions which share the same mean. The width of the two Gaussians are 3.2 µm and 9.6 µm, which can be compared with a "digital" resolution of 14.4 µm in case of no charge sharing. This indicates that charge sharing improves the position resolution of

113

this detector and diamond detectors are well suited for applications which requires a good tracking performance.
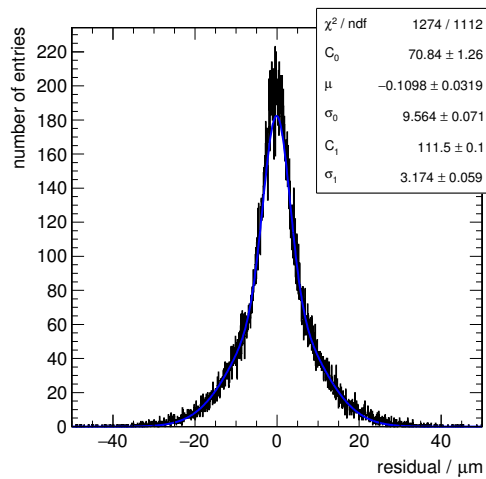
Figure 3.41.: Residual distribution for the pCVD diamond sample *POLY A* irradiated to $1.2 \times 10^{16}\,\mathrm{p/cm^2}$. A sum of two normal distributions with the same mean is used to fit the measurement.

4. 3D Diamond Detectors

The idea of 3D sensors was created in 1997 by Parker, et. al. [70]. With the insertion of the electrodes into the sensor material it is possible to reduce the drift distances of the charge carriers to less than the sensor thickness and thereby increase the collected charge for detectors with a limited MFP, e.g. irradiated or trap dominated detectors. A sketch of an array of four adjacent quadratic 3D cells is shown in Figure 4.1. Each cell consists of four bias electrodes (red) in the corners and one readout electrode (green) in the center of the cell. Each bias electrode biases with up to four adjacent cells.

To fabricate the 3D geometry in a CVD diamond a technique using a laser to machine the bulk electrodes was used. It has been shown that a femto-second laser pulse can be used to prompt a phase transition of diamond into a conductive material consisting of diamond-like-carbon, amorphous carbon and graphitic material [140, 141]. The physical concept behind this phase transition is described in [142]. Detailed studies of the phase transition showed that the time scale of this transition is picoseconds [143].

In this chapter the fabrication of 3D detectors is described and the first beam test results for a 3D scCVD and a 3D pCVD diamond are presented. With the 3D scCVD diamond the proof of principle was established, as scCVD diamond sensor material combines high signal response with a uniform material. The results of the scCVD sample, presented in the following, are published in [144]. Large scale applications of the 3D CVD diamond concept require pCVD diamonds, as only these are available in larger sizes. As discussed in Section
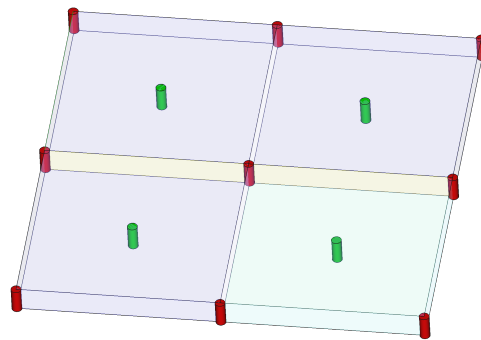
Figure 4.1.: Illustration of four 3D cells next to each other. The readout electrodes are marked in green, the bias electrodes in red.

2.3.3, the drawbacks of pCVD are lower signal response and inhomogeneities within the material due to grain boundaries. As the MFP is already reduced for unirradiated pCVD diamonds, the concept of 3D detectors can show its full power for such a trap dominated material. In such a detector it is possible to reach a larger signal response than in a planar strip detector.

The chapter ends with a discussion of differences between the scCVD and pCVD samples and an outlook of the next steps towards a large scale 3D detector based on CVD diamond.

4.1. Detector Fabrication

The detector fabrication consists of four steps, the initial cleaning, the fabrication of the conductive electrodes, the metalization and the construction of the detector assembly. The micro machining of the conductive electrodes was performed by the Laser Processing Research Center at the University of Manchester, while all other steps were carried out at OSU. In this section the process of electrode fabrication is briefly discussed, further details can be found in [145].

4.1.1. Electrode Formation

The conductive electrodes in the 3D geometry are formed with a pulsed laser. In the focal point of the laser the energy density is high enough to initiate a phase transition of diamond into a partially conductive material. A sketch of the electrode formation process is shown in Figure 4.2.
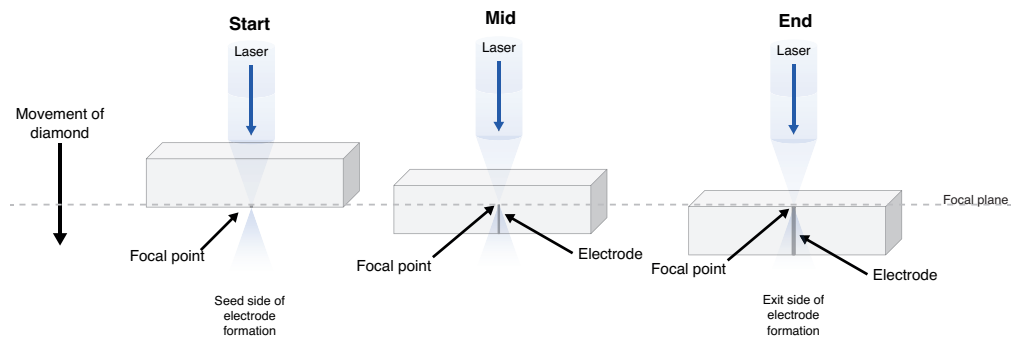
Figure 4.2.: Illustration of the formation process of the electrodes. At the focal point of the laser the energy is high enough to prompt a phase transition. By the movement of the diamond with respect to the focal point the electrode is formed across the diamond.

To prevent light absorption by the electrode itself, electrodes are formed from the back to the front side of the diamond sample by moving the diamond through the beam spot. Starting with a beam spot focused at the back of the diamond, the plate is moved with a constant translation speed.

It was found that the phase transition prompted with the laser results in a density change of the carbon material from $3.5\,\text{g/cm}^2$ to $2.5\,\text{g/cm}^2$ [140, 141]. Figure 4.3 shows Scanning Electron Microscope (SEM) pictures of the entry/seed and exit side of the laser within the diamond.

(a) SEM - Seed side. (b) SEM - Exit side.
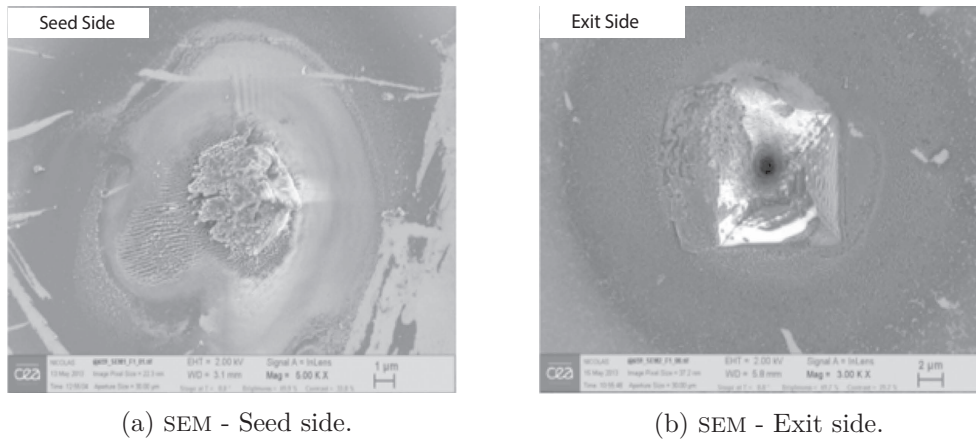
Figure 4.3.: The SEM pictures shows a single electrode of the laser processed diamond at the seed (a) and exit side (b) of the processing.

On the seed side, Figure 4.3 (a), an excess of material is observed due to the smaller density of the electrode material in comparison to that of diamond. On the exit side a small crater is observed, which indicates that the pressure build-up inside the diamond was sufficient to expel a few micrograms of material before the laser reached the surface.

4.1.2. Laser Setup

The laser used for electrode fabrication was a Coherent Libra Ti Sapphire femto-second laser [146] with a wave length of $800\,\text{nm}$ and a pulse duration of $100\,\text{fs}$. It was operated in a TEM_{00} beam mode. The pulse repetition rate was fixed to $1\,\text{kHz}$ for the fabrication. The intensity of the pulses was varied by using neutral-density filter attenuators. With additional beam optics the beam was focused to a beam spot with a size of about $4\,\mu\text{m}$.

A picture of this setup is shown in Figure 4.4. By moving the diamond plate with a motorized 3-axis micro controlled stage the position of the focal-point within the diamond can be changed. The fabrication was monitored using a camera.
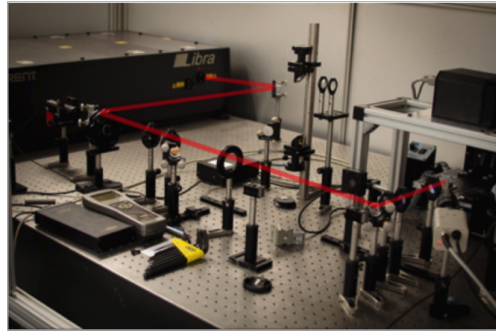
Figure 4.4.: Setup of the Laser for electrode formation including the beam optics. The diamond sample is placed on the right. A camera is used to monitor the formation.
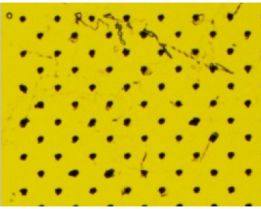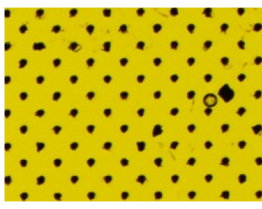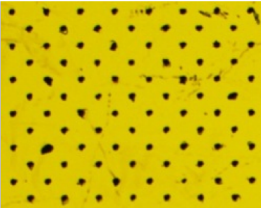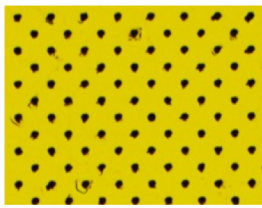
Seed Side	low power	high power
low speed		
high speed		

Figure 4.5.: Pictures of seed side for different laser power-densities and translation speed configurations.

Exit Side	low power	high power
low speed		
high speed		
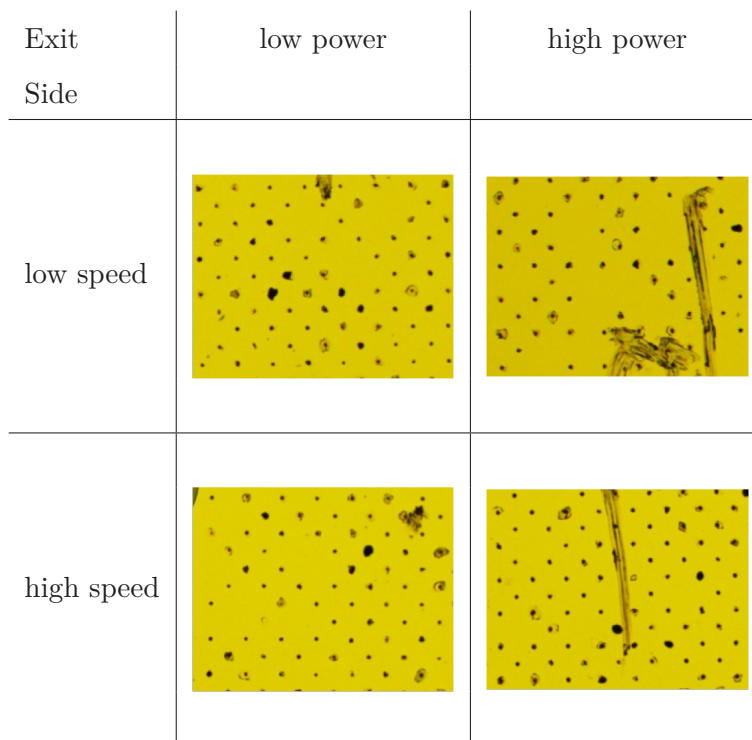
Figure 4.6.: Pictures of exit side for different laser power-densities and translation speed configurations.

4.1.3. Optimization of the Setup

In order to yield high efficiencies in electrode production an optimization of the energy-density at the focal point with respect to the translation speed was performed with an optical grade pCVD diamond. A complete electrode is defined as an electrode with a continuous conducting path over the whole thickness of the diamond sample. With optical microscopy each electrode is checked and this definition is used to define the efficiency of electrode formation as the fraction of completed electrodes divided by the total number of electrodes attempted. Two different translation speeds and two different energy densities were used for this scan. In Figures 4.5 and 4.6 the pictures of the different combinations are shown for the seed and the exit side. No missing electrodes can be seen on the seed side, indicating the correct formation of a seed. In the high power - low speed configuration the diameter of the electrodes is strongly varying. On the exit side some electrodes are missing, indicating that the process of electrode formation stopped inside the diamond. In total 371 electrodes were produced for each configuration. Every electrode was checked by optical inspection individually. Assuming a binomial distribution for the error calculation, the error of the efficiencies can be calculated to 2 %.

In Table 4.1 the results are summarized. The highest yield of 93.3 % was achieved in the combination of low power with high translation speed. This combination uses the following parameters: an energy density of $2\,\mathrm{J/cm^2}$, translation speed of $20\,\mathrm{\mu m/s}$ and a laser pulse repetition rate of $1\,\mathrm{kHz}$. In a $500\,\mathrm{\mu m}$ thick diamond the formation of one electrode can be calculated to last $25\,\mathrm{s}$ using this settings. Further research is ongoing in order to increase the speed in column formation.

4.1.4. Fabrication of the scCVD diamond

A scCVD diamond plate from Element Six [147] with a size of $4.7 \times 4.7\,\mathrm{mm^2}$ was used as a starting material. The diamond sample was mechanically polished by Element Six. As any surface imperfection may alter the laser focus the diamond was cleaned. This ensured the highest electrode formation efficiencies. Before electrode formation a two step cleaning procedure was used. In the first step, the diamond was cleaned at OSU using the standard cleaning procedure, described in Section 2.3.4 to remove any residuals on the surface. In the second step $10\,\mathrm{\mu m}$ of material were removed from top and bottom

	low power ($2\,\mathrm{J/cm^2}$)	high power ($3\,\mathrm{J/cm^2}$)
low speed ($15\,\mathrm{\mu m/s}$)	$92.4 \pm 1.4\,\%$	$78.7 \pm 2.1\,\%$
high speed ($20\,\mathrm{\mu m/s}$)	$93.3 \pm 1.3\,\%$	$87.6 \pm 1.7\,\%$

Table 4.1.: Electrode production yield for different laser parameters.

using RIE in order to reduce the damage of the diamond material due to mechanical polishing. After electrode formation and before metalization the surface was cleaned again with the standard cleaning procedure using chemical cleaning with acids and using an oxygen plasma etch process. After these steps the thickness of the diamond was measured to be $440 \pm 4\,\mu\text{m}$.

The cleaned diamond was tested with a Sr^{90} radioactive source setup at OSU (as described in Section 3.6.2.1. At a thickness $d = 440\,\mu\text{m}$ a signal of $15\,840\,e$ is expected for full charge collection. At a bias voltage $500\,\text{V}$ a signal of $(15\,770 \pm 250(\text{stat.}) \pm 350(\text{calib.} + \text{syst.}))\text{e}$ was measured. This is shows the full collection of the deposited charge at a bias voltage of $500\,\text{V}$. At lower bias voltages full charge collection is not yet reached. At a bias voltage of $300\,\text{V}$ the signal was measured to be $14890 \pm 250(\text{stat.}) \pm 350(\text{calib.} + \text{syst.}))e$, corresponding to $94.4\,\%$ of the full charge collection. Figure 4.7 shows the measured CCD as a function of the bias voltage. Full charge collection is only reached between $400\,\text{V}$ to $500\,\text{V}$. At $100\,\text{V}$ a charge of $(9\,290 \pm 200(\text{stat.}) \pm 350(\text{calib.} + \text{syst.}))e$ was measured, corresponding to a charge collection distance of $(258 \pm 5.5(\text{stat.}) \pm 9.7(\text{calib.} + \text{syst.}))\,\mu m$. This measurement shows that this diamond is only fully collecting charge at bias voltages of $500\,\text{V}$ or higher, below this bias voltage a reduced charge collection can be observed.

The optimized laser parameters were used to form the electrodes. Two arrays of square cells consisting of bias electrodes in the four corners and a readout electrode in the center were produced. The two arrays had cell sizes of $100 \times 100\,\mu\text{m}^2$ and $150 \times 150\,\mu\text{m}^2$. Each array consisted of 9×11 cells. The yield of electrode formation was measured to be $92 \pm 3\,\%$ by optical inspection,. Inspections with a SEM were used to estimate the diameter of the electrodes to be $6 \pm 1\,\mu\text{m}$.
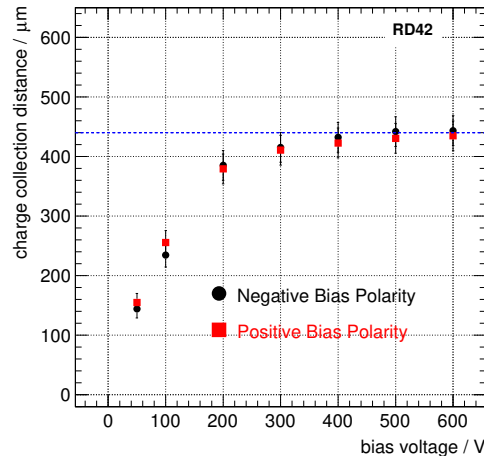
Figure 4.7.: The CCD as a function of bias voltage for the scCVD diamond sample. The sample reaches full charge collection between $400\,\text{V}$ and $500\,\text{V}$. From these measurements the CCD at $25\,\text{V}$ is estimated to be between $50\,\mu\text{m}$ to $150\,\mu\text{m}$.

(a)   (b)
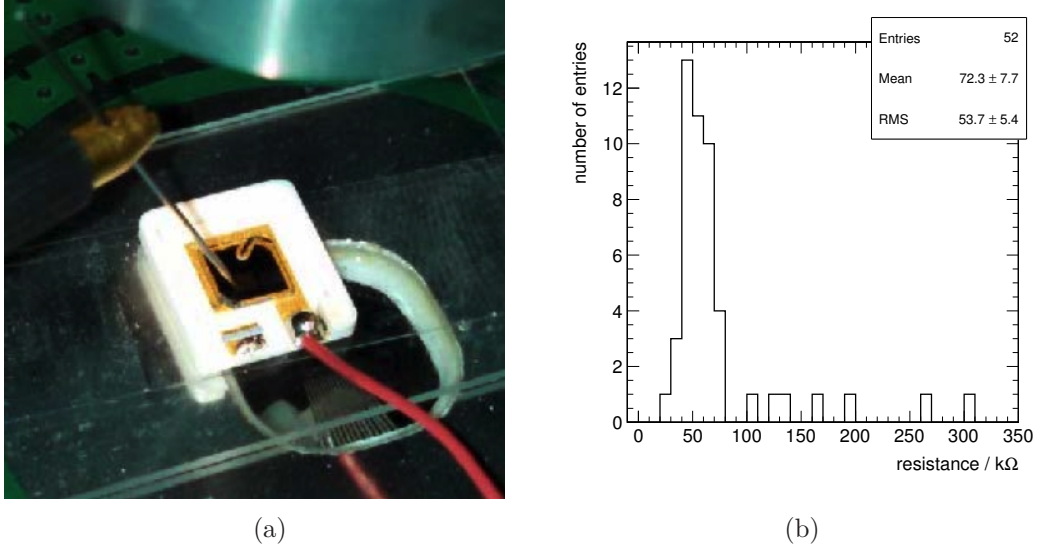
Figure 4.8.: Resistivity measurements of the electrodes with a probe needle setup.
(a): The setup for the measurement of the electrode resistances with a probe needle contacting the electrode.
(b): The distribution of the resistance of the measured subset of readout electrodes.

For the following tests only the array with $150 \times 150\,\mu m^2$ cells was used. The resistance of a subset of 77 readout electrodes was measured with a probe needle setup at OSU. For this measurement the detector was metalized with $Cr - Au$. On one side the metalization was used as a contact. On the other side a probe needle was placed at the electrode. A picture of the actual measurement is shown in Figure 4.8 (a). For 52 out of 77 electrodes a resistance below $R_{electrode} \leq 1\,\text{G}\Omega$ was measured. These measurements are shown in Figure 4.8 (b). The distribution peaks at $45 \pm 5\,\text{k}\Omega$ with a FWHM of $32\,\text{k}\Omega$. It has a mean of $72 \pm 8\,\text{k}\Omega$ and a RMS of $54\,\text{k}\Omega$. With the formula

$$\rho = \frac{R \cdot \pi r^2}{d} \,, \tag{4.1}$$

where R is the resistance, r is the radius of the electrode and d the thickness of the diamond, the resistivity was estimated to be $0.29 \pm 0.10\,\Omega\,\text{cm}$ for a typical electrode. The error is deduced from the uncertainties on the central value of the electrode resistance, the diameter of the electrode ($r = 6 \pm 1\,\mu\text{m}$), and the thickness of the diamond sample ($d = 440 \pm 4\,\mu\text{m}$). This value of resistivity is more than four orders of magnitude higher than for graphite ($\rho_{Graphite} = 7.8 \times 10^{-6}\,\Omega\,\text{cm}$, [148]) and three orders of magnitude lower than diamond-like carbon ($\rho_{DLC} = 10^2 - 10^{16}\,\Omega\,\text{cm}$, [149]). This indicates the presence of multiple phases of carbon in the electrodes, being consistent with measurements reported by other groups on photo induced amorphous structures in diamond [150]. With optical inspection in combination with the resistivity a total of nine readout electrodes have

been found in which the electrode was not formed continuously through the full bulk of the material.

4.1.5. Fabrication of the pCVD sample

For the 3D pCVD detector a diamond from II-VI Incorporated [151] with a thickness of 525 µm was used. In initial source test at OSU the CCD was measured for different bias voltages, shown in Figure 4.9.
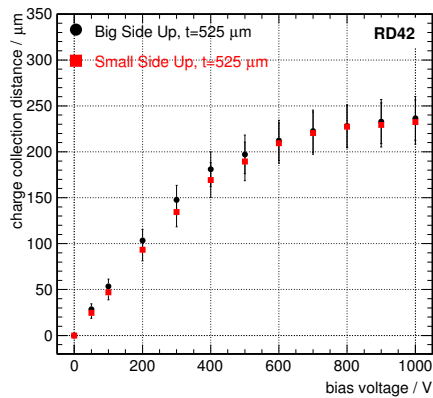
Figure 4.9.: The CCD of the 3D pCVDdiamond sensor as a function of the bias voltage. The CCD at a bias voltage of 70 V was interpolated to be 35 ± 5 µm.

At a bias voltage of 500 V a CCD of 193 ± 21 µm was measured. With increasing the bias voltage further up to 1000 V, corresponding to an electric field of 1.9 V/µm, a CCD of 234 ± 24 µm is reached. In optical measurements it was found that the yield in electrode formation was lower than in the scCVD diamond, which might be an indication that the laser was not operating with optimal settings for this material.

The resistance of a subset of 22 readout electrodes was measured using the probe needle setup at OSU, shown in Figure 4.8 (a). For 21 out of 22 electrodes resistances below $R_{electrode} \leq 1\,\text{G}\Omega$ were measured and the distribution is shown in Figure 4.10. The distribution has a mean of 61 ± 15 kΩ with a RMS of 67 ± 10 kΩ. The MPV is at 35 ± 5 kΩ with a FWHM of 30 kΩ. The diameter of the electrode was measured to be 6 ± 1 µm, the same as in the scCVD sample. This results in a resistivity of $\rho = 0.19 \pm 0.10\,\Omega\,\text{cm}$ for a typical electrode. This measurement shows a slight indication that the electrode resistivity for the pCVD sample is smaller than the one for the scCVD sample. Further measurements are required to check this.
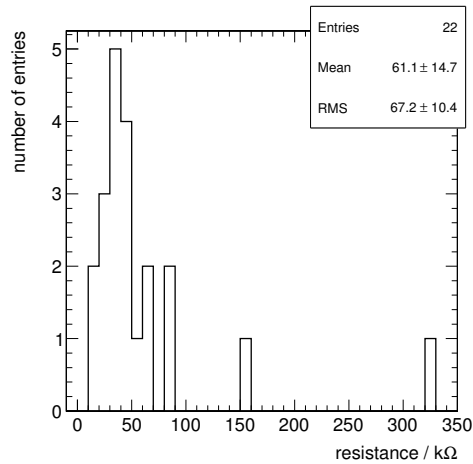
Figure 4.10.: Resistance measurement of 22 readout electrodes of the 3D pCVD diamond
detector.

4.1.6. Metalization

On the $150 \times 150\,\mu\mathrm{m}^2$ array a structured metalization with $Cr - Au$ was applied using a photo-lithographic process. The deposition of the metalization was performed with sputtering. After deposition the diamond was annealed at $400\,°\mathrm{C}$ for $4\,\mathrm{min}$ in a N_2 atmosphere to ensure a good ohmic contact to the electrodes.

The design of the metalization pattern is shown in Figure 4.11. With this metalization pattern it was possible to combine three three different patterns on one diamond sensor. A strip pattern (left), a 3D pattern, with electrodes in the bulk (right) and a pattern with the same structured metalization as the 3D detector, but with no electrodes underneath (middle). This pattern will be referred to as *3D phantom* in the rest of this thesis. With this partitioning two control regions were created next to the 3D detector. The strip pattern used a strip pitch of $50\,\mu\mathrm{m}$. By operating this part of the device with a bias voltage of $500\,\mathrm{V}$ the planar strip detector is expected to collect full charge, serving as a reference for charge collection, as can be seen from Figure 4.7. With the 3D phantom the signal pick-up due to the interdigitated surface metalization can be measured. Only the planar detector required a back plane metalization to provide the bias electrode. It consisted of a pad with dimensions of $810 \times 1605\,\mu\mathrm{m}^2$. Even though the planar strip detector is operated at high voltage no additional guard rings were added to the design due to lack of space.
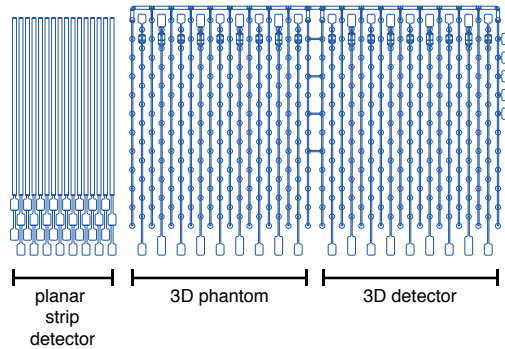
Figure 4.11.: The design of the metalization pattern with the three regions of planar strip detector, 3D phantom and 3D detector as described in the text.

To realize a threshold free, low noise readout; the same readout electronics as for the irradiation studies are used, see Section 3.2. These consisted out of the *VA2.2* readout chip [122] and the SIROCCO readout system [123]. The 3D cells of each column were ganged together and read out as one single channel. The planar strip detector, the 3D phantom and the 3D detector columns were each connected to one of the charge sensitive amplifier channels of the same readout chip. In total 16 planar strips, 9 ganged columns from the 3D phantom and 9 ganged columns from the 3D detector are connected. A picture of the scCVD detector bonded to the multi-channel readout is shown in Figure 4.12. While the bias of the 3D phantom and the 3D detector are applied from the top side, the planar strip detector's bias is applied from the back. While the 3D phantom and the 3D detector were biased together using one power supply, a separate power supply was used for biasing the planar strip detector.
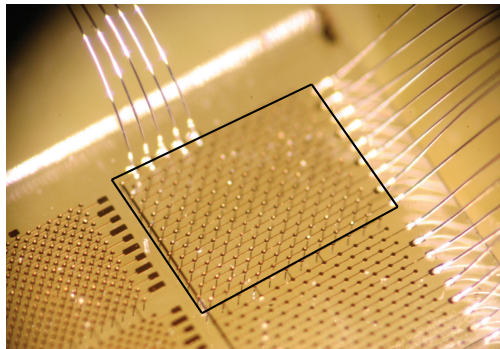
Figure 4.12.: A picture of the scCVD prototype detector bonded to the multi-channel readout chip. The location of the 150 µm cell size 3D detector with the bulk electrodes is indicated by the black frame. The readout chip is connected with the bond-wires on the right; the HV bias for the 3D phantom and the 3D detector is supplied by the five bond-wires visible at the top.
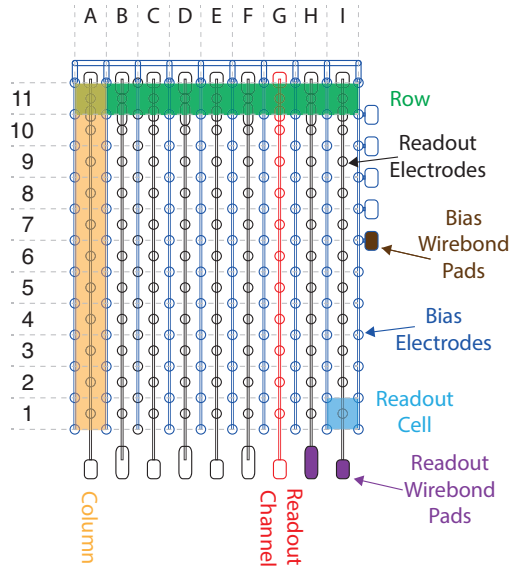
Figure 4.13.: The metalization pattern of the 3D detector including the naming convention used in the following.

In Figure 4.13 a zoomed view of the 3D detector metalization mask is shown. The bias circuit is colored in blue while the readout circuit is colored in black. Each circle defines the position of one bulk electrode. One cell, marked in light blue, consists of four bias electrodes and one readout electrode. As discussed above, the readout electrodes of 11 cells are ganged together to one readout channel. One single readout channel is highlighted in red. In total the pattern has 99 cells, ordered in 11 rows and 9 columns. One row (green) and one column (orange) are highlighted. Each readout channel corresponds to one column of 11 cells. At the bottom the 9 wire bond pads (purple) for the readout chip are placed, the four wire bond pads on the right are used for connecting the bias (brown). The position of a cell is determined by the column, $A - I$, and the row, $1 - 11$.

While wire bonding the pCVD sample, the wire bonding pad of the 22nd channel of the *VA2.2* readout chip was damaged. This meant that the wire bonding scheme for this sample had to be adjusted. In the planar strip detector the 21st readout channel was used to readout two strips of the detector (strips 7 and 8). The 22nd channel was not connected and the wire bonding continued with the 9th strip and the 23rd channel. This wire bonding scheme results in slight differences in the analysis, described later in this chapter.

4.2. Beam Tests

The diamond prototypes have been tested in two different beam test campaigns at *CERN* to investigate the signal spectrum induced by highly energetic particles and

the spatial resolution of the devices. The beam tests were performed in August 2012 for the scCVD sample and in October 2015 for the pCVD sample. In the following sections the 3D detector based on a scCVD diamond is referred as "3D scCVD detector", while the 3D detector based on a pCVD diamond is referred as "3D pCVD detector".

4.2.1. Set-up

The beam test was performed at CERN. In the H6 beam line of the SPS [152] the "Strasbourg" telescope setup was used. This setup is the same setup used for the irradiation studies, described in Section 3.2. Protons with an energy of 120 GeV were selected for these tests. The energy loss of these protons can be considered to be close to the energy loss of a MIP.

To fill the traps within the diamond material the pumping routine was applied as described in Section 3.6.3.2. Each sample was pumped with a $\sim$54 MBq ^{90}Sr source for 4 h before being transported to the setup. At the test site it it was pumped again for 20 min with a $\sim$23 MBq ^{90}Sr source. Before changing the polarity of the bias voltage the same pumping procedure was repeated.

The intensity of the beam was optimized for recording single hits in each silicon plane within the 2 µs shaping time of the *VA2.2* chip in order to suppress events with multiple particle tracks. For every 7 s spill, 10 k to 50 k coincidence triggers were counted in the telescope scintillators depending on beam conditions. The data acquisition system was capable to record 3.6 k of these events.

As the 3D scCVD diamond was meant to be used as a proof-of-principle for the 3D detector concept in diamond, it was decided to test the diamond only at one bias voltage, but with both polarities. The diamond strip detector was biased with a Keithley 237 [153] at $\pm$500 V, while the 3D phantom and the 3D detector were biased with one channel of a CAEN N1471 [154] at $\pm$25 V. With this two power supplies the strip detector could be operated at a different bias voltage than the 3D phantom and the 3D detector. The leakage current of both devices was checked multiple times during each run. The polarity of both power supplies was always chosen to be the same due to limitations of the readout electronics. In each run at least 1.1 M events were recorded. The bias voltages, the leakage currents, the number of collected events and the duration of both runs are listed in Table 4.2.

The 3D pCVD diamond was tested at multiple bias voltages to measure the signal response as a function of bias voltage. The planar strip detector was biased at $\pm$500 V, while 3D and 3D phantom detectors were biased with +50 V, +60 V, +70 V or +80 V, and −60 V, −70 V or −75 V. A total of 1.1 M to 2 M events were recorded for each run. An overview of the performed runs can be found in Table 4.3. During run 19108

Run	Bias		Leakage current		Collected	Duration
number	Strip [V]	3D [V]	Strip [nA]	3D [nA]	events	[h]
17107	$+500$	$+25$	<1	<2	1.10 M	$5:30$ h
17108	-500	-25	<0.2	<2	1.27 M	$6:15$ h

Table 4.2.: Overview of all runs performed with the 3D scCVD diamond in the beam test in August 2012.

Run	Bias		Leakage current		Collected	Duration
number	Strip [V]	3D [V]	Strip [nA]	3D [nA]	events	[h]
19105	$+500$	$+50$	<0.2	<5	2.0 M	$9:15$ h
19106	$+500$	$+60$	<0.2	<5	2.0 M	$9:20$ h
19107	$+500$	$+70$	<0.2	<5	2.0 M	$14:20$ h
19108	$+500$	$+80$	<0.2	5 to 10	1.1 M	$3:00$ h
19110	-500	-60	<1	<5	1.5 M	$6:20$ h
19111	-500	-70	<0.2	<5	2.0 M	$6:50$ h
19112	-500	-75	<0.2	5 to 10	1.5 M	$5:40$ h

Table 4.3.: Overview of all runs performed with the 3D pCVD diamond in the beam test in October 2015. The analysis of run 19107 is presented in this chapter.

($V_{3D} = +80\,$V) and 19112 ($V_{3D} = -75\,$V) the 3D detector started to draw current, therefore these runs were not analyzed.

In this chapter only the results of positive polarity measurements are presented. For the pCVD sample the highest voltage at which the diamond operated stable ($+70\,$V) has been chosen for the analysis. Therefore the results of the scCVD diamond in run 17107 and the results of the pCVD diamond in run 19106 are presented here. The 3D detector of the scCVD device was biased at $+25\,$V, while the 3D detector of the pCVD device was biased at $+70\,$V.

4.2.2. Data Analysis

The same analysis framework as for the radiation analysis, see Section 3.3, is used for processing the data and as a basis for further analysis. To study the signal response within single cells, it was required to precisely predict the hit position with good resolution in the 3D detector in x and in y-direction. As the original alignment method only included an alignment in x-direction, an additional alignment step of the 3D detector for the y-direction was added. The last analysis step, the transparent analysis, is replaced by an dedicated analysis step for 3D detectors. This step is based on the transparent analysis, which was developed for the radiation analysis, and is performed after the alignment.

Each of the three detector regions are treated independently and each analysis step was checked for each region separately. The following analysis steps are performed for each run:

- Conversion from the raw data into the *ROOT* data format.
- Pedestal calculation and subtraction, including a common mode correction for the DUT.
- Creation of clusters in each detector of the telescope by using a seed and hit threshold in units of the average noise σ_{Noise}. For the DUT the seed threshold is chosen to be $5 \times \sigma_{Noise}$ and the hit threshold to be $3 \times \sigma_{Noise}$.
- Event selection,
    - Requiring one and only one hit in each silicon detector
    - The average hit position of all silicon planes must be in a fiducial region.
    .
- Alignment of the telescope with respect to the beam, see Figure 3.1.
    - Alignment in the x and y- direction of each silicon detector.
    - Alignment in the x-direction of the DUT using the planar strip detector.
- Alignment of the DUT in y-direction, described in Section 4.2.2.1.
- Final analysis step
    - using the standard cluster definition, see Section 3.3.2.
    - using the transparent cluster definition, see Section 3.3.6.

4.2.2.1. Alignment in y-direction

Since the metalization pattern of the planar strip detector of the DUT is not segmented in y-direction, a method has been developed to align the DUT in the y-direction. The method is described with the data of run 17107. It is applied to the other run in a similar way.

The alignment of the DUT in x-direction also includes an rotational alignment around the z-axis, therefore it is only necessary to find the right offset in y-direction. For events with one and only one hit in each silicon plane a predicted hit position in the global frame is calculated. This hit position is then converted into a hit position within the DUT frame. In the first step the edges of the 3D detector are used to find a rough alignment. Figure 4.14 shows the predicted hit positions in the detector for events which have a cluster within one of the three diamond detectors. One can see an approximately 4000 µm wide and 2000 µm high structure which defines the active region of the detector. With a projection on the y-axis it is possible to get a first rough alignment of the detector.

This alignment can be improved by a detailed study of the pulse height response at the edges of the detector. Figure 4.15 (a) shows the average pulse height distribution as a function of the predicted hit position in x-direction. Since the alignment in the x-direction is known very precisely due to the alignment of the planar strip detector, the edge of the 3D detector is known precisely as well and is marked with a red line. The distribution is relatively flat up to the edge of the 3D detector and then decreases to almost zero. This shows that the position of the edge is known within 50 µm. By comparing this
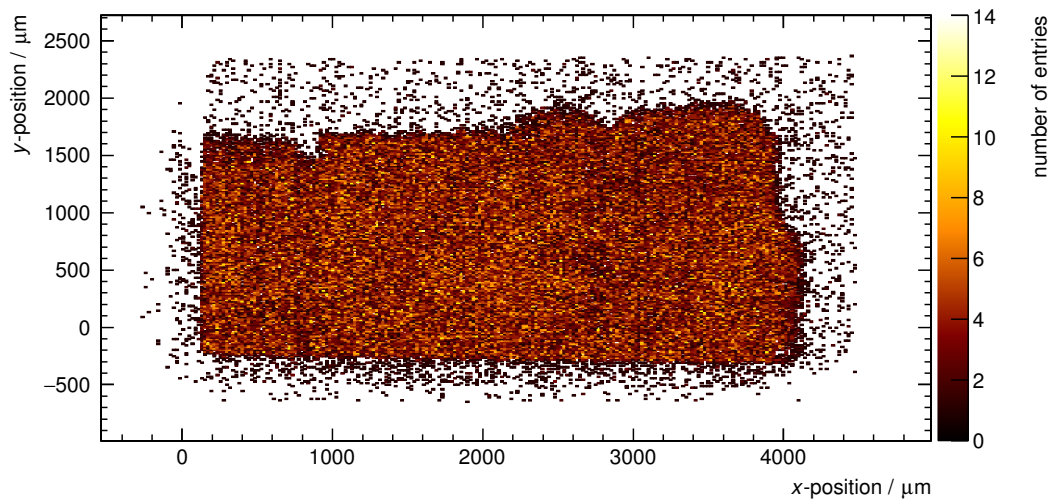
Figure 4.14.: Predicted hit position for events with at least one cluster in one of the three diamond detectors.
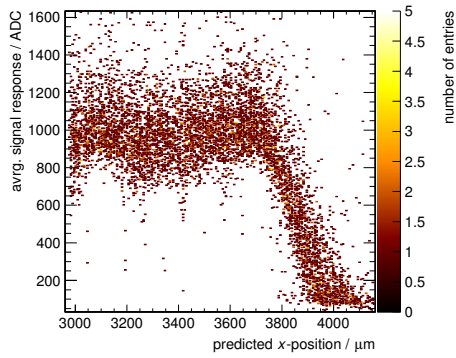
(a) Predicted hit position in the x-direction of the 3D detector versus the pulse height of cluster.
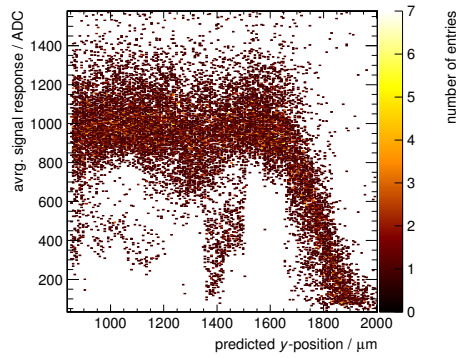
(b) Predicted hit position in the y-direction of the 3D detector versus the pulse height of cluster.
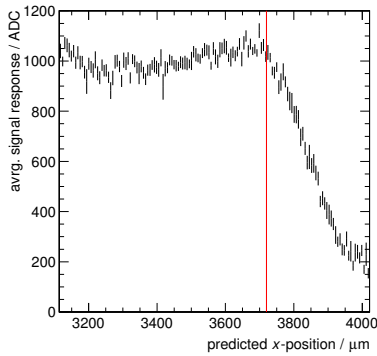
(c) Profile of the 2D histogram of Figure (a). The edge position of the $3D$ detector is marked with a red vertical line.
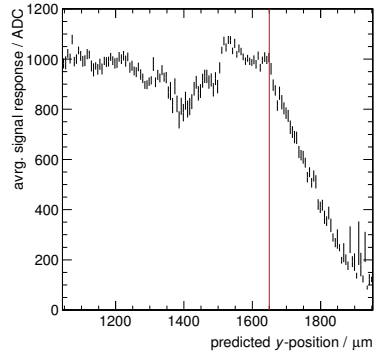
(d) Profile of the 2D histogram of Figure (b). The estimated edge position of the $3D$ detector is marked with a red vertical line.

Figure 4.15.: Alignment in the y-direction found by using the edges of the 3D detector.

distribution for the y-direction with the distribution in the x direction a rough align-
ment can be achieved. Figure 4.15 (b) shows the same distribution for the y-direction.
The distribution shows a similar drop in signal response as seen in the distribution for
the x-direction. Events with signal responses between 200 ADC and 600 ADC can be
observed in the distribution for the y direction at predicted positions between 1400 µm
and 1500 µm. These reduced signal responses might be an additional feature caused by
broken readout or bias electrodes. By using the profiles of the 2-dimensional distribu-
tions, shown in Figures 4.15 (c) and 4.15 (d), it is possible to estimate the position of
the edge comparing both profiles.

The rough alignment by edge finding is further improved in a second step using cells
with broken readout electrodes. The signal response of a cell with an imperfect readout
electrode is different to the response for a fully working cell. Figure 4.16 (a) shows the
average signal response for each cell after the rough alignment step. The cell containing
the hit was extracted from the predicted hit position from the silicon strip telescope. The
distribution of cell responses is shown in Figure 4.16 (b). The response of 9 cells is below
9000 e counts. These cells were selected to improve the alignment further, due to their
low signal response. In the following these cells are called "dead cells", as this low signal
response could be caused by a broken or not connected ("dead") electrode. Around these
cells the average signal response is plotted against the predicted hit position in the y-
direction. The signal response is lower for the cell with the dead readout electrode. The
charge collection of the two adjacent cells is modeled to be flat and equal. The step from

(a) 2D
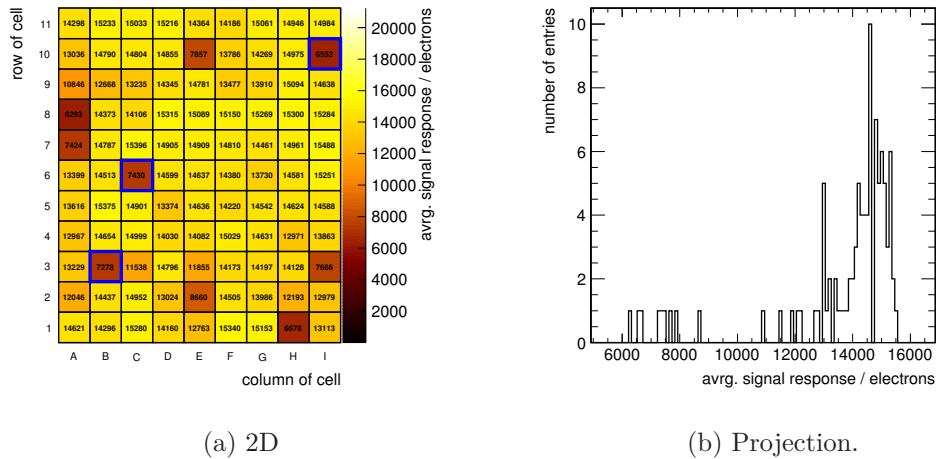
(b) Projection.

Figure 4.16.: Average signal response for each cell. In Figure (a) as a function of pre-
dicted hit position. In this Figure the three cells shown in Figure 4.17 are
highlighted in blue. Figure (b) shows the projection of the average signals.
In total 9 cells have an average signal response below 9000 e.

high charge collection to low charge collection and vice versa is assumed to be described by an error function. For this reason the data is fitted with the following function:

$$f(x) = A \cdot \sqrt{\frac{\pi}{2}} \cdot \sigma_x \cdot \left(\mathrm{erf}\left(\frac{75\,\mu\mathrm{m} - (x - \Delta x)}{\sqrt{2}\sigma_x} \right) + \mathrm{erf}\left(\frac{75\,\mu\mathrm{m} + (x - \Delta x)}{\sqrt{2}\sigma_x} \right) \right) + B$$

(4.2)

where A and B define the signal height of the working and the dead cells, Δx is the alignment offset and σ_x is the width of the Gaussian used in the error function. In Figure 4.17 the signal response of three dead cells, highlighted in Figure 4.16, is shown with respect to the predicted hit position, The expected edges of the cell are marked

(a) Dead Cell $B3$.

(b) Dead Cell $C6$.

(c) Dead Cell $I10$.
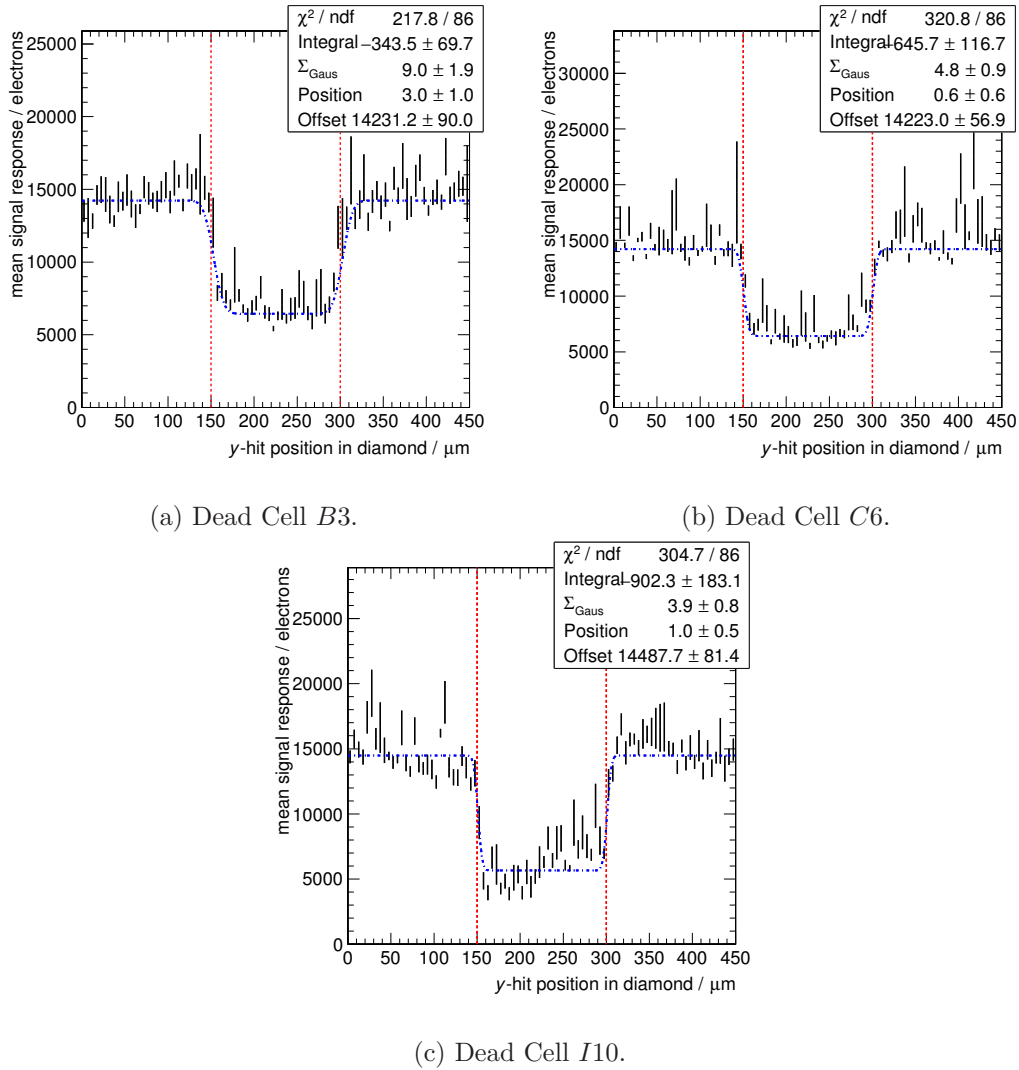
Figure 4.17.: Signal response of dead cells.

133

with two vertical red lines. By comparing the extracted position of the cells with respect to each other the alignment can be adjusted. As adjacent cells could have a distorted signal response as well, the fit does not work for each dead cell. By adjusting the alignment parameters based on good fits an alignment precision of approximately 5 µm was achieved.

4.2.2.2. Further analysis changes

To study 3D detectors with the analysis framework of the irradiation analyis, further changes have been introduced for the specific 3D analysis step.

The performance of the diamond test detector was analyzed with two methods: a 'clustered' and a 'transparent' analysis. The 'clustered' analysis uses the above mentioned definition to construct clusters starting from a seed channel and adding adjacent channels fulfilling the cluster criteria as used in the silicon detectors. The 'transparent' analysis sums the three closest read-out channels to the predicted track position as determined from the track fitting to form a 'transparent' cluster.

In order to understand effects due to broken readout electrodes three different categories were defined: *good cells*; *all but bad cells*; and *bad cells*. *Bad cells* are defined as cells which probably have broken readout electrode. In case of the scCVD sample these cells were identified before hand with optical inspection and resistive measurements of the electrodes. For the pCVD sample these measurements were only performed on a subset of the detector and hence were not used. Therefore, the broken readout electrodes were identified by the signal response of the corresponding cell. In order to study the expected performance of a fully working detector, a continuous region, in which there are no cells with broken readout electrode, is selected. All cells in this region are called *good cells*. All cells but the ones which have a broken readout electrode are called *all but bad cells*.

With a good alignment it is possible to study the signal response within a single cell. The predicted hit position is used to get a relative hit position within the cell. For these measurements the $150 \times 150\,\mu\mathrm{m}^2$ cell is divided into 15×15 bins with a size of $10 \times 10\,\mu\mathrm{m}^2$. As the statistics per cell are not very high, multiple cells are overlaid to increase the statistics.

4.2.3. Results

In the following the results of the 3D scCVD and the 3D pCVD diamond detectors are presented. After a proof-of-principle with the 3D scCVD diamond detector the capabilities of the concept of 3D detectors based on diamond material is shown with the 3D pCVD sample. This section is closed by a discussion about the differences between the two detectors.

4.2.3.1. 3D Detector based on a scCVD Diamond

The 3D scCVD diamond detector was tested in August 2012 at a bias voltage of $+25\,$V. A total of $1.1\,$M events were collected for this run. The corresponding electric field distribution for this bias voltage is shown in Figure 4.18. It can be seen that the field is strongest around the electrodes, reaching field strengths of more than $10^4\,$V/cm, corresponding to $10\,$V/µm. In between the bias electrodes, there are regions with relatively low electric fields.

After an explanation of the calibration method, the noise of the three regions is studied, followed by a first comparison of the charge spectra. It was found that events with negative signals in the adjacent readout channel occur, which cannot be explained by noise fluctuations. These events were studied and their cause are discussed. With the understanding of these events the the final charge spectra comparison can be performed. The section is finished with the results for the expected resolution and the charge response within the cell.

Calibration   A detailed description of the calibration method can be found in Section 3.6.4. As this device is based on an unirradiated scCVD diamond, the charge calibration from ADC to electrons was performed by using the signal response of the strip detector. Figure 4.19 shows the signal distribution for the strip detector: Figure 4.19 (a) shows the ADC distribution, in Figure 4.19 (b) the same distribution is shown after applying the calibration. The calibration constant is applied in such a way that the mean of this distribution ($1119\,$ADC) corresponds to a collected charge of $C = 440\,\text{µm} \cdot 36\,\text{e}/\text{µm} =$
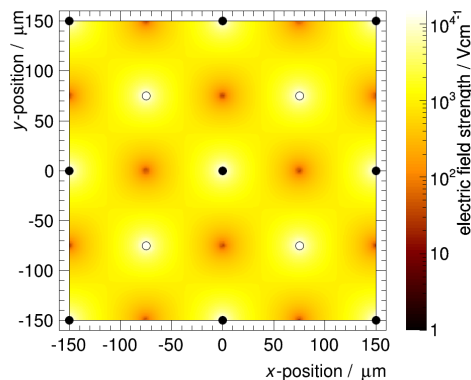
Figure 4.18.: The calculated electric filed distribution of a four cell array for a bias of $+25\,$V. Bias electrodes are marked with solid circles and readout electrodes are marked with empty circles.

(a) Raw distribution in ADC.

(b) Calibrated distribution in electrons.
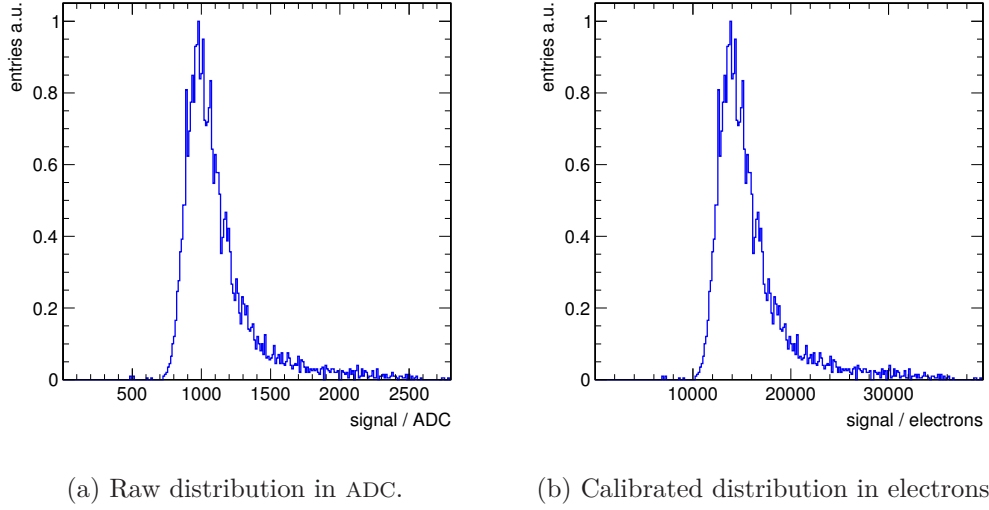
Figure 4.19.: Calibration of the 3D detector setup using the strip detector.

15 840 e. Resulting in a calibration constant of 7.06 ± 0.10 ADC/100e. This constant is also checked by comparing the noise distributions and by a pulser calibration on the test bench, performed before the beam test at OSU, see Section 3.6.2.1 and the different calibration methods result in the compatible calibration constants within the errors.

Electronic Noise The electronic noise for all channels before common mode correction was measured to be 109 e by measuring the width of the Gaussian. The common mode was measured on an event by event base. A Gaussian fit was performed and a width of 4.5 ADC was extracted, corresponding to 31.8 e. After applying a correction for common mode noise the noise was reduced to 91 e. In Figure 4.20 the electronic noise distribution of all readout channels connected to the diamond test device are shown, while Figure 4.21 shows the separate distribution for each detector. The common mode corrected noise (σ) is measured to be 82 e for the planar strip detector (Figure 4.21 (a)), 92 e for the 3D phantom (Figure 4.21 (b)) and 95 e for the 3D detector (Figure 4.21 (c)). The noise of the planar strip detector is in full agreement to the measured noise distributions of the radiation analysis and the order of the noises is expected as the capacitance of the detectors the strip detector is the lowest and the capacitance of the 3D detector is the highest. As no measurement of the exact capacitances was performed it cannot be checked if the quantitative differences are correct.

The measured noise for the planar strip detector is in full agreement with the expected noise, as shown in Section 3.6.4. This indicates that used calibration constant is correct. This means that the planar strip detector is collecting full charge at the applied bias voltage of $+500$ V.
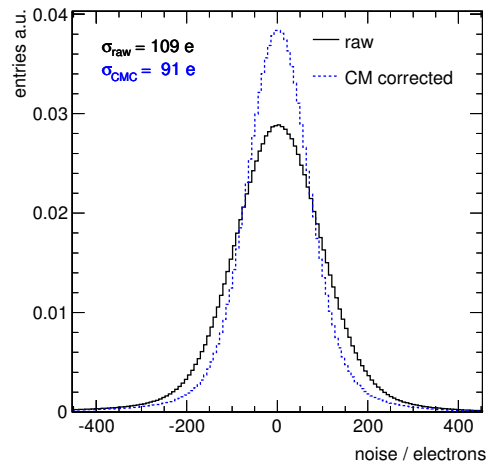
Figure 4.20.: Noise distribution for all connected channels within all three DUT.

(a) Strip detector   (b) 3D phantom   (c) 3D detector
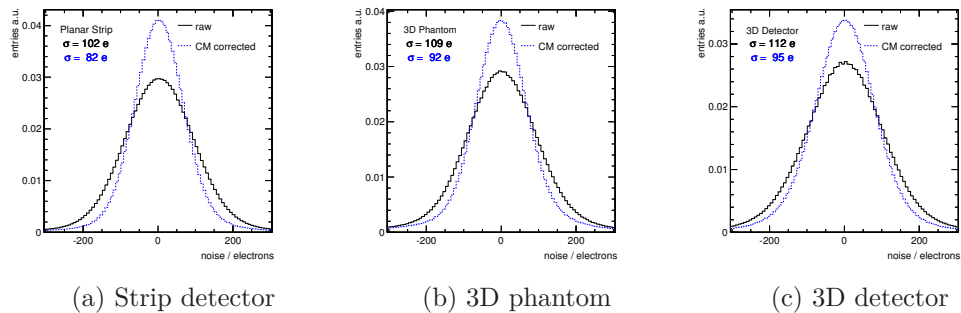
Figure 4.21.: Noise distributions of all channels connected to the three active regions. The raw noise distribution is shown in black, the common mode corrected distribution is indicated by the blue dashed line.

Charge Spectra   Only events with a track passing through one of the diamond test device active regions are kept for further analysis. This reduced the data sample from 1.1 M events to a data sample of 250 k events.

In a first step the performance of the three detectors is investigated by using a clustered analysis. 85 % of the events have single clusters, the remaining 15 % have multiple clusters. It is observed that the majority of two cluster events occur when the predicted hit position is within the 3D phantom detector. This can be seen in Figure 4.22. The predicted hit positions for single cluster events are shown in green, while the predicted hit positions for multi-cluster events are shown in blue. Almost all multi-cluster events are observed in 2 regions: The region between the strip detector and the 3D phantom and in the right half of the 3D phantom detector. In events occurred in the both regions, clusters are observed in both adjacent detectors, either in the planar strip detector and the 3D phantom, or in the 3D detector and in the 3D phantom detector. Since no guard rings were use to isolate the three detectors from each other, charge sharing could occur in between the various detector geometries.

Figure 4.23 shows the average charge signal as a function of predicted track position in the diamond. Here the charge signal is calculated by summing over all cluster charges in the three regions. The three detector regions on the diamond are marked as strip, 3D phantom, and 3D and correspond to the regions of Figure 4.11. The strip detector extends past the trigger scintillator and only the strips in the trigger shadow are included in the analysis which follows. It can be observed that the response of the 3D phantom is position dependent. This distortion occurs due to the different electric field configurations of the adjacent detectors. On the right side the 3D detector with its electrodes in the material is picking up charge. On the left side the strip detector with its back
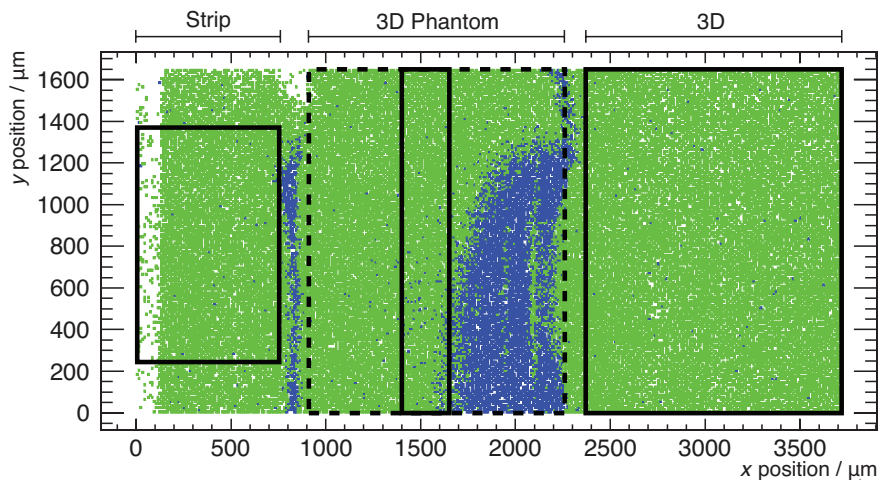
Figure 4.22.: The predicted hit position of all events. Events with a one cluster are shown in green, events with more than one cluster are shown in blue.
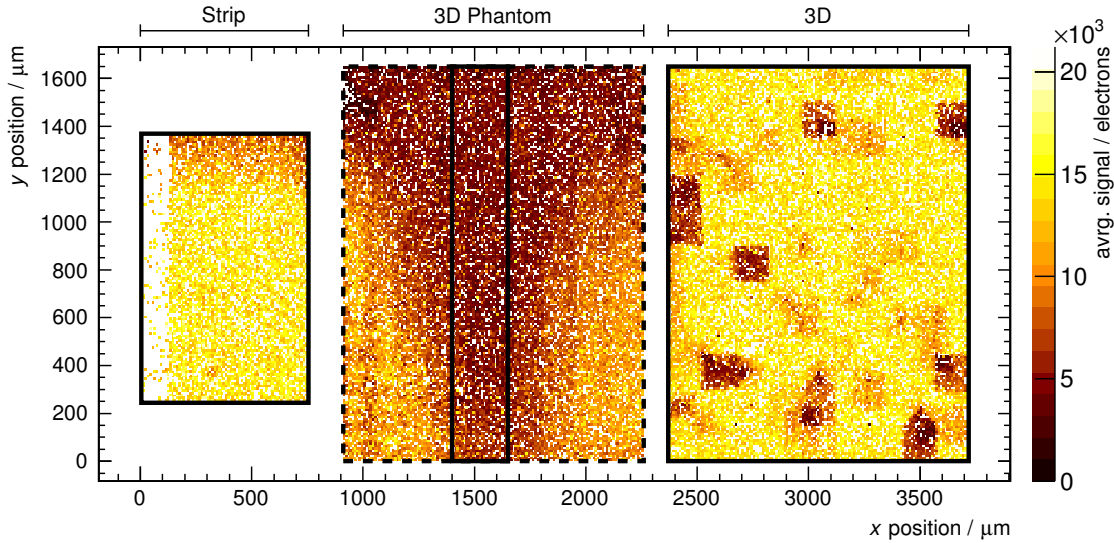
Figure 4.23.: The average charge signal of the prototype detector as a function of the predicted track position. In this plot the charge signal is defined as the sum over all cluster charges. The strip, 3D phantom and 3D detector areas are marked.

metalization collects the charge. Here the effect due to the higher bias voltage seems to results in almost all charge being collected with the planar detector and the 3D phantom collects only a small fraction of the charge. For the following analysis steps only the marked central region of the 3D phantom was analyzed to reduce the influence due to these distortions.

Charge Spectrum Comparison In the following sections, the transparent cluster definition is used, consisting of the three closest channels to the predicted hit position. For ease of comparison the following pulse height spectra are scaled in such a way that the most probable peak position has a height of 1. The transparent cluster charge spectra of the three detector regions are shown in Figures 4.24 (a) and 4.24 (b). The cluster charge of the planar strip detector exhibits a typical Landau-Vavilov distribution [155], with a MPV of about $13\,700\,e$. With a FWHM of $\sim3700\,e$ the fraction of FWHM over the MPV can be calculated to be 0.27. This is in agreement with other measurements for scCVD diamonds. The 3D detector shows a more complex distribution consisting of two approximately Gaussian peaks, an upper peak around $13\,500\,e$ and a lower peak around $6600\,e$, where the upper peak coincides with the MPV of the strip detector spectra.

The dashed line in Figure 4.24 (b) indicates the cluster charge spectrum of the 3D phantom obtained from the entire region, while the solid line corresponds to the spectrum of the central region only. The central region exhibits a Landau-Vavilov shape, with a
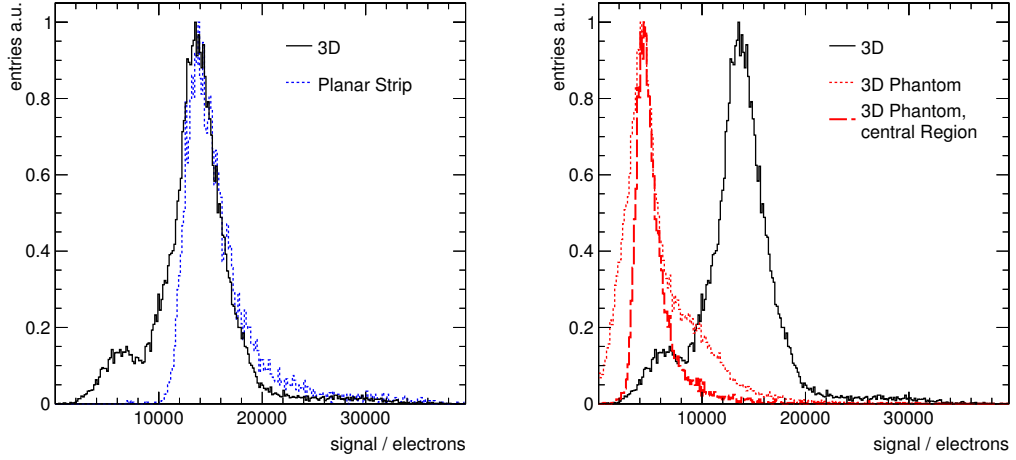
(a) The cluster charge spectra from the strip (dashed blue) and 3D detectors (solid black).

(b) The cluster charge spectra from the 3D phantom and the 3D detector are. The 3D phantom (red lines) exhibits a significantly lower cluster charge spectrum.

Figure 4.24.: Comparison between the charge spectra of the 3D detector with planar strip detector and 3D phantom.

most probable value at approximately $4450\,e$, being considerably lower than MPVs of the strip and 3D detector. The mean of this distribution is $5430\,e$. Assuming that all charge up to a certain depth is collected with such a device, the measured mean corresponds to an average drift distance of $150\,\mu m$, twice the electrode spacing. This is expected as only charge near the surface contributes to the charge signal since the 3D phantom is essentially an interdigitated surface device with $150\,\mu m$ pitch.

The charge spectra of the 3D phantom central region and 3D detector start at a similar value. Hence, the lower peak is most likely caused by incomplete cells only collecting a fraction of the deposited charge; these are cells with a defective or non-contiguous readout electrode.

A map of the pulse height response of the 3D detector is shown in Figure 4.25. A grid which shows the position of the cells is overlaid. Each square represents one single cell with a readout electrode in the middle and four bias electrodes in the corners. In total there are 99 cells labeled from A1 to I11. It can be observed that nine cells, A7, A8, B3, C6, E2, E10, H1, I3, and I10, show a strongly reduced signal response, below $9000\,e$. It was found that these are the same cells for which a broken bias electrode has been found. Therefore the mean signal response of the cell is an indication for broken or non-connected readout electrodes. The yield for the electrode production can therefore be extracted as $91 \pm 3\,\%$. This is in full agreement with the yield of $92 \pm 3\,\%$, found with optical inspection (cf. Section 4.1.4). As there is no difference in the fabrication of
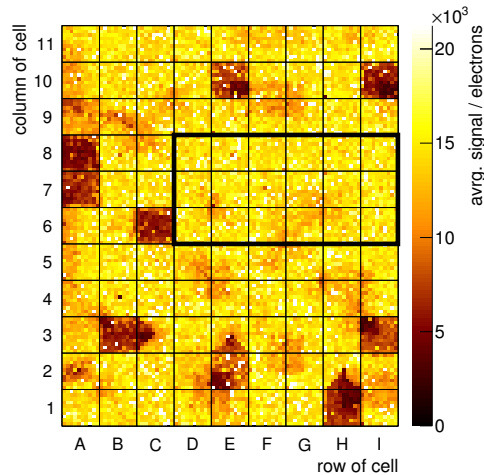
Figure 4.25.: The average cluster charge versus predicted hit position in the 3D detector. The individual cells are marked by the overlay. Each cell has a readout electrode at its center and bias electrodes in the corners. The thick rectangle highlights the *good* cell region.

readout and bias electrodes ~10 % of the bias electrodes are expected to be defective. It can be observed that the signal response around some bias electrodes is reduced and might indicate a broken or non-connected bias electrodes. As bias electrodes are shared by four cells, a single broken bias electrode is influencing the charge collection in a big region and therefore it is important to investigate in detail which bias electrodes are broken.

Negative Charges   During the analysis it was found that events occur in which one of the channels of the transparent cluster has a negative signal response. For this reason the minimum signal response within the three channels is calculated. The negative charge is defined as this minimum and can be associated with one channel of the transparent cluster. Only events in which the *negative signal* is actually below zero were considered for the further analysis. In Figure 4.26 the negative charge contributions of the channels contained in the transparent clusters are shown. In 70 % the biggest negative charge is observed in the second closest strip with respect to the predicted hit position. The distributions of the second and third closest strip show a peak close to zero, with a steep fall. In the distribution of the second closest strip a broad peak with signals below $-700\,e$ is visible. A negative charge of $-700\,e$ would correspond to noise fluctuations of about $7.7\,\sigma$, this shows that these events cannot be explained by pure noise fluctuations.

When plotting the predicted hit position for events with charges below the $-700\,e$, shown in Figure 4.27, it is apparent that these events are clustered around the positions of bias electrodes. This leads to the assumption that defect bias electrodes can cause negative signals.
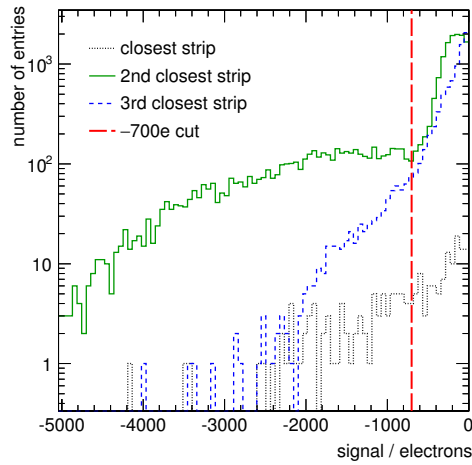
Figure 4.26.: The negative charge contributions of the channels contained in the transparent clusters. The three channels are sorted by distance to the predicted track position. The threshold of $-700\,e$ to define a negative signal is indicated by the red vertical dashed line. After applying the selection 88 % of all negative signals appear in the second nearest strip (green solid line) to the predicted position.
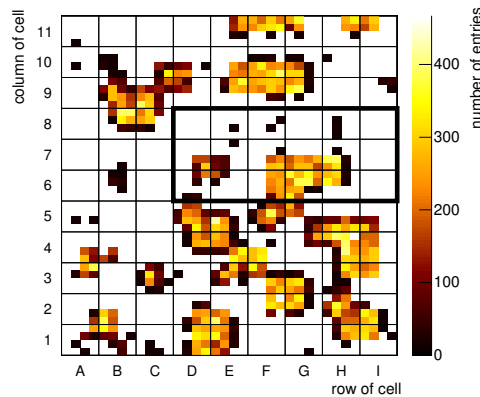
Figure 4.27.: Predicted hit position within the 3D detector for all events where a negative charge below $-700\,e$ has been observed. Bias lines are located at the crossing of the grid overlay. There is a clustering of these events around bias electrodes. The black rectangle marks a subset of adjacent cells used in further analysis as the fiducial region.

The experimental observation of negative signals could be reproduced with a simulation based on the TCAD Sentaurus package [156], using a model for single crystal diamond taking into account the electric field distribution, the field dependent hole and electron mobilities, and the finite lifetime of charge carriers [157]. The negative signals are likely due to the finite lifetime of the electrons and holes.

(a) (b)
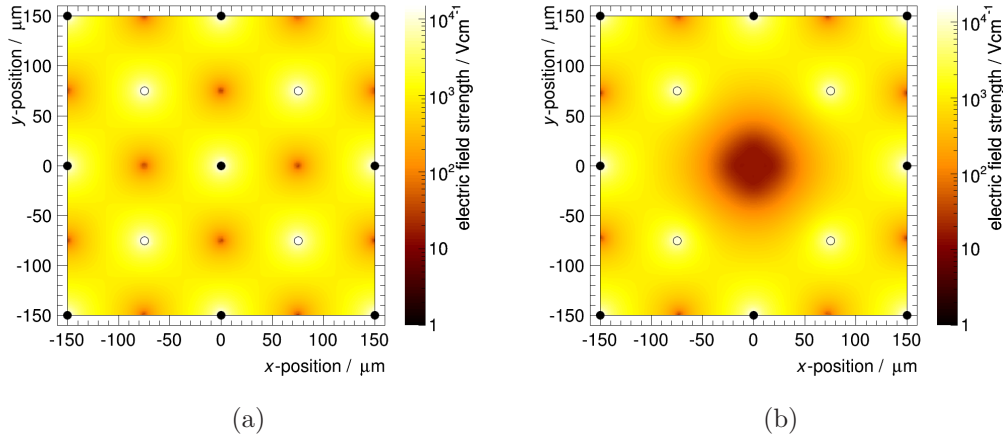
Figure 4.28.: The calculated electric field strength distributions of a four cell array in the case of fully functional cells for a bias voltage of 25 V. Bias electrodes are marked with solid circles and readout electrodes are marked with empty circles.
In Fig. (a): A electrodes are connected.
In Fig. (b): The middle bias electrode is missing.

In the case of a missing bias electrode the field strength in the region around this electrode is significantly reduced, leading to lower drift speeds of the charge carriers in this region. This can be seen in Figure 4.28 which shows the electric field strength distributions of a four cell array in the case of fully functional cells (a) and in the case of a missing bias electrode (b). The finite lifetime of the charge carriers lead to trapping of the carriers before they can reach an electrode. Thus they can induce a charge with opposite sign on the next nearest signal electrode with respect to the nearest signal electrode due to the shape of the weighting field. Similar observations have been made with 3D detectors based on silicon [158].

When mapping the predicted position of negative charge events onto the full 3D detector, it appears that most are clustered around 20 bias electrodes. This results in a yield for bias electrode formation of $83 \pm 4\%$, which is slightly lower, but still consistent with the measured yields from optical inspection ($\varepsilon = 92 \pm 3\%$) and the yield extracted from the signal response of the cells ($\varepsilon = 91 \pm 3\%$). With the simulation based evidence

that negative charge signals are an indicator of a missing bias electrode, an additional method for measuring the electrode production yield was developed. The negative charge response is further used for rejecting events close to broken bias electrodes, as discussed in the following paragraph.

Charge Spectra Comparison of 3D and Strip Detector To exclude the contribution of cells with defective readout electrodes to the signal spectrum of the 3D detector, a continuous region, in which there were only fully functional readout electrodes, was selected as indicated in Figure 4.25 by the thick rectangle rectangle. To reduce the effect of broken bias electrodes, events containing significant negative charge below $-700\,e$ are removed.

Figure 4.29 shows the transparent charge signal spectra of the selected region of the 3D and the strip detector overlaid. The average charge in the strip detector is $16\,800\,e$, the average charge of the 3D detector is $15\,900\,e$. The peak of the strip detector charge distribution is $14\,700\,e$ and the peak of the charge distribution of the 3D detector is $15\,000\,e$. The two spectra are consistent in their most probable value and their width of the distributions. The strip detector exhibits a slightly larger tail towards events with large signal, which can be associated with large energy transfers. The discrepancy might by caused by the size of the negative charge selection criteria and needs to be investigated further. Nevertheless, the comparison shows that the 3D detector collects equivalent charge to the planar strip detector at a twentieth of the bias voltage.
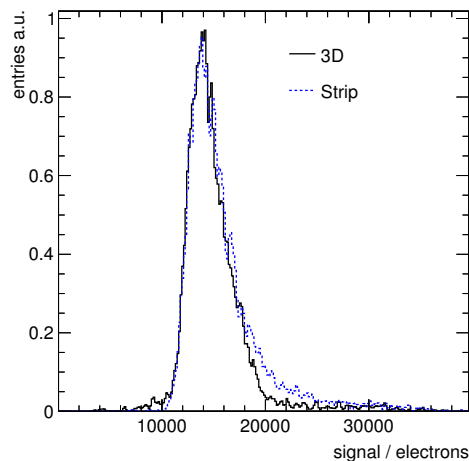
Figure 4.29.: The transparent charge pulse height spectra of the strip detector and 3D detector continuous fiducial region, as highlighted in Figure 4.25.

Resolution The spatial resolution of the 3D detector was investigated by reconstructing the position using the centroid of the two channels with the highest signal within 3 strips of the incident beam track. Since the cells were ganged along the y-axis only the resolution in x-direction could be assessed. The residual of the reconstructed centroid position in the continuous fiducial region on the 3D detector is shown in Figure 4.30. The flat top distribution has a standard deviation of $\sigma(x) = 40.2 \pm 0.3\,\mu\text{m}$. This indicates no significant charge sharing between the 3D cells as this is only slightly lower than the 'digital' resolution of $150\,\mu\text{m}/\sqrt{12} = 43.3\,\mu\text{m}$.
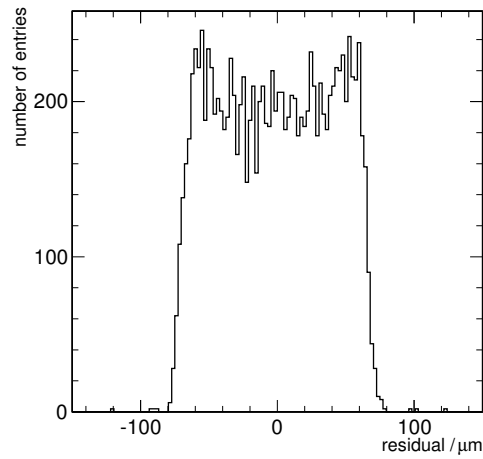
Figure 4.30.: The residual distribution of the 3D detector showing no significant charge sharing between the 3D cells.
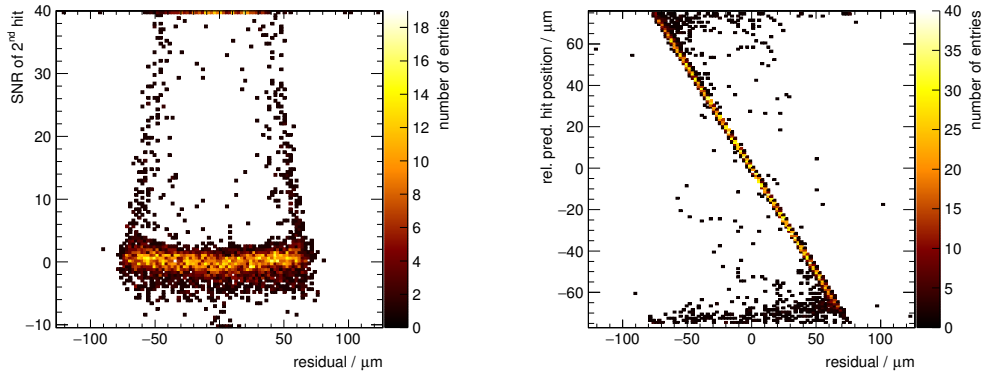
(a) The residual as a function of the SNR of the second hit for the 3D scCVD sample.

(b) The residual as a function of the relative predicted hit position.

Figure 4.31.: The residual distribution of the 3D detector versus relative predicted hit position with respect to the closest readout strip (a) and versus the SNR of the second highest hit of the cluster (b). Events with slight charge share occur close to the edges of the cell.

Figure 4.31 shows the residual distribution as a function of the relative hit position in the cell and as a function of the SNR of the second highest hit in the cluster. From Figure 4.31 (a) one can see that most events do not have SNRs of the second highest hit below four. For events with higher SNRs the residual becomes smaller. By studying Figure 4.31 (b) it can be observed that in the range between $-60\,\mu m$ to $60\,\mu m$ no charge sharing is apparent. In the outer most regions of the cell the residual distribution indicates that charge sharing can occur. In these regions the electric field is lowest and the drift distances furthest.

(a)   (b)
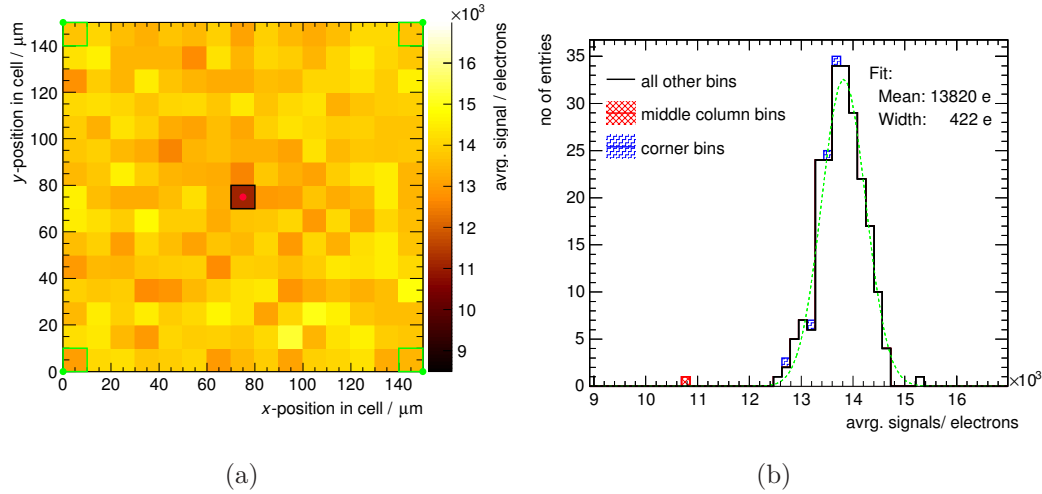
Figure 4.32.: In (a) the average cluster charge as a function of the predicted hit position within the cell is shown. The dots indicate the position of the electrodes of the cell. In Figure (b) the 1D distribution of the average cluster charge in the $10 \times 10\,\mu m^2$ bins within (a) is plotted. The bins with readout and bias electrode are highlighted.

Charge Response Within The Cell The 2D charge distribution of all cells with a functional readout electrode (*all but bad* cells) were overlaid as explained in Section 4.2.2.2. The distribution is shown in Figure 4.32 (a). Therefore this plot contains the overlay events of 90 cells. In order to have sufficient statistics in each bin, a bin size of $10 \times 10\,\mu m^2$ has been chosen. There is a significant reduction in the average charge of the central bin, where the readout electrode is located, relative to the overall average value of bins. Through optical measurements the bias electrode was estimated to have a diameter of ~6 μm, therefore in a $10 \times 10\,\mu m$ bin 30 % of the bin is covered by the electrode. The signal distribution of events in the central bin shows two distinct distributions with about 30 % of the total entries below 7000 e, corroborating the view that particles traversing the electrode yield very low or no signals. The bins in the corners contain a quarter of a bias electrode, therefore, only about 7 % of events are expected to yield lower charge.

Figure 4.32 (b) shows the pulse height distribution of the 225 bins. The bins including a bias or readout electrode are highlighted in red and blue. By excluding those bins and fitting a Gaussian a mean of 13 820 e with a standard deviation of 422 e can be extracted, resulting in a width of 3 %. This shows that the charge response within the cell is very uniform when excluding areas containing either readout or bias electrodes.

4.2.3.2. 3D Detector based on a ₚCVD Diamond

In the following section, the results of the 3D ₚCVD diamond detector, biased at $+70\,$V, are presented. These data were taken during the October 2015 beam test campaign. Similar to the discussion of the 3D scCVD detector results, the calibration is presented and confirmed by the noise distributions. With the calibration a first comparison of the charge spectra of the three detector regions is possible. In this detector negative signal responses within the transparent cluster were found, which cannot be explained by only statistical fluctuations. The cause of these negative signals was investigated by comparing the collected data with simulations. The results of these studies were used to develop a method for distinguishing broken bias electrodes. By selecting events in a contiguous region with fully working readout electrodes, a final comparison of the signal response in the 3D detector and the strip detector was possible. This section concludes with the results for resolution and the charge response within a cell.

Calibration   In the October 2015 no unirradiated scCVD diamonds were tested, therefore a different way for extracting the calibration constant was needed. The diamond *SINGLE A*, described in Section 3.7, was tested in the same beam test and the the same repeater card was used, which resulted in the same gain. Thus the same calibration constant is valid for both detectors.

The calibration constant for *SINGLE A* was obtained using the following procedure. The diamond *SINGLE A* was tested in two different beam tests with the same irradiation level (see Table 3.7), in November 2014 and October 2015. During the November 2014 beam test campaign an unirradiated scCVD diamond was tested. That scCVD diamond was used to extract a calibration constant for that beam test. The common mode corrected noise and the average pulse heights of both beam tests agree within less than $3\,\%$. This leads to the conclusion that the calibration constants for both beam test are the same. The resulting calibration constant is $7.80 \pm 0.12\,$ADC/100 e.
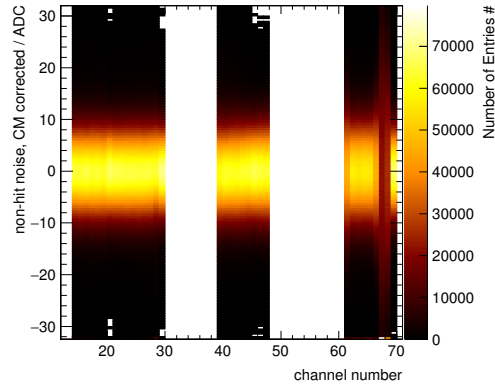
Figure 4.33.: Common mode corrected noise distribution as a function of channel number for the 3D pCVD sample.

Electronic Noise   The noise distributions for each channel are shown in Figure 4.33. It can be observed that three channels, channels 67 to 69, have a much broader noise distribution. These channels are connected to the 3D detector and bias the average noise of the detector. For this reason the noise is two different noise estimations are caulcluated. One for the full 3D detector region and a second noise estimation, which is calculated for 5 adjacent non-noisy channels (channels 62 to 66), this estimate is referred as the non-noisy region in the following paragraph. The common mode distribution is centered around zero and the width of the Gaussian fit was measured to be 8.14 ADC, corresponding to 103 e. The separate noise distributions, with and without common mode noise correction, are shown in Figure 4.34.

(a) Strip detector

(b) 3D phantom

(c) 3D detector, no noisy channels
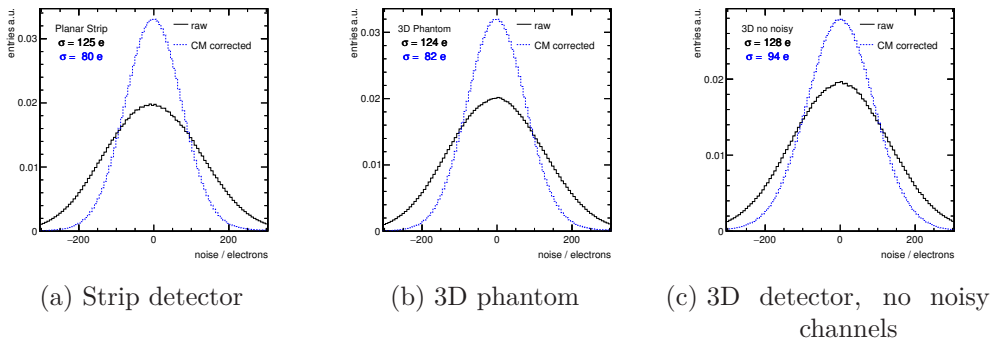
Figure 4.34.: Noise distributions of all channels connected to the three active regions. The raw noise distribution is shown in black, the common mode corrected distribution is indicated by the blue dashed line. For the 3D detector the region with no noisy channels is shown. The common mode corrected noise is 80 e for the planar strip detector (a), 82 e for the 3D phantom (b) and 94 e for the 3D detector (c).
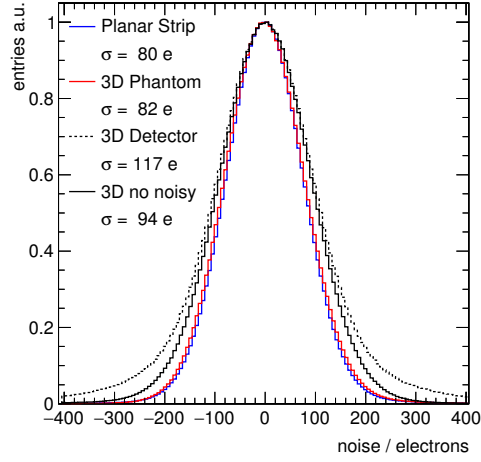
Figure 4.35.: Noise distribution for the three detectors of the 3D pCVD sample. For the 3D detector a region with no noisy channels is additionally shown.

The electronic noise after common mode correction was measured for each detector separately. For the planar strip detector it was measured to be $80\,e$, for the 3D phantom $82\,e$, for the full 3D detector $117\,e$ and for the non-noisy region $94\,e$. An overlay of all common mode corrected noise distributions is shown in Figure 4.35. It can be seen that the noise of the planar strip detector is in agreement with the noise measurements performed for the irradiation analysis, see Section 3.6.4 and is similar to the noise measured for the planar strip detector of the 3D scCVD detector. This confirms that the calibration constant is valid and that the method used for extracting the calibration constant gives the correct results. The noise of the 3D detector is also similar to the one of the 3D scCVD detector when excluding the noisy channels. While the noise of the scCVD 3D phantom is similar to the noise of the scCVD 3D detector, the noise of the pCVD 3D phantom is smaller and close to the noise of the pCVD planar strip detector region.

Charge Spectra In order to take account of the smaller charge response expected from a pCVD diamond, especially for the 3D phantom, the cluster seed and hit factor were reduced to $\mathrm{Thr_{seed}} = 4 \times \sigma_{\mathrm{Noise}}$ and $\mathrm{Thr_{hit}} = 3 \times \sigma_{\mathrm{Noise}}$. When requiring one and only one hit in every silicon detector and a predicted hit position within one of the three detectors, the dataset contains a total of $220\,000$ events. After applying the final selection criteria on the χ^2/NDF of the track, requiring $\chi^2/NDF < 5$, the total number of events was reduced to $168\,800$, consisting of $23\,700$ events with a predicted hit position in the planar strip detector, $68\,800$ within the 3D phantom and $76\,300$ within the 3D detector.

As discussed in Section 4.1.6 the wire bonding scheme for the strip detector was adjusted as one pad of the *VA2.2* readout chip was broken. Due to this change the strip detector was split into two parts and multi-cluster events could be observed within the strip

detector, as seen in Figure 4.36. In this figure the position of 500 000 events in a region around the DUT are shown. Events without a cluster in one of the three regions are marked blue, with exactly one cluster are marked black and events with more clusters are colored green. In Figure 4.36 (b) the three regions of the detector are additionally highlighted in red.
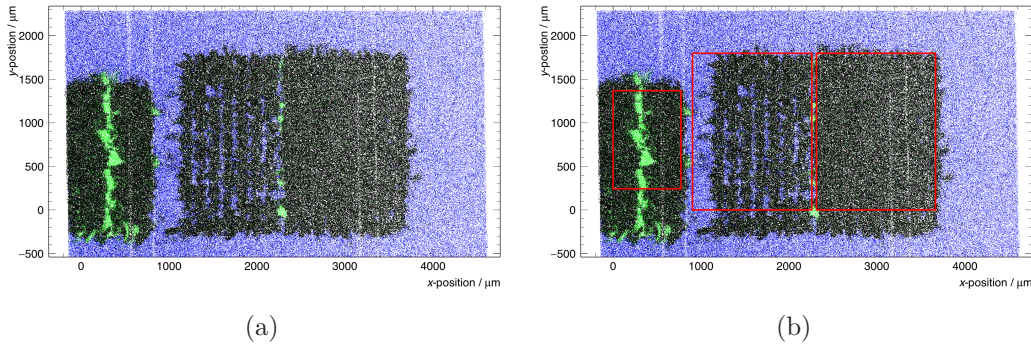
Figure 4.36.: Predicted hit positions of events in the rough fiducial cut. The events with no cluster are marked in blue, with one cluster in black, with two clusters in green and with more clusters in orange. In Figure (b) the regions of the three detectors are additionally marked in red.

In between the 3D phantom and the 3D detector at several positions events with multi-clusters are clustered. These events might be caused by non functional bias electrodes, in which charge can be collected by the adjacent detector. With the highlighted region of the 3D phantom, a 200 µm wide region in the left part of the 3D phantom detector can be seen in which most events do not contain a cluster in any detector region. This indicates that the left most strip of the 3D phantom detector was broken or not read out correctly. Further a pattern within the one cluster hit positions can be observed. The distance of the strips is in agreement with the readout pitch of 150 µm, indicating that the pure surface device is collecting charge only in a region close to the readout strips and that the signal response close to the bias strips is smaller than the seed threshold of $Thr_{\mathrm{noise}} = 4 \times \sigma_{noise} \approx 330\,\mathrm{e}$.

In Figure 4.37 the average charge within the three detectors is shown as a function of the predicted hit position. As for the 3D scCVD sample the charge signal is defined as the sum over all cluster charges within the three detector regions.
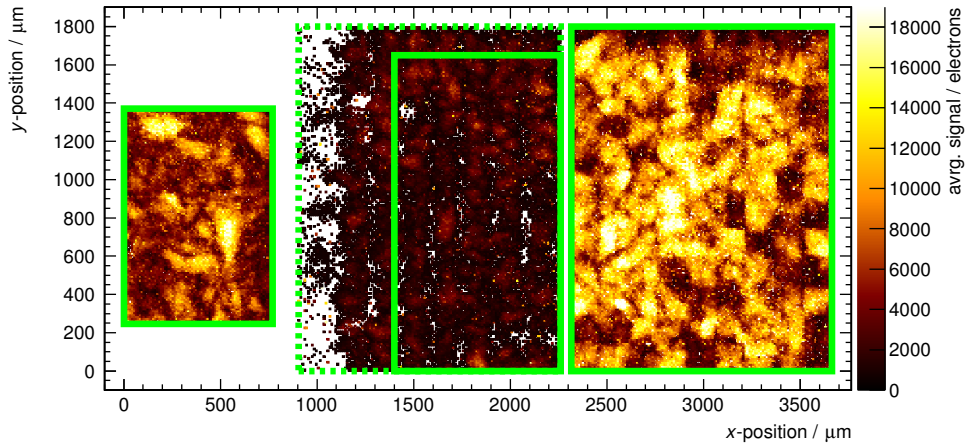
151

Figure 4.37.: The average charge signal of the prototype detector as a function of the predicted track position. In this plot the charge signal is defined as the sum over all cluster charges. The strip , 3D phantom and 3D detector areas are highlighted in green. For the full region of the 3D phantom a dotted line is used, the region without the left part is marked with a solid line. The strip detector was operated at a bias voltage of $+500\,\text{V}$, the 3D phantom and the 3D detector were operated at $+70\,\text{V}$.

The three detector regions on the DUT are highlighted in green, as strip, 3D phantom, and 3D; and correspond to the regions of metalization pattern, shown in Figure 4.11. For the 3D phantom two different regions are investigated; the full detector, marked by a dotted line, and a smaller region ignoring the left part of the 3D phantom, marked by a solid line. The fiducial cut applied for the planar strip detector is smaller than the full metalization pattern in order to reduce the effect due to inhomogeneous electric fields close to the edges.

In the planar strip detector the charge response variation is large. Regions of high signal responses with charges up $18\,000\,\text{e}$ can be observed, while in other regions the average signal response is below $5000\,\text{e}$. These differences may be caused by inhomogeneities within the pCVD diamond material. The charge response in the 3D phantom is much lower compared to the planar strip detector: In a huge fraction of the detector the average signal is below $3000\,\text{e}$; with some areas were the charge response is increased up to $6000\,\text{e}$. These higher responses areas are clustered along vertical lines, indicating that the highest signals are generated in regions close the readout strips. The low signal collection is expected as the 3D phantom acts like a pure surface device and therefore the electric field within the detector is very low.

Comparing the three detector regions it can be seen that in the 3D detector, the regions with signal response above $10\,000\,\text{e}$ are larger than in the strip detector region. In

this region a variation in signal response can be observed as well, but the regions with low signal response are smaller than in the strip detector. In addition to the signal fluctuations due to the inhomogeneities in the pCVD diamond material, regions with low response can be observed which have sharp vertical and horizontal edges. These regions are most likely caused by the effects of broken electrodes. In the further analysis the electrode production yield will be studied. It can be concluded that the charge response in the pCVD sample is more complex than the response in the scCVD sample. Therefore it is more difficult to distinguish broken from working readout electrodes.

Charge Spectrum Comparison   In the following sections the transparent cluster method is used. Therefore the charge is defined as the sum of the two highest signals in the three channel cluster. In Figure 4.38 the charge spectra of the three detectors are compared with each other using this charge definition.

The spectrum of the strip detector starts at approximately 700 e, showing that there are no regions in which the detector is inefficient. With its steep rising edge and the long tail towards high deposited charges due to high energy transfers the distribution shows the expected characteristics of a Landau distribution The distribution peaks around 4000 e and has a mean of 6200 e. This corresponds to a CCD of 172 μm, resulting 35 % of full charge collection. The FWHM of distribution is 4300 e. This results in a fraction of FWHM over the MPV of 1.08 which compatible with other measurements for pCVD diamonds.

The charge spectrum of 3D phantom exhibits a steep falling distribution starting at 0 e. This shows that the pure surface device biased at 70 V on a pCVD diamond sample collects a small amount of charge. The mean of the distribution is 1190 e for the full 3D phantom and 990 e for the central region.
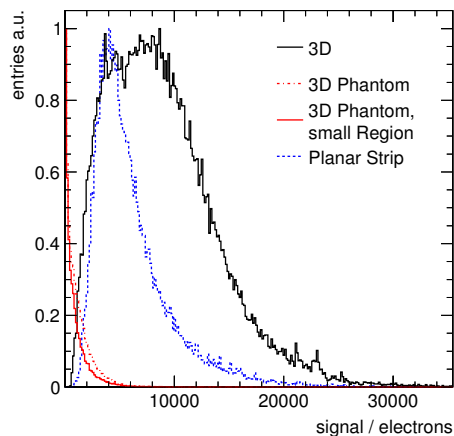
Figure 4.38.: Charge spectra for the three detectors of the 3D pCVD sample.

The full raw charge spectrum of the 3D detector is the broadest of the three spectra. It starts slightly below the strip detector spectrum around 500 e, but does not show a distinct peak position. In the region between 3000 e to 10 000 e the distribution is relatively constant. Above this value the distribution is falling with a long tail towards high signals. Events with signals above 25 000 e can be observed. The mean of this distribution is 8870 e and is therefore 43 % higher than the mean of the planar strip distribution. The FWHM was measured to be 11 200 e. As no distinct MPV can be found, the calculation of the FWHM-MPV-fraction was not performed. The broad distribution most likely can be explained by different charge responses of cells due to broken electrodes.

Figure 4.39 (a) shows the average pulse height in the 3D detector with the cell grid overlaid; It can be seen that there is variation in charge response. There are cells, such as E1, with low charge response. Additionally, cells with a low charge response within a small region, such as $C5$, are noticeable. To study the charge response of the 3D detector, the cells of the detector were graded as *good*, *bad* or in-between (*all but bad*). The corresponding signal responses of the single cells is shown in Figure 4.39 (b). This distribution shows a low peak at 5000 e and a broad peak with responses between 8000 electrons and 12 000 electrons. The threshold to identify cells with defective readout electrodes was chosen to be 7300 e. Thin colored boxes around each cell are used to

(a)   (b)
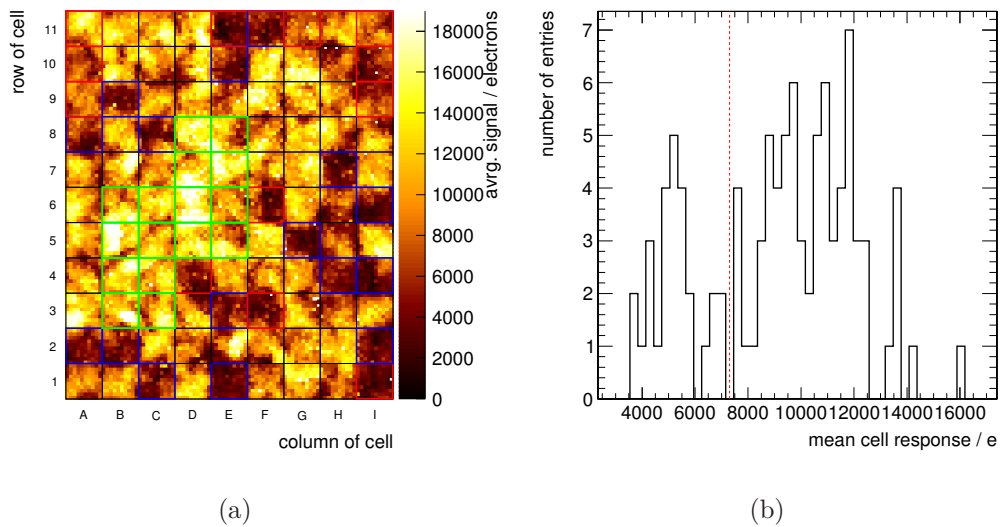
Figure 4.39.: Figure (a): The average cluster charge versus predicted hit position in the 3D detector. The individual cells are marked by the overlay. Each cell has a readout electrode at its center and bias electrodes in the corners. The good cell region, containing 16 cells is marked in green. Cells highlighted in red and blue are cells which might have issues with the readout electrode, the blue cells are used to check the alignment in y direction.
Figure (b): The mean signal response of each cell. The threshold of 7300 e has been chosen to identify broken readout electrodes.

highlight the different kinds of cell types. Cells colored in red and blue are cells in which the low signal response below the threshold could be the cause of readout electrode issues, the blue cells are used to check the alignment in the y-direction. In total 28 cells were graded as bad by using a threshold of $7200\,\mathrm{e}$ on the mean signal response of the cell; from which a yield for electrode fabrication of $72 \pm 5\,\%$ can be extracted. From these 28 cells a subset of 12 cells was chosen to check the alignment in y direction. For the following analysis a region with 16 adjacent cells was chosen as a good cell region, which are colored in green. In Table 4.4 all *good* and *bad* cells are listed.

Negative Charges   For this study the same negative charge definition is used as for the scCVD sample. For each event the smallest signal within the transparent cluster is chosen. This signal is associated to one specific readout channel of the transparent cluster. The counting of the readout channel is performed relatively to the predicted hit position, resulting in a closest, a second closest and a third closest strip. All events in which the smallest signal is below zero are shown in Figure 4.40. The spectra of the second and third closes strip have a peak close to zero. The width of this peak is approximately $130\,\mathrm{e}$. This is expected from noise fluctuations of the pedestal. In the spectrum of the second closest strip, this distribution is overlaid with a second, much broader, distribution, peaking around $-900\,\mathrm{e}$. By comparing this distribution with Figure 4.27, the one of the scCVD sample, one realizes that negative charges occur more often for the pCVD sample. In order to investigate the difference to the scCVD sample and to understand the cause of these negative charges, events with a negative charge below $-250\,\mathrm{e}$ have been selected for further analysis.

The positions of these events is shown in Figure 4.41 (a). In comparison to the structure seen for the scCVD sample, this hit distribution looks different. While in the case

Cell	Count	List
All	99	–
Bad	28	A2, A8, A9, A10, A11, B2, B9, C1, C8, D4, E1, E3, E10, E11, F3, F6, F11, G5, G11, H4, H7, I1, I2, I4, I6, I9, I10, I11
Good	16	B3, B4, B5, B6, C3, C4, C5, C6, D5, D6, D7, D8, E5, E6, E7, E8

Table 4.4.: List of all cells in each category. The good cell region is chosen such that all cells are adjacent without any bad cells included.

(a) Linear.

(b) Logarithmic.
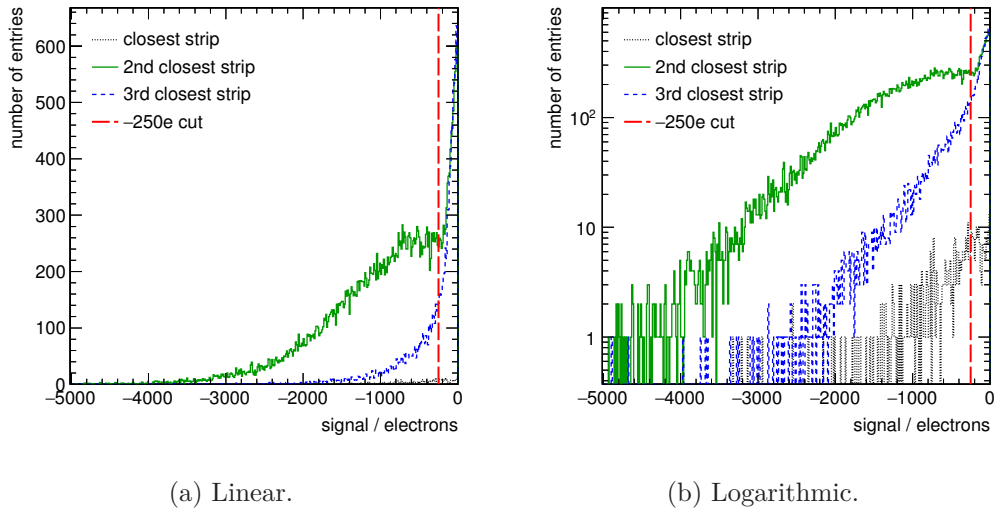
Figure 4.40.: The negative charge contributions of the channels contained in the transparent clusters. The three channels are sorted by distance to the predicted track position. Figure (a) shows the distribution in linear scale, while (b) shows the distribution with a logarithmic scale on the y axis.

(a) Absolute Position

(b) Relative Position.
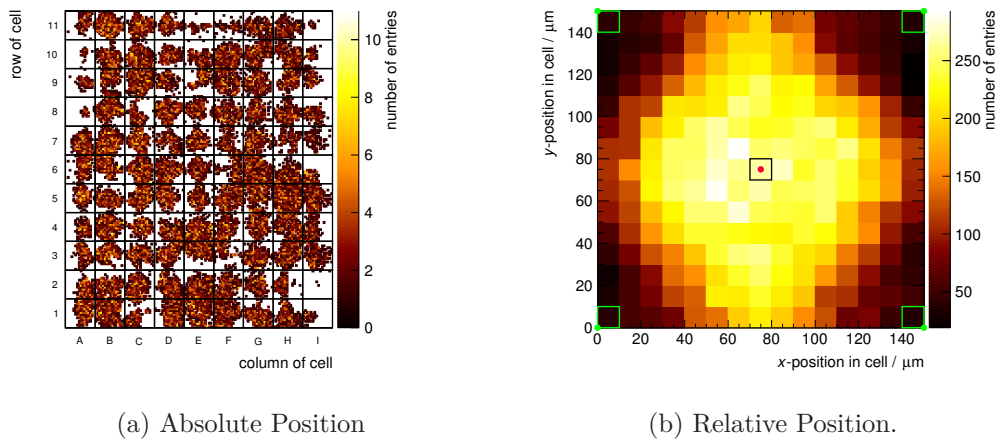
Figure 4.41.: Predicted hit position within the 3D detector for all events where a negative charge below $-200\,$e has been observed. The metalization for the bias is located at the crossing of the grid overlay. Figure (a) shows the absolute position. In Figure (b) this positions are mapped into one cell.

of the scCVD sample almost all events with negative charges are clustered around the bias electrodes, the hit distribution is more complex in the pCVD case. Most of these events can be observed in the center of the cell, close to the readout electrode. This clustering can be enhanced by looking at the relative position within the cell. The events with negative charges are clustered around the readout electrode in a lozenge-shaped structure, as shown in Figure 4.41 (b). In most cases the region around the bias electrodes only contain very few events with negative charges, but at some bias electrodes negative charges can be observed as well. In order to understand the differences in the distribution compared to the scCVD sample, the effect of negative charges was studied further.

For this study a new variable, called *adjacent charge ratio*, is defined. For this definition the signal of the second channel of the transparent cluster S_{2nd} is divided by the signal of the first channel of the transparent cluster S_{1st}. In order to take alignment uncertainties into account this ratio is only calculated for events in which S_{1st} is greater than S_{2nd}. The distribution of this variable is shown in Figure 4.42, for the three different cell definitions *all* cells (Figure (a)), *all but bad* cells (Figure (b)) and, *good* cells (Figure (c)). A narrow distribution, peaking around zero, contains the events without negative charges. The long tail towards positive ratios is caused by charge sharing in the region between the cells. The distribution has more events with a negative charge ratio than with a positive charge ratio. When increasing the 'quality' of cells, switching from *all* cells to *all but bad* cells and further to *good* cells, it can be observed that the peak at zero gets more and more suppressed. For the *good* cells region this peak is completely gone and a peak around -4.2% can be seen. In Figure 4.43 the number of entries at this peak position is used to scale the distributions with respect to each other. It can be seen that the distributions agree with each other for the positive charge ratios above 10%. In all three distributions a peak around -5% can be observed. For lower ratios the good cells distribution is lower than the other two indicating less negative charges

| (a) All cells. | (b) *all but bad* cells. | (c) Good cells. |
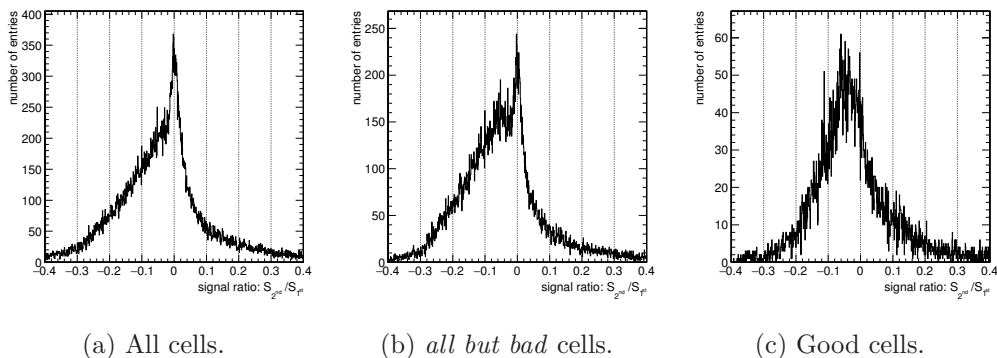
Figure 4.42.: Adjacent charge ratio for the three different regions. This ratio is defined by the signal of the second channel divided by the signal of the first channel of the transparent cluster.
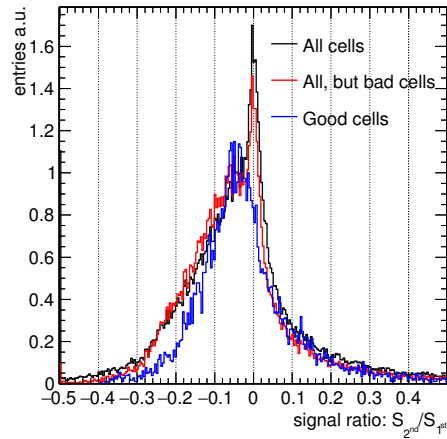
Figure 4.43.: Adjacent negative charge ratios for *all*, *all,but bad* and *good* cells, scaled such that the distributions are one at the peak position of the *good* cells distribution.

for these cells. The events with an adjacent charge ratio smaller than -0.3 show that negative charges can be a strong effect.

This charge ratio is then used to investigate where negative charge is observed within the cell. For this analysis *all,but bad* cells are used. The mean of the adjacent charges is calculated for different positions within the cell and used as a figure of merit. Figure 4.44 shows this average adjacent charge ratio within the cell for all events with a predicted hit position within a cell classed as *all but bad*. In order to reduce effects due to alignment uncertainties, all events with a predicted hit position within 5 µm of one of the edges of the cell are rejected. A lozenge-shape structure, similar to the one of Figure 4.41 (b) is observed. The distribution shows a horizontal and a vertical symmetry through
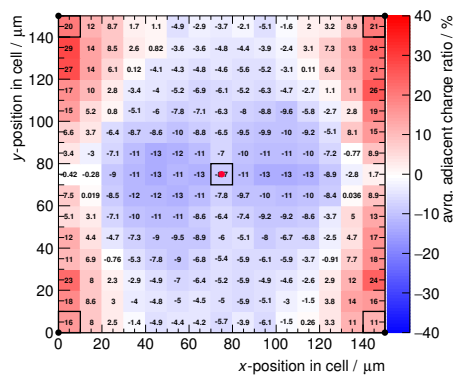
Figure 4.44.: Average adjacent charge ratio within the cell for all but bad cells.

the readout electrode, which is positioned at $75\,\mu m/75\,\mu m$. While the ratio within the lozenge-shape is negative, it tends to be positive outside. On the left and on the right side of the cell the highest values of $+10\,\%$ to $+27\,\%$ can be observed close to the bias electrodes. On the top and the bottom parts of the cell the average adjacent charge ratio is smaller, reaching a maximum of $+10\,\%$. Within the lozenge-shape, two regions of low ratios are found, one on the left and one on the right of the readout electrode. On both sides the smallest average charge ratio found is $-13\,\%$.

To understand these results a simulation of the cells based on the TCAD Sentaurus package [156] was used. The simulation was performed on a 2D mesh. With this simulation effects within the diamond material can be simulated, changes of the electric field due to the metalization are not included. More details can be found in [157]. An area of 2×2 cells was simulated. As in the real sample multiple cells are ganged together in y-direction, this is accounted in the simulation by summing the charges of cells within each column. As the effect of negative charges around the readout electrodes was not observed in the scCVD sample, the idea was developed that this effect is caused by the limited MFP of charge carriers. As the pCVD sample has a CCD lower than its thickness, the MFP of the material is lower. This limited MFP can be introduced in the simulation by limiting the charge carrier lifetime. A shorter charge carrier lifetime results in smaller MFP. This lifetime was then varied to the the effect of this parameter on the signal response within a 3D cell. In Figure 4.45 the adjacent charge ratio is simulated for 9 different lifetimes. A similar lozenge-shape as in Figure 4.44 can be seen in all plots. For lifetimes greater than $5\,ns$ the effect is strongly reduced. At carrier lifetimes in the range of $1\,ns$ to $5\,ns$ the simulation is in good agreement with the data. All main features of the data agree with the simulation: the global lozenge-shape, the horizontal and vertical symmetry, the position of the lowest and the highest ratio. Even the size of the adjacent charge ratios are in agreement. For a charge carrier lifetime of $3\,ns$ the lowest charge ratios are $-15\,\%$, found at $x = \pm40\,\mu m$ and $y = 0\,\mu m$. The biggest charge ratios can be found close to the left and right edges at $y = \pm40\,\mu m$. These charge ratios are simulated to be $+20\,\%$.

With this simulation it is possible to reproduce the measured negative charges and this simulation suggest that these effect is caused by the limited MFP in the pCVD diamond material. By comparing the simulation of different lifetimes with the data, this simulation can explain the data if the intrinsic charge carrier lifetime in that sample is of the order of $3\,ns$. The lozenge-shape can be identified to be caused by the weighting field of the adjacent readout channels.

Broken Bias Electrodes   As discussed for the scCVD diamond detector, negative charges around the bias electrodes are an indicator of broken bias electrodes. In the pCVD diamond sample this effect is combined with the negative charges due to the limited MFP in the diamond material. In order to measure the bias electrode production yield for the

(a) $\tau = 0.01$ ns.

(b) $\tau = 0.1$ ns.

(c) $\tau = 1$ ns

(d) $\tau = 2$ ns

(e) $\tau = 3$ ns

(f) $\tau = 4$ ns

(g) $\tau = 5$ ns.

(h) $\tau = 10$ ns

(i) $\tau = 20$ ns
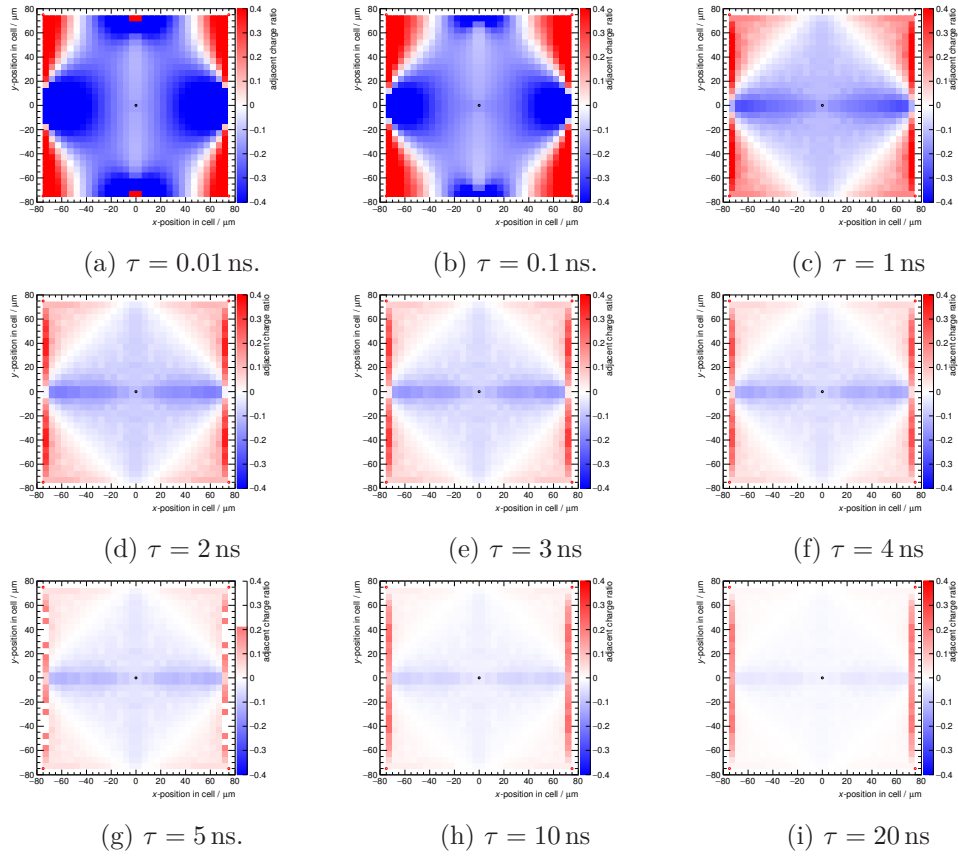
Figure 4.45.: Simulation of adjacent charge ratio within the cell for 9 different charge carrier life times τ: 0.1 ns, 0.1 ns, 1 ns, 2 ns, 3 ns, 4 ns, 5 ns, 10 ns and 20 ns (Simulations performed by G. Forcolin [157]).

pCVD sample, a study of negative charges around the bias electrodes was performed and is described in the following paragraph.

To identify broken bias electrodes, the fraction of negative charges was investigated in a lozenge-shaped region around each bias electrode. The lozenge has a side length of 84.8 µm, corresponding to a maximum distance of 60 µm to the bias electrode. In Figure 4.46 the position of the selected events for this analysis is shown. The selected region corresponds to 31 % of the full cell. The regions used for this simulation are highlighted with a hatch pattern. The size of the lozenge was chosen based on the simulation results with a charge carrier lifetime of 3 ns. The simulation showed that in this region the average charge ratio is positive. Therefore events with negative charges caused by the finite charge carrier lifetime are reduced to a minimum.

The negative charge spectrum for this region compared to the spectrum of the whole cell is shown in Figure 4.47. Both spectra are scaled in such a way that their peaks have a height of 1. The distributions agree for negative charges above $-150\,\mathrm{e}$. This falling distribution describes events in which the negative charge is the result of noise fluctuations. In the region below $-150\,\mathrm{e}$ the negative charge spectrum of the full cell is clearly above the one of the bias electrode region. This shows that the selection of events in this region reduces the number of events with strong negative charges.

For each bias electrode the *negative charge fraction* is studied. For this fraction all events with a predicted hit position in the lozenge-shape region around the bias electrode are considered. The fraction is then defined by the ratio of events with the negative charge below $-400\,\mathrm{e}$ and the ratio of all events in this region. In Figure 4.48 the fraction is plotted in a 2D histogram, each bin is representing the negative charge fraction around one bias electrode. This fraction is below 30 % for most of the bias electrodes, around some electrodes this fraction is increased, reaching a maximum above 80 %. This indicates that differences between bias electrodes can be found with this method. By projecting
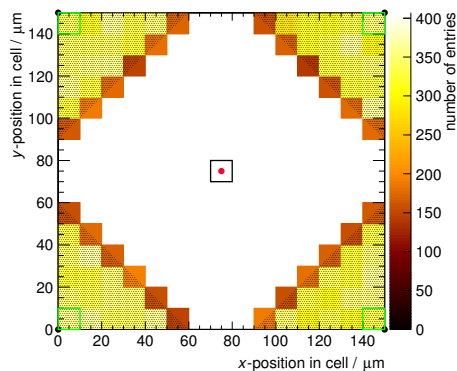
Figure 4.46.: Events selected for the investigation of broken bias electrodes. The region of the selected events is highlighted by the dotted area.

(a) Normal.

(b) Logarithmic.
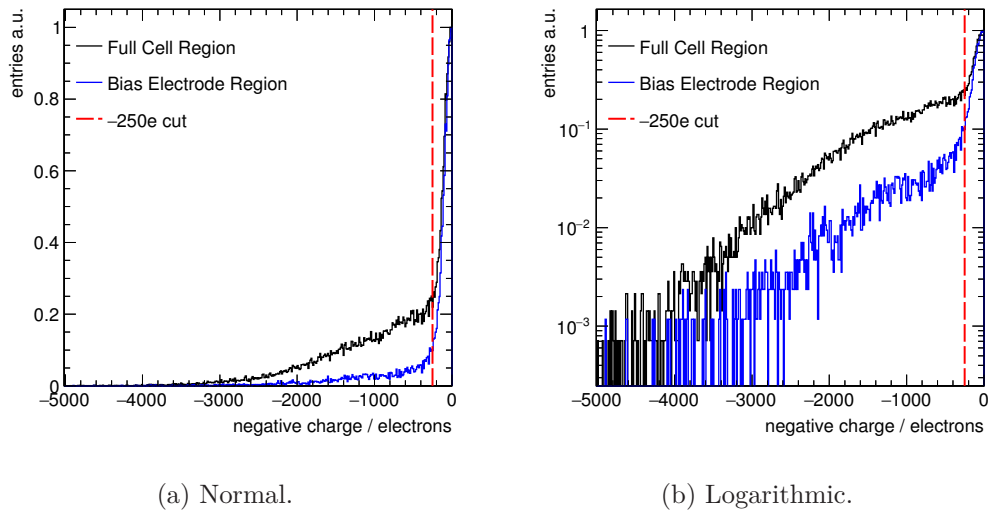
Figure 4.47.: Comparison of negative charge spectra of the full cell and of a region around the bias electrode, as shown in Figure 4.46. High negative charges are surpressed by the position cut.
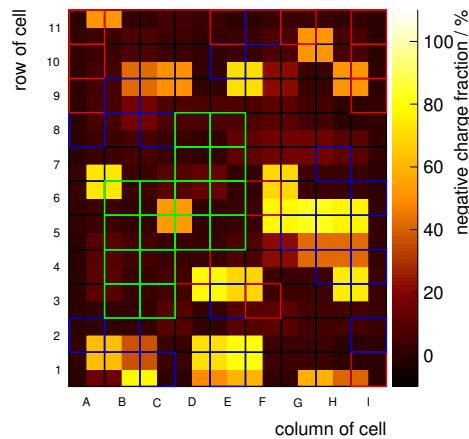
Figure 4.48.: Fraction of events with negative charges below 420 e and a predicted position in the region around the bias electrode with respect to the predicted hit position. Each bin represents one bias electrode. Cells are colored to highlight the cell type with the same color scheme as in Figure 4.39 (a).

these fractions in one distribution, it is possible to define a selection criteria which indicates that a bias electrode is broken. This distribution is shown in Figure 4.49 (a). The majority of bias electrode regions have negative charge fractions below 20 %. No regions with fractions between 25 % to 35 % can be observed. All other regions have fractions between 35 % and 85 %. A selection criteria for broken bias electrodes was chosen at 30 %. With the corresponding cumulative distribution, shown in Figure 4.49 (b), it is possible to extract the yield for bias electrode production. In total 22 bias electrodes are marked as broken, resulting in bias electrode production yield of 82 ± 4 %. This is higher than the yield extracted from the identified *bad* cells, but consistent, especially with having in mind that broken bias columns could reduce the signal in cells as well.

Comparison of 3D and Planar Strip Detector   For the comparison of the 3D detector with the planar strip detector, a continuous region of 16 cells was chosen in which there are no indications that a readout electrode is broken. The cells of this region are listed in Table 4.4 and are highlighted in Figure 4.39 (a) in green. This region contains two bias electrodes which have a high negative charge fraction, indicating that these bias electrodes are broken. They are positioned in the left upper corner of $B6$ and between the cells $C5$, $C6$, $D5$ and $D6$. A similar rejection of events with negative charges to that applied for the 3D scCVD sample could not be used for the 3D pCVD sample. In the case of the pCVD diamond the negative charges can be found in every cell in a lozenge-shape structure around the readout electrodes, while in the scCVD sample events with negative

(a) 1D.

(b) Integral
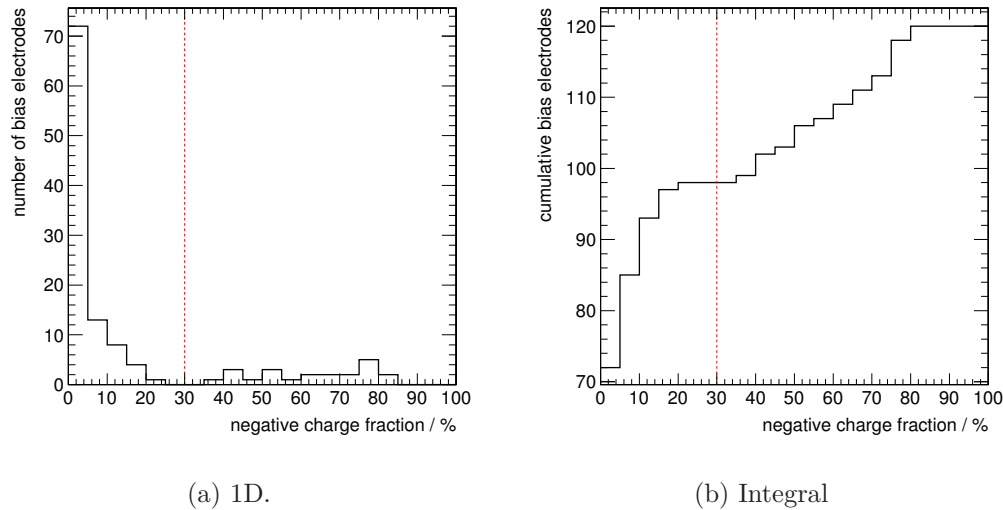
Figure 4.49.: Distribution of the negative charge fractions of Figure 4.49 is shown in Figure (a). The cumulative distribution is shown in Figure (b), it is used to measure the yield for bias electrode production. In both distributions the applied selection criteria for broken bias electrodes is chosen to be 30 % and is highlighted with a red dashed line.

charges were clustered around a small fraction of bias electrodes. With this rejecting all events with negative charge, Only events predicted outside of the lozenge-shaped region around the readout electrodes would be used.

For the analysis of the charge spectra transparent clusters with a cluster size of three were used. In Figures 4.50 (a) and 4.50 (b) the pulse height spectra are shown. Two different definitions for the signal are chosen. In Figure 4.50 (a) the *positive signal* definition is used. A *positive signal* is defined as the sum of all signals within the transparent cluster which are positive. Figure 4.50 (b) uses the *full signal* definition, in which the signal is defined as the sum of all signals, both positive and negative, within the transparent cluster. For the signal in the planar strip detector the *positive signal* definition is used. In both figures the signal spectrum of the planar strip detector is shown as a blue dashed line.

It can be seen that for both signal definitions the pulse height of the 3D detector is significantly higher than the pulse height of the planar strip detector. The mean of the planar strip spectrum is $\sim 6200 \pm 600$ e, corresponding to a CCD of $172 \pm 16\,\mu m$, and its MPV is 5200 ± 500 e. This measurement is in agreement with the measured CCD of $193 \pm 21\,\mu m$ in the source setup at $500\,V$. For the *positive signal* definition a mean of $12\,100 \pm 600$ e and a MPV of $10\,600 \pm 1000$ e can be extracted. As the *full signal* definition can add negative charges to the signal, the mean and the MPV of the spectrum are lower. The mean is measured to be $11\,500 \pm 600$ e and the MPVs to be 9700 ± 1000 e. The MPVs of the distributions are extracted by a Gaussian fit around the peak position. Due to the broad distribution the error on that fit is large, resulting in an large error on the MPV. The measured means result in an equivalent CCD of $336 \pm 17\,\mu m$ using the positive signal
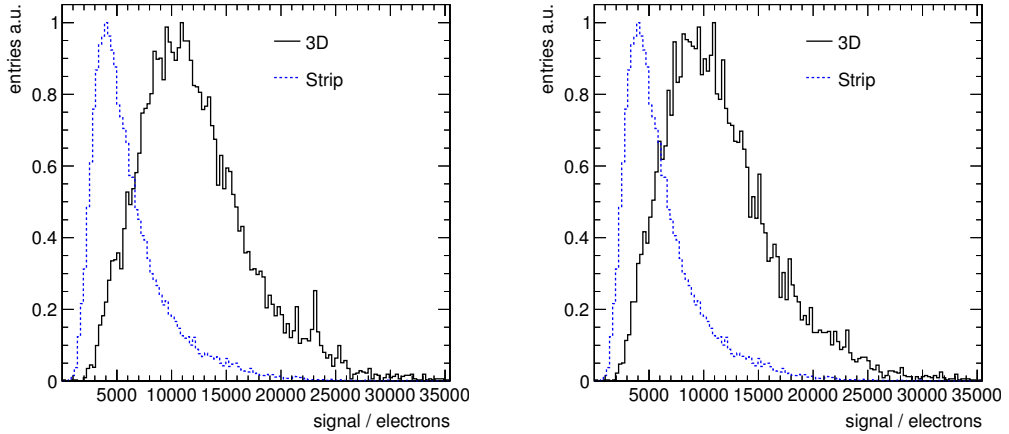
(a) Positive signal definition.

(b) Full signal definition.

Figure 4.50.: Comparisons of the signals of the 3D detector, biased at $70\,V$, and the planar strip detector, biased at $500\,V$, using two different signal definitions.

definition and $319 \pm 17\,\mu m$ using the full signal definition. This corresponds to $67 \pm 3\,\%$ and $63 \pm 3\,\%$ of the expected signal response of a full charge collecting detector.

By comparing these results with the signal of the planar strip detector, it can be seen that the 3D detector at a bias voltage of $+70\,V$ collects more than 1.8 times the charge of the planar strip detector, biased at $+500\,V$. In the source measurement the CCD of this diamond sensor in the planar configuration was measured to be $234 \pm 24\,\mu m$ at a bias voltage of $1000\,V$. By switching to the 3D geometry it is possible to collect $50\,\%$ more charge at a bias voltage of only $70\,V$, showing the potential of this technology.

In Figure 4.51 the spectra of the two different signal definitions are compared with each other. The *positive signal* spectrum is slightly shifted to higher signal responses, compared to the *full signal* spectrum. This is expected, as in the *postive signal* definitions negative charges are not added. For very high signal responses, above $26\,000\,e$, both distributions completely overlap. Two peaks in the spectrum of the *positive signal* definition can be seen at $21\,500\,e$ and $23\,000\,e$. Both peaks are not observed in the *full signal* spectrum. These peaks cannot be explained by random fluctuations or binning effects. On the low side of the signal spectrum the *positive signal* indicates that an additional peak at $\sim 5000\,e$ is resulting in additional events with low signals. In order to understand these additional peaks, the position of events with these signal response values was investigated.

In Figure 4.52 (a) the positions of events with a signal below $6400\,e$ is shown, while Figure 4.52 (b) shows the position of events with a signal between $21\,000\,e$ and $24\,000\,e$. Events with a low signal response are clustered in column E. More than $40\,\%$ of the events with a signal response below $6400\,e$ in the good cell region have a predicted hit position in this column and only $8\,\%$ of these events occur in column D. Additionally
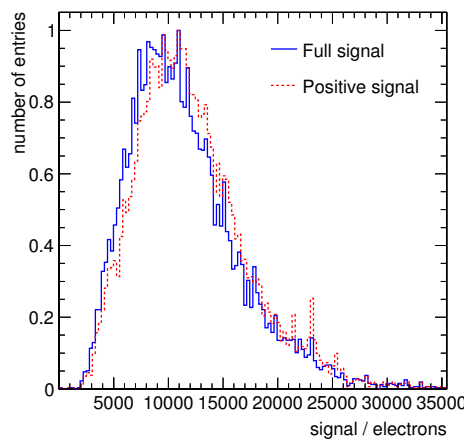
Figure 4.51.: Comparison of signal sepctra for both signal definitions. The *full signal* definition in solid blue and the *positive signal definition* in red dotted.
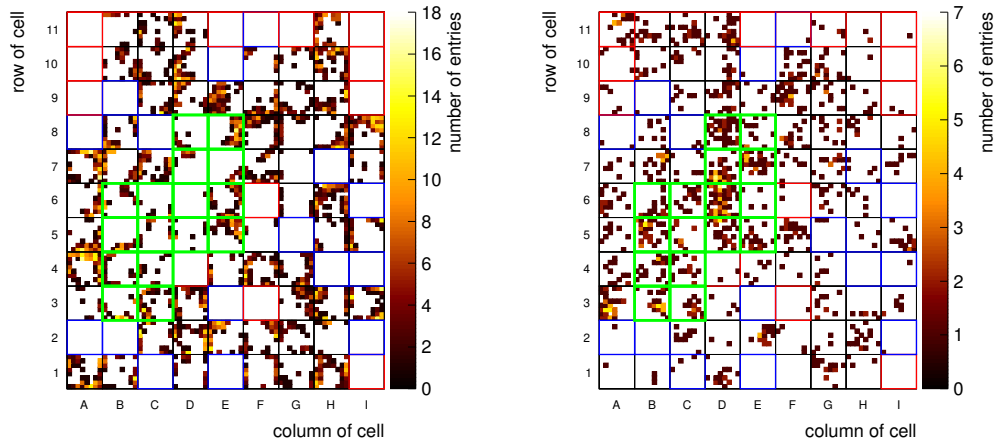
(a) Position of events with a signal below 6400 e.

(b) Position of events with a signal between 21 000 e and 24 000 e.

Figure 4.52.: Position of events from the low peak and the two high peaks of the charge spectrum shown in Figure 4.50 (a).

it can be seen that these events are often clustered along lines. A horizontal or vertical clustering along the borders of the cells can be explained by the low electric field in these regions. Clustering in the along lines through a cell might be caused by grain boundaries in the material. One theory is that part of the charge gets trapped in these boundaries resulting in a reduced signal response. In order to study these low pulse height regions in more detail, a dataset with higher statistics is needed, additionally simulations of the signal response of cells with grain boundaries are ongoing [157], which will investigate if grain boundaries are a possible cause for low signal responses.

The position of events with signals between 23 000 e and 27 000 e shows a clustering in only a few regions. This clustering cannot be explained with statistical fluctuations. Most of these events have predicted positions in in the columns B and D. It was found that if one investigate the pulse height distribution of each readout channel individually, a narrow peak at high signals between 20 000 e and 30 000 e can be observed in every single distribution. The position of that peak varies between each channel. The physical reason for these peaks has not been found yet and a more detailed investigation is needed to understand the cause.

Resolution To investigate the spatial resolution of the 3D detector, the residual distribution as a function of the SNR of the highest adjacent channel is shown in Figures 4.53 (a) and 4.53 (b). For this analysis the good cell region was used. In Figure (a) the position of the highest signal is used as an estimate for the position. It can be seen that events with a high SNR in the adjacent channel, having a residual close to $\pm 75\,\mu m$, indicating that significant charge sharing can only be observed in the outer 25 µm. By using

the signal response of the adjacent channel and using the centroid position of the two highest signals for position calculation, the resolution of the detector can be improved. For events with a SNR above 5 in the adjacent channel the residual is reduced, compared to the maximum signal position calculation method.

Figure 4.54 shows the projected residual distributions for both position definitions. The standard deviation of the residual of the highest signal position is $44.0 \pm 4.0\,\mu m$, which is consistent with the expected digital residual of $43.3\,\mu m$. The standard deviation for the two highest centroid calculation methods is $36.8 \pm 4.0\,\mu m$. In the central region no significant charge sharing can be observed, while in the outer regions the slight charge sharing improves the resolution of the detector.

Charge Response within the Cell   For the study of the charge response within the cell, the *all but bad* grade cells are used. The 2D charge distributions of these cells were overlaid. The cluster size of the transparent cluster was varied between one and three to study the effects of charge sharing. The corresponding distributions are shown in Figures 4.55 (a) and 4.55 (b). In both distributions the four bias electrodes are highlighted in green and the readout electrode is highlighted in red. A vertical and a horizontal symmetry through the readout electrode can be observed in both distributions. The signal response in the outer bins in the x-direction is reduced for the cluster size one distribution. This reduction cannot be observed in the y-direction.

By adding the signal of the two adjacent readout channels, this effect is reduced. For this distribution the signal response is above $>12\,600\,e$ in the central region of the cell (from $30\,\mu m$ to $120\,\mu m$ in the x and the y-direction). In the middle of the four edges a lower

(a) using the position of the maximum signal.   (b) using the highest two centroid position.
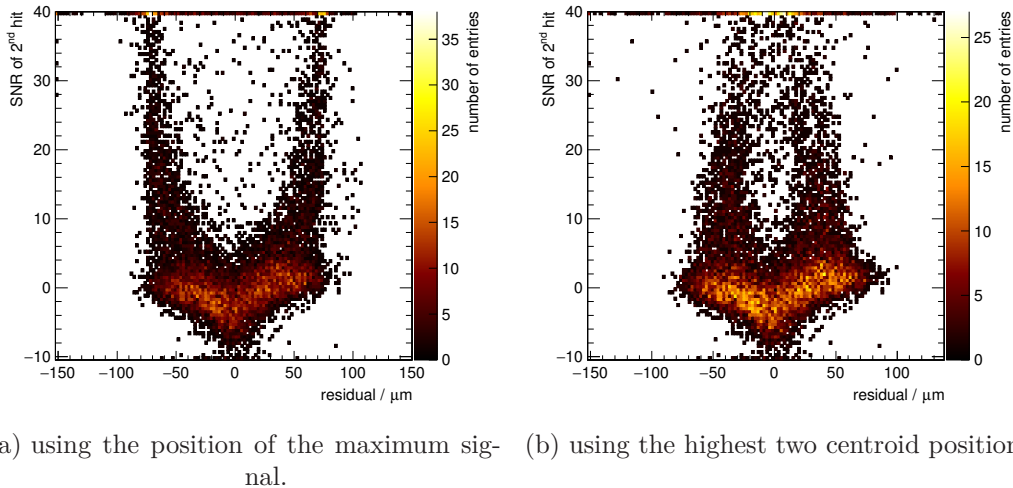
Figure 4.53.: Residual distribution for the good cell region as a function of the SNR of the highest adjacent strip.
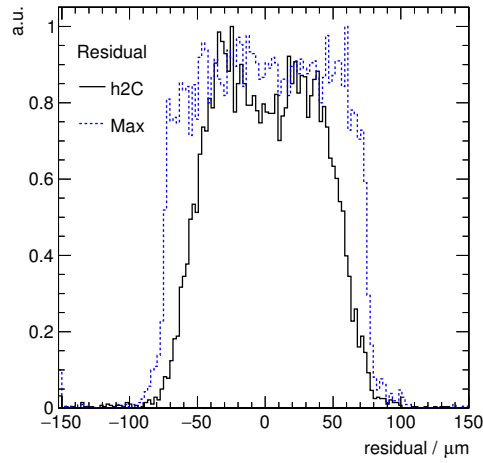
Figure 4.54.: Residual distribution for the good cell region using two different methods for position calculation: the blue dashed line shows the residual using the position of the highest signal. The black solid line shows the residual using the position calculated with the centroid of the two highest channels.
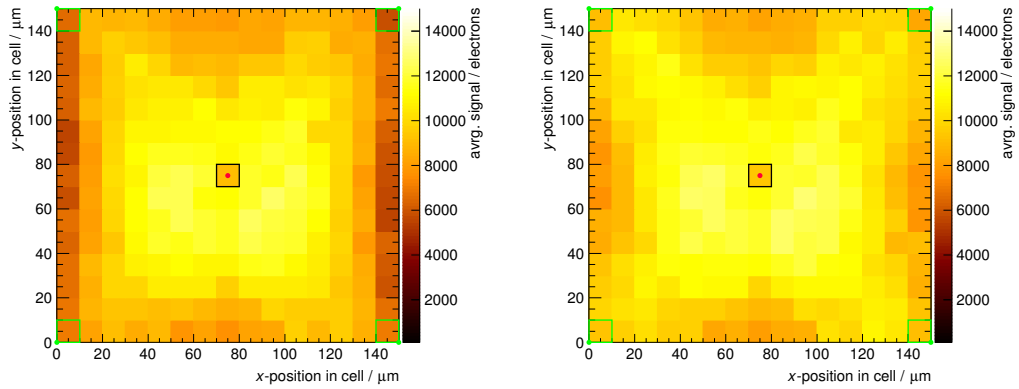
(a) Cluster size 1.

(b) Cluster size 3.

Figure 4.55.: The average cluster charge as a function of the predicted hit position within the cell for cluster size 1 (a) and 3 (b). The green dots indicate the position of the bias electrodes of the cell, while the red dot indicates the position of the readout electrode. A reduction of pulse height in the middle of each edge can be observed.

signal response can be observed. These lower regions show a by ∼20 % reduced signal response compared to the central region. These regions have a triangular shape and can be can be associated with low electric field regions within the cell. TCAD simulations showed similar distributions for charge carrier lifetimes of 1 ns to 5 ns.

By comparing the distributions with cluster size of one and cluster size three, one can observe a significant reduction on the left and right edge of the cell in case of the cluster size one distribution. This shows that in the outer regions (5 µm to 10 µm) of the cell the charge is split between the readout channels and confirms the slight charge sharing observed in the residual distributions. The effect cannot be measured in y-direction as cells above and below are connected to the same readout channel.

4.2.4. Comparison of scCVD and pCVD results

The results of the first 3D detectors based on scCVD and pCVD diamond material have been presented. As both detectors were based on the same detector layout, a direction comparison between the 3D scCVD and the 3D pCVD detectors is possible.

As the planar strip detector of the scCVD sample collected full charge, a direct calibration was possible and the charge collection of the 3D detector could be directly compared with that of a full charge collecting device. This is not possible for any pCVD sample as planar strip detectors using pCVD material have smaller CCDs than its thickness. With the planar strip region on the pCVD detector a charge collection of 172 ± 16 µm at 500 Vwas measured, which is in agreement with the measurements with the source setup at OSU. This corresponds to ∼33 % of full charge collection.

With the sampled using scCVD diamond material it was possible to show that the 3D detector collected full charge. This was achieved at a bias voltage of +25 V. In source measurements it was found that a corresponding planar strip detector requires a bias of more than 400 V to reach the same signal response.

Due to the limited MFP in the pCVD material, the advantages of the 3D detectors based on diamond could be demonstrated. The 3D detector, biased at +70 V, collected 1.8 times the charge of the planar strip detector, biased at +500 V. The source measurements showed a maximum CCD of 234 ± 24 µm at a bias voltage of 1000 V. This is approximately 100 µm less than the equivalent CCD measured in the 3D geometry. This means that with the 3D geometry biased with 70 V it was possible to increase the charge collection by more than 50 % compared to the planar geometry biased at 1000 V. Therefore the charge collection can be significantly improved if the material has limited MFP.

The comparison of average signal maps of the two 3D detectors (Figures 4.23 and 4.37) shows, that the charge collection of the pCVD sample is less homogeneous than the charge collection of the scCVD sample. A possible cause of this inhomogeneities could be the difference in the pCVD and scCVD material. Instead of a pure crystal the pCVD

diamond material consist out of grains, resulting in a more inhomogeneous material. An important factor for charge collection could be the behavior of charge carriers, when crossing grain. Trapping in these boundaries could result in reduced signal responses. Further studies are needed to understand the reasons for this inhomogeneous signal responses in detail.

Another big difference between the 3D scCVD and 3D pCVD results was found when studying the position of negative charges, see Figures 4.27 and 4.41. In the scCVD sample negative charges predominantly appeared close to a subset of bias electrodes. This leads to the assumption that negative charges occur when bias electrodes are broken and was confirmed with simulations. For the pCVD sample the situation is more complex. Negative charges were observed in all cells of the detector. These events were clustered around the readout columns in a lozenge-shaped structure. Simulations of the detector were performed and it was observed that the shape of the structure and the magnitude of the signals could be reproduced by reducing the charge carrier life times to approximately 3 ns. The simulations (shown in Figure 4.45) lead to a basic understanding of this effect and allowed the estimation of the charge carrier life time in the pCVD material.

4.3. Summary and Outlook

In this chapter the fabrication and testing of the first 3D detectors based on CVD diamond was described. An array of conductive electrodes was fabricated within the CVD diamond material using a femto second laser. An electrode formation yield of $92 \pm 3\%$ was achieved for the scCVD sample. The yield for the pCVD sample was measured to be $83 \pm 4\%$. Both detectors were tested in a beam test with $120 \, \text{GeV}/c$ protons. By including a planar strip detector and a 3D phantom detector in addition to the 3D detector on the same diamond, a detailed study of the new detector geometry could be performed, including a direct comparison between the two geometries.

By using the the homogeneous scCVD material, it was possible to demonstrate the proof of principle. The 3D detector biased at $25 \, \text{V}$ collected charge equivalent to the planar strip detector biased at $500 \, \text{V}$. The 3D phantom, an interdigitated surface detector, collected only one-third of the charge collected by the 3D detector. This indicates that that the bulk electrodes significantly improve charge collection. Detailed studies of the 3D detector charge spectrum showed the appearance of negative charges if the bias electrode was broken or not connected. This effect could be reproduced in TCAD simulations. No major charge sharing was observed in the 3D detector, resulting in a residual distribution close to the digital resolution. With this device the concept of 3D diamond detectors was shown to be viable.

The first 3D pCVD diamond detector was used to investigate the potentials of this concept. Optical inspection indicated a lower yield in electrode formation, this was confirmed by measuring the bias electrode yield. With the presented method a yield of

$82 \pm 4\,\%$ in bias electrode formation has been measured. By using the same metalization scheme as for the scCVD sample it was possible to compare the signal response of the three detectors with each other, as well as a direct comparison with the scCVD sample. The 3D detector, biased with $70\,\mathrm{V}$, collected more than 1.8 times the charge of the planar detector, biased with $500\,\mathrm{V}$, showing its great promise as a detector layout for pCVD diamond material. The comparison with initial source measurements even showed that the 3D geometry collects $50\,\%$ more charge than the planar configuration at a bias voltage of $1000\,\mathrm{V}$. Compared to the negative charge spectra seen for the 3D scCVD, the situation for the 3D pCVD detector is more complex. In addition to the appearance of negative charges due to broken bias electrodes, negative charges were also observed in a region around the readout electrodes. The limited MFP in pCVD diamond material was introduced in simulation by using a limited charge carrier life time. It was found that the best agreement with the measurements can be found for charge carrier life time around $3\,\mathrm{ns}$. In comparison to the scCVD sample the signal distribution is much broader, which might be associated with the grain boundaries and the lower electrode production yield. Charge sharing between cells is slightly higher compared to the scCVD detector resulting in smaller residual distributions.

While the charge collection within the cell is uniform for the scCVD sample, the pCVD sample shows a reduced signal response in the regions with the lowest electric fields. By changing the cell layout or increasing the electric field it might be possible to reduce the low electric field regions, such that the signal response within each cell becomes more uniform for detectors with limited MFP, such as pCVD detector.

These results show the promise of this detector layout. The prospective of increasing the charge collection in pCVD diamonds from that of the planar configuration indicates the advantage of such a technology for diamond based particle detectors. The measured charge for the 3D pCVD detector is more than $50\,\%$ higher than the maximum charge collection measured in a planar geometry on the same diamond. By increasing the electric fields and reducing the drift distances the signal response in 3D pCVD detectors might be increased even further.

An important step towards a high quality 3D diamond detector is the understanding of electrode formation process. The electrode formation yield must be improved significantly to close to $100\,\%$. Resistivity of $0.29 \pm 0.10\,\Omega\,\mathrm{cm}$ for the scCVD sample and $0.19 \pm 0.10\,\Omega\,\mathrm{cm}$ for the pCVD sample have been measured for typical electrodes. In the perspective of building a pixelated 3D detector for the HL-LHC environment, it is important to get lowest possible resistivities. The time constant of signal response is linearly dependent on the resistivity. Only with small resistivities it will be possible to build 3D detectors with shaping times small enough for LHC purposes. In addition the speed of the electrode formation must be significantly increased to produce large area devices.

A major advantage of 3D diamond detectors compared to 3D silicon detectors is the electrode production mechanism. Compared to the etching process used for 3D silicon

detectors the laser processing has a high flexibility in terms of electrode positioning and properties. This allows a cheaper and faster development cycles of electrode geometries compared to 3D silicon.

The studies of 3D diamond detectors are ongoing. New cell layouts, like honeycomb structures and smaller cell sizes; as well as larger area detectors are in development and tests are planned in 2016. Another important step in the development of 3D diamond detectors is the measurement of their radiation hardness. The combination of high intrinsic radiation hardness of the diamond with the improved charge collection of the 3D geometry could lead to particle detectors which are well suited for the use in very high radiation environments, such as HL-LHC.

5. Determination of the Sensitivity of Diamond Detectors to Particle Flux

During the operation of the PLT pilot run, described in Section 1.3.1, an unexpected pulse height decrease with increasing particle flux was observed. This decrease prompted the RD42 collaboration to undertake a systematic study of this effect.

In several beam tests at Paul Scherrer Institute (PSI) the pulse height as a function of the incident particle flux was studied. Initially it was possible to measure pad and pixel detectors with particle fluxes up to $\sim$300 kHz/cm^2. During these beam tests the following observations were made [33]:

(1) Non-irradiated scCVD diamonds do not show any significant flux dependence in the pad (less than 3 %) or pixel (less than 4 %) geometries.

(2) In tests of scCVD diamond pixel samples using diamonds which were removed from the PLT pilot run, a similar pulse height dependence as in the PLT pilot run was observed (50 % loss of pulse height at 20 MHz/cm^2).

(3) In tests of scCVD diamond pad samples, which were removed from the PLT pilot run, a pulse height decrease of 10 % was observed for particle fluxes of 300 kHz/cm^2. This shows that the same pulse height dependence on the incident particle flux can be reproduced outside of LHC experiments in particle beam test campaigns.

(4) pCVD diamond detectors irradiated to 5×10^{13} neutrons/cm^2, a similar irradiation level as in the PLT pilot run, did not show a decrease of the pulse height up to particle flux of 300 kHz/cm^2 (less than 3 %).

An upgrade of the initial setup was required to extend these observations to higher particle fluxes. In this chapter the new beam test setup is introduced, followed by a discussion of the new analysis method including a description of the final selection criteria. In Section 5.4, the first results of diamond pad detectors at higher rates which were tested in August and October 2015 are presented. This chapter closes with a summary of the results and an outlook for the future.

5.1. The Compact CMS Pixel Telescope

The original telescope setup was a six plane beam telescope which was constructed using the CMS analog pixel ROC PSI46v2 [159]. The fast trigger output from this ROC, called FAST-OR, was used as a trigger signal which is adjustable in trigger area using a pixel mask. This system was used to test pixel and pad detectors. For testing of pad detectors an ORTEC 142A preamplifier combined with an ORTEC 450 amplifier[160] with 200 ns shaping time was used. Up to four pixelated DUTs or one pad DUT could be tested in parallel. The following limitations were observed during operation:

- The system could only measure pad detectors at fluxes up to $\sim 300\,\mathrm{kHz/cm^2}$

- Only one pad detector could be tested at one time.

- The pixel ROC had a high pixel threshold (3500 e).

- No synchronization between telescope and pad detector data streams possible

- No on-line analysis was available.

- The data buffer size limited the run length.

- The entire system took a long time to setup (days).

In the frame of the thesis the Compact CMS Pixel Telescope was developed which addressed the limitations and included additional functionality. In this section, the design goals are discussed, followed by a description of the new hardware and software design. Additional information about the commissioning of the setup can be found in [161].

5.1.1. Design Goals

Our experience with the original setup lead to the specifications of a new setup. Following specifications were made for the new beam telescope

- Have the capability of measuring pad detectors at much higher particle fluxes (up to $20\,\mathrm{MHz/cm^2}$).

- Be able to test multiple pad detectors in parallel to minimize the testing procedure.

- Have the capability to use all versions of the CMS pixel ROCs, especially the ones with reduced pixel threshold

- Add an on-line monitor system to check data quality and get first results while the beam test is running.

- Solve the data taking limitations of the pixel readout system.

- Reduce the setup time to optimize the data taking.

- Synchronize events between DUT and telescope data streams to provide tracking for pad detectors.

	PSI46v2	PSI46dig	PROC600
ROC size	$7.9 \times 9.8 \, \text{mm}^2$	$7.9 \times 10.2 \, \text{mm}^2$	$7.9 \times 10.6 \, \text{mm}^2$
Pixel size	$150 \times 100 \, \text{µm}^2$	$150 \times 100 \, \text{µm}^2$	$150 \times 100 \, \text{µm}^2$
Pixel array	52×80	52×80	52×80
Charge readout	analogue	digitized - 8 bit	digitized - 8 bit
Readout	multi level, 40 MHz	160 Mbit/s	160 Mbit/s
Hit rate	$80 \, \text{MHz/cm}^2$	$120 \, \text{MHz/cm}^2$	$600 \, \text{MHz/cm}^2$
Radiation Tolerance	$200 \, \text{kGy}$	$1 \, \text{MGy}$	$\sim 5 \, \text{MGy(exp.)}$
In-time threshold	$3500 \, \text{e}$	$\gtrsim 1500\text{e}$	$\gtrsim 1000\text{e}$
Trigger	hit multiplicity logic	none	simple OR
DAC / registers	26 / 3	16 / 3	14 / 3
Power up condition	not defined	default values	default values
Time stamp buffer size	12	24	40
Data buffer size	32	80	$56 \times 4^{\diamond}$
ROC readout buffer	0	64	64
Output buffer FIFO	no	yes	yes
Double column speed	20 MHz	40 MHz	40 MHz (DCCD)$^{\diamond}$
Metal layers	5	6	6
PLL	no	yes	yes
Data loss at max operating flux	$\sim 3.8\,\%$ at $120 \, \text{MHz/cm}^2$	$\sim 1.6\%$ at $150 \, \text{MHz/cm}^2$	$\sim 3\,\%$ at $600 \, \text{MHz/cm}^2$
available since	2004	Fall 2014	Spring 2016

Table 5.1.: Specifications of the different CMS pixel ROCs.

$^{\diamond}$ The concept of Dynamic Cluster Column Drain is developed to address inefficiencies due to the column drain mechanism. It uses the fact, that pixel hits usually appear in clusters and therefore transfer clusters with sizes up to 2×2 pixels instead of single pixels [162, 163].

5.1.2. Hardware

The new telescope is capable of using all versions of the CMS pixel ROC. Due to the different data formats different ROCs cannot be mixed within one readout chain. Table 5.1 summarizes the specifications of all existing CMS pixel ROCs. One important feature for testing detectors smaller than the telescope sensor size is a adjustable trigger region. By deactivating single pixels, the active trigger region can be set. Two versions of the CMS pixel ROC, PROC600 and PSI46v2, provide a trigger out signal, the FAST-OR signal. As the FAST-OR trigger signal is not provided in all versions of the ROC and the telescope should be capable of using all versions of the ROC, the setup uses two readout chains. One readout chain includes the ROCs of the telescope and one readout chain includes all other pixelated ROCs. The Digital Testboard (DTB) [164], developed at PSI, was originally designed to readout the PSI46dig ROC, but the firmware was extended such that it is capable to work with all ROC versions. This board allows the readout of the data buffer via USB 2.0 during operation. All versions of the ROC are designed to operate at the 40 MHz clock frequency of the LHC.

A modular approach of telescope planes was used. The telescope can be arranged with an arbitrary number of telescope modules. Each telescope module consists of up to three telescope planes. Multiple modules can be daisy-chained to create one readout chain. Figure 5.1 shows one such telescope module. The schematics of possible configurations are shown in Figure 5.2. The pad configuration, shown in Figure 5.2 (a), uses two daisy chained telescope modules to provide tracking for two pad DUTs. In the pixel
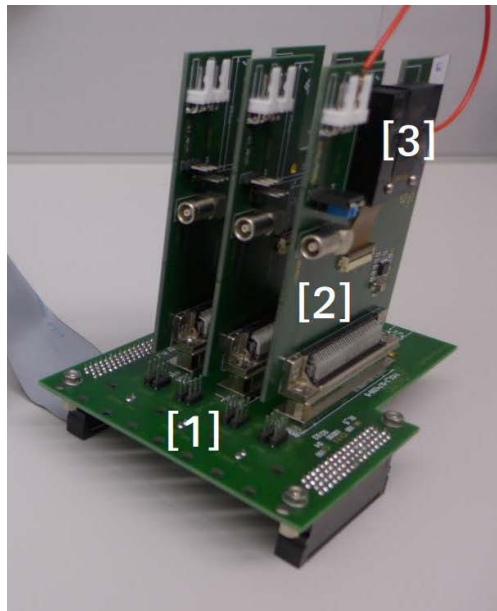
Figure 5.1.: One telescope module , consisting of a motherboard ([1]) and up to three telescope planes ([2]). The ROC ([3]) shielded light with a black plastic cap.

configuration, shown in Figure 5.2 (b), one additional telescope module is placed in the middle on which three pixel DUTs can be installed and read out with a separate readout chain.

The telescope plane is the link between the telescope module and the ROC. The readout of each version of the ROC requires a specific version of the telescope plane. The sensor bias of the pixel detectors can be provided either via the DTB or individually via a connection on each telescope plane.

A custom made fast amplifier with short shaping time and low noise behavior was chosen to be able to measure pad detectors at the particle fluxes of $20\,\mathrm{MHz/cm^2}$ in combination with the $20\,\mathrm{ns}$ beam structure of the cyclotron. This CVDFE1 amplifier has an adjustable rise time of $3\,\mathrm{ns}$ to $7\,\mathrm{ns}$ and a noise level of $600-800\mathrm{e}$. For digitization a DRS4 Evaluation Board is used. The DRS4 Evaluation Board provides a four channel readout and has a dead time of approximately $1\,\mathrm{ms}$.

5.1.3. Software

The readout and control of the hardware was performed with the Data Aquisition (DAQ) framework EUDAQ [165, 166]. With its modular design EUDAQ can be easily modified to work with the new setup. The adaption of the pixel readout system into the EUDAQ framework is described in detail in [161].

The data format of EUDAQ was designed to work with pixel and strip tracking detectors. Events are saved as *StandardEvent* objects. This data format was extended by introducing new classes to work with the waveform data from digitizers. The readout and control of the DRS4 Evaluation Board was included into the EUDAQ framework.

5.1.4. Trigger Logic

Trigger logic is used to select events where particles transverse the telescope, pass through a well defined region of the DUTs and trigger the readout of the experiment. The readout of the pad DUTs requires a stable time between the actual particle crossing and the trigger decision. Only then is it possible to precisely measure the signal response of DUTs with fast electronics. In order to have high efficiency in data taking, it is important that the trigger area is matched to the size of the DUTs. As different readout devices are integrated into one setup, the trigger logic needs to ensure the data of the different devices is synchronized.

In the following paragraph the main ideas of the trigger logic are described. A schematic view of the full trigger logic can be found in the Appendix B.1. The FAST-OR signals of two ROCs are put into an AND gate to form a coincidence, referenced as Fast-Or
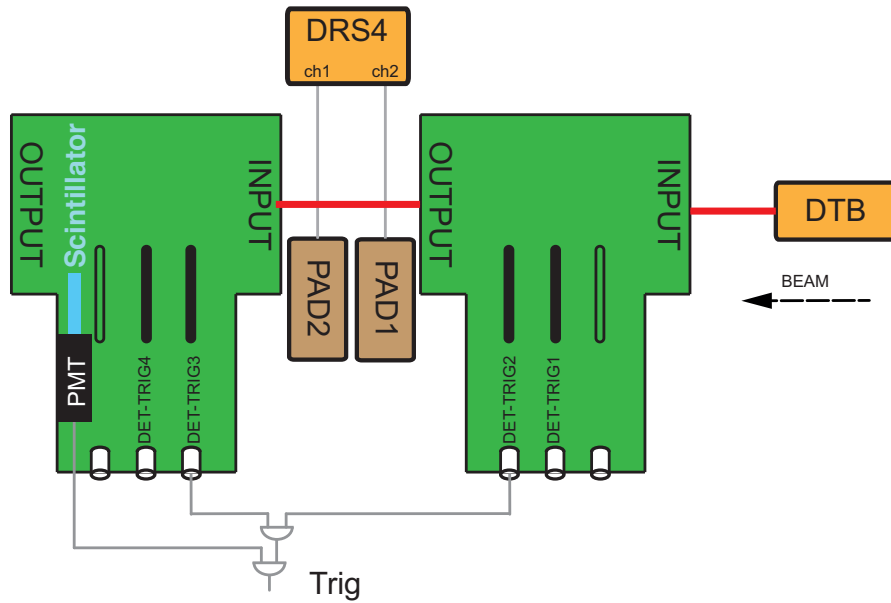
(a) Schematic view of a pad configuration. The two innermost pixel planes and the scintillator are used for triggering. Two pad detectors are read out with one DRS4 board. The two motherboards are daisy-chained and readout with one DTB. The trigger coincidence is build out of FAST-OR2, FAST-OR3 and the scintillator signal.
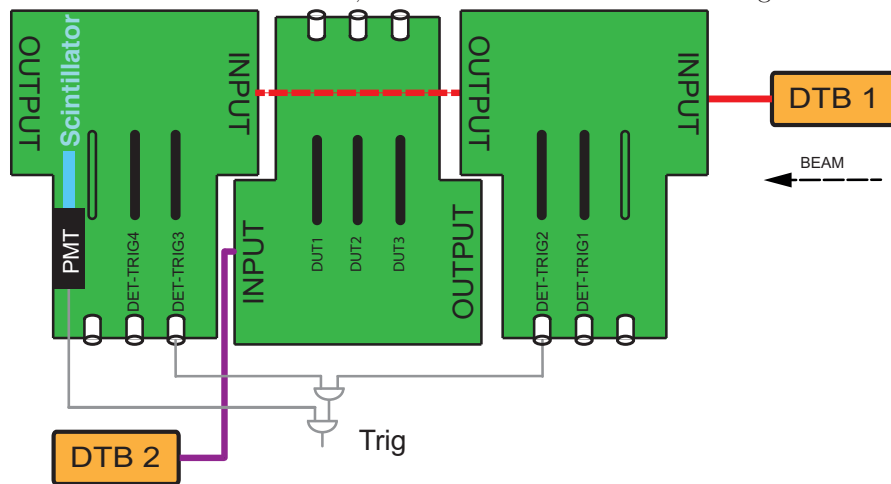
(b) Schematic view of a pixel configuration. DTB1 is used for the readout of the analog readout-chain, while DTB2 is used for the digital readout-chain. Up to three DUTs can be installed in the digital readout chain. The trigger coincidence is build out of FAST-OR2, FAST-OR3 and the scintillator signal.

Figure 5.2.: Schematic views of a pad and a pixel configuration

Coincidence. By disabling single pixels of each ROC the trigger area can be scaled. This coincidence ensures that the particle crossed all DUTs in the telescope. As the FAST-OR signals only occur every 25 ns, the time resolution of these signals is limited. In order to obtain more precise timing, a scintillator read out with a PMT [167] was added to the setup. After discriminating the scintillator signal and requiring it be in coincidence with the Fast-Or Coincidence signal, precise event timing was obtained. The principle of using the FAST-OR signals for providing a scalable trigger area is shown in the timing diagram in Figure 5.3. The trigger area of the two ROCs was chosen to be smaller than the active region of the DUTs in order to guarantee particle crossing through the DUTs.

In addition to using the FAST-OR signals for the data acquisition decision, measurement of the FAST-OR rate was used to obtain the incident particle flux. At the beam settings with the lowest particle flux, FAST-OR rates of 700 Hz to 1000 Hz were measured, resulting in a particle flux of $9.5\,\text{kHz/cm}^2$ to $13.7\,\text{kHz/cm}^2$ for a typical trigger area of $2.7 \times 2.7\,\text{mm}^2$. At the beam settings with the highest particle flux the FAST-OR rates were measured to be around 700 kHz, resulting in a particle rate of the order of $9 - 10\,\text{MHz/cm}^2$. The requirement to have a coincidence of two FAST-OR signals and the scintillator signal reduces the trigger rate by approximately 70 %. In order to collect a similar amount of data for each particle flux, a prescaler was used to reduce the trigger rates by selecting only every n^{th} event. The settings of the prescaler were adjusted between 2^0 and 2^8 such that the average data taking rate was in a range between 300 Hz and 500 Hz. The limiting factor in data taking rate is the readout time of the DRS4 Evaluation Board.

In order to allow particle tracking the data streams of the different detectors must be synchronized. For this reason the EUDET Trigger Logic Unit (TLU) [168] was used. After each trigger signal the DRS4 Evaluation Board acknowledges the data acquisition, as soon as the device is capable for recording the next event. During the beam test campaigns the main fraction of the trigger logic was built with NIM-modules.
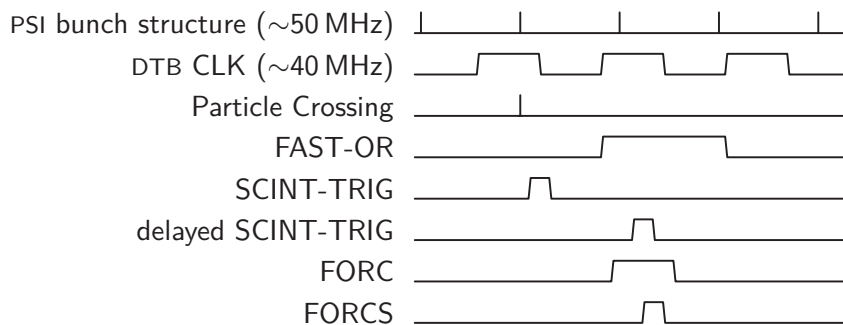
Figure 5.3.: Main principle of the trigger logic. The ROC provides a scalable trigger area with limited time resolution, the scintillator provides precise timing without the scalability of the trigger area.

To measure the gain of the pad amplifiers during operation, additional calibration pulses were injected into the amplifier during data taking. These calibration pulses were used as an additional trigger source. With these events it was also possible check the synchronization of the detector's data streams.

5.1.5. Analysis

After the conversion of the raw data into *ROOT* files, the data of the pixel planes was used to align the setup in space. The procedure of measuring the signal in the waveform of the pad DUT is described in Section 5.1.6. For each event the pixel hits in the pixel planes were used to reconstruct the particle track in the telescope by performing independent linear fits in the two directions specified by the pixel detectors. The hit position within each DUT was predicted and this position as well as the goodness of the fit was used in further analysis. A detailed discussion of the different selection criteria can be found in Section 5.3. Further details to the analysis framework can be found in [169] and [161].

5.1.6. Signal Extraction from Waveform Analysis

An important step in the analysis of the pad detector is the extraction of the signal response from the recorded waveform. A full waveform with a length of approximately $512\,\mathrm{ns}$ and 1024 data points was digitized for each triggered event. A detailed discussion of the signal extraction can be found in [169]. In Figure 5.4 an overlay of twenty waveforms digitized with the DRS4 Evaluation Board are shown for a low ($\Phi = 13\,\mathrm{kHz/cm^2}$) and a high particle flux ($\Phi = 9.2\,\mathrm{MHz/cm^2}$) run. It can be seen that all waveforms have a distinct peak in a region between $60\,\mathrm{ns}$ to $80\,\mathrm{ns}$. Outside of this region, the waveform of the low particle flux run fluctuates around zero (noise). In the high particle flux run, the fluctuations around zero can be seen as well, but additional peaks occur within the $512\,\mathrm{ns}$ digitization time. These peaks are caused by additional particles crossing the DUT during the digitization (pile-up).

By overlaying 5000 waveforms of the high particle flux run, shown in Figure 5.5, the beam structure of the $50.6\,\mathrm{MHz}$ High Intensity Proton Accelearator (HIPA) beam can be seen. The peak at $70\,\mathrm{ns}$ is caused by the signal of a particle, which triggered the readout. Due to the high particle flux additional particles can cross the DUT during the length of the recorded waveform. Therefore, additional peaks can be observed in the overlay. The distance of these peaks is $19.7 \pm 0.1\,\mathrm{ns}$, which is in agreement with the $50.6\,\mathrm{MHz}$ cyclotron frequency of the PSI accelerator. From this measurement it can be observed that particle signals can be observed in every bunch cycle, except the one before the trigger bunch. This effect is caused by the design of the trigger logic, which does not allow events with a FAST-OR signal in the bunch crossing before the trigger.
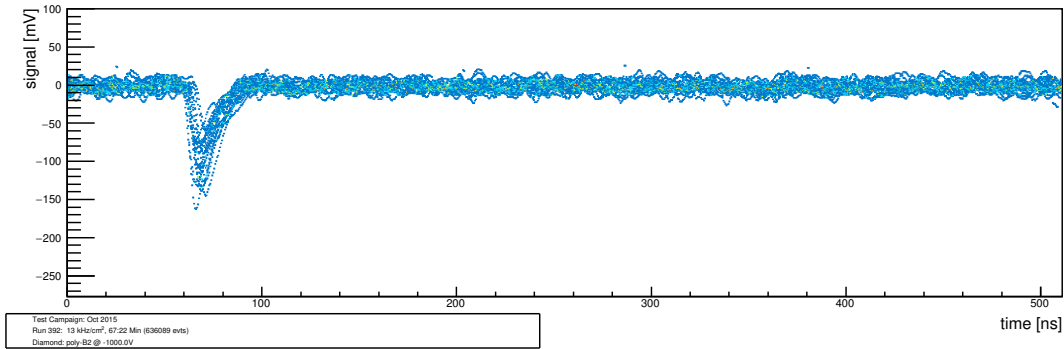
(a) At a particle flux of $13\,\mathrm{kHz/cm^2}$.
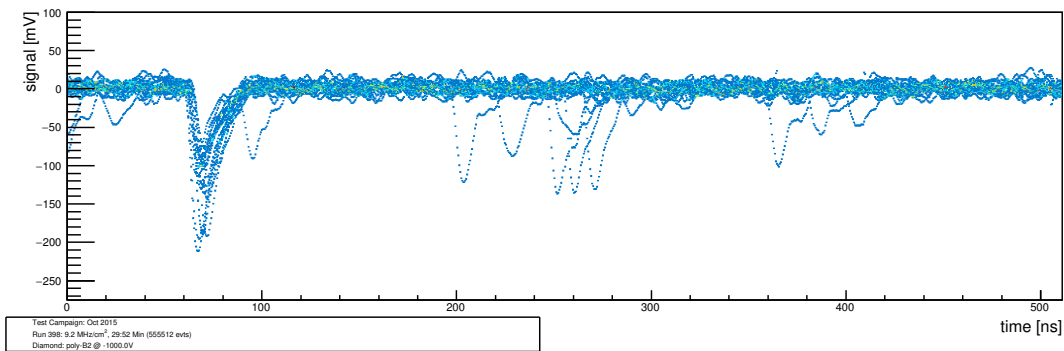
(b) At a particle flux of $9.2\,\mathrm{MHz/cm^2}$.

Figure 5.4.: Twenty waveforms of the DRS4 evaluation board overlaid for two runs with different particle fluxes.
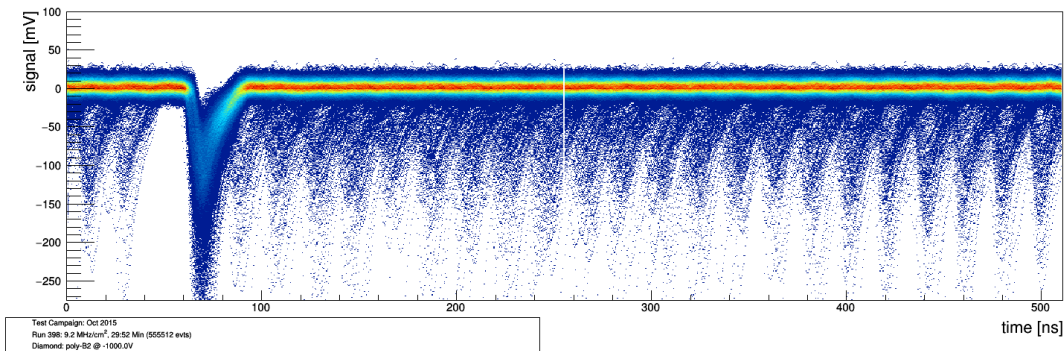
Figure 5.5.: Overlay of waveforms of one run at a particle flux of $9.2\,\mathrm{MHz/cm^2}$, for which the trigger was generated by the coincidence of FORC and Scintillator.

By counting the number of additional particles within each waveform it was possible to verify the measurements of particle flux with the FAST-OR rates, within $\sim 20\,\%$.

Events which are triggered by the pulse injection (in the following sections called pulser events) have a different shape of the waveform. Two different versions of the amplifier assembly were constructed which uses the same ASIC, but differ in the way the calibration pulse is injected. One version uses an external pulse to trigger an internal circuit to generate the calibration pulse, this version is referred as *internal pulser*. In the second version the external pulse is directly used as the calibration pulse and is therefore referred as *external pulser*. The signal response of pulser events is different in time and in shape. This allows an easy identification of these events.

The CVDFE1 circuit is based on a charge-sensitive preamplifier. As the result the collected charge is proportional to the integral of the signal waveform. To measure the zero offset of the waveform (pedestal), the waveform was integrated in a region in front of the expected peak position. For each event the pedestal correction was performed individually. The signal response of the detector can be extracted with this method. As the gain of the amplifiers was not measured, the signal response of each measurement is given in arbitrary units (a.u.). A comparison of different integration widths was performed to evaluate the influence of this parameter.

In the following paragraph, the method used to extract the signal is described. This method is illustrated for one example waveform in Figure 5.6. An important aspect for the measurement of the signal charge, is the exact position of the peak in order to integrate the signal in this region. In the DRS4 the observed signal peak generated by the crossing particle is not exactly at the same position relative to the trigger pulse but varies due to the limited timing precision of the trigger. In order to integrate the signal around the peak position, the peak position is extracted for each waveform individually.

As multiple signal peaks can be observed, especially at high particle fluxes, the window in which the maximum amplitude is search needs to be restricted. The interval, in which the position of the maximum amplitude is found, is called PeakSearchRegion. Around the found peak position, the signal of the waveform is integrated. The width of the integration window can be adjusted and is given by the interval IntegralRange, which defines the integration length left and right of the found peak. A signal definition is based on the combination of one PeakSearchRegion and one IntegralRange. In order to have an unbiased measurement of the pedestal, the same IntegralRange is used, but the position of the integral is fixed in time.

In the example in Figure 5.6, the signal peak is fluctuating around 84.5 ns. This position is marked with an orange arrow. A signal PeakSearchRegion with a width of one bunch cycle is defined from 75 ns to 95 ns. The pedestal peak position is fixed at 64.5 ns. In the first step, the highest signal within the signal PeakSearchRegion is found at 83.5 ns. In this case three different IntegralRanges are defined, that are colored in green and
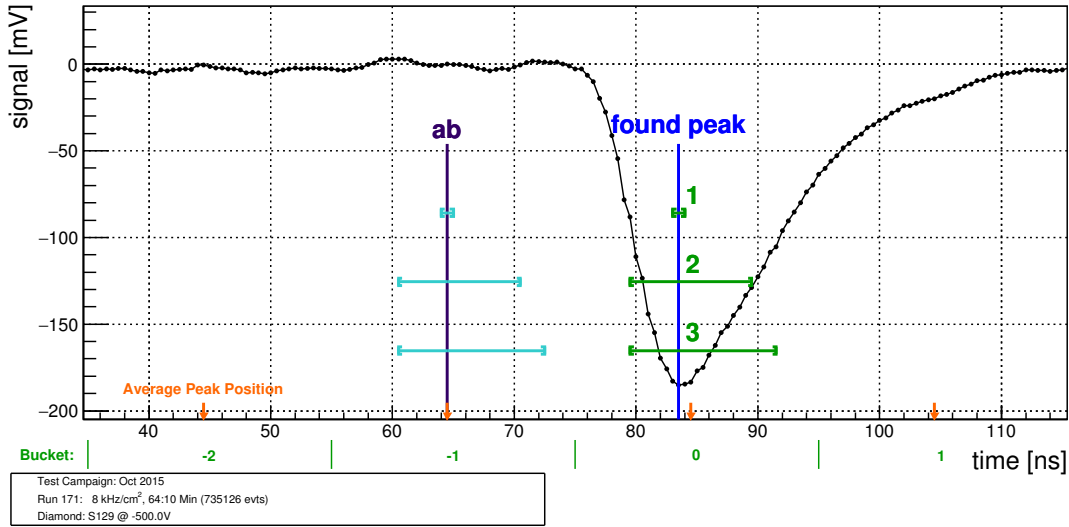
Figure 5.6.: One single waveform showing the integration windows for the signal and pedestal PeakSearchRegion. The signal PeakSearchRegion is defined from 75 ns to 95 ns, while the pedestal PeakSearchRegion is defined as a single point at 64.5 ns. Three different integral width are defined using three different IntegralRanges, these are highlighted in green for the signal and in turquoise for the pedestal region.

marked with 1,2 and 3. For each signal integral one corresponding pedestal integral is calculated around the fixed pedestal position.

Detailed studies of different IntegralRanges have shown that the best SNR is reached when an asymmetric integration window from around the peak position is used. In Figure 5.7 the SNR optimization for one diamond is shown. The right and the left length of the are varied and for each combination the SNR is distinguished. In the Figure 5.7 (a) the two dimension optimization procedure is shown. In Figure 5.7 (b) the profiles for the left and the right integral length around their maximum SNR are shown. For this irradiated pCVD diamond sample the best SNR of 18.85 is reached for an integral from 4 ns left of the peak to 6.5 ns right of the peak. This optimization was performed for several DUTs with different signal responses. The best SNR was achieved for a similar IntegralRange, small variations in the best IntegralRange by ±0.5 ns in each direction have been observed. This means that the pulse shape of the signal pulse is independent of the actual height of the signal. Therefore the shape of the measured signals is primarily caused by the shaping times of the amplifier circuit. This is in agreement with the fast charge collection times in diamond materials, as it means that these collection times must be comparatively small compared to the shaping times of the amplifier circuit.

(a) Two dimensional optimization.
(b) SNR profiles.
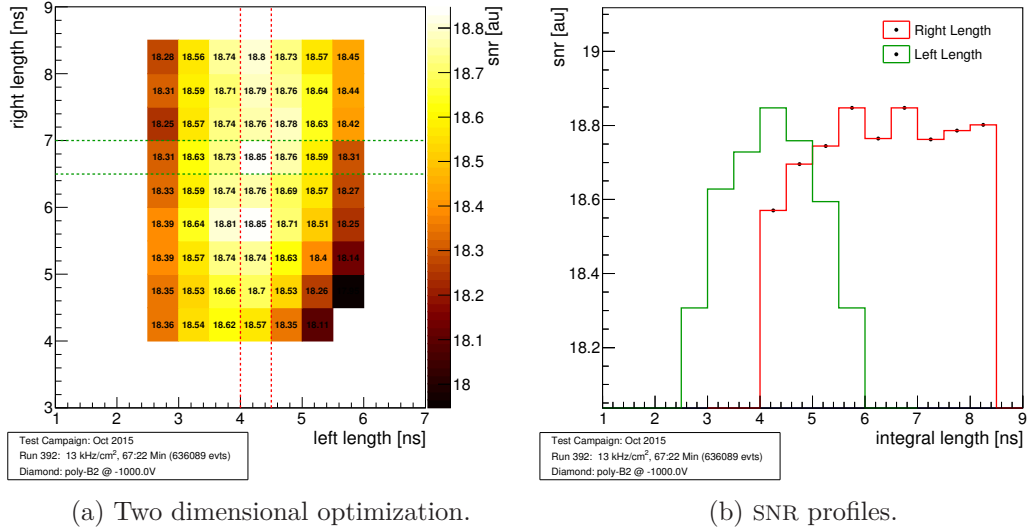
Figure 5.7.: SNR optimization for an irradiated pCVD diamond in the October 2015 beam test campaign. In the two dimension plots the two profiles are highlighted.

5.2. Setup Configurations in the August 2015 and October 2015 Beam Tests

The $\pi M1$ beam line at the HIPA facility of PSI provides a constant high intensity beam up to particle rates of $10\,\mathrm{MHz/cm^2}$ which is suitable for these studies. The beam has a bunched structure of $50.6\,\mathrm{MHz}$, corresponding to a time difference of $19.8\,\mathrm{ns}$ between two particle bunches.

5.2.1. Beam Test Parameters

The beam was tuned to provide π^+ with a momentum of $250\,\mathrm{MeV}/c$, with small contaminations of muons and protons(less than $1\,\%$). The pion flux was varied between $\sim\!10\,\mathrm{kHz/cm^2}$ and $10\,\mathrm{MHz/cm^2}$ by controlling two sets of intermediate collimators (FS11 and FSH13). In each beam test, the optimal position of the telescope was found by moving the telescope with respect to the beam and measuring the particle flux. After finding the position with the highest intensity, the telescope was aligned with respect to the beam. The collimator settings were varied to find the optimal parameters for the different particle fluxes and the hit rates were measured.

In addition to the secondary beam lines the accelerator complex was also used to provide a beam for other experiments. Every five minutes the particle beam of the accelerator was routed to the Ultra Cold Neutron (UCN) facility. This caused a beam interruption of several seconds.

5.2.2. Setup

In both, August and October 2015, beam test campaigns the upgraded beam test setup, described in Section 5.1, consisting of the new telescope, a scintillator for timing was used. The data acquisition was performed with the EUDAQ framework and the full trigger logic, as shown in Appendix B.1, was used for event selection.

In Figure 5.8, a picture of the pad setup is shown. It consists of two telescope modules, each with two pixel planes, two diamond pad detectors in the center and the scintillator on the left hand side.

5.2.2.1. Trigger Timing Optimization

The DRS4 chip has an external trigger input which is used to start the readout of the waveforms. As the DRS4 chip has a circular buffer, the readout of each event may start at a different position within this buffer. This position of the start of the readout is called the *trigger cell*. Due to differences in the signal propagation times to the *trigger cell*, the time resolution using the an external trigger is limited [170]. In Figure 5.9, the peak position of the signal *PeakSearchRegion* is shown as a function of the *trigger cell*. The dependence of the peak position on the *trigger cell* can be observed.

A method to correct the trigger timing for the *trigger cell* effect and to improve the time resolution was developed based on the measured dependency. The average peak position for each *trigger cell* was extracted and used to correct the time of each measurement based on the trigger position. The timing resolution was improved with this method. In Figure 5.9 (b), the trigger timing with the correction is shown as a function of the
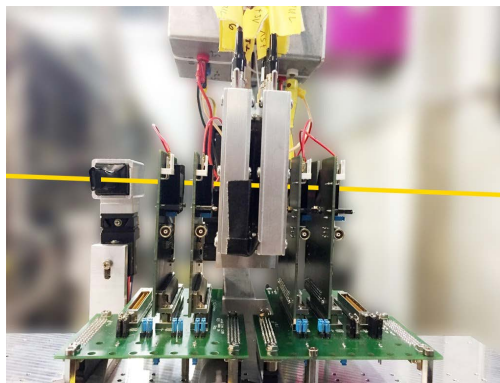
Figure 5.8.: A side view on the telescope setup for pad testing in the October 2015 beam test. The particles enter the telescope from the right side. On each telescope module two telescope planes are installed. In the middle the two pad detectors are placed. On the left the scintillator can be seen.

(a) Before timing correction

(b) After timing correction.
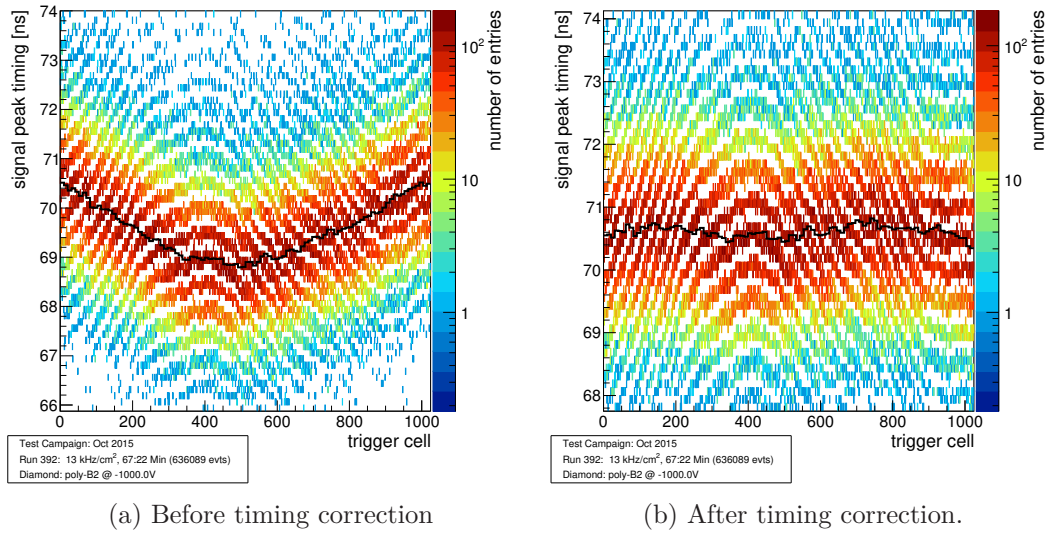
Figure 5.9.: Peak position with respect to the *trigger cell* before and after the timing correction.

trigger cell. It can be seen that the dependency was reduced. If one fits the corresponding projection in the region of the FWHM, a width of 0.99 ns can be extracted for the original timing. With the timing correction the width of the Gaussian can be reduce by 33 % to 0.67 ns. This shows the good timing resolution of the upgraded setup.

5.2.3. Test Procedure

Each detector was pumped, see Section 2.3.3.1, for at least 6 h with a $\sim$37 MBq ^{90}Sr source and then tested. Before switching the bias polarity the same routine was repeated.

In the August 2015 beam tests the following procedure was used for data taking. The beam shutter was closed after each run, followed by the change of the collimator settings. As soon as the new collimator settings were reached, the run was started and only then the beam shutter was reopened.

During the October 2015 beam test, the above procedure was compared to a procedure in which the beam was not shuttered between runs. It was observed that the opening and closing of the beam shutters did not have any effect on the pulse height. Therefore, the routine was simplified during the October 2015 beam test and the beam stop at the end of each run was not used. In between two runs, the collimator settings were updated and a short delay until the collimators reached their new set point was required.

The data taking procedure for the August 2015 test beam was defined as followed:

- 3 h to 4 h run at $3\,\mathrm{kHz/cm^2}$ until pulse height was stable

- Rate up scan: six rate points ($3\,\mathrm{kHz/cm^2}$, $20\,\mathrm{kHz/cm^2}$, $60\,\mathrm{kHz/cm^2}$, $600\,\mathrm{kHz/cm^2}$, $2\,\mathrm{MHz/cm^2}$ and $5\,\mathrm{MHz/cm^2}$), each run lasting at least 1 h

- Rate down scan at the same fluxes ($2\,\mathrm{MHz/cm^2}$, $600\,\mathrm{kHz/cm^2}$, $60\,\mathrm{kHz/cm^2}$, $20\,\mathrm{kHz/cm^2}$, and $3\,\mathrm{kHz/cm^2}$), data taking at each point for at least 1 h

- Second rate up scan at the same fluxes ($3\,\mathrm{kHz/cm^2}$, $20\,\mathrm{kHz/cm^2}$, $60\,\mathrm{kHz/cm^2}$, $600\,\mathrm{kHz/cm^2}$ and $2\,\mathrm{MHz/cm^2}$), data taking at each point for at least 1 h

For the October 2015 beam test the procedure was adjusted, in order to guarantee a stable operation of the DUTs. The procedure was defined in the following way: The first run was reduced to be at least 1 h and was extended if the pulse height was not stable after this time period. Then the August 2015 procedure was executed with the difference that the run time was reduced to be at least 20 min, but requiring a stable signal response. Within the data taking it was observed that an additional flux of $200\,\mathrm{kHz/cm^2}$ can be useful for analysis, such that during the beam test it was decided to add another measurement point to each scan procedure. After the August 2015 beam test it was observed that during the first up scan the pulse height is increasing with increasing particle flux. This might be an indication that the detector has not yet reach stable operation. In order to guarantee stable operation the number of flux-up and flux-down scans was increased to three.

5.3. Event Selection

Events which were not caused by a particle crossing the DUT were removed from the full data set. This includes events which were triggered by the pulser or events in which the reconstructed particle track did not cross the DUT in a region of interest. In the following, the different selection criteria are defined and the influence of each selection criteria on the shape of the signal distribution and on the average signal response is discussed.

5.3.1. Definition of Selection Criteria

5.3.1.1. Event Range

After starting a new run several settings of the trigger logic, e.g. prescaler settings and pulser frequency, were adjusted to ensure high quality data taking. These adjustments could take several minutes, therefore, the first 5 min of each run was removed from the analysis.

5.3.1.2. Beam Interruptions

There were beam interruptions due to the filling of UCN and due to problems with the accelerator complex. Beam interruptions can be recognized by the fraction of pulser events in a certain time window. All beam interruptions plus $5\,\mathrm{s}$ before and $15\,\mathrm{s}$ after each beam interruption were removed from the data set. This ensures that only events with a real particle crossing are included in the further analysis.

5.3.1.3. Saturated Events

In all events the waveform was checked to insure the DRS4 was not saturated. Only events which have no saturated waveform were used for further analysis.

5.3.1.4. Pulser Events

The pulser signal was digitized with another channel of the DRS4 board and was used to identify pulser events. These events were analyzed separately to check the amplifier gain. The actual fraction of these events depends on the run parameters, like particle flux, the pulser rate and the prescaler settings, which were adjusted in such a way that the fraction was between $5\,\%$ to $20\,\%$.

5.3.1.5. Pedestal Sigma

As described in Section 5.1.6, the pedestal of each event was measured in front of the actual triggered bunch. The pedestal may be biased due to additional particle crossings before the actual trigger or due to baseline shifts. Therefore the pedestal distribution was fitted with a Gaussian in the FWHM range. The fitted width was used for defining the event selection. Only events which have a pedestal within $3 \times \sigma$ were used for the further analysis. This ensures that a pedestal subtraction on an event-by-event base can be performed. In Figure 5.10, one can see the distribution for a low ($\Phi = 13\,\mathrm{kHz/cm}^2$) and a high ($\Phi = 9.2\,\mathrm{MHz/cm}^2$) particle flux run. In the low particle flux run, the distribution has a Gaussian shape. For the high particle flux run, a long tail towards higher signals can be observed. These events arise due to the higher particle flux. Only events in the green band were selected for further analysis, events from the long tail were rejected.

(a) Low flux.

(b) High flux.
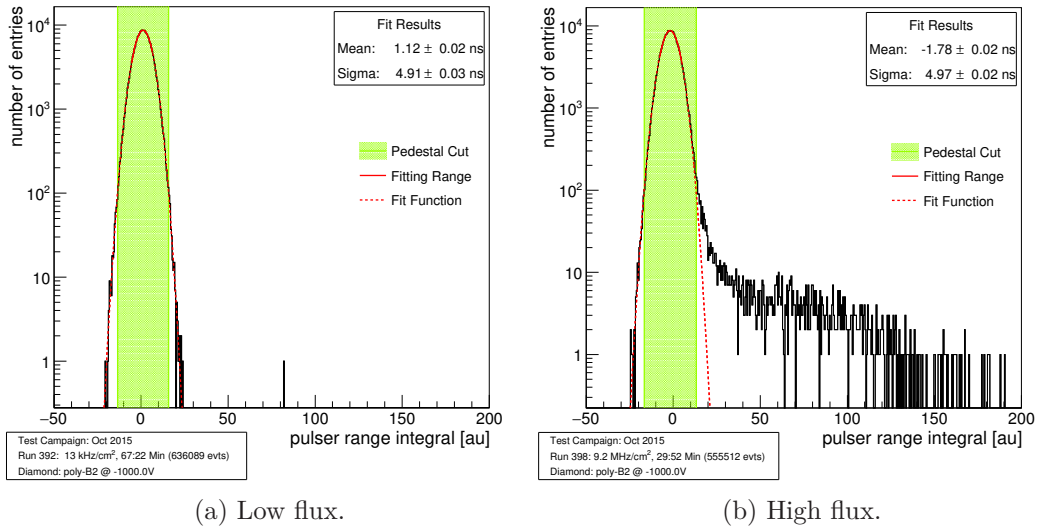
Figure 5.10.: Pedestal distributions for a low and a high particle flux run. The FWHM of the distribution was fitted with a Gaussian and the fit parameters were used to define the selection criteria, based on the mean and the width of the distribution.

(a) Low Flux.

(b) High Flux.
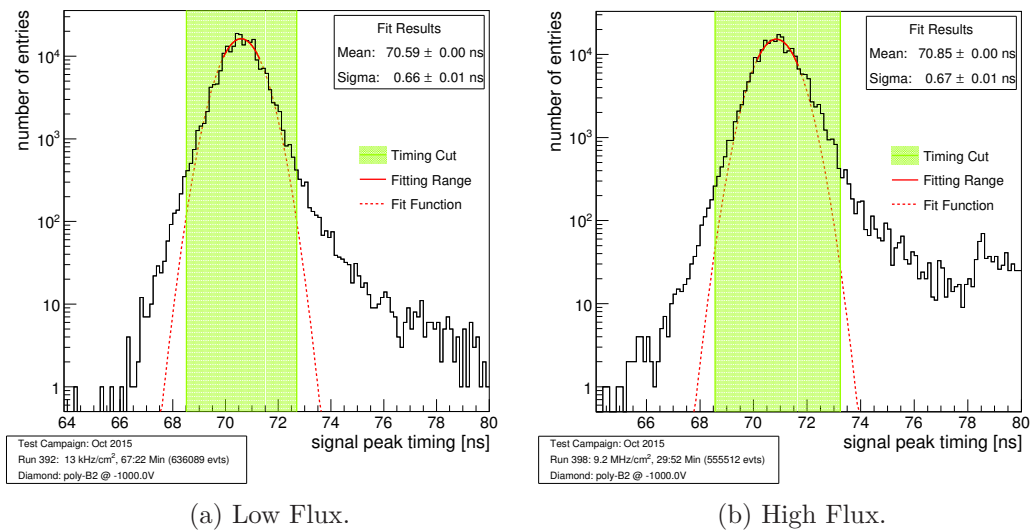
Figure 5.11.: Peak position timing fitted with a Gaussian for a low and a high particle flux run. The green area indicates the $4 \times \sigma$ band of the fit, which was used as the selection criteria.

5. Determination of the Sensitivity of Diamond Detectors to Particle Flux

5.3.1.6. Peak Position Timing

With the timing correction, explained in Section 5.2.2.1, a time resolution of 0.67 ns was achieved. Therefore the position of the peak can be used to select events which are shifted with respected to the predicted timing. The corrected timing distribution of the signal peaks is shown in Figure 5.11 for a low and a high flux run. In the region around the FWHM the distribution was fitted with a Gaussian and all events which have a peak timing outside of the $4 \times \sigma$ band of the fit were rejected. The long tail towards higher peaking times indicates events in which a second particle crossed the detector in the following bucket and its signal response was higher than the trigger bucket. This could lead to an incorrect measurement of the signal and therefore these events were rejected.

5.3.1.7. Bucket Selection Criteria

A trigger ambiguity due to the different clock frequencies of the cyclotron (50.6 MHz) and the DTB(40 MHz) can cause trigger problems. These frequencies correspond to cycles of 19.8 ns and 25 ns respectively. For optimal trigger timing the width of the FAST-OR signals needs to be adjusted to accept triggers within a certain range of the clock cycle. The width was optimized by a manual procedure to have a maximum signal acceptance window. Due to the different clock frequencies, two particles may cross the telescope within one clock cycle of the DTB. This can cause trigger ambiguity which leads to a shift of the signal with respect to the trigger timing.

In Figure 5.12 this situation is sketched. Two particles cross the telescope in consecutive bunch cycles of the cyclotron. The particle of the first bunch (marked in red) crosses the telescope outside of the active trigger area, but hits the scintillator. The particle of the second bunch (marked in green) crosses the active area of the telescope and causes
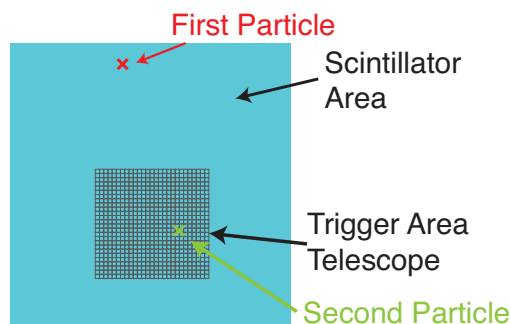
Figure 5.12.: Situation of the trigger ambiguity. The particle of the first bunch crosses the telescope outside its active area, but hits the scintillator. The second particle defines the timing of the trigger.

190
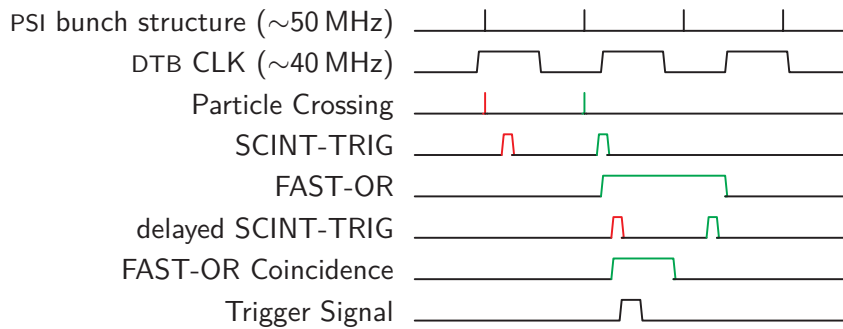
Figure 5.13.: Timing for the trigger ambiguity.

a FAST-OR signal. In a certain fraction of such events this can generate a trigger decision. Figure 5.13 shows the timing diagram for such an event. The signal of the SCINT-TRIG of the first particle overlays with the coincidence of the FAST-OR signals which is generated by the second particle. In such a case, the trigger signal is generated. The actual particle which triggered the FAST-OR and the particle which caused the SCINT-TRIG are not the same. Therefore, the signal in the DUT is shifted by one 20 ns clock cycle with respect to the typical trigger timing. In Figure 5.14 the waveforms of three different events are shown. The green waveform shows an event with the correct trigger timing. The purple waveform corresponds to an event in which two particles crossed the detector in adjacent bunches. The orange waveform corresponds to an event which has a trigger ambiguity. The peak position is shifted by ~20.0 ns due to the trigger
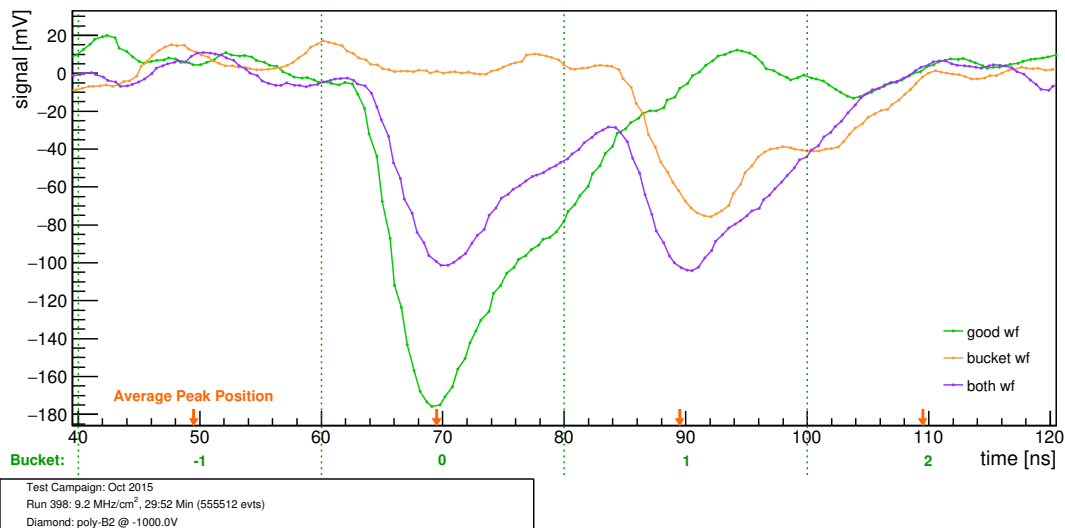
Figure 5.14.: Waveforms of three different events. The green waveform shows an event with the correct timing, the purple waveform has two particle crossings in two adjacent buckets and the orange waveform is shifted by ~20.0 ns due to the trigger ambiguity.

ambiguity. Events which are caused by the trigger ambiguity have signal responses close to zero and therefore need to be rejected as they bias the measurement. This selection is called *bucket* selection criteria.

Due to this bucket shift the peak of the signal is outside of the original signal Peak-SearchRegion, in the following paragraphs this PeakSearchRegion is referenced as s_b. The shape of the signal in this PeakSearchRegion is similar to the shape in the pedestal region. Due to pedestal fluctuations the maximum in this region is arbitrarily distributed and the integral is similar to the one of the pedestal region. In order to identify these events an extended PeakSearchRegion s_e was defined. This extended Peak-SearchRegion added one particle bunch in front and one in the back of the original signal bunch, resulting in a total width of $\sim$60 ns. This corresponds to three adjacent particle bunches.

In Figure 5.15 the peak position of the extended PeakSearchRegion s_e is plotted versus the standard signal definition, calculated in the PeakSearchRegion s_b. While most of the events have an IntegralPosition between 67 ns to 74 ns and a signal clearly above zero, a fraction of the events has an IntegralPosition between 84 ns to 94 ns. For these events the two different contributions can be observed. On the one hand there are events with signals around zero which are caused by the trigger ambiguity. One such example is shown in the orange waveform in Figure 5.14. On the other hand there are events which have a signal response separated from zero. These events are caused by two particles crossing the detector in two adjacent bunches. Such an example is shown in the purple waveform of Figure 5.14.
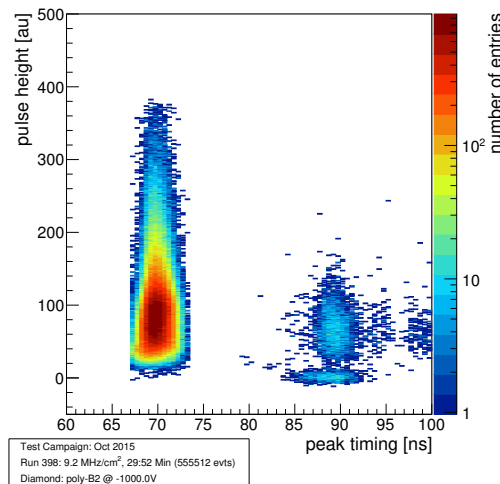
Figure 5.15.: Effect due to an ambiguity coincidence of scintillator and Fast-Or Coincidence signal. On the x axis the IntegralPosition for a $[40, 100]$ PeakSearchRegion is plotted versus the signal integral for the $[60, 80]$ PeakSearchRegion.

This can also be verified by the comparison of the signal for the "normal" PeakSearchRegion s_b with the signal of the extended PeakSearchRegion s_e for events which have an IntegralPosition between 84 ns to 94 ns. This is shown in Figure 5.16. Two contributions can be observed in the s_b signal integral. There are events, in which the s_b signal integral is close to zero and a second component with signals in s_b separated from zero. For both components the signal response in the extended region s_e is clearly separated from zero.
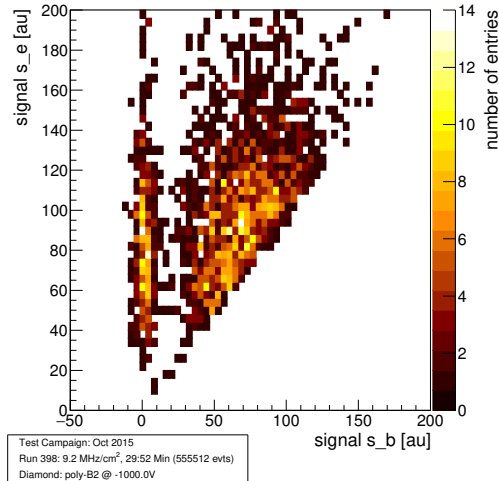
Figure 5.16.: Comparison of signals for the "normal" PeakSearchRegion with the signal of the extended PeakSearchRegion for events which have an IntegralPosition between 84 ns to 94 ns.

By removing events from the second contribution, such as the purple waveform in Figure 5.14, the majority of the removed events would have relatively low signal response events. Therefore the final signal distribution would be biased towards high signal responses. In order to reduce this bias, the event was only removed, if the IntegralPositions did not agree with each other and the signal response in the signal PeakSearchRegion s_b was compatible within $3 \times \sigma$ with a pedestal measurement.

5.3.1.8. Tracks

In order to remove events with multiple particle crossings, only events with exactly one cluster in each pixel plane were used for further analysis. Up to 20 % of the events, depending on the particle flux, were removed when applying this selection criteria.

5.3.1.9. Chi2 Cut

To predict the hit position in the DUT, two independent linear fits in x and in y direction are performed. The error in the pixel planes is approximated using digital resolution ($150\,\mu m/\sqrt{12} = 43\,\mu m$ for the x-direction and $100\,\mu m/\sqrt{12} = 29\,\mu m$ for the y-direction). By using four pixel planes for tracking this results in a linear fit with two degrees of freedom each.

The goodness of the fit was determined with χ^2. In Figure 5.17, the χ^2 distributions of the linear fits in the x and y-direction are shown for several particles fluxes from $13\,kHz/cm^2$ up to $9.2\,MHz/cm^2$. The distributions are completely overlapping, therefore no dependence on the incident particle flux can be observed. A comparison with the expected χ^2 distribution with two degrees of freedom indicates that the estimated error on the measurement is too small. Therefore it was decided to define the selection criteria based on the quantile of the distributions. Events in which the χ^2 in x or in y direction exceeded the 90 % quantile of the distribution were removed from the further analysis, resulting in a reduction by 5 % to 8 %.

5.3.1.10. Track Angle Cut

Due to the changes of the collimator settings, track angles change when the particle flux is changed. If a particle crosses the DUT with a different angle the signal response of the detector could be changed. In Figure 5.18, the track angle distributions for the x

(a) In x-direction   (b) In y-direction
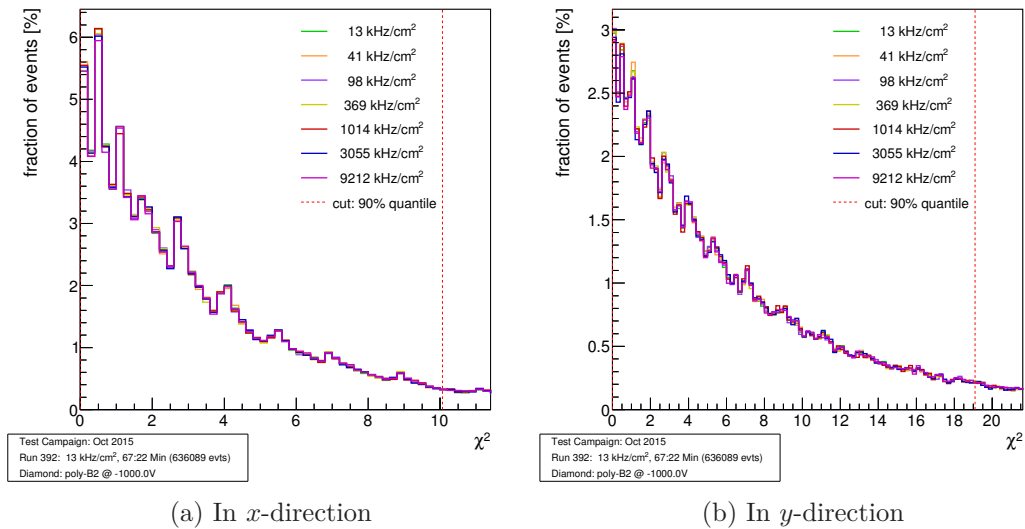
Figure 5.17.: χ^2 distribution in the x and in the y-direction for one rate scan. The regular substructure is caused by the limited resolution of the pixel planes. Events above the 90 % quantile were rejected.

and the y-direction at different particles fluxes are shown. In these figures the track angle is restricted by the reduced trigger area on the pixel detectors. The observed regular substructures in the x-direction can be explained by the larger pitch of 150 μm compared to 100 μm for th y-direction. Slight changes in the tails of the distribution can be observed. Therefore, fixed intervals for the track angle are defined for each direction separately. These two selection criteria exclude 0.1 % to 0.4 % of the events.

5.3.2. Final Cut Flow

In Figure 5.19, the cut-flow diagrams for the lowest ($\Phi = 13\,\text{kHz/cm}^2$) and the highest ($\Phi = 9.2\,\text{MHz/cm}^2$) particle flux runs are shown. For these two runs the relative fraction of events after applying the selection criteria in a consecutive order are summarized in Table 5.2. After applying all selection criteria 40.2 % (for the $9.2\,\text{MHz/cm}^2$ run) and 55.9 % (for the $14\,\text{kHz/cm}^2$ run) of the original data set can be used for further analysis. Differences due to the *event_range* selection can be explained due to the differences in the duration of the run. The effect of *pulser* selection criteria depends on the pulser frequency, the particle rate and the prescaler settings, therefore differences are expected. With the *ped_sigma*, the *bucket* and the *timing* selection criteria more events are rejected for high particle fluxes. This is in agreement with the expected reduction by removing overlapping events in data due to the increased flux.

(a) Track angle in the x-direction.   (b) Track angle in the Y-direction.
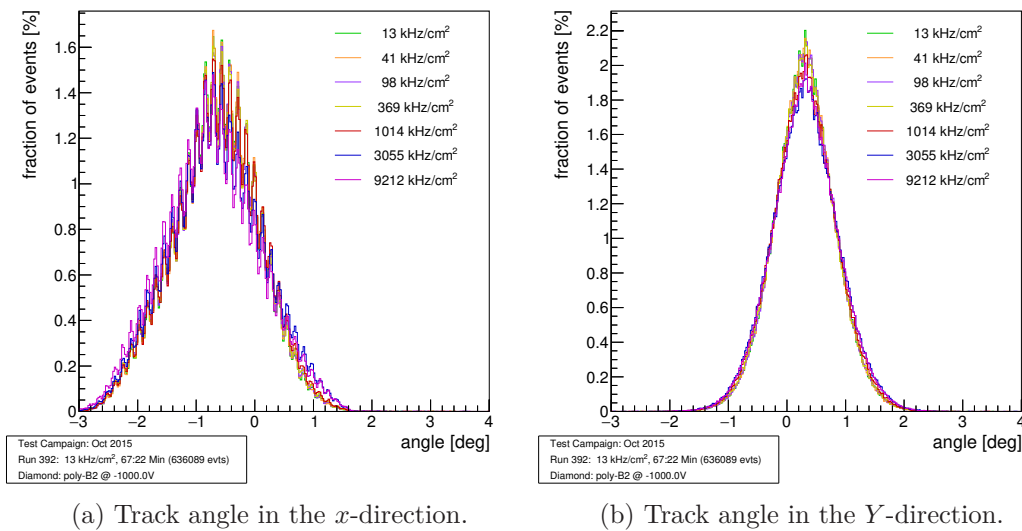
Figure 5.18.: Track angle distributions in the x and y-direction for a single rate scan. restricted by the reduced trigger area on the pixel detectors for trigger events. By constraining the trigger area, the spread of the track angle distribution is greatly reduced.

195

(a) At a particle flux of $13\,\mathrm{kHz/cm^2}$ (b) At a particle flux of $9.2\,\mathrm{MHz/cm^2}$
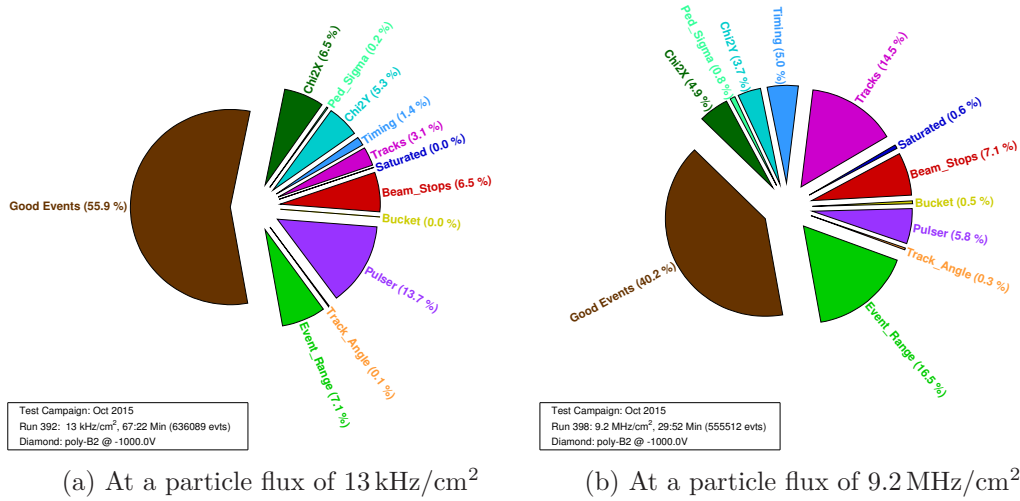
Figure 5.19.: Pie chart of the different selection criteria contributions for two runs in the October 2015 beam test.

At high rates, the probability of having multiple tracks in one bunch crossing increases. Therefore, more events are excluded by the *tracks* selection criteria. An estimate assuming Poisson-distributed beam showed a probability of $14\,\%$ for two track events at a particle flux of $10\,\mathrm{MHz/cm^2}$, when requiring at least one particle crossing. This is in agreement with the observed reduction by this selection.

5.3.3. Influence of Different Selection Criteria

The influence of the different selection criteria is described for the pCVD diamond *Poly-B2*. As the pCVD diamond material is less homogeneous than scCVD diamond material, the signal response in the diamond is depending on the position of the particle crossing. This position dependence results a much broader pulse height distribution compared a pure Landau-Vavilov distribution.

Influence on the Signal Shape   Figure 5.20 shows the pulse height distributions after each step in the event selection process in a linear and in a logarithmic y scale for a low and a high particle flux run. Figure 5.21 shows the distributions after normalizing the maximum of each distribution to one allowing a direct comparison of the shapes among each other.

The raw pulse height distribution shows a distinctive peak at zero and a wide distribution peaking at approximately $100\,\mathrm{a.u.}$ with a long tail towards higher values. By applying the *saturation* selection criteria (Section 5.3.1.3), the small peak at $400\,\mathrm{a.u.}$ gets removed,

Selection	Criteria	Low flux run [%]	High flux run [%]	Relative Dif. [%]
all		100.00	100.00	0.00
+ event_range	reject first 5 min	7.14	16.55	−9.41
+ beam_interruptions	$[-5\,\mathrm{s},+15\,\mathrm{s}]$	6.52	7.08	−0.56
+ saturated	$\mathrm{ph} < 0.5\,\mathrm{V}$	0.04	0.62	−0.58
+ pulser	remove pulser trigger	13.69	5.83	+7.86
+ ped_sigma	ped in $3 \times \sigma$)	0.22	0.81	−0.60
+ timing	timing in $4 \times \sigma$	1.44	4.99	−3.55
+ bucket	$Peak_b! = Peak_e,$ signal $< 3 \times \sigma_{ped}$	0.01	0.44	−0.43
+ tracks	one cluster in each plane	3.10	14.54	−11.44
+ chi2X	90 % quantile	6.49	4.89	+1.60
+ chi2Y	90 % quantile	5.29	3.74	+1.55
+ track_angle	$<2°$	0.14	0.28	−0.14
Final Sample		55.93	40.23	−15.70

Table 5.2.: Relative contribution to selection for the different criteria for a low and a high flux run. This corresponds to the fraction of events rejected by each cut. The difference of the two contributions (low flux fraction minus high flux fraction) are shown in the fourth column.

(a) Low flux - Linear.

(b) Low flux - Logarithmic.

(c) High flux - Linear.

(d) High flux - Logarithmic.
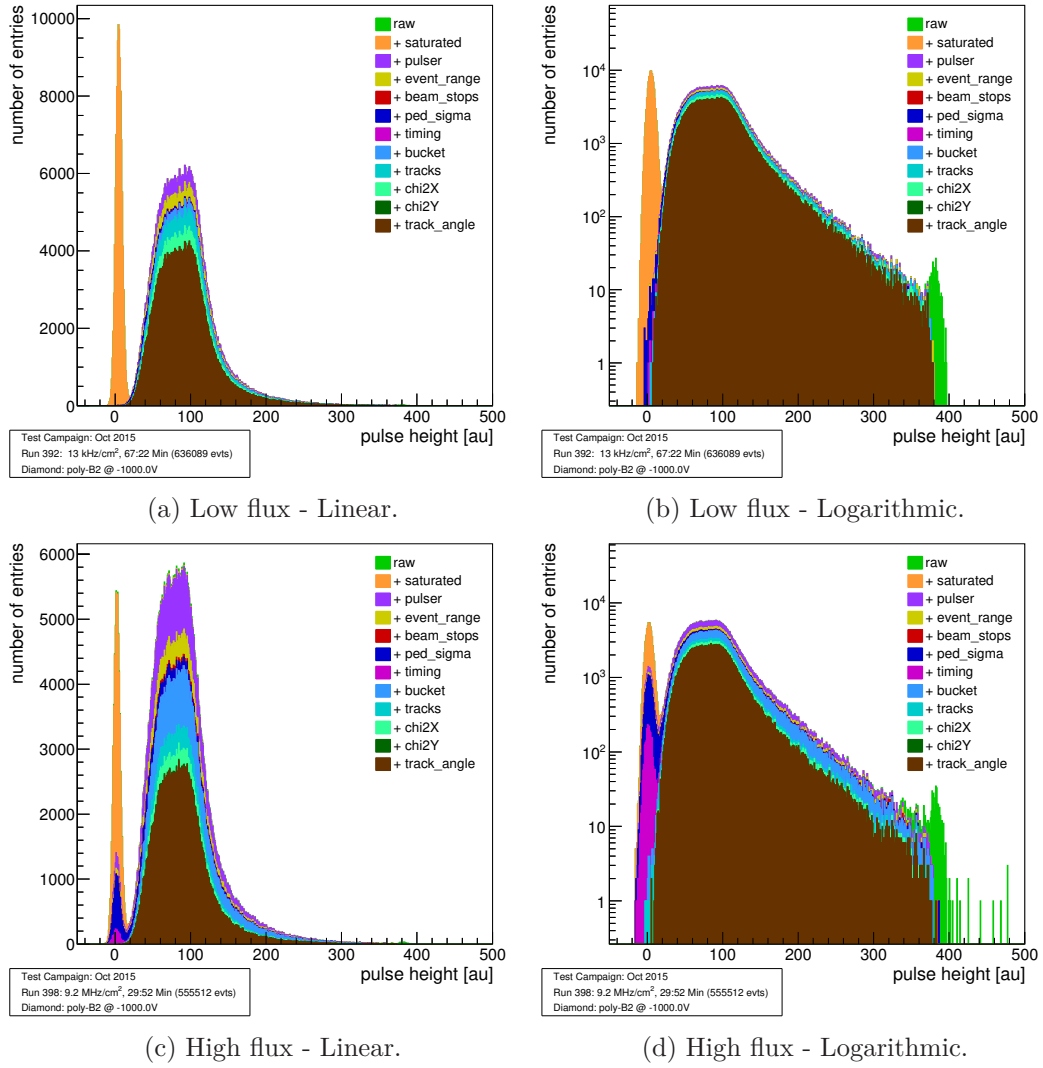
Figure 5.20.: Pulse height distribution applying one selection criteria after the other for a low and a high flux run. Both distributions are shown in normal and logarithmic scale.
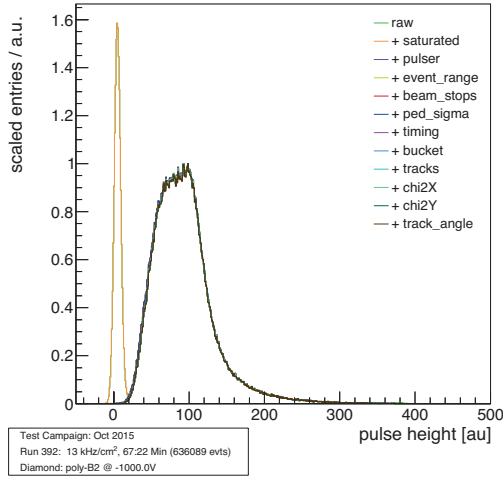
(a) Low flux - Linear.
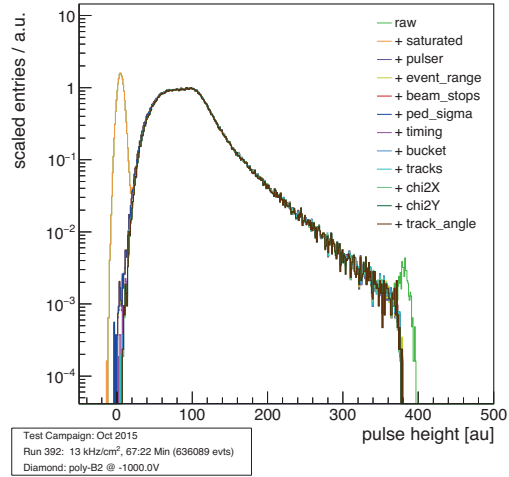
(b) Low flux - Logarithmic.
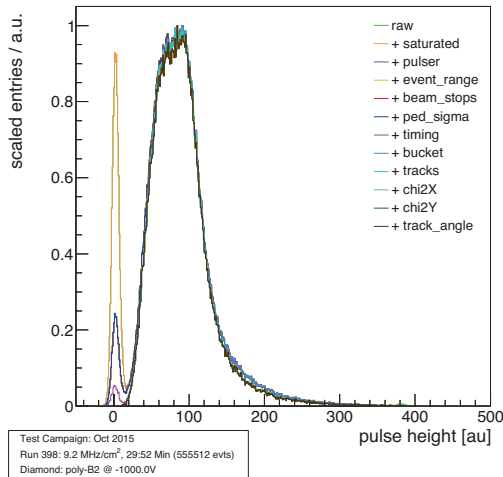
(c) High flux - Linear.
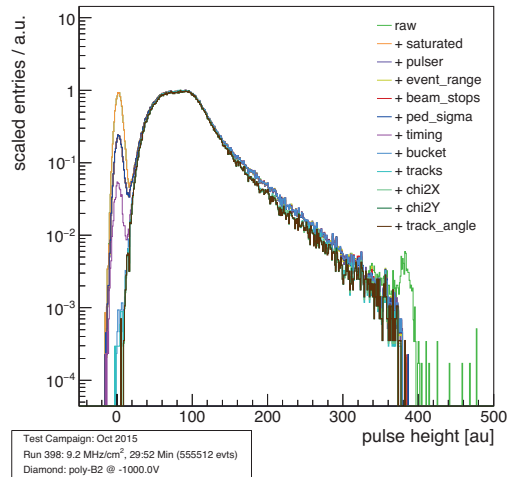
(d) High flux - Logarithmic.

Figure 5.21.: Pulse height distributions when applying each selection criteria after each other. This are the same distributions as in Figure 5.20, but the distributions are scaled such that the maximum for signals above 10 a.u. is at one.

while the rest of the distribution stays unchanged. At both particle fluxes, the pedestal at zero is strongly reduced when the *pulser* events (Section 5.3.1.4) are rejected. After this selection, the pedestal contribution is completely removed for the low flux run, while the peak is reduced, but can be still observed for the high flux run. The following selection criteria *event_range* (Section 5.3.1.1), *beam_interruptions* (Section 5.3.1.2) and *ped_sigma*(Section 5.3.1.5) do not have a strong influence on the shape of the distribution. By applying the *timing* (Section 5.3.1.6) on the high flux run the pedestals peak is further reduced and vanishes after applying the *bucket* selection criteria (Section 5.3.1.7). Applying these last two selection criteria does not change shape of the signal distribution. The *tracks* selection criteria (Section 5.3.1.8) is changing the shape of the distribution in the high signal region for the high particle flux run. A slight reduction for signals above 140 a.u. can be observed in Figure 5.21 (d). This selection criteria removes events with more than one cluster in any of the telescope planes, events with multiple tracks are removed. These events have a higher signal response and the tracks selection criteria removes them.

It can be seen that the combination of all selection criteria suppresses the peak at zero. The shape of the signal is essentially constant, indicating that the selections do not bias the sample towards low or high signal responses.

Influence on the Mean Pulse Height   For the measurement of the signal response of a DUT the mean pulse height for each run was calculated after applying every selection criteria. The effect of each selection criteria on the mean pulse height was studied. In Figure 5.22, the mean pulse height is shown when one applies the selection criteria in

(a) Low flux.   (b) High flux.
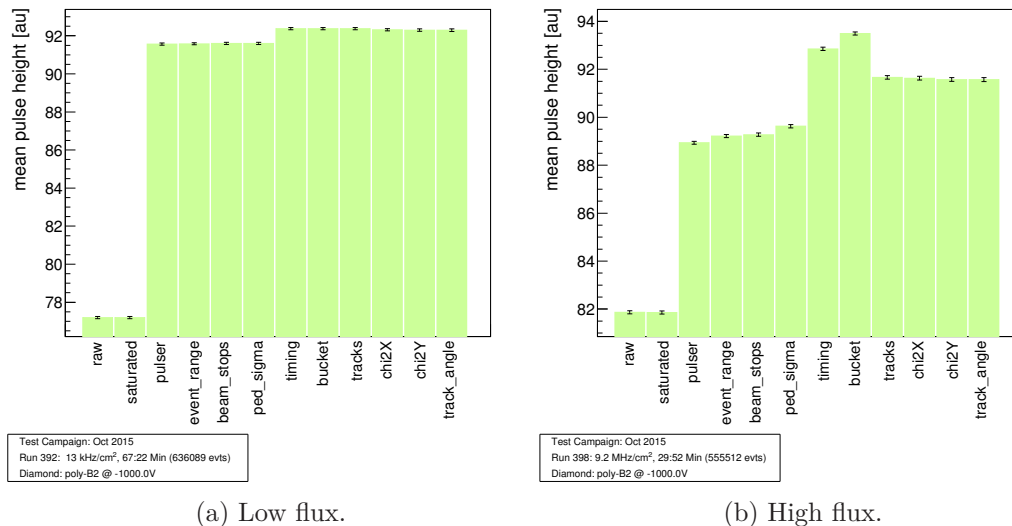
Figure 5.22.: Influence of the difference selection criteria on the mean of signal distribution.

consecutive order for a low particle flux run in Figure 5.22 (a) and for a high particle flux run in Figure 5.22 (b). The indicated errors correspond to the statistical errors on the mean calculation and do not take into account any systematic errors. It can be observed that the raw distribution has the smallest mean signal as it contains many events in which no particle crossed the detector.

Applying the *pulser* selection criteria, the mean is increased strongly as most events with no particle crossing are removed. While the *event_range*, the *beam_stops*, and the *ped_sigma* criteria do not have any influence at low particle flux, a slight increase of the mean can be observed for the high particle flux. Additional events with no particle crossing and events with a biased pedestal due to a particle crossing are removed. The *timing* selection criteria also removes events where no particle crossed, as it requires a peak position in a region around the average peak position. Events without a particle crossing have peak position uniformly distributed in the full PeakSearchRegion and therefore are rejected. The rejection of these events further increases the mean.

All following selection criteria do not have an influence on the mean signal for the low particle flux run. The mean signal stays constant within the statistical errors. For the high particle flux run the situation is slightly different. The *bucket* selection increases the mean slightly as the probability for triggering on the wrong bucket increases with higher particle flux. The pulse height of these events is close to zero. By rejecting these events, the mean signal is increased. The application of the *track* selection criteria rejects events that have multiple tracks and therefore reduces the mean signal. The selections on *chi2X*, *chi2Y* and *track_angle* do not affect the mean signal indicating that the selected trigger area already demands a straight track through the telescope.

This analysis shows that the applied selection criteria are well understood and that the influence of each selection criteria on the mean pulse height behaves as expected for the different particle fluxes. After applying all selection criteria the signal distributions do not show any pedestal contribution. For all further analyses the mean pulse height of the detector during the run was used.

5.4. Results

In this section first results of the analysis of the beam test data for the 2015 beam tests are presented. The analysis presented is based on the `RatePadAnalysis`-framework [169]. This framework processes digital logbooks to extract the parameters of each run, converts the data using the EUDAQ framework and combines the results of the different particle fluxes. For each telescope configuration the pixel data was used to align the telescope, such that it was possible to perform a straight line fit for each event and extract a predicted hit position for each DUT.

For each beam test campaign a separate optimization of the SNR was performed. In both beam test campaigns in August 2015 and October 2015, the best SNR was achieved with an *IntegralRange* $[-4\,\mathrm{ns}, 6\,\mathrm{ns}]$. For each beam test campaign the PeakSearchRegion was adjusted in such a way that the most probable peak position was centered in the region. The corresponding pedestal IntegralPosition was defined $20\,\mathrm{ns}$ in front of the most probable IntegralPosition of the signal PeakSearchRegion. In all runs an event-wise pedestal subtraction was performed. The pulse height (signal response) was defined as the difference of the signal integral and the pedestal integral. For each run the average pulse height after event selection was calculated. For the final comparison of different runs the average pulse height versus the incident particle flux was plotted on an absolute and a relative scale. In addition, the average pulse height of the pulser calibration was measured for each run. It was required that at each particle flux the pulser calibrations agree with each other. Runs which showed a significant difference in the average pulser signal were removed.

5.4.1. Diamonds Tested

The scCVD diamond *S129* was produced by Element 6 [147] with a thickness of $528\,\mathrm{\mu m}$. After RIE the final thickness was measured to be $509\,\mathrm{\mu m}$. It was one of the spare detector parts of the PLT pilot run detector, which have not been used during operation of the PLT pilot run. Since 2014 this diamond has been used as a reference detector in several beam tests at PSI and was also tested as a strip detector with the Strasbourg telescope at CERN. The diamond has not been exposed to any specific radiation, but as it was tested in several beam tests it has received a small fluence due to the incident particle flux in these beam tests. A total integrated particle flux of the the order of $10^{11}\,\mathrm{p/cm^2}$ to $10^{12}\,\mathrm{p/cm^2}$ is estimated as its total fluence received.

In a source measurement at OSU the measured CCD as a function of bias voltage was measured and is shown in Figure 5.23. It can be seen that this diamond has a higher CCD than its thickness, even after RIE. It reaches a maximum CCD of $565\,\mathrm{\mu m}$ at a bias voltage of below $100\,\mathrm{V}$. This difference of measured CCD and thickness is not completely understood, but was observed in all diamonds of this production batch.

The pCVD diamond *Poly-D* was produced by II-VI technologies [151]. After a first processing step the thickness of the diamond was measured to be $535\,\mathrm{\mu m}$. It was irradiated to $1 \times 10^{14}\,\mathrm{n/cm^2}$ in April 2014 and was initially tested as a pixel detector in May 2014. After this test the detector was processed again. By RIE the thickness of the diamond was reduced by $25\,\mathrm{\mu m}$ to the new thickness of $510\,\mathrm{\mu m}$. This processing step was meant to validate industrial processing. In the October 2015 beam test this diamond was tested as a pad detector The CCD as a function of bias is shown in Figure 5.24, measured with a $^{90}\mathrm{Sr}$ source setup at OSU. The measurements were performed before irradiation, after irradiation and after reprocessing. In the unirradiated state it reached a CCD of $300\,\mathrm{\mu m}$ for positive and negative bias of $\pm1000\,\mathrm{V}$. After irradiation with $10^{14}\,\mathrm{n/cm^2}$ the CCD
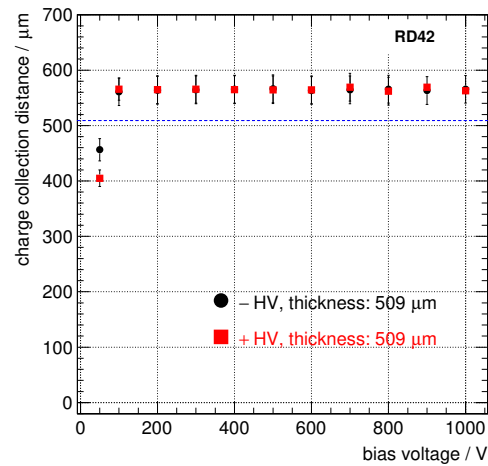
Figure 5.23.: The CCD as a function of applied bias voltage for the unirradiated scCVD diamond *S129*. The dashed line represents the expected signal based on the thickness of the material.
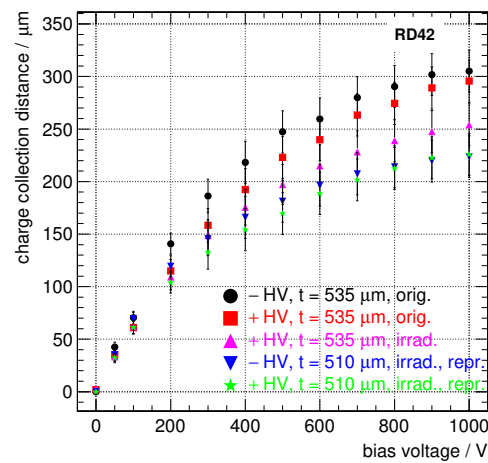
Figure 5.24.: The CCD as a function of applied bias voltage for the unirradiated pCVD diamond *Poly-D*. The unirradiated diamond reached a CCD of 300 μm at a bias voltage of ±1000 V. After the irradiation the CCD reduced by ∼50 μm. The additional processing step which removed 25 μm diamond material reduced the CCD by another ∼25 μm.

was reduced by 40 µm. After the industrial reprocessing the CCD of the detector decreased by 25 µm. This reduction of the CCD after industrial reprocessing corresponds to a reduction of the MFP from 4300 µm to 1300 µm, indicating that an issue may have occurred during the processing.

The third diamond *Poly-B2* is also a pCVD diamond, produced by II-VI technologies [151]. Its thickness was measured to be 545 µm. In the August 2015 beam test it was first tested unirradiated. After that beam test it was irradiated to 5×10^{14} n/cm^2 and retested in the October 2015 beam test. In the bias scan it can be seen that this diamond the CCD plateaus at 250 µm for the positive polarity and approximately 280 µm for the negative polarity. At high bias voltage the diamond starts to draw current (larger than 2 nA), which affects the gain of the amplifier and therefore distorts the CCD measurement. For the negative polarity this effect was observed above 900 V, for the positive polarity the effect occurred between 800 V and 900 V. By cleaning and re-metalization of the diamond it was possible to remove this effect. All of the above effects and the fact that these effects went away after cleaning indicate that it was a surface related effect and not a bulk effect.

All neutron irradiations of the pCVD diamonds were performed at the Jozef Stefan Institute in Ljubljana with a TRIGA Mark II research reactor [171]. In Table 5.3 an overview of all rate scans performed with these diamonds is given.
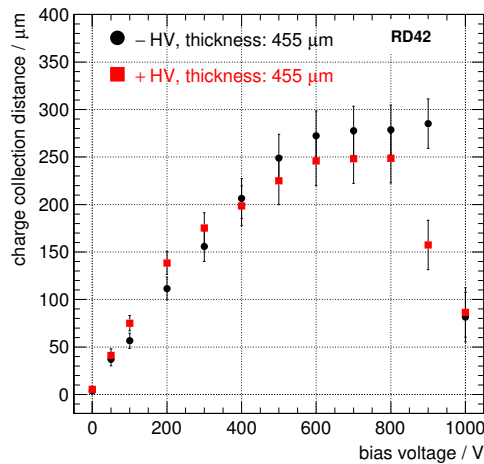
Figure 5.25.: The CCD as a function of applied bias voltage for the unirradiated pCVD diamond *PolyB2*. At high bias voltage the diamond starts to draw leakage current and the CCD seems to be reduced as the gain of the charge sensitive amplifier is reduced.. At -900 V a maximum CCD of 280 µm was measured.

Name	Type	Prod.	Beam Test.	Radiation [n/cm^2]	Thick. [µm]	Bias [V]	Pulser Type	Polarities Sig.	Pul.
S129	scCVD	E-6	Aug	none	509	-500	ext.	neg.	neg.
S129	scCVD	E-6	Oct	none	509	-500	ext.	neg.	neg.
S129	scCVD	E-6	Oct	none	509	$+500$	ext.	pos.	pos.
Poly-B2	pCVD	II-VI	Aug	none	455	$+1000$	ext.	pos.	neg.
Poly-B2	pCVD	II-VI	Aug	none	455	-1000	ext.	neg.	neg.
Poly-B2	pCVD	II-VI	Oct	5×10^{14}	455	-1000	int.	neg.	neg.
Poly-B2	pCVD	II-VI	Oct	5×10^{14}	455	$+1000$	int.	pos.	neg.
Poly-D	pCVD	II-VI	Oct	1×10^{14}	510	-1000	int.	neg.	neg.
Poly-D	pCVD	II-VI	Oct	1×10^{14}	510	$+1000$	int.	pos.	neg.

Table 5.3.: Overview of the diamonds tested, including the corresponding irradiation levels, which have been analyzed.

5.4.2. Analysis Method

Each full scan consisted of several flux-up and flux-down scans. The actual procedures are described in Section 5.2. For each run the mean signal pulse height and the mean pulser pulse height were extracted. In order to ensure a stable operation of the detector the current was monitored continuously during the full scan. The first flux-up scan was not used, so that the diamond operates in a stable regime and was fully pumped. For the final comparison of the signal responses of different particle fluxes the runs needed to fulfill certain criteria.

The electronics was setup so that a particle crossing the detector which was biased with negative bias voltage resulted in a negative signal, while at positive bias voltage the signal was positive. In order to simplify the comparison of both polarities, the mean pulse height was calculated as the absolute value of the pedestal subtracted signal. It is known that the responses of the amplifier for positive and negative signal polarities were different, therefore the mean signal responses for positive and negative signal polarities are different. In the last two columns of Table 5.3 the polarities of the signals of the pulser and of particle tracks are listed. In full scans in which signal and pulser have opposite polarities, the graphs, showing the pulser response as function of particle flux, have to be considered with great caution. In this configuration the response might be not correlated with the gain.

5.4.3. Discussion of the Errors

In order to study the errors in the measurement different procedures were compared with each other. The error is modeled by sum of a purely statistical error $\sigma_{stat.}$ and an error

on the reproducibility of the measurement $\sigma_{rep.}$. The statistical error can be reduced with $\sigma_{stat.} \propto 1/\sqrt{N}$, where N is the number of recorded events increasing the number of recorded events N, the reproducibility is assumed to be constant. This analysis was performed individually for each diamond and each bias polarity. In Table 5.4 the results are summarized.

The pulser response of each run was studied as a function of particle flux. For each run the mean pulse height of the pulser was calculated. With this information a mean and a sigma was extracted combining all runs with the same particle flux. The relative errors were compared with each other and the minimum and maximum is shown in the Table 5.4. In addition, the mean and the sigma when averaging the all means pulser pulse heights of the runs are shown. This average is smaller for the full scans with the internal pulser. In all runs in which the external pulser was operated with negative polarity the mean pulser pulse height decreases with increasing particle flux. In the full scan in which the pulser was operated with positive polarity the pulse height is rather increasing than decreasing. For the full scans in which the internal pulser was used the differences between the runs are smaller than 0.2 %.

The mean signal pulse height of each run was used to calculate the mean and sigma for each particle flux. These are used to calculate the relative error for each particle flux. From all particle fluxes the minimum and the maximum of this relative error are shown in the Table 5.4. The corresponding distributions can be found in the Appendix B.3. It can be observed that variations for the scCVD sample are smaller than the variations for the pCVD samples, while the maximum (minimum) relative error for the scCVD sample is 0.63 % (minimum: 0.33 %), the maximum error for the pCVD samples is 1.24 % (minimum: 0.75 %).

In all previous tests of diamonds in beam tests no particle flux dependence was observed. These tests were performed at particle fluxes of the order of $50\,\mathrm{kHz/cm^2}$. Therefore the relative errors for all runs below $80\,\mathrm{kHz/cm^2}$ and below $150\,\mathrm{kHz/cm^2}$ were calculated. It can be observed that for all scans except the ones of the unirradiated *Poly-B2* the relative error becomes larger when including the runs between $80\,\mathrm{kHz/cm^2}$ to $150\,\mathrm{kHz/cm^2}$. The relative errors for runs below $80\,\mathrm{kHz/cm^2}$ is of the order of 0.5 % for scCVD and 1 % for the pCVD. In the distributions of the scans of the unirradiated pCVD sample *Poly-B2* (Figures B.13 in Appendix B.3) two contributions can be observed while in all other distributions the data are consistent with a single Gaussian. This indicates that a different effect occurs in that case and the error for is under-estimated rather than over-estimated.

In addition the spread of the pedestal distribution was studied individually for each particle flux. The minimum and the maximum spread for one particle flux, as well as the total spread for the full scan are shown in the last columns of the Table 5.4. It can be observed that the full pedestal spread is between 2.55 a.u. and 7.18 a.u.. This is most-likely an intrinsic property of the amplifier. The maximum spread for each individual particle flux is 0.46 a.u.. This is an indicator for the repeatability of the measurements performed with this setup.

The following procedure was used for the estimation of the error on the reproducibility. The relative error on the signal for all runs with a particle flux was taken as the relative error on each measurement. This error was calculated for each bias polarity and each diamond individually. In addition it was required that the absolute error must be at least the maximum pedestal spread.

5.4.4. Discussion of the pulser response

It was planed to use the pulser to check the gain of the amplifiers during each run and during the full scan. For this reason the response of the pulser signal was studied for each run and compared with all runs of the full scan. As mentioned in Section 5.1 two different versions of the amplifier were used, an *internal pulser* and an *external pulser* version. The *internal pulser* uses negative polarity signals as calibration pulses, while the *external pulser* can be operated with both polarities depending on the input signal. During the August 2015 beam test campaign only the amplifier version with the *external pulser* was used. In the October 2015 beam test beam campaign both versions were used. In Figure 5.26 the pulser response for windows of 10 000 events is shown during one run. After the applying all selection criteria a total of 700 to 800 events were included in each calculation of the average. The constant fit indicates that the pulser response during the run is very constant. As the behavior of the two versions with external and internal pulser are different, the results are discussed separately.
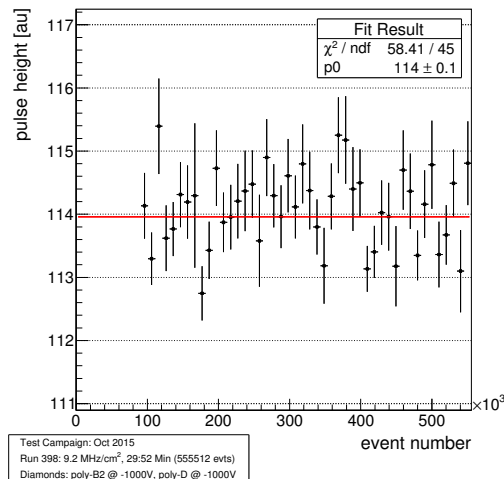
Figure 5.26.: Mean pulser pulse height as a function of event number during one run. Each point corresponds to 10 000 events. After applying all selection criteria a total of 700 to 800 events are used for calculation of the average.

Diamond name	Bias [V]	type	Pulser			Signal Flux				Pedestal Spread		
			min [%]	max [%]	rel. σ_{tot} [%]	min [%]	max [%]	<150 [%]	<80 [%]	full [a.u.]	min [a.u.]	max [a.u.]
S129	−500	ext.	0.04	0.17	2.76	0.48	0.63	0.50	0.50	7.18	0.08	0.46
	+500	ext.	0.11	0.22	0.35	0.33	0.50	0.44	0.39	3.81	–	–
	−500	ext.	0.08	0.19	2.80	0.42	0.58	0.45	0.46	3.76	–	–
unirrad.												
Poly-B2	−1000	ext.	0.05	0.88	2.43	0.77	0.90	1.19	1.41	5.26	0.09	0.28
	+1000	ext.	0.07	0.37	0.72	0.83	1.17	1.28	1.38	4.69	0.01	0.43
irrad..												
Poly-D	−1000	int.	0.04	0.21	0.17	0.75	1.04	1.10	1.04	3.72	0.08	0.42
	+1000	int.	0.04	0.17	0.06	0.83	1.14	1.18	1.10	3.69	0.12	0.39
irrad..												
Poly-B2	−1000	int.	0.04	0.18	0.06	0.85	1.24	0.98	0.88	2.90	0.04	0.40
	+1000	int.	0.04	0.09	0.03	0.76	1.01	0.87	0.84	2.55	0.07	0.37

Table 5.4.: Summary table of the systematic errors study. The highlighted cells are mentioned explicitly in the text.

208

5.4.4.1. External Pulser

By changing the height and the polarity of the input signal the signal response of the *external pulser* can be changed in height and in polarity. It was planned to operate the pulser in such a way that the pulser response is of the same polarity as the signal response. For all scans, but the scan of the unirradiated *Poly-B2* operated at $+1000\,$V, this was the case. During the scan of *Poly-B2* at $+1000\,$V in August 2015 the polarity of the pulser signal was not changed, therefore the signal response was positive and the pulser response was negative.

In Figure 5.27 the pulser response as a function of particle flux is shown for the negative bias polarity scans and for the positive bias polarity scans. In every scan the data was scaled in such a way that the average pulser responses for particle fluxes below $80\,$kHz/cm^2 were the same. The scan of *Poly-B2*, operated with $-1000\,$V bias, was taken as the reference.

In Figure 5.27 (a) the pulser response for negative bias polarity is shown. The two scans in August 2015 show a similar behavior. In the three low particle fluxes the pulser responses are close to $76\,$a.u., while the pulser responses for the three high particle fluxes are lower at $\sim 72\,$a.u.. This corresponds to a change of $\sim 5\,\%$ when changing the particle flux between $120\,$kHz and $1.2\,$MHz. The behavior of the scan in the October 2015 beam test campaign is similar with the difference that the drop in pulser response occurs at a high particle flux. The pulser response at $\sim 1\,$MHz is similar to the three
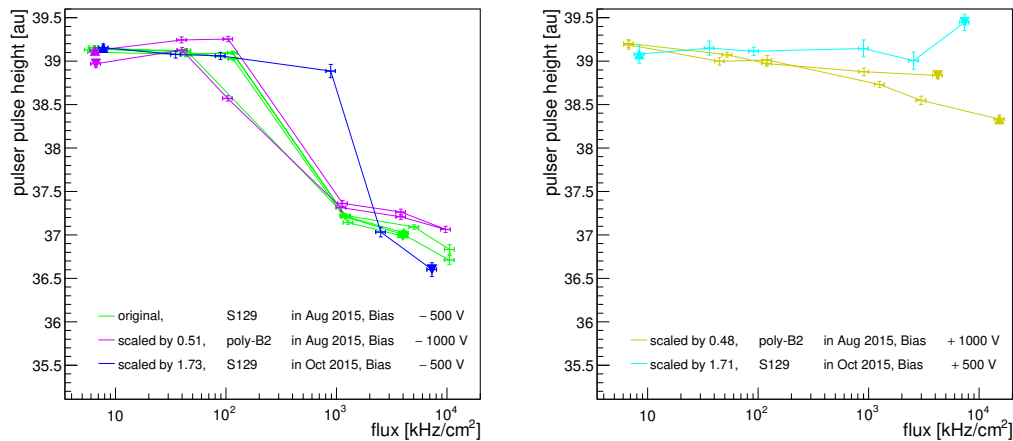
(a) Negative bias polarity.

(b) Positive bias polarity

Figure 5.27.: External pulser response for positive an negative polarity. For all scans but *Poly-B2* at a bias of $+1000\,$V the polarity of the pulser is chosen to be the same as for the signal. For *Poly-B2* at a bias of $+1000\,$V the signal was positive, while the pulser was negative.

low flux points and the drop from $\sim$76 a.u. to $\sim$72 a.u. occurs between $890\,\mathrm{kHz/cm^2}$ and $2500\,\mathrm{kHz/cm^2}$.

In Figure 5.27 (b) the pulser response for positive sensor bias is shown. While the pulser response for the scan of *S129* was adjusted such that the polarity of both the pulser and the signal were the same, this polarity change of the pulser signal was not performed for the scan of *Poly-B2*. The response for the negative pulser signal(blue line) is going down with particle flux. The reduction is $2.5\,\%$ and therefore only half of the reduction for the negative bias polarity scans. For the scan with positive pulser polarity a slight increase can be observed. The four measurements below $2.6\,\mathrm{MHz/cm^2}$ are in complete agreement with each other using only the pure statistical error. At the highest particle flux of $7.5\,\mathrm{MHz/cm^2}$ the response is above the other measurements, in a linear fit including this measurement the goodness of the fit χ^2 was found to be 13.44 for 5 degrees of freedom, corresponding to a probability of $2.0\,\%$.

The response of the pulser for negative polarity pulses are not understood. Further investigations are needed to understand the effect. Due to the different behavior of positive and negative pulser polarity it was decided to not perform any gain corrections based on this measurement but use the pulser only to check the stability within the run and at each particle flux separate.

5.4.4.2. Internal Pulser

With the circuit of the *internal pulser* only pulses with negative polarity can be injected. Therefore only for negative bias polarity the signal of the pulser and of a crossing particle are of the same polarity.
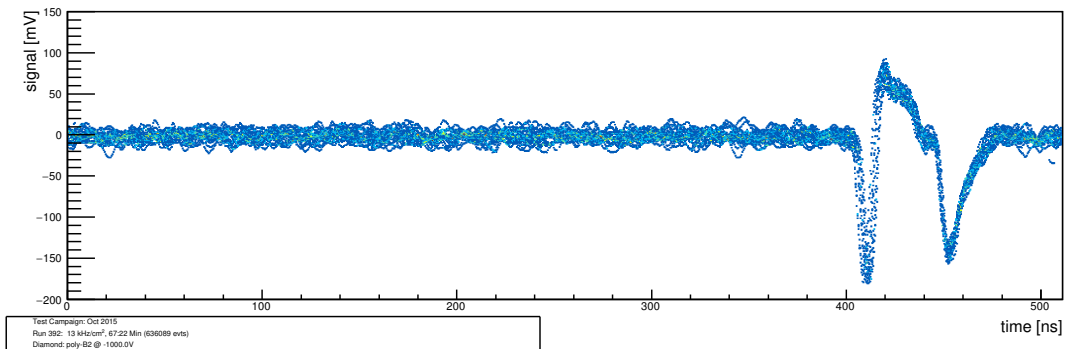
Figure 5.28.: Twenty example waveforms for the pulser response when using the *internal pulser*.

In Figure 5.28 twenty example waveforms are shown for one run in which the *internal pulser* was used. During the pulse injection into the circuit a coupling was observed which caused one additional pulse in front and one in the back of the actual injected

signal. The additional pulses in front can be observed in this overlay at a peak position of $\sim$410 ns. The pulse in the back is outside of the digitization window. The pulse caused by the coupling is overshooting before it returns to zero. The injected pulse can be observed at 455 ns.

In Figure 5.29 the pulser response for all scans performed with an *internal pulser* are shown. The data of each scan was rescaled such that the mean for particle fluxes below 80 kHz/cm^2 agree. All measurements are spread within less than 0.9 %. The biggest spread can be observed the scan of *Poly-D* biased at -1000 V.

Fitting all measurements with a Gaussian, a mean of 103.7 a.u. with a width of 0.12 a.u. can be extracted. This indicates that the pulser response for the internal pulser is constant for all scans no matter if the signal of the crossing particles was of the same or of the opposite polarity than the pulser signal.

The different behavior between *external* and *internal pulser* circuit needs additional studies. It is not clear if the constant response of the *internal pulser* is caused by the different way of injecting the pulse or by other effects. The difference of the pulse shape due to the coupling needs to be removed in order to see if this additional pulse superpose any changes in the injected pulse.
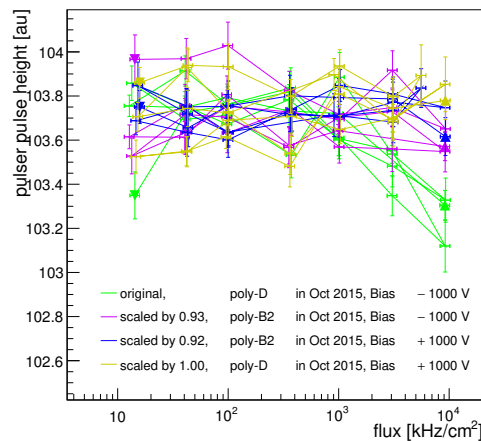
Figure 5.29.: Internal pulser response for the October 2015 beam test for the diamonds *Poly-B2* and *Poly-D* biased with $\pm$1000 V. For positive polarity the signal of the pulser is always negative, therefore the signals of pulser and crossing particles are of the same polarity for negative bias polarity and of opposite polarity for positive bias polarity.

5.4.5. Results of the scCVD Diamond Pad Detector *S129*

The scCVD diamond pad detector *S129* was tested in both beam test campaigns. It was used as a reference detector to check the stability and measure the systematic errors of the system. As the system is optimized to work with signals of pCVD diamond detectors, the input signal to the DRS4 Evaluation Board was attenuated by a factor of two using a 6 dB attenuator.

In the August 2015 beam test the detector was only tested with a bias voltage of -500 V due to limited beam time. In order to study the systematics of the setup a slightly modified testing routine was used. It was observed that the mean pulser pulse height was reduced in some runs of the flux scan. Therefore a total of five runs were removed from further analysis. In the last run of the scan at a particle flux of $10 \, \text{MHz/cm}^2$ the amplifier died during the run, therefore the data was not used for analysis. In October 2015 the diamond was only tested for one single flux up scan for each bias voltage. The signal distributions, shown in Figures 5.30 in normal and logarithmic scale, completely overlap for all six runs of one flux-up-scan. Small differences can be seen in the very low pulse height regime below 70 a.u. in Figure 5.30 (b), these events are still under investigation, as the reason for them is not yet understood. As the influence of these events on the mean signal pulse height is small, it can be concluded that at all particle fluxes a similar pulse height distribution can be extracted.

In Figure 5.31 the mean signal pulse heights of the all three flux scans performed in August 2015 and October 2015 are shown. Due to the usage of a different amplifier and a different attenuator a difference in pulse height can be observed for the two scans with

(a) Linear Scale.　　　　　　　　(b) Logarithmic Scale.
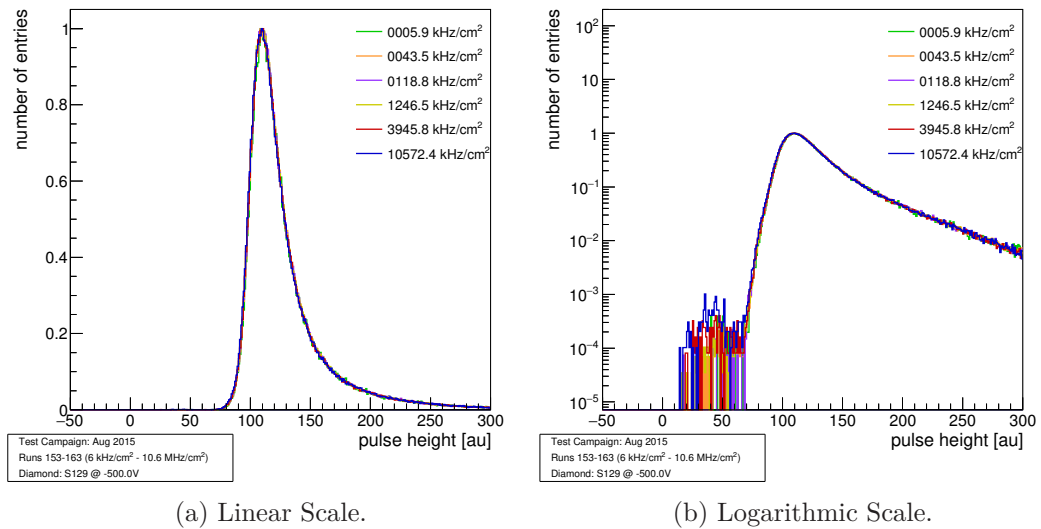
Figure 5.30.: Pulse height distribution of the signal for *S129* unirradiated biased with -500 V, tested in August 2015.
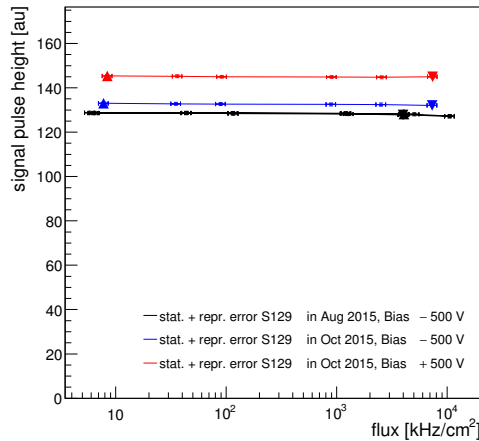
Figure 5.31.: Signal response of *S129* in the August 2015 and October 2015 beam test campaign. In both beam tests different attenuators were used, therefore the signal responses had slightly different gain. The amplifier gain for positive and negative signals is also slightly different.

a negative bias of $-500\,\mathrm{V}$. In addition a difference between positive an negative bias polarity can be observed which is caused by different amplifier responses for positive and negative signals.

In Figure 5.32 the measurements are scaled in such a way that the mean pulse height for all runs below $80\,\mathrm{kHz/cm^2}$ agree with the mean of the $-500\,\mathrm{V}$ scan in October 2015. In Figure 5.32 (b) showing the signal response as a function of particle flux, the response is slightly decreasing with increasing particle flux for both scans with negative bias polarity. The total spread of all measurements total change of less the $1.4\,\%$ over the full range of all particle fluxes. The differences between the mean pulse heights of the same particle flux is less than $0.3\,\%$. The measurements at positive bias polarity do not show the same decrease. For these a relative spread of $0.4\,\%$ can be extracted and is consistent with a flat signal response over the full range of particle fluxes.

In order to understand the underlying reason for this effect the mean pulser signal was studied as a function of incident particle flux, shown in Figure 5.32 (b). In all scans the amplifier version with the *external pulser* was used. Both types, the signal and the pulser, waveforms used the same signal polarity and could be therefore compared directly with each other. A decrease by approximately $5\,\%$ can be observed. This could be caused by a change of the gain in the amplifier circuit or by issues in the pulser circuit. Further studies, comparing external and internal pulser and changing the size of the calibration charge, are needed to understand this effect in detail.

It can be seen that the signal response is very stable within less than $0.5\,\mathrm{a.u.}$ up to a particle flux of $100\,\mathrm{kHz/cm^2}$. For higher particle fluxes the signal for scans with negative
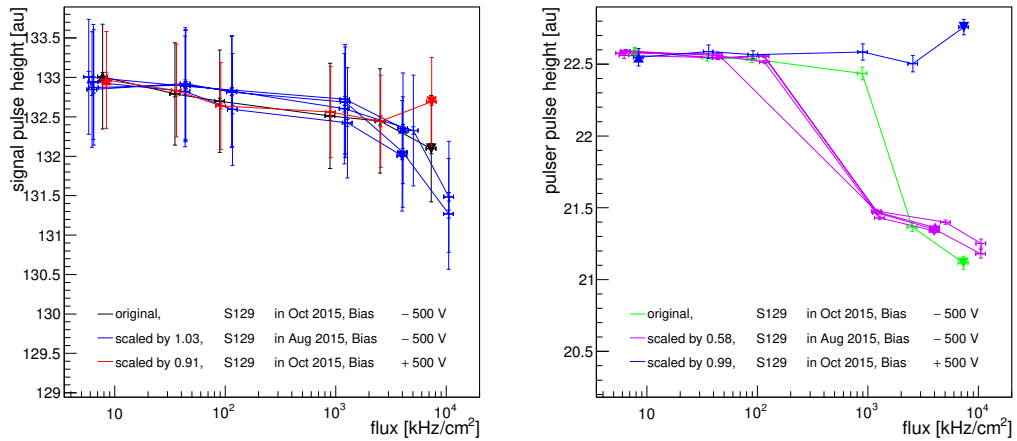
(a) Signal response.

(b) Pulser response.

Figure 5.32.: Mean signal and pulser pulse height for all scans of *S129* in the August 2015 and October 2015 beam test campaign. The data were rescaled such that the mean of the pulse heights below $80\,\text{kHz/cm}^2$ for each scan agree with each other. In Figure (a) the errors are the combined errors, linearly adding the statistical and the reproducibility errors. The errors in Figure (b) corresponds to the width of the distribution divided by the square root of the number of event.

bias polarity are slightly decreasing, while the full scan with positive bias polarity is flat or slightly increasing. As the diamond is already slightly irradiated and the response of the pulser is changing with particle flux, it is not clear if the reduced pulse height response is caused by changes in the gain of the amplifier with rate or by actual effects due to the increasing particle flux.

The slight decrease (1.4 %) for negative bias polarity in both beam test campaigns might be caused by a systematic effect such as a change of the gain in the amplifier or it could be an intrinsic effect of the slightly irradiated scCVD diamond. In order to improve the understanding of systematic effects in this setup, further studies of the signal response of unirradiated scCVD diamonds is needed. By testing new unirradiated scCVD diamonds and varying the pulser settings the understanding of the cause of the slight signal decrease could be improved.

5.4.6. Results of pCVD Diamond Pad Detectors

In the following sections the results of the two pCVD diamond pad detectors *Poly-B2* and *Poly-D* are presented. The diamond *Poly-B2* was tested with the new setup in both beam test campaigns, once unirradiated and once after the irradiation with $5 \times 10^{14} \, \mathrm{n/cm^2}$. The diamond *Poly-D* was tested in the October 2015 beam test campaign. It was irradiated to a dose of $10^{14} \, \mathrm{n/cm^2}$. With these measurements it is possible to check the hypothesis that pCVD diamond detectors do not show a pulse height decrease with increasing particle flux. Compared to the original publication [33] the tests are performed at particle fluxes approximately 30 times higher and the tested diamonds were irradiated to 10 times higher radiation doses.

5.4.6.1. Results of the unirradiated pCVD Diamond Pad Detector *Poly-B2*

These tests were performed in the August 2015 beam test campaign. The diamond was unirradiated.

The two Figures 5.33 (a) and 5.33 (b) show an overlay of pulse height distributions of several runs at different particle fluxes. The detector was biased with $\pm 1000 \, \mathrm{V}$. The distributions are much wider than the distributions of the unirradiated scCVD diamond *S129*. This difference is expected as scCVD diamond material is more homogeneous than pCVD diamond material. In addition the distributions for the different particle fluxes do not overlay as well as for the scCVD sample. The rising edge of the distribution shifts slightly and slight differences in the long tail can be observed.

In Figure 5.34 the mean pulse height response as a function of particle flux is shown for positive and negative bias polarity. The difference in Figure 5.34 (a) is caused by the different amplifier gain for positive and negative signals. For both polarities a

(a) At -1000 V.

(b) At $+1000$ V.
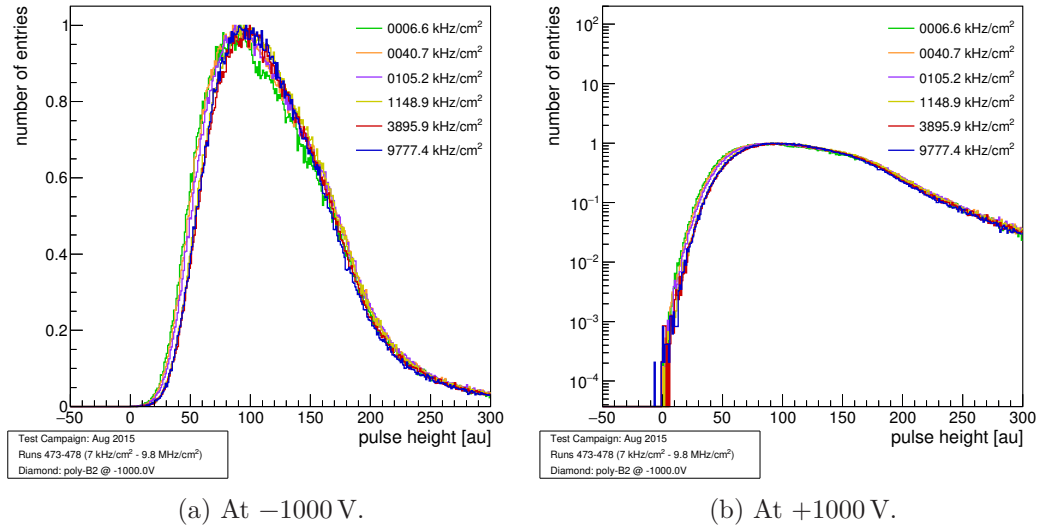
Figure 5.33.: Pulse height distribution for the different particle fluxes of the unirradiated pCVD diamond *Poly-B2* at a bias voltage of ± 1000 V.

(a) Unscaled.

(b) Scaled.
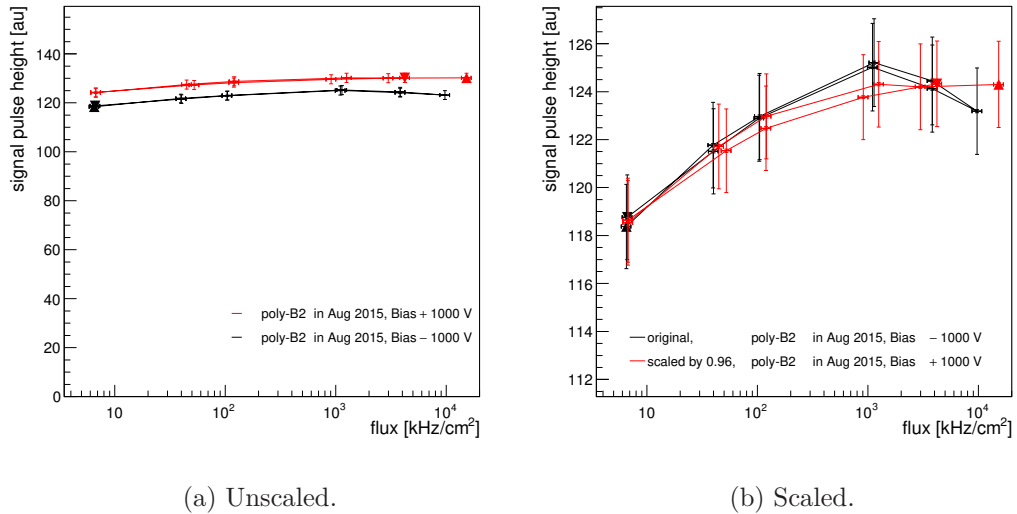
Figure 5.34.: Signal response as a function of particle flux for the pCVD diamond *Poly-B2* unirradiated and biased with ± 1000 V. The errors are the combined statistical and reproducibility errors. The amplifier has different gain for positive and negative polarity. In Figure (b) the scan with positive bias polarity is rescaled such that the mean for runs at particle fluxes below 80 kHz/cm^2 agree with the one of negative bias polarity.

signal increase from the lowest to the highest particle flux by approximately 4 % can be observed.

In Figure 5.34 (b) the positive bias polarity scan is scaled with one factor for the full scan to agree with the scan at negative bias polarity for particle fluxes below $80\,\text{kHz/cm}^2$. A scaling factor of 0.96 was found, which is of the same order as the scaling factor of 0.91 found for *S129* in the same beam test campaign. Slight difference between this factor are expected due to the use of different amplifiers. It can be seen that the total signal spread of all runs is below 5 %. An increase of the mean signal up to a particle flux of ∼1 MHz can be observed. The measurements of positive and negative bias polarity are in agreement with each other. Due to the increasing signal response the error calculated by using all runs with particle fluxes below $80\,\text{kHz/cm}^2$ is maybe overestimated. From the lowest flux to the second lowest particle flux an increase of 2.5 % can be observed. This decrease is below the sensitivity of the original setup and therefore consistent with the results of the original paper [33].

While the measurements of the unirradiated scCVD diamond for negative bias voltage indicated a ∼1.4 % decrease in the signal response from lowest to highest particle flux, the measurements for positive voltage indicated a flat signal response over the full flux range. The measurements of the unirradiated pCVD sample for positive and negative bias polarity rather indicate an signal increase of 3 % to 5 % from the lowest to th highest particle flux. For a better understanding of the underlying physics the measurement program needs to be extend to several flux-up and flux-down scans. In addition the test of other unirradiated pCVD diamond detectors are needed to check if this increase occurs for other diamonds as well.

5.4.6.2. Results of the irradiated pCVD Diamond Pad Detector *Poly-D*

This sample was irradiated with $1 \times 10^{14}\,\text{n/cm}^2$ and was tested with the new setup as a pad detector during the October 2015 beam test.

Figure 5.35 shows the pulse height distributions for the different particle fluxes for positive and negative bias of $\pm1000\,\text{V}$. The distributions of positive and negative polarity have slightly different shapes. The distribution for positive polarity is broader than the one for negative polarity. The distributions are wider than the ones of the unirradiated scCVD sample *S129* shown in Figure 5.30 and slightly wider than the ones of the unirradiated pCVD sample *Poly-B2*, shown in Figure 5.33. The distributions show a steep rising edge, reaching a maximum between 80 a.u. and 100 a.u.. Above this maximum the distribution is falling, with an additional kink at ∼150 a.u. for the negative bias and a kink at ∼200 a.u. in the case of positive bias. A long tail towards high signals responses can be observed. The different shape compared to the distributions of *Poly-B2* might be caused by the issues when processing the diamond, explained in Section 5.4.1.

(a) At $-1000\,$V.

(b) At $+1000\,$V.
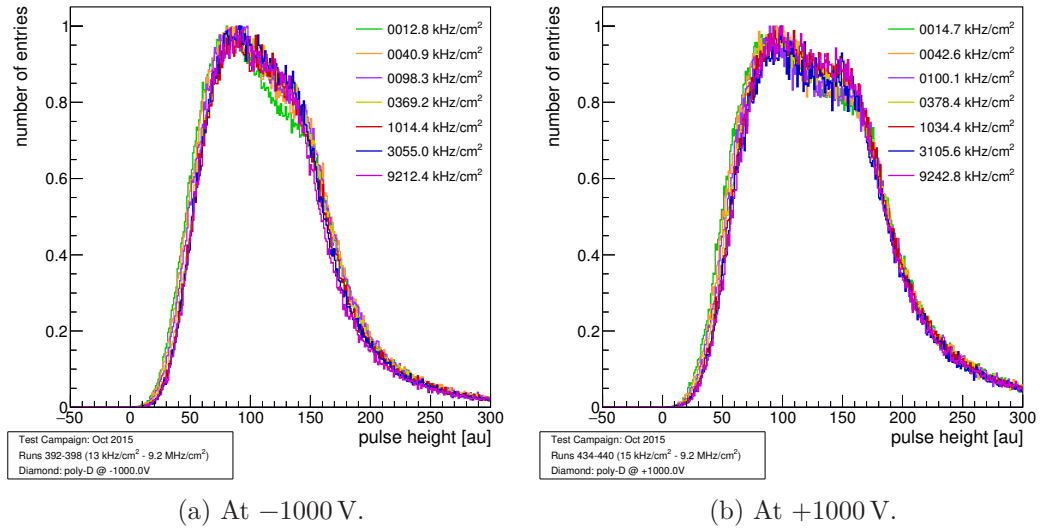
Figure 5.35.: Signal pulse height distributions of the pCVD diamond *Poly-D* after an irradiation with $1 \times 10^{14}\,$n/cm² for bias voltages of $\pm 1000\,$V.

(a) Unscaled.

(b) Positive bias polarity runs rescaled.
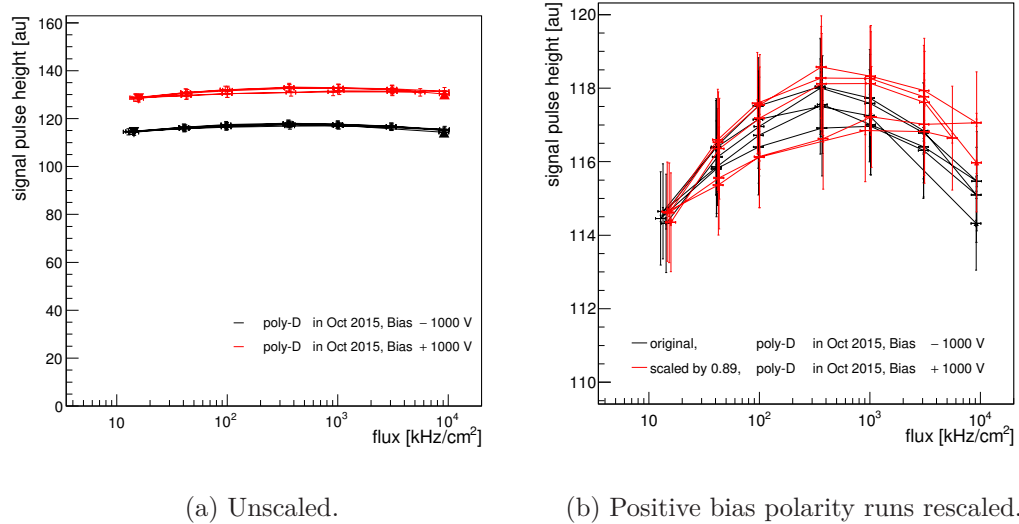
Figure 5.36.: Signal response as a function of particle flux for the pCVD diamond *Poly-D* irradiated to $1 \times 10^{14}\,$p/cm² for positive and negative bias polarity of $\pm 1000\,$V. In Figure (b) the runs for positive polarity are scaled by a factor such the mean pulse height below $80\,$kHz/cm² agree for both bias polarities.

In Figure 5.36 the signal responses as a function of particle flux are shown for the full scans where *Poly-D* was biased with ±1000 V. In Figure 5.36 (a) the two scans are shown without rescaling. The difference in pulse height for positive and negative bias polarity are caused by the different amplifier gains for positive and negative signals. The full spread of the mean pulse height is 4 a.u., corresponding to less than 3.5 %. No decrease between lowest and highest particle flux can be observed. In Figure 5.36 (b) the data of the positive bias polarity is rescaled by 0.89, similar to the scaling factors of the scans before. The shape for positive and negative bias polarity is similar, but slight difference can be observed for the highest particle fluxes.

In Figures 5.37 (a) and 5.37 (b) the mean signal responses for both polarities are shown in separately. The green error bars correspond to the purely statistical error, while the blue error bars correspond to the summed error of statistical and reproducibility error. The signal response increases with particle flux, reaching a maximum around $\sim$350 kHz/cm^2. Above this particle flux the signal response decreases. This decrease is a little more pronounced for a bias of $-$1000 V. In the comparison of the measurements at high particle fluxes with the ones at the lowest particle flux, no signal decrease with respect to the lowest particle flux can be measure for this sample at positive and negative polarity.

For positive bias voltage a slight hysteresis effect can be observed. For each particle flux the signal response for the measurements during the flux-down scans are higher than the ones of the flux-up scans. For a particle flux of $\sim$350 kHz/cm^2 maximum difference of

(a) At $-$1000 V.

(b) At $+$1000 V.
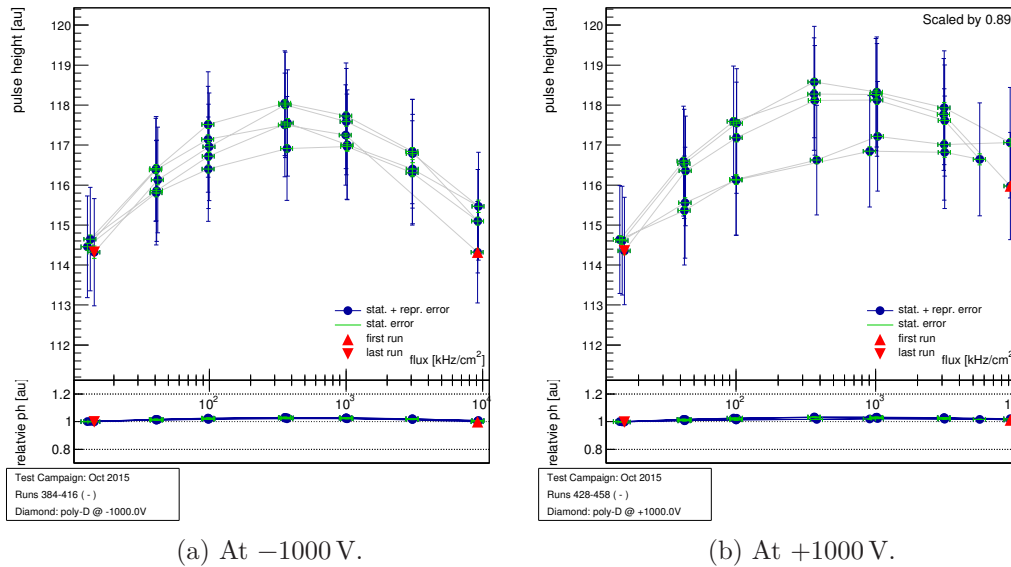
Figure 5.37.: Mean signal response of *Poly-D* unirradiated biased with ±1000 V: The positive runs are scaled by 0.89, such that the means for all runs below 80 kHz/cm^2 are the same for positive and negative bias polarity.

(a) Sorted by scan direction.

(b) Hysteresis.
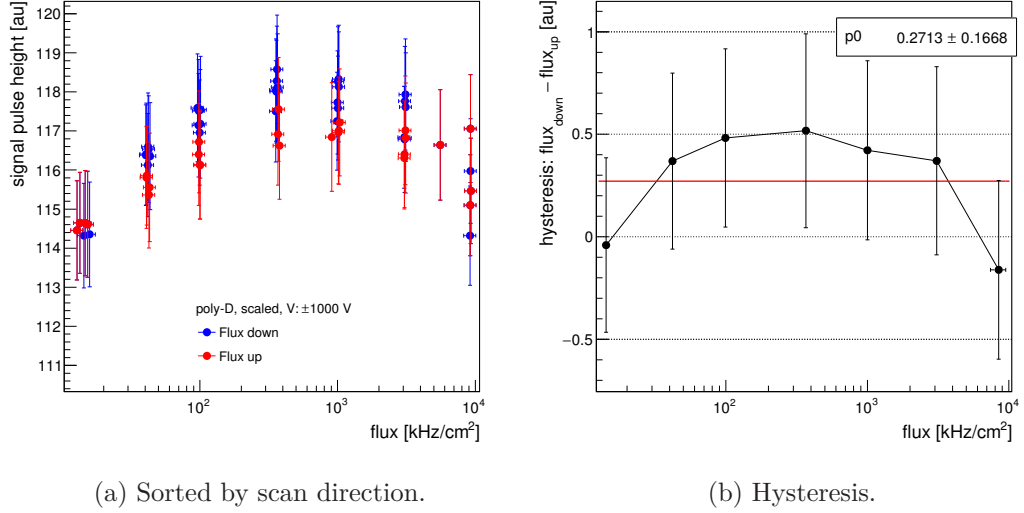
Figure 5.38.: Mean signal response for the pCVD sample *Poly-D* after an irradiation to 1×10^{14} n/cm^2. The positive runs are scaled with a fixed factor such that the mean pulse heights for the runs below 80 kHz/cm^2 agree with the same mean of negative bias polarity.

1.5 a.u. can be observed, corresponding to a relative difference of 1.3%. This hysteresis effect is visualized in Figure 5.38. The two scans of positive and negative polarity are combined. In Figure 5.38 (a) the measurements during the flux-up scans are highlighted in red, while the measurements of the flux-scan downs scans are highlighted in blue. The trend that the flux-down scans have higher signal responses is seen in this distribution as well. For each particle flux all measurements performed during a flux-up(down) scan are used to calculate the weighted mean signal response at this particle flux. The difference for both scan directions is then used as an indicator for the hysteresis. This difference as a function of particle flux is shown in Figure 5.38 (b). A constant fit is performed in order to check the agreement with the hypothesis that no hysteresis can be observed. The difference is zero at the lowest particle flux and increases to a maximum of 0.52 ± 0.45 a.u. at ~350 kHz/cm^2 and decreases for higher particle fluxes reaching -0.15 ± 0.45 a.u. at the highest particle flux. The constant fit results in an offset of 0.27 ± 0.17 a.u., which corresponds to a $1.62 \times \sigma$ deviation from zero. This offset is mainly caused by the measurements at positive bias polarity which deviates by 1.55 sigma on its own.

No signal decrease with respect to the lowest particle flux can be measure for this sample at positive and negative polarity. The signal response is increasing when the particle flux is increased. The highest signal response is measured at a particle flux of about 350 kHz/cm^2, a slight indication for a hysteresis effect was observed, mainly caused by the measurements at positive polarity. This hysteresis is within the errors of the original publications [33] and therefore are consistent with this publication.

5.4.6.3. Results of the irradiated ᴘCVD Diamond Pad Detector *Poly-B2*

These tests were performed in the October 2015 beam test campaign after the irradiation to $5 \times 10^{14}\,\mathrm{n/cm^2}$.

The pulse height distributions for positive and negative bias voltage of $\pm 1000\,\mathrm{V}$ are shown in Figure 5.39. It can be seen that the distributions for each polarity are over-lapping and only small difference in the long tail can be observed. In comparison the distributions of the unirradiated diamond these distributions are narrower indicating that the ᴘCVD material becomes more homogeneous with irradiation. Slight differences in the shapes of the distributions for positive and negative polarity can be observed. This could indicate differences in the collection of electrons and holes.

Figure 5.40 (a) shows the original and the rescaled signal response as a function of particle flux for the scans at positive and negative bias of $\pm 1000\,\mathrm{V}$. For Figure 5.32 a scaling factor of 0.96 was applied to the positive bias polarity run. No decrease of the signal response with increasing particle flux can be observed for fluxes up to $10\,\mathrm{MHz/cm^2}$ in both polarities. All measurements are within a range of $3.2\,\%$. If the first measurement at $-1000\,\mathrm{V}$ is ignored all measurements are within $2.5\,\%$.. In Figure 5.41 the two scans are shown separate. It can be observed that the signal for the first flux-down and the following flux-up scan are slightly reduced compared to the other flux-up and flux-down scans, this effect cannot be seen in case of positive polarity. This might be an indication that the detector was not yet fully pumped and therefore not operating in a stable regime. For positive polarity the measurements at each particle flux are in agreement with its purely statistical errors when flux-up and flux-down measurements considered

(a) At $-1000\,\mathrm{V}$.　　　　　　　　(b) At $+1000\,\mathrm{V}$
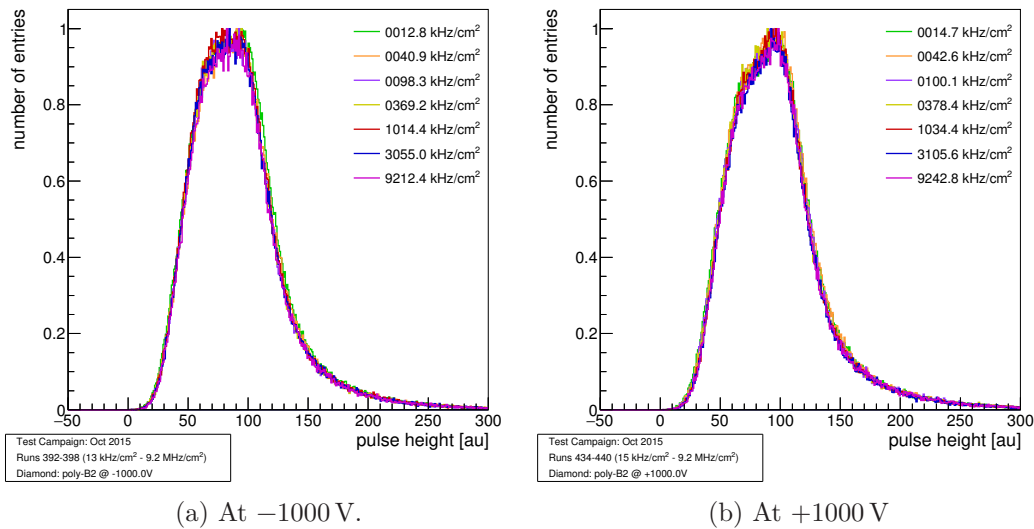
Figure 5.39.: Overlays of the pulse height distributions of one flux-down of the ᴘCVD diamond *Poly-B2* irradiated to $5 \times 10^{14}\,\mathrm{p\ /cm^2}$ biased with $\pm 1000\,\mathrm{V}$.

(a) Unscaled.

(b) Positive bias polarity runs rescaled.
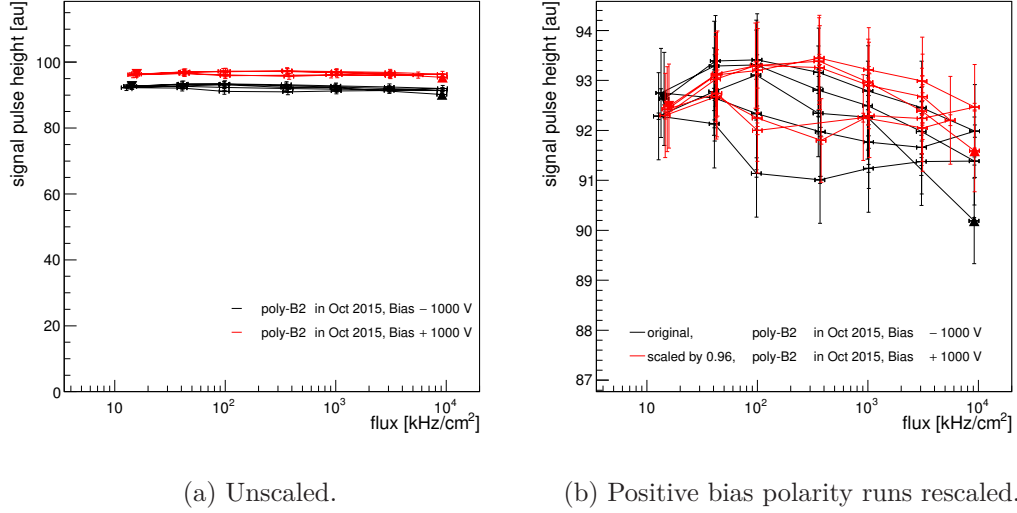
Figure 5.40.: Signal response as a function of particle flux for the pCVD sample *Poly-B2* after an irradiation to $5 \times 10^{14}\,\mathrm{n/cm^2}$ biased with $\pm 1000\,\mathrm{V}$. The errors are the combined statistical and reproducibility errors. In Figure (b) the positive runs are scaled in such a way that the means for all runs below $80\,\mathrm{kHz/cm^2}$ are the same for positive and negative bias polarity.

separate. In both cases a small hysteresis effect can be observed, similar to the one seen for the irradiated pCVD diamond *Poly-D*. The maximum difference of $1.5\,\mathrm{a.u.}$ between flux-down and flux-up measurements can be found at a particle flux of $\sim 350\,\mathrm{kHz/cm^2}$ for the run at positive bias voltage. This corresponds to a relative difference of $1.6\,\%$.

In Figure 5.42 the two scans are combined and each measurement is categorized as a flux-up or a flux-down measurement. In Figure 5.42 (a) the measurements performed during the flux-down scans are colored in blue, while the measurements performed during the flux-up scan are highlighted in red. A higher signal response for the flux-down scan measurements can be observed compared to the measurements performed during the flux-up scan. For each particle flux a weighted mean of all flux-up and flux-down scan measurements is calculated and the difference of these two is shown in Figure 5.42 (b). At the lowest particle flux the difference is close to zero, but at the highest particle flux a difference of $-0.2\,\mathrm{a.u.}$ can be observed. This difference is shifted to negative by the first measurement point of the $-1000\,\mathrm{V}$ bias voltage scan. Being the first measurement it is only associated to a flux-down and not a flux-up scan. Excluding that point the difference is zero. With the constant fit an offset of $0.315 \pm 0.108\,\mathrm{a.u.}$ was found. This results in a 2.9σ deviation from zero. As the errors on the reproducibility are based on the assumption that no differences can be observed for particle fluxes below $80\,\mathrm{kHz/cm^2}$, these errors are over-estimated rather than under-estimated and this hysteresis can be seen as a lower limit. For a better understanding of the observed effect the reproducibility error needs to be decreased and more studies are needed.

(a) At −1000 V.

(b) At +1000 V.
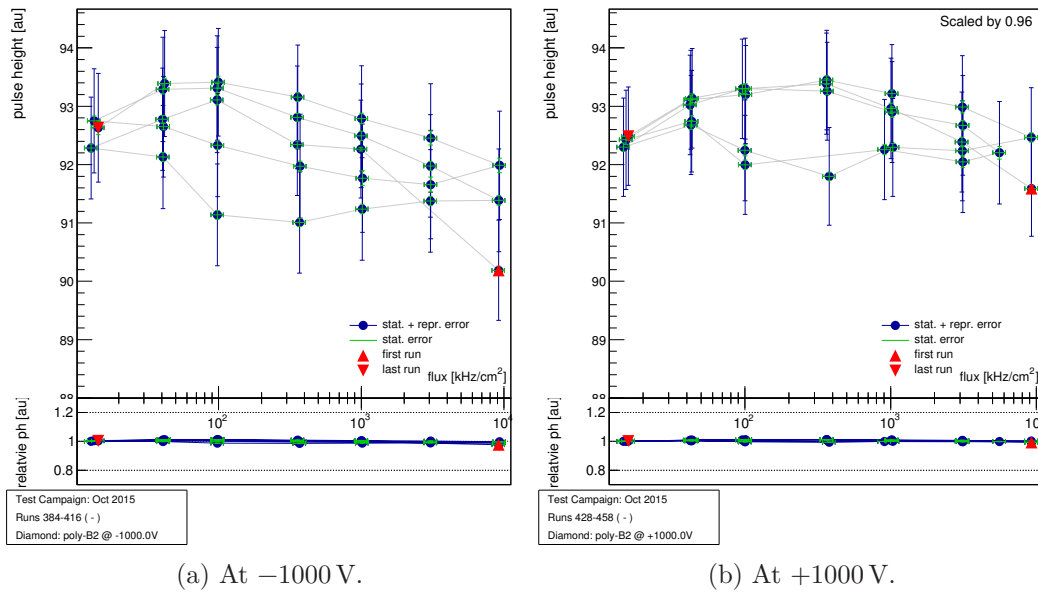
Figure 5.41.: Signal response as a function of particle flux for the pCVD sample *Poly-B2* after an irradiation to $5 \times 10^{14}\,\mathrm{n/cm^2}$ biased with $\pm 1000\,\mathrm{V}$: The positive runs are scaled in such a way that the means for all runs below $80\,\mathrm{kHz/cm^2}$ are the same for positive and negative bias polarity. The purely statistical error is shown in green and the combined error, adding the reproducibility errors, is shown in blue. The positive polarity scan is rescaled by a factor 0.96 in order to correct for the amplifier gain differences for positive and negative signals.

(a) Sorted by scan direction.

(b) Hysteresis.
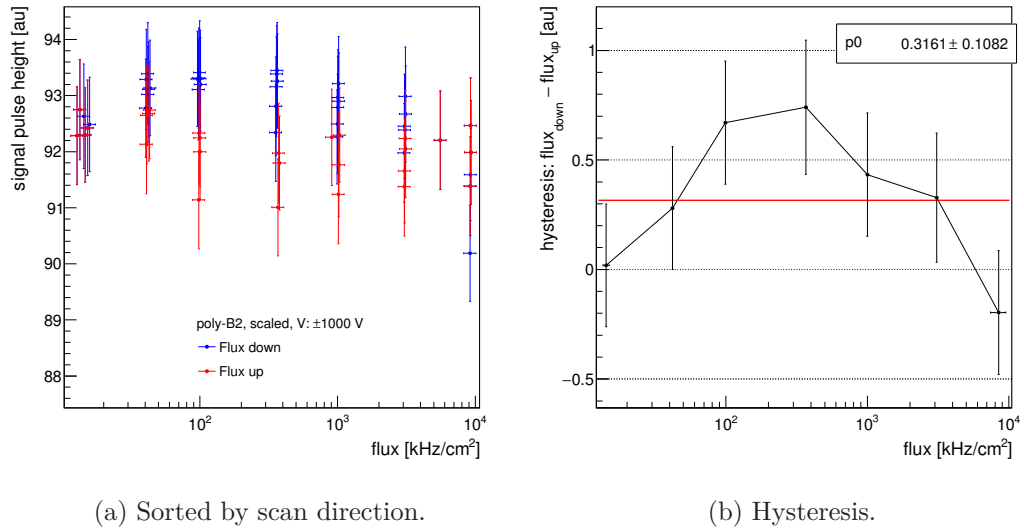
Figure 5.42.: Mean signal response for the pCVD sample *Poly-B2* after a irradiation to 5×10^{14} n/cm^2 for positive and negative bias polarity of ± 1000 V combined and sorted by flux-up and flux-down scans. The positive runs are scaled with a fixed factor such that the mean pulse heights for the runs below 80 kHz/cm^2 agree with the same mean of negative bias polarity.

5.4.7. The Signal Response as a Function of Predicted Hit Position

As the upgraded setup provides tracking it is possible to analyze the signal response as the function of the position of the crossing particle. A study of how homogeneous the CVD diamond material is can be performed. In Figure 5.43 the signal response for two runs at the highest particle flux are shown for the scCVD diamond *S129* and the irradiated pCVD diamond *Poly-B2*. As the scCVD diamond material is a single crystal it is homogeneous and the signal response is flat in the analyzed region. In the signal response of the pCVD diamond regions with high and low signal responses can be observed. In order to understand the cause of the observed structures more detailed studies are needed. The errors on the predicted hit position needs to be understood and comparison between different particle fluxes is needed. This may allow an association of the observed structures to effects occurred in the diamond.

5.5. Conclusion and Outlook

The pulse height dependence on the particle flux observed in the PLT Pilot Run was the starting point for a major beam test campaign to understand this issue. In several beam tests the pulse height dependence on incident particle flux was studied. The first results for pad diamond detectors presented in [33] suggest that pCVD diamond pad detectors

(a) *S129* biased at −500 V.

(b) *Poly-B2* biased at −1000 V.
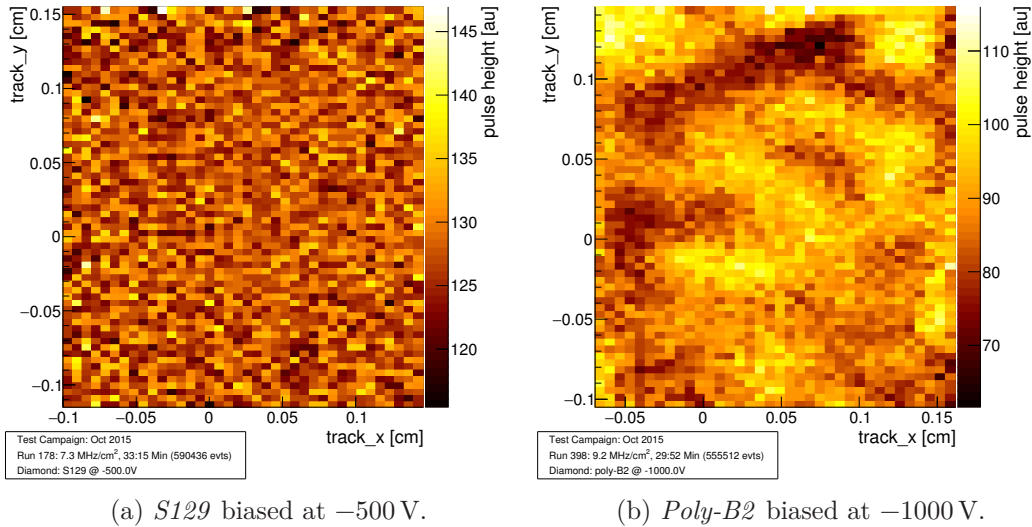
Figure 5.43.: Signal response as a function of the predicted hit position for the unirradiated scCVD diamond *S129* and the irradiated pCVD diamond *Poly-B2*.

do not show a pulse height dependence up to at least $300 \, \text{kHz/cm}^2$ and irradiation levels of $5 \times 10^{13} \, \text{neutrons/cm}^2$.

In order to verify these results at higher particle fluxes, an upgrade of the original setup was developed in 2015. With the upgraded setup it was possible to test pCVD diamond pad detectors at particle fluxes of up to $9.2 \, \text{MHz/cm}^2$. The tested diamonds, irradiated to $1 \times 10^{14} \, \text{n/cm}^2$ and $5 \times 10^{14} \, \text{n/cm}^2$ did not show a decrease in the signal response when the particle flux is increased. This validates the statement of the publication up to a 30 times higher particle flux and to an 10 times higher radiation level. For both irradiated pCVD diamonds a slight hysteresis of the order of $1 \, \%$ to $2 \, \%$ may be observed. The combination of the hysteresis measurements for both irradiated pCVD samples results in an 3.3 sigma deviation from zero. In addition the signal response at particle fluxes of several $100 \, \text{kHz/cm}^2$ is slightly increased. In order to understand these effects in more detail additional studies are required. A signal difference of $4 \, \%$ to $10 \, \%$ was observed between positive and negative bias polarity, this effect was associated with differences in gain of the amplifier for positive and negative signals and is most likely not a diamond material related property.

The signal reduction with increasing particle flux measured for the scCVD diamond of the PLT pilot run [172] and the measured polarization effect in pCVD diamonds of the CMS BCM seem to be an effect caused by manufacturing process related issues and cannot be generalized to be intrinsic properties of all CVD diamond sensors.

After these measurements for pad detectors the next step is the validation of this result for diamond pixel detectors. The new setup is prepared for testing pixel detectors with low pixel thresholds. The first devices, irradiated up to $5 \times 10^{14} \, \text{n/cm}^2$, have recently

been tested. Testing pixel detectors with the second generation of the CMS pixel ROC the internal threshold of each pixel is reduced from 3500 e to 1500 e, compared to the data taken with the CMS PLT pilot run. With the third generation of the CMS pixel ROC the threshold will be further reduced. The upgraded setup is already prepared for testing these devices.

These presented studies are continuing in order to validate that pCVD diamonds can be operated in the radiation environment expected at HL-LHC and to understand the cause of the observed decrease in scCVD diamond detectors. In order to study the slight hysteresis in more detail the measurement program needs to be extended by scans with random order of the particle fluxes and the reproducibility error needs to be decreased. In the coming years tests with higher particle fluxes, higher radiation levels with different metalization and cleaning methods and tests of diamonds from other suppliers are planned. The upgraded setup is a major step on the way towards a compact, fast to use setup. For the validation of the measurements at higher particle fluxes a new beam line which is capable to deliver a constant beam and the required fluxes is needed as with particle fluxes of $10\,\mathrm{MHz/cm^2}$ the limit in the $\pi M1$ beam line is reached.

5.5.1. Proposed Improvements to the Setup

During the operation of the beam telescope in 2015 several ideas were developed to further improve the setup. A short overview of suggested changes is given in this section.

In order to reduce the setup time further, a specialized Trigger Unit integrating the full trigger logic into one single module was proposed during the design of the telescope and will replace the hand-built logic in the 2016 beam test campaigns [173].

The timing correction, explained in Section 5.2.2.1, was required as the external trigger input of the DRS4 Evaluation Board has a limited timing resolution due to differences in internal signal propagation times. This effect can be avoided in future beam tests by digitizing the actual trigger signal on a separate channel and measuring the peak time with respect to that channel. As all channels of the DRS4 Evaluation Board were already used, this was not an option during the beam test campaigns in 2015.

A VME-based readout system with a CAEN 1742 digitizer board is under development. This system will maximize the readout speed and will be capable of digitizing up to 32 channels. Therefore additional signals can be added to the readout. By digitizing the scintillator signal and the cyclotron clock it will be possible to use the relative timing for particle identification.

The trigger ambiguity, described in Section 5.3.1.7, can be addressed in upcoming beam tests by running the DTB clock with the cyclotron's frequency of 50.6 MHz. First tests indicate that stable operations of the ROCs with an increased clock speed are possible.

A new frame was designed during the past year. This frame will combine the whole setup for easier installation and will reduce the setup time. In addition the material budget of the telescope can be reduced as the detectors will not need separate light shielding. This might improve the resolution of the telescope as multiple scattering will be reduced.

6. Summary and Outlook

In order to continue the search for new particles and to find answers to fundamental questions in particle physics, a major upgrade of the LHC is planned in the end of the next decade. With the HL-LHC program the total number of collisions will increase by a factor of ten which results in a very harsh environment in the experiments. Therefore the requirements to each detector system will be very challenging. The highest particle fluence occurs in the inner most tracking layers of the experiments. After the expected particle fluences for these layers no sensor technology is available which fulfill these requirements. Therefore new sensor technologies need to be developed which are capable to work in these conditions. In this thesis diamond was investigated as a such a radiation tolerant sensor material with the focus on the construction of diamond based pixel detectors for the inner-most tracking layers of HL-LHC experiments.

The radiation tolerance of the diamond material was tested in a radiation campaign with $800\,\mathrm{MeV}$ protons. The results of this radiation campaign were presented in Chapter 3. The corresponding damage constant for this type of radiation was extracted for scCVD and pCVD diamond sensors separately. The two measured damage constants are in agreement within the uncertainties, confirming that the damage constant is an intrinsic material property and is valid for all kinds of CVD diamond materials. In this radiation campaign one scCVD diamond has been irradiated up to $7.8 \times 10^{15}\,\mathrm{p/cm^2}$ and pCVD diamonds exceeding $1 \times 10^{16}\,\mathrm{p/cm^2}$. With a radiation fluence of $1.2 \times 10^{16}\,\mathrm{p/cm^2}$ one pCVD sample was irradiated to the expected particle fluence in the inner most tracking layers of HL-LHC experiments at the full integrated luminosity of 3000/fb. For this sample a mean signal response of approximately $1900\,\mathrm{e}$ and a most probable response of approximately $1650\,\mathrm{e}$ was measured using a strip detector configuration. This corresponds to a SNRs of 23.5 for the mean signal response and 20.5 for most probable signal response. The residual distribution of this detector has been measured to be a convolution of two Gaussian distributions with the same mean and widths of $10\,\mathrm{\mu m}$ and $3.6\,\mathrm{\mu m}$ respectively for a strip detector with a $50\,\mathrm{\mu m}$ strip pitch. This shows the capabilities of diamond as a radiation hard tracking detector.

In this thesis the results of the first prototypes of a 3D detector based on scCVD and pCVD diamonds were presented in Chapter 4. To demonstrate the feasibility of the 3D detector concept using diamond sensors, a scCVD diamond was used, as the charge collection properties of scCVD material are well understood. With a femto-second laser an array of conductive electrodes was formed within the bulk of the diamond material. In the tests with a high energy beam the charge collection of the 3D scCVD diamond detector

was compared with the charge collection of a planar strip detector on the same diamond. The 3D detector reached full charge collection at a bias voltage of 25 V, while the planar detector geometry required a minimum bias of >400 V. The full power of 3D detector concept using diamond sensors was shown the first time by using a 3D detector based on a pCVD diamond. This 3D detector at bias voltage of 75 V collects more than 1.8 times the charge of an adjacent planar detector build on the same substrate, biased at 500 V. Even when the planar detector is biased with 1000 V, corresponding to an electric field of ∼2 V/µm, the charge collection is still 50 % lower than the one of the 3D detector. The effective CCD in this 3D detector is the highest CCD ever measured in beam test using pCVD diamond sensors with a thickness of about 500 µm. This shows that using the 3D geometry will increase the charge collection for trap dominated sensor materials, such as irradiated sensors. In order to use this technique at larger scales the yield in electrode formation needs to be further increased and techniques to produce a pixelated 3D detector need to be developed.

The results of the recent publications on the signal dependence of CVD diamond detectors on particle flux led to a systematic study of this effect. As described in Chapter 5, in several beam tests unirradiated and irradiated CVD diamonds were tested at particle fluxes of more than $9\,\text{MHz/cm}^2$. The performed measurements show that the signal response of pCVD diamond detectors is flat within 1 % for particle fluxes up to at least $9\,\text{MHz/cm}^2$ and radiation levels of $5 \times 10^{14}/\text{cm}^2$. This validates the statement of the first publication [33] up to a 30 times higher particle flux and to a ten time higher radiation level. This shows that the recently observed dependency of the signal on the particle flux is not a barrier in the construction of tracking detectors for the experiments in the HL-LHC, because the measurements presented in this thesis indicate that the effect is not a universal diamond property. The measurements suggest that this dependency can be avoided by using high quality pCVD diamond sensor material.

For large-scale applications, such as a layer of pixelated diamond detectors, only pCVD diamond sensor material is a potential candidate as the size of scCVD diamonds is limited. In comparison to scCVD diamond material the MFP in that material is reduced, resulting in a lower charge collection for pCVD diamond sensor material. To further pursue the construction of a working diamond-based pixel detector for HL-LHC environment, it is important to maximize the SNR of the detector. This can be achieved by research in several directions.
The charge collection in the diamond detector assembly can be increased by improving the quality of pCVD diamond material. The research on pCVD diamond material is continuing. The improvement of the material to higher CCD is progressing. In the past five years the CCD of pCVD material was increased from 200 µm to above 300 µm [174]. Recently first wafers with CCDs close to 350 µm have been reported [175].
By using the presented 3D geometry, the drift distances of the charge carriers can be reduced, resulting in higher signals compared to planar detectors and therefore a better SNR.
The noise and the threshold of the pixel electronics need to be further reduced to work

with the lower signals of CVD diamond detectors. Specialized electronics for diamond sensors can take advantage of the low leakage current in comparison with silicon. Already now the newest generation of the pixel ROCs of the CMS and the ATLAS experiment reach noise levels below 200 e and thresholds below 1000 e, when connected to a diamond sensor.

In this thesis the signal response of diamond sensors which were irradiated to the expected fluences in the inner most tracking layers of the HL-LHC experiments were studied and SNRs of above 20 were reached which shows that diamond sensors are a viable sensor technology for the innermost tracking layers of HL-LHC experiments. For the first time it was shown that 3D detectors using scCVD or pCVD diamond sensors achieved similar or better signal responses than planar detectors. Therefore it is possible to overcome the intrinsically smaller signal response of diamond compared to silicon by using the 3D geometry. In addition it was shown that the pulse height dependency of diamond detectors is not an intrinsic property of the diamond and can be avoided by using high quality pCVD diamond material. Achieving these three milestones — the high SNRs after heavy irradiation, the successful realization of the 3D geometry in diamond detectors, and the absence of pulse height dependency on particle flux — pave the way for constructing radiation tolerant pixel detectors based on CVD diamond sensors for future high luminosity particle experiments.

Acknowledgments

6. Summary and Outlook

A. Appendix for Chapter 3

A.1. Names of the Diamonds

Acronym	Name	Type	Thickness [µm]	Size [mm^2]	CCD [µm]	Current Dose [10^{15} p/cm^2]
SINGLE A	*PW205B*	scCVD	466	5×5	466 / 466	7.82 ± 0.51
POLY A	*L114-13*	pCVD	516	10×10	230 / 227	$12.6 \ \pm 1.3$
POLY B	*L107-11*	pCVD	510	10×10	218 / 223	3.50 ± 0.35
POLY C	*L107-10*	pCVD	466	10×10	227 / 241	10.30 ± 0.73

Table A.1.: Conversion table of tested diamonds to real names.

A.2. Example Configuration File for Radiation Hardness Analysis

```
runNo = 17000
Events = 180000
repeaterCardNo = 2
voltage = 500
diamondName = PW205B
currentBegin = 2.0
currentEnd = 1.6


diamondPattern0 = {}
diamondPattern1 = {}


Iter_Size = 500#buffer size


#which sirroco input should we use
dia_input = 1# 0 corresponds to sirocco 4,
             # 1 => sirocco 5 (used for oct2006 and aug2010 runs)


# Channels to Screen
# Diamond Channels
Dia_channel_screen_channels = {1, 2, 55-57, 63-69,  84 - 127}
Dia_channel_noisy_channels = {56}
Dia_channel_not_connected = {0, 56, 65-67, 86- 127}


#D0X_channel_screen_channels = {0,1,127,128,254,255}
#D0Y_channel_screen_channels = {0,1,127,128,129,130,254,255}
#D1X_channel_screen_channels = {0,1,127,128,129,254,255}
#D1Y_channel_screen_channels = {0,1,127,128,254,255}
#D2X_channel_screen_channels = {0,1,128,215,254,255}
#D2Y_channel_screen_channels = {0,1,7,8,127,128,254,255}
#D3X_channel_screen_channels = {0,1,127,254,255}
#D3Y_channel_screen_channels = {0,1,2,3,4,5,6,127,254,255}


#D3X_channel_screen_regions = {128,255}


#For SlidingPedestal (floats)
Si_Pedestal_Hit_Factor = 5
Di_Pedestal_Hit_Factor = 5


#Common Mode Noise (CMN)
D0_CMC = 1
```

```
#For Clustering (floats)
clusterSeedFactors = {16,24,18,20,30,28,24,22,5}
clusterHitFactors = {10,16,14,14,14,14,12,10,3}

#AUTO FID CUT
UseAutoFidCut = 0
nDiamonds = 2

#Silicon Fiducial Cut on Diamond
si_avg_fidcut_xlow = 75.0
si_avg_fidcut_xhigh = 125.0
si_avg_fidcut_ylow = 75.0
si_avg_fidcut_yhigh = 125.0
selectionfidCut0 = {075-125,075-125}
selectionfidCut1 = {165-190,075-125}

#Alignment
#alignment_training_method = 0
#alignment_training_track_fraction = 0.1
alignment_training_track_number = 100000
alignment_training_method = 1# 1 corresponds to cut after n Eventsy
alignment_chi2 = 4

#Telescope geometry (looks like this is the same geom for all runs)
#wide geometry:  edges: 0, 2.40, 9, 18, 20.40
#          (si modules 2.40cm wide, x/y planes spaced 2mm,
#           D0/D1 interspacing 9mm, dia module 1.9cm wide)

Double_t detectorD0Z = 0.725# by definition
Double_t detectorD1Z = 1.625# by definition
Double_t detectorD2Z = 18.725# by definition
Double_t detectorD3Z = 19.625# by definition
Double_t detectorDiaZ = 10.2# by definition


#compact geometry: edges: 0, 2.40, 6, 12, 14.40
#          (si modules 2.40cm wide, x/y planes spaced 2mm,
#           D0/D1 interspacing 9mm, dia module 1.9cm wide)
#Double_t detectorD0Z = 0.725 # by definition
#Double_t detectorD1Z = 1.625 # by definition
#Double_t detectorD2Z = 12.725 # by definition
#Double_t detectorD3Z = 13.625 # by definition
```

```
#Double_t detectorDiaZ = 7.2 # by definition

#Alignment constants
alignment_x_offsets = {0,0,0,0,0}
alignment_y_offsets = {0,0,0,0}
alignment_phi_offsets = {0,0,0,0,0}
alignment_z_offsets = {0,0,0,0,0}

#Resolutions
alignment_x_resolution = {0,0,0,0,0}
alignment_y_resolution = {0,0,0,0}
alignment_phi_resolution = {0,0,0,0,0}
alignment_z_resolution = {0,0,0,0,0}

#How should charge interpolation be done for two hit clusters?
bool eta_correction = true

TransparentAlignment = 1
Comment = ""
lastChannel = 64
firstChannel = 1
```

A.3. Example Beam Configuration H6B

Magnet/Collimator	Reference	Polarity
BEND.041.022	−660.0	S
BEND.049.029	−870.0	S
QUAD.041.033	−427.1	S
QUAD.041.040	−40.4	N
QUAD.041.050	−56.4	N
BEND.041.055	564.0	N
QUAD.041.078	−62.6	N
QUAD.041.096	149.9	N
QUAD.041.106	−211.7	N
BEND.041.124	−625.0	N
SEXT.041.129	300.0	N
TRIM.041.130	0.0	S
BEND.041.132	−609.0	N
QUAD.041.160	149.9	N
QUAD.041.178	62.8	S
SEXT.041.193	300.0	S
TRIM.041.194	0.0	S
TRIM.041.195	0.0	S
QUAD.041.288	149.9	N
QUAD.041.306	−62.6	N
BEND.041.311	566.4	S
QUAD.041.362	214.8	S
BEND.041.375	596.0	S
TRIM.041.385	0.0	S
QUAD.041.397	−193.1	N
QUAD.041.426	−125.7	N
QUAD.041.434	142.7	N
QUAD.041.453	−131.5	N
QUAD.041.461	91.9	N
TRIM.041.473	0.0	S
TRIM.041.474	−120.0	N
BEND.041.516	0.0	N
XCBHV.041.043	±8.0	-
XCBHV.041.047	±30.0	-
XCBHV.041.064	±8.0	-
XCBHV.041.128	±3.0	-
XCBHV.041.129	±14.0	-
XCBHV.041.192	±15.0	-
XCBHV.041.193	±20.0	-
XCBHV.041.384	±2.0	-
XCBHV.041.414	±20.0	-

Table A.2.: Magnet and Collimator settings in the May 2016 beam test

A.4. Logbook of scCVD Diamond *PW205B*

date	step	comment
10/xx/2010	cleaning	Standard cleaning
10/xx/2010	metalized	Cr/Au pad detector
10/13/2010	source tests	
06/15/2011	cleaning	Standard cleaning
06/18/2011	metalized	Cr/Au strip detector/strips on big side
06/30/2011	beam test	tot=0.0×10^{15} p/cm^2
07/25/2011	cleaning	Au & Cr etch + Chromic acid + 1× residual removal
08/xx/2011	irradiation	tot=0.775×10^{15} p/cm^2
08/18/2011	metalized	Cr/Au pad detector
08/19/2011	source tests	
08/21/2011	cleaning	Au & Cr etch + Chromic acid + 1× residual removal +2min O2
10/xx/2011	metalized	Cr/Au strip detector/strips on big side
10/14/2011	beam test	tot=0.775×10^{15} p/cm^2
12/05/2011	cleaning	Au & Cr etch + Chromic acid + 2× residual removal
12/xx/2011	irradiation	tot=2.385×10^{15} p/cm^2
02/14/2012	cleaning	Chromic acid + residual removal + 2min 02
05/31/2012	metalized	Cr/Au pad contacts
05/31/2012	source tests	
06/04/2012	cleaning	Au & Cr etch + Chromic acid + 1× residual removal + 2min O2
08/10/2012	metalized	Cr/Au strip detector/strips on big side
08/15/2012	beam test	tot=2.385×10^{15} p/cm^2
09/17/2012	cleaning	Au & Cr etch + 1× residual removal **NO Chromic acid**
09/xx/2012	irradiation	tot=3.05×10^{15} p/cm^2
10/04/2012	cleaning	Chromic acid + 1× residual removal + 2min O2
10/04/2012	metalized	Cr/Au strip detector, **metalization failed**
10/04/2012	cleaning	Au & Cr etch + 2×Chromic acid + 1× residual removal + 2min O2
10/05/2012	metalized	Cr/Au strip detector/strips on big side
10/09/2012	beam test	tot=3.05×10^{15} p/cm^2
12/04/2012	cleaning	Au & Cr etch + 2×Chromic acid + 1× residual removal
12/xx/2012	irradiation	tot=7.82×10^{15} p/cm^2
10/07/2014	cleaning	Au & Cr etch + 2×Chromic acid + 2× residual removal + 2min O2
10/08/2014	RIE	15min/side remove 0.1-0.3um/side
10/13/2014	metalized	Cr/Au pad detector
10/31/2014	cleaning	2× Au & Cr etch + 2× Chromic acid + 2× residual removal + 2min O2
11/03/2014	problem	residue on surface
11/07/2014	cleaning	Al etch + 2× Chromic acid + 2× residual removal + 10min O2
11/12/2014	Metalized	Cr/Au strip detector/strips on big side
11/26/2014	beam test	tot=7.82×10^{15} p/cm^2

Table A.3.: Logbook of scCVD diamond *PW205B*.

B. Appendix for Chapter 5

B.1. Trigger Logic of the New Telescope Setup
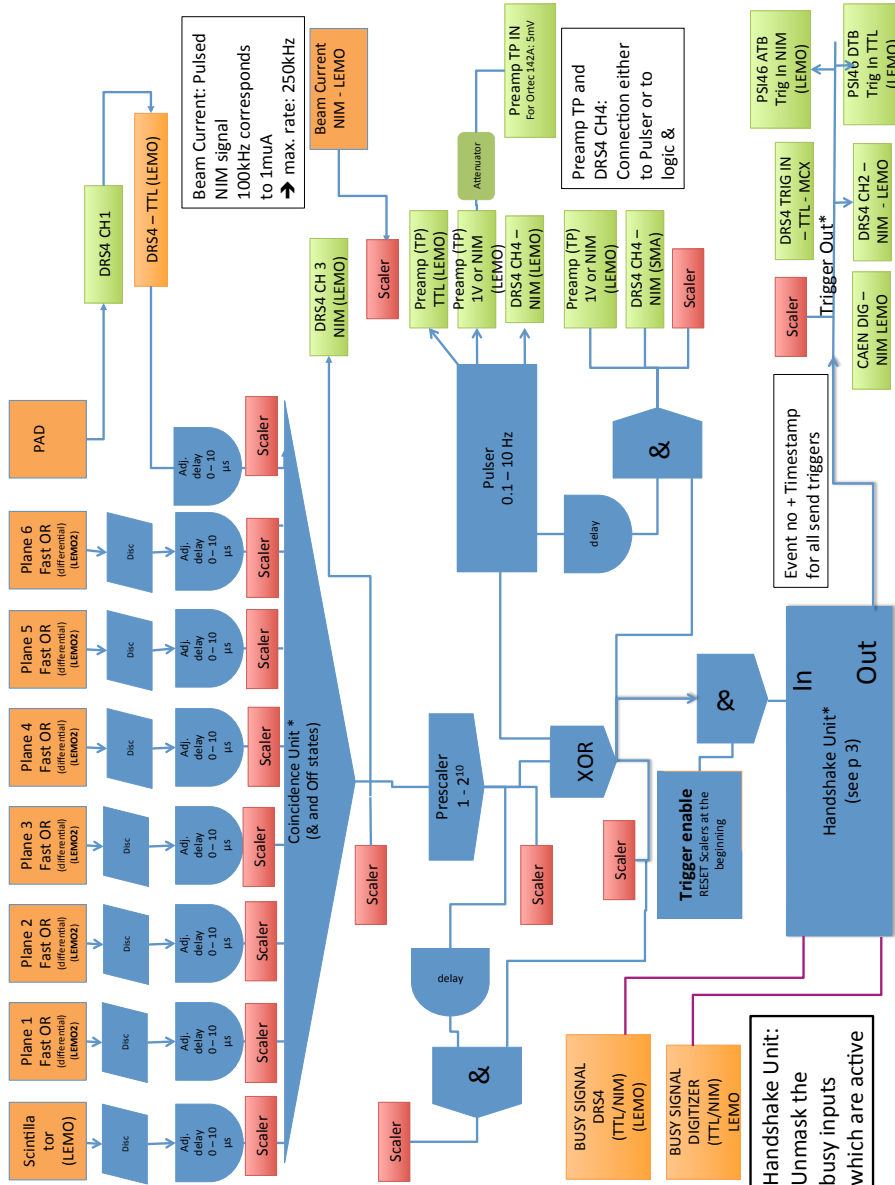
B.2. Example Waveforms
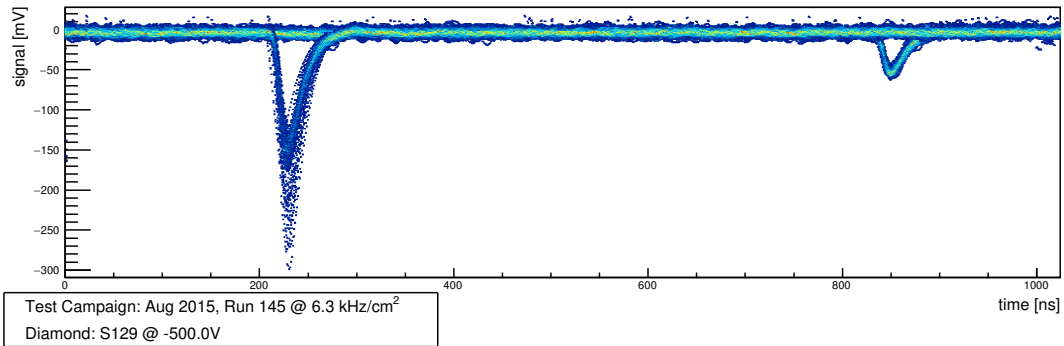
Figure B.1.: Waveforms for *S129* in August 2015, biased at −500 V
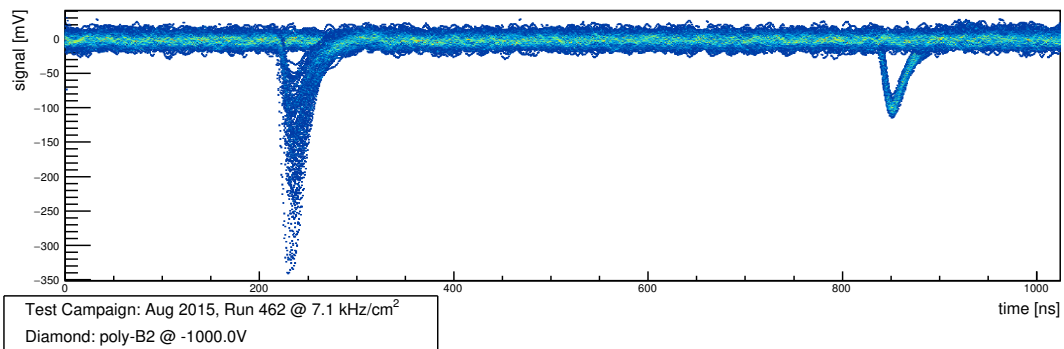
Figure B.2.: Waveforms for *Poly-B2* in August 2015, biased at −1000 V
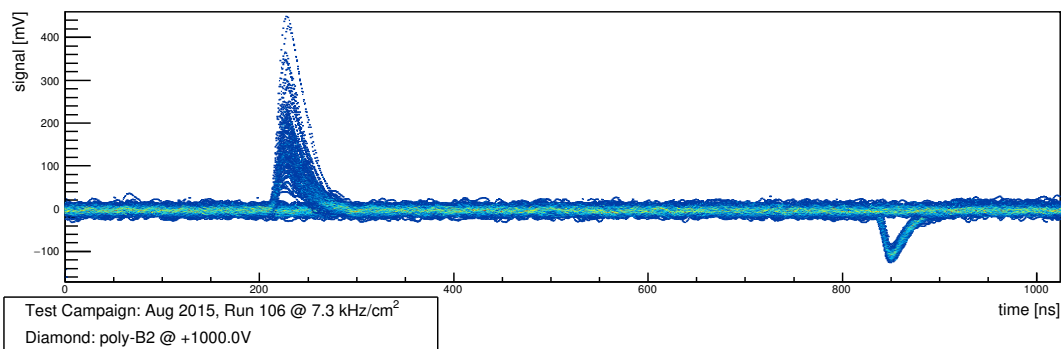
Figure B.3.: Waveforms for *Poly-B2* in August 2015, biased at +1000 V
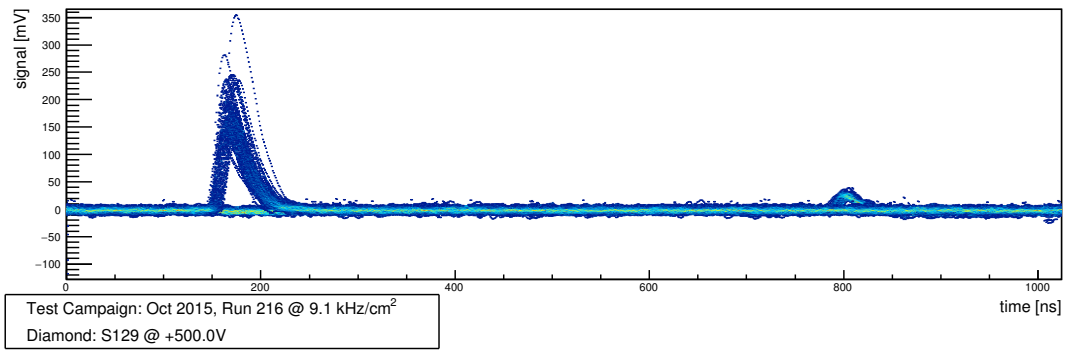
Figure B.4.: Waveforms for *S129* in October 2015, biased at $+500\,\mathrm{V}$
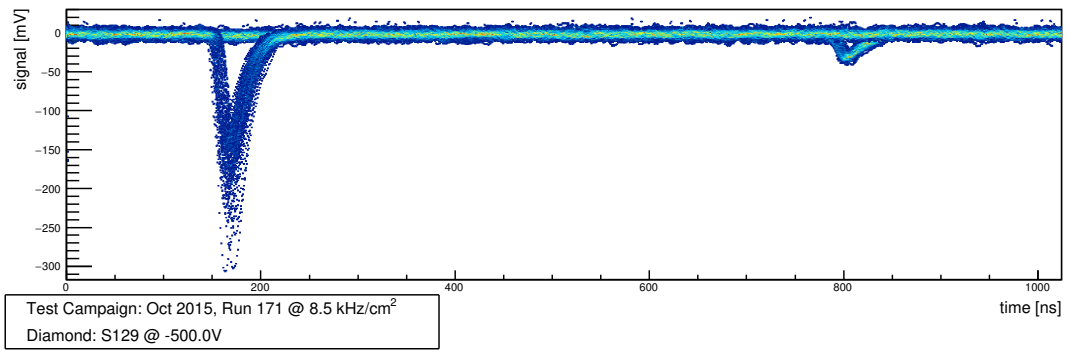
Figure B.5.: Waveforms for *S129* in October 2015, biased at $-500\,\mathrm{V}$
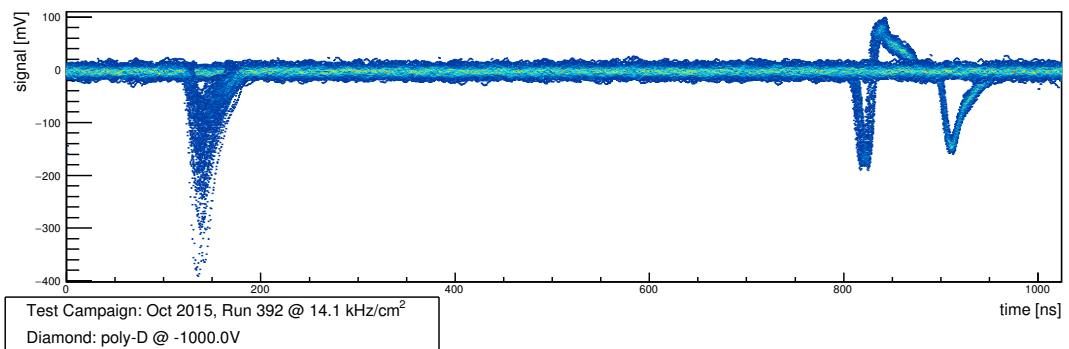
Figure B.6.: Waveforms for *Poly-D* in October 2015, biased at $-1000\,\mathrm{V}$
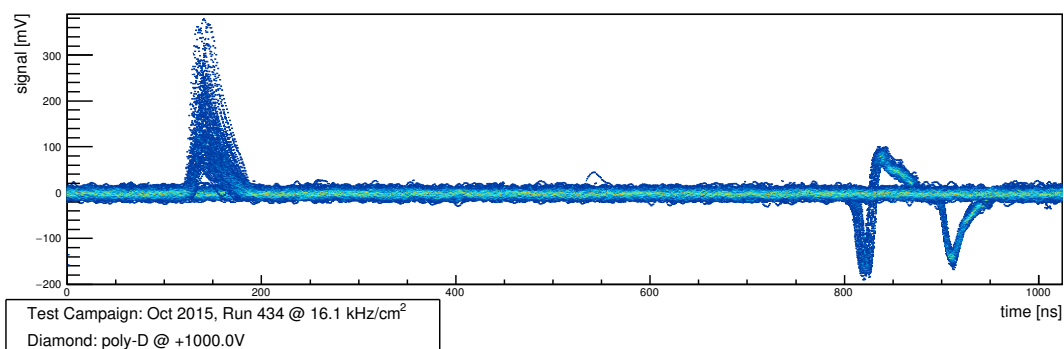
Figure B.7.: Waveforms for *Poly-D* in October 2015, biased at $+1000\,\mathrm{V}$
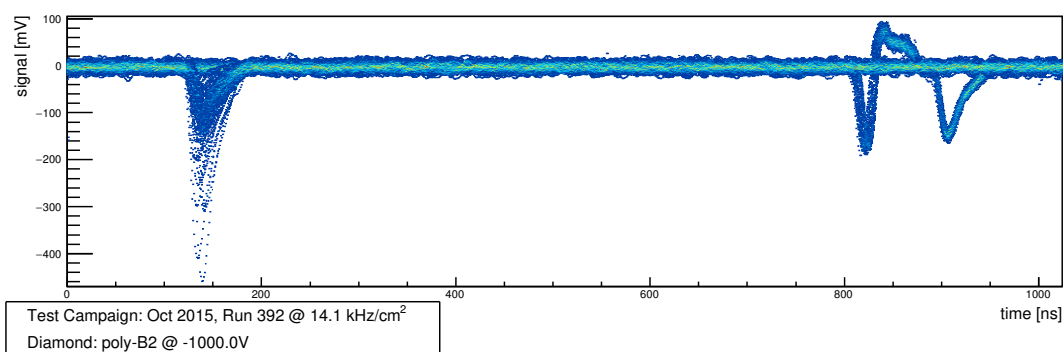
Figure B.8.: Waveforms for *Poly-B2* in October 2015, biased at $-1000\,\mathrm{V}$
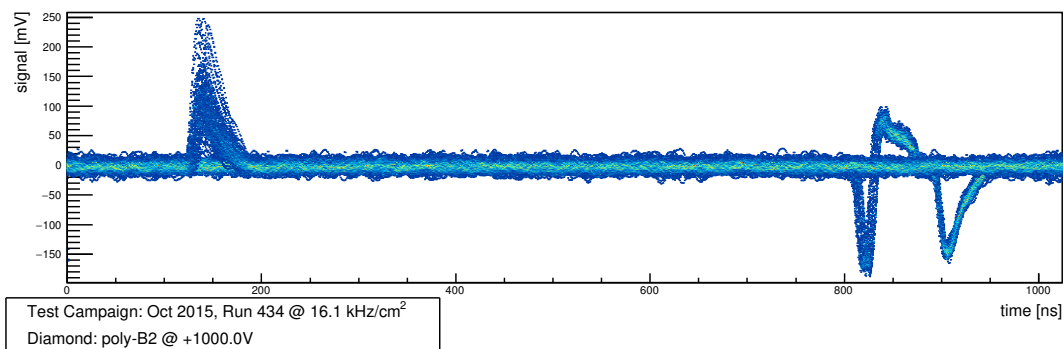
Figure B.9.: Waveforms for *Poly-B2* in October 2015, biased at $+1000\,\mathrm{V}$

B.3. Reproducibility Error for each Rate Scan

For each diamond, each beam test campaign and each bias polarity the distribution for the extraction of the reproducibility error is shown. In each distribution all runs with particle fluxes below $80 \, \text{kHz/cm}^2$ are used. A fit of the distribution with a Gaussian is performed to extract the error.
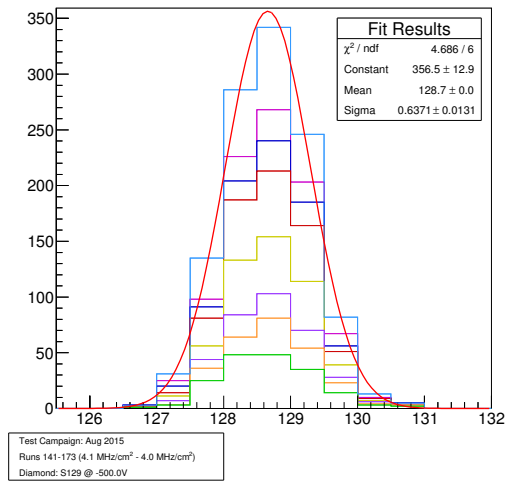
Figure B.10.: Reproducibility error for *S129* in August 2015, biased at $-500 \, \text{V}$

(a) biased at $-500 \, \text{V}$

(b) biased at $+500 \, \text{V}$
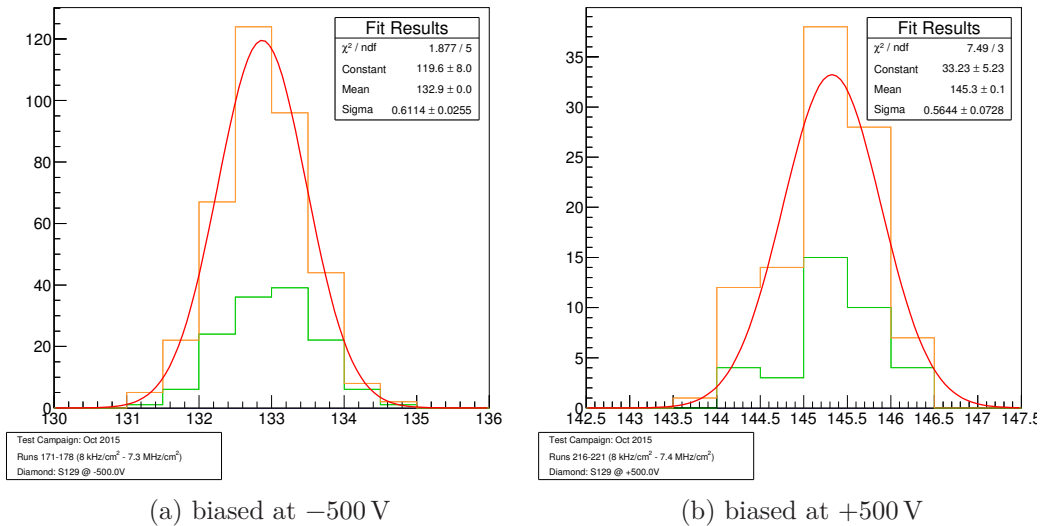
Figure B.11.: Reproducibility error for *S129* in October 2015

(a) biased at $-1000\,\mathrm{V}$ (b) biased at $+1000\,\mathrm{V}$
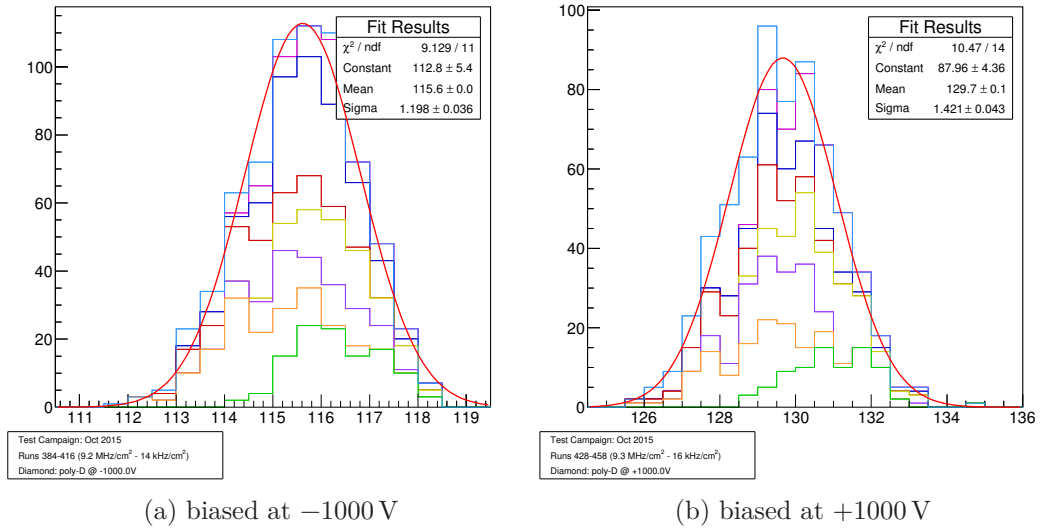
Figure B.12.: Reproducibility error for *Poly-D* in October 2015

(a) biased at $-1000\,\mathrm{V}$ (b) biased at $+1000\,\mathrm{V}$.
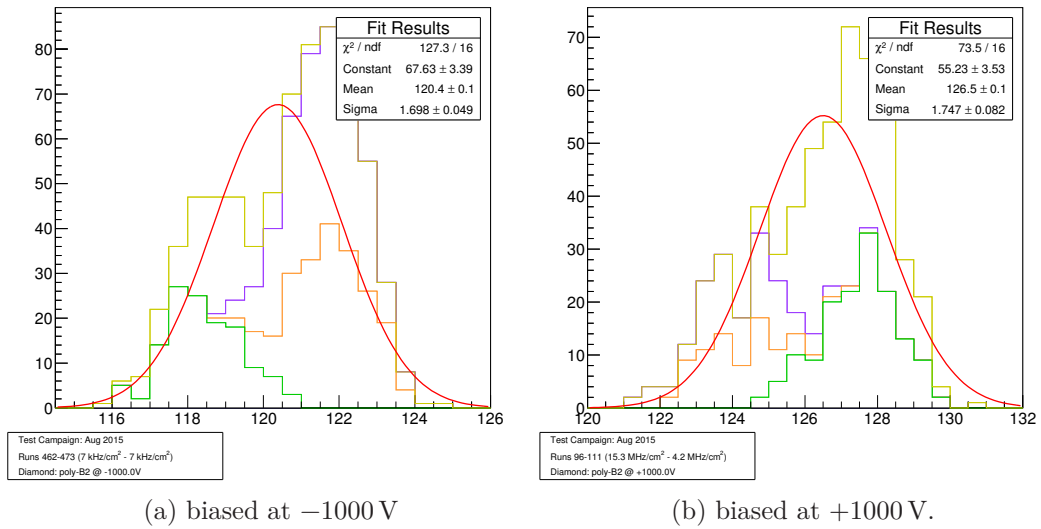
Figure B.13.: Reproducibility error for *Poly-B2* in August 2015

(a) biased at $-1000\,\text{V}$

(b) biased at $+1000\,\text{V}$

Figure B.14.: Reproducibility error for *Poly-B2* in October 2015

Acronyms

ADC	Analog to Digital Converter
ALICE	A Large Ion Collider Experiment
ASIC	Application Specific Integrated Circuit
ATLAS	A Toroidal LHC ApparatuS
BCM	Beam Condition Monitor
BCM1F	BCM1F
BCM1L	BCM1L
BCM2L	BCM2L
BLM	BLM
c.o.m.	centre-of-mass
CCD	Charge Collection Distance
CERN	European Organization for Nuclear Research
CMN	Common Mode Noise
CMS	Compact Muon Solenoid
CVD	Chemical Vapor Deposition
DAC	Digital to Analog Converter
DAQ	Data Aquisition
DBM	Diamond Beam Monitor
DCCD	Dynamic Cluster Column Drain
DSSD	Double Sided Strip Detector
DTB	Digital Testboard
DUT	Device Under Test
ENC	Equivalent Noise Charge
fcc	face-centered cubic
FWHM	Full Width Half Maximum
HAPS	Hybrid Active Pixel Sensors
HIPA	High Intensity Proton Accelearator
HL-LHC	High Luminosity LHC
HPHT	High-Pressure High-Temperature
IBL	Insertable B-Layer
IP	Interaction Point
LANSCE	Los Alamos Neutron Science Center

Acronyms

LEP	Large Electron-Positron Collider
LHC	Large Hadron Collider
LHCb	Large Hadron Collider beauty
LVDS	Low-voltage differential signaling
MAPS	Monolithic Active Pixel Sensors
MC	Monte Carlo
MCA	Multi Channel Analyzer
MCX	Micro Coaxial Connector
MFP	Mean Free Path
MIP	Minimal Ionizing Particle
MP	Most Probable
MPV	Most Probable Value
NIEL	Non Ionizing Energy Loss
NIM	Nuclear Instrumentation Module
OSU	Ohio State University
pCVD	polycrystalline CVD
PLL	Phase Lock Loop
PLT	Pixel-Luminosity-Telescope
PMT	PhotoMultiplier Tube
PSI	Paul Scherrer Institute
RIE	Reactive Ion Etching
RMS	Root Mean Square
ROC	ReadOut Chip
scCVD	single crystalline CVD
SDR	Strip Detector Read-out System
SEM	Scanning Electron Microscope
SLAC	Stanford Linear Accelerator Center
SM	Standard Model
SMA	SubMiniature version A connector
SNR	Signal-to-Noise Ratio
SPS	Super Proton Synchrotron
SUSY	SUperSYmmetry
TID	Total Ionizing Dose
TLU	Trigger Logic Unit
TOF	Time Of Flight
ToT	Time-over-Threshold
TTL	Transistor-transistor logic
UBM	Under Bump Metallization
UCN	Ultra Cold Neutron
VME	Versa Module Eurocard-bus

List of Figures

264

267

List of Tables

271

Bibliography

[1] CERN. ECFA-CERN Workshop on Large Hadron Collider in the LEP Tunnel, Mar 1984. URL `http://cds.cern.ch/record/154938`. 1

[2] S. Chatrchyan, V. Khachatryan, A.M. Sirunyan, et al. Observation of a new boson at a mass of 125 GeV with the CMS experiment at the LHC. *Phys. Lett.*, B716:30–61, 2012. doi: 10.1016/j.physletb.2012.08.021. 1

[3] G. Aad, T. Abajyan, B. Abbott, et al. Observation of a new particle in the search for the Standard Model Higgs boson with the ATLAS detector at the LHC. *Phys. Lett.*, B716: 1–29, 2012. doi: 10.1016/j.physletb.2012.08.020. 1

[4] Peter W. Higgs. Broken Symmetries and the Masses of Gauge Bosons. *Phys. Rev. Lett.*, 13:508–509, 1964. doi: 10.1103/PhysRevLett.13.508. 1

[5] F. Englert and R. Brout. Broken Symmetry and the Mass of Gauge Vector Mesons. *Phys. Rev. Lett.*, 13:321–323, 1964. doi: 10.1103/PhysRevLett.13.321. 1

[6] Oliver Sim Brüning, Paul Collier, P Lebrun, et al. *LHC Design Report.* CERN, Geneva, 2004. URL `https://cds.cern.ch/record/782076`. 2

[7] CERN European Organization for Nuclear Research. Cern accelerating science. online, 2016. URL `http://home.cern/`. 2

[8] J. H. Christenson, J. W. Cronin, V. L. Fitch, and R. Turlay. Evidence for the 2 pi Decay of the k(2)0 Meson. *Phys. Rev. Lett.*, 13:138–140, 1964. doi: 10.1103/PhysRevLett.13.138. 3

[9] Wikimedia Commons. Map of the cern accelerator complex, 2016. URL `https://commons.wikimedia.org/wiki/File:Cern-accelerator-complex.svg`. File: Cern-accelerator-complex.svg. 3, 259

[10] K A Olive, K Agashe, C Amsler, et al. Review of Particle Physics. *Chin. Phys.*, C38: 090001, 2014. doi: 10.1088/1674-1137/38/9/090001. 4, 16, 17, 18, 19, 20, 21, 25, 50, 259

[11] W. J. Stirling. Parton luminosity and cross section plots, 2016. URL `http://www.hep.ph.ic.ac.uk/~wstirlin/plots/plots.html`. 5, 259

[12] CERN. HL-LHC Preliminary Design Report: Deliverable: D1.5. Technical report, CERN, Nov 2014. URL `https://cds.cern.ch/record/1972604`. 6

[13] CERN. LHC/ HL-LHC Plan. online, 02 2016. URL `http://hilumilhc.web.cern.ch/sites/hilumilhc.web.cern.ch/files/HL-LHC-plan-2016-01.png`. 7, 259

[14] Collaboration ATLAS. Letter of Intent for the Phase-II Upgrade of the ATLAS Experiment. Technical Report CERN-LHCC-2012-022. LHCC-I-023, CERN, Geneva, Dec 2012. URL `https://cds.cern.ch/record/1502664`. Draft version for comments. 7

[15] J Butler, D Contardo, M Klute, J Mans, and L Silvestris. Technical Proposal for the Phase-II Upgrade of the CMS Detector. Technical Report CERN-LHCC-2015-010. LHCC-P-008, CERN, Geneva. Geneva, Jun 2015. URL `https://cds.cern.ch/record/2020886`. 7

[16] Ashish Kumar Suny. Near future upgrades of the CMS pixel detector. talk at PIXEL 2014, Sept 2014. URL `https://indico.cern.ch/event/302139/contributions/691616/attachments/570968/786464/Pixel2014_v3.pdf`. 7

[17] Anna Sfyrla, Ricardo Eusebi, Rick Tesarek, et al. Beam Condition Monitoring with Diamonds at CDF. *IEEE Trans. Nucl. Sci.*, 55:328–332, 2008. doi: 10.1109/RTC.2007.4382739,10.1109/TNS.2007.913492. 8

[18] M. Domke, C. Ilgner, S. Kostner, et al. Commissioning of the beam conditions monitor of the LHCb experiment at CERN. In *IEEE Nucl. Sci. Symp. Conf. Rec.*, pages 3306–3307, 2008.

[19] N Bernardino Rodrigues, R Hall-Wilton, W Lange, et al. Fast beam conditions monitor BCM1F for the CMS experiment. *Nuclear Instruments and Methods in Physics Research Section A: Accelerators, Spectrometers, Detectors and Associated Equipment*, 614(3):433 – 438, 2010. ISSN 0168-9002. doi: http://dx.doi.org/10.1016/j.nima.2009.12.056.

[20] V Cindro, D Dobos, I Dolenc, et al. The ATLAS beam conditions monitor. *JINST*, 3: P02004, 2008. 8

[21] Hempel M., Baer T., S. Bart Pedersen, et al. Bunch-by-Bunch Beam Loss Diagnostics with Diamond Detectors at the LHC. *Proceedings, 52nd ICFA Advanced Beam Dynamics Workshop on High-Intensity and High-Brightness Hadron Beams (HB2012)*, 2013. URL `http://accelconf.web.cern.ch/AccelConf/HB2012/index.htm`. 8

[22] H. Kagan and W. Trischuk. *The Snowmass 2013 Proceedings*, chapter 38.8: Diamond Sensors. American Physical Society, 2013. 8, 259

[23] N Bernardino Rodrigues, R Hall-Wilton, W Lange, et al. Fast Beam Conditions Monitoring (BCM1F) for CMS. *Topical Workshop on Electronics for Particle Physics*, 2008. URL `http://cds.cern.ch/record/1158637`. 8

[24] Jessica Lynn Leonard. Performance of New and Upgraded Detectors for Luminosity and Beam Condition Measurement at CMS. *PoS*, EPS-HEP2015:233, 2015. 8

[25] Nathaniel Jay Odell. Measurements of the luminosity and normalised beam-induced background using the CMS Fast Beam Condition Monitor. Technical Report CMS-CR-2012-342, CERN, Geneva, Nov 2012. URL `https://cds.cern.ch/record/1497744`. 9

[26] E. Bartz, J. Doroshenko, V. Halyo, et al. The PLT: A luminosity monitor for CMS based on single-crystal diamond pixel sensors. *Nucl. Instrum. & Meth. B (Proc. Suppl.)*, 197(1): 171 – 174, 2009. ISSN 0920-5632. 9

[27] Steve Schnetzer. Diamond Sensors for Energy Frontier Experiments. *PoS*, Vertex2013:029, 2013. 9

[28] Dean Andrew Hidas. The Pixel Luminosity Telescope: LHC/CMS pilot run. In *PIXEL conference*, 2012. 10

[29] A. Kornmayer. The CMS pixel luminosity telescope. *Nuclear Instruments and Methods in Physics Research Section A: Accelerators, Spectrometers, Detectors and Associated Equipment*, pages –, 2015. ISSN 0168-9002. doi: http://dx.doi.org/10.1016/j.nima.2015.09.104. URL `http://www.sciencedirect.com/science/article/pii/S0168900215011936`. 9

[30] A Gorisek. The ATLAS Beam Condition Monitor Commissioning. *Topical Workshop on Electronics for Particle Physics*, 2008. URL `https://cds.cern.ch/record/1158638`. 11, 259

[31] Kock Kiam Gan. Diamond particle detectors systems in high energy physics. *PoS*, TIPP2014:103, 2015. 11, 12, 259

[32] J Albert, Markus Alex, Gianluca Alimonti, et al. Prototype ATLAS IBL Modules using the FE-I4A Front-End Readout Chip. *JINST*, 7:P11010, 2012. doi: 10.1088/1748-0221/7/11/P11010. 11

[33] R. Wallny. Beam test results of the dependence of signal size on incident particle flux in diamond pixel and pad detectors. *JINST*, 10(07):C07009, 2015. 13, 173, 215, 217, 220, 224, 228

[34] Walter H. Barkas, Wallace Birnbaum, and Frances M. Smith. Mass-Ratio Method Applied to the Measurement of L-Meson Masses and the Energy Balance in Pion Decay. *Phys. Rev.*, 101:778–795, 1956. doi: 10.1103/PhysRev.101.778. 17

[35] H. H. Andersen and J. F. Ziegler. *Hydrogen stopping powers and ranges in all elements.* New York : Pergamon Press, 1977. ISBN 0080216056. Includes bibliographical references. 18

[36] J. Lindhard and M. Scharff. *Range concepts and heavy ion ranges: (Notes on atomic collisions, II).* Mathematisk-fysiske meddelelser. Munksgaard, 1963. 18

[37] Claus Grupen and Boris Schwartz. *Particle detectors.* Cambridge Monographs on Particle Physics, Nuclear Physics and Cosmology. Cambridge University Press, 2008. 19, 25

[38] Wikimedia Commons. Photon absorption coefficient in lead, 2016. URL `https://commons.wikimedia.org/wiki/File:Pb-gamma-xs.svg`. File: Pb-gamma-xs.svg. 21

[39] W.R. Leo. *Techniques for Nuclear and Particle Physics Experiments: A How-to Approach.* Springer, 1994. ISBN 9780387572802. 21

[40] L. Landau. On the energy loss of fast particles by ionization. *J. Phys.(USSR)*, 8:201–205, 1944. 22

[41] Hans Bichsel. Straggling in thin silicon detectors. *Rev. Mod. Phys.*, 60:663–699, Jul 1988. doi: 10.1103/RevModPhys.60.663. URL `http://link.aps.org/doi/10.1103/RevModPhys.60.663`. 22

[42] Stefan Meroli. *Interaction of radiation with matter: from the theory to the measurements.* online, 2013. 22

[43] H. A. Bethe. Molière's theory of multiple scattering. *Phys. Rev.*, 89:1256–1266, Mar 1953. doi: 10.1103/PhysRev.89.1256. URL `http://link.aps.org/doi/10.1103/PhysRev.89.1256`. 22

[44] W. T. Scott. Mean-Value Calculations for Projected Multiple Scattering. *Phys. Rev.*, 85: 245–248, 1952. doi: 10.1103/PhysRev.85.245. 22

[45] Virgil L. Highland. Some Practical Remarks on Multiple Scattering. *Nucl. Instrum. Meth.*, 129:497, 1975. doi: 10.1016/0029-554X(75)90743-0. 23

[46] David Barney. CMS Detector Slice. CMS Collection., Jan 2016. URL `https://cds.cern.ch/record/2120661`. 24, 259

[47] R. L. Gluckstern. Uncertainties in track momentum and direction, due to multiple scattering and measurement errors. *Nucl. Instrum. Meth.*, 24:381–389, 1963. doi: 10.1016/0029-554X(63)90347-1. 25

[48] O. Steinkamp. Experimental methods of particle physics - track reconstruction: introduction. lecture, 2015. URL `http://www.physik.uzh.ch/lectures/empp/15/lectures/empp15_OS_intro.pdf`. 25

[49] Vardan Khachatryan. CMS Tracking Performance Results from early LHC Operation. *Eur. Phys. J.*, C70:1165–1192, 2010. doi: 10.1140/epjc/s10052-010-1491-3. 25

[50] Ashish Kumar. Commissioning of the cms forward pixel detector. Talk at PIXEL 2008, September 2008. URL `https://indico.fnal.gov/contributionDisplay.py?contribId=50&confId=1588`. 26

[51] Katja Klein. The Phase-1 Upgrade of the CMS Pixel Detector. Technical Report CMS-CR-2016-036, CERN, Geneva, Mar 2016. URL `https://cds.cern.ch/record/2140071`. 26

[52] Geoffrey Mullier. The upgraded Pixel Detector of the ATLAS Experiment for Run-II at the Large Hadron Collider. Technical Report ATL-INDET-PROC-2015-013, CERN, Geneva, Nov 2015. URL `https://cds.cern.ch/record/2108892`. 27, 271

[53] Timon Heim. Status and performance of the ATLAS Pixel Detector after 3 years of operation. *Nucl. Instrum. Meth.*, A765:227–231, 2014. doi: 10.1016/j.nima.2014.04.058. 44

[54] M Capeans, G Darbo, K Einsweiller, et al. ATLAS Insertable B-Layer Technical Design Report. Technical Report CERN-LHCC-2010-013. ATLAS-TDR-19, CERN, Geneva, Sep 2010. URL `http://cds.cern.ch/record/1291633`.

[55] A Dominguez, D Abbaneo, K Arndt, et al. CMS Technical Design Report for the Pixel Detector Upgrade. Technical Report CERN-LHCC-2012-016. CMS-TDR-11, CERN, Sep 2012. URL `https://cds.cern.ch/record/1481838`. Additional contacts: Jeffrey Spalding, Fermilab, Jeffrey.Spalding@cern.ch Didier Contardo, Universite Claude Bernard-Lyon I, didier.claude.contardo@cern.ch.

[56] D Kotliński. Status of the cms pixel detector. *Journal of Instrumentation*, 4(03):P03019, 2009. URL `http://stacks.iop.org/1748-0221/4/i=03/a=P03019`. 27, 271

[57] CMS Collaboration. Commissioning and Performance of the CMS Pixel Tracker with Cosmic Ray Muons. *JINST*, 5:T03007, 2010. doi: 10.1088/1748-0221/5/03/T03007. 27, 259

[58] C. W. Fabjan and F. Gianotti. Calorimetry for particle physics. online, Oct 2003. URL `http://lappweb.in2p3.fr/~chefdevi/Detector_reports/Calorimetry/Fabjan.pdf`. 28

[59] W. Trischuk. The ATLAS Beam Conditions Monitor at University of Toronto. online, Oct 2008. URL `http://www.physics.utoronto.ca/~william/bcm/bcm_toronto.html`. 30

[60] Moritz Guthoff. Instrumentation for beam radiation and luminosity measurement in the CMS experiment using novel detector technologies. *Nuclear Instruments and Methods in Physics Research Section A: Accelerators, Spectrometers, Detectors and Associated Equipment*, pages –, 2016. ISSN 0168-9002. doi: http://dx.doi.org/10.1016/j.nima.2016.06.028. URL `http://www.sciencedirect.com/science/article/pii/S0168900216305708`. 31

[61] Douglas Schaefer. The ATLAS Diamond Beam Monitor : Luminosity Detector on the LHC. Technical Report ATL-INDET-PROC-2015-009, CERN, Geneva, Jul 2015. URL `https://cds.cern.ch/record/2034225`. 31, 259

[62] H. Spieler. Semiconductor detector systems. *Ser. Semicond. Sci. Tech.*, 12:1–489, 2005. 32, 33, 35, 37, 40, 41, 42, 43, 64, 69, 259, 260

[63] B. Van Zeghbroeck. Principles of electronic devices. online, `http://ecee.colorado.edu/~bart/book/`, University of Colorado, Department of Electrical, Computer, and Energy Engineering,, 2011. 33

[64] Wikimedia Commons. Pn junction in equilibrium, 2016. URL `https://commons.wikimedia.org/wiki/File:Pn-junction-equilibrium-graph.svg`. File: Pn-junction-equilibrium-graph.svg. 34, 260

[65] F. Hartmann. *Evolution of Silicon Sensor Technology in Particle Physics*. Springer Tracts in Modern Physics. Springer Berlin Heidelberg, 2008. ISBN 9783540250944. 38, 45, 64, 260

[66] Steffen Müller, W Boer, and T Müller. *The Beam Condition Monitor 2 and the Radiation Environment of the CMS Detector at the LHC*. PhD thesis, Karlsruhe U., Karlsruhe, 2011. Presented on 14 Jan 2011. 39

[67] Michael Moll. *Radiation damage in silicon particle detectors: Microscopic defects and macroscopic properties*. PhD thesis, Hamburg U., 1999. URL `http://www-library.desy.de/cgi-bin/showprep.pl?desy-thesis99-040`. 39, 40, 260

[68] S. Zhao. *Characterization of the electrical properties of polycrystalline diamond films*. PhD thesis, Ohio State U., 1994. 41, 86

[69] Manfred Krammer. Detector structures. Lecture, Jan 2010. URL `http://fisica.cab.cnea.gov.ar/particulas/html/icfa/wiki/images/3/32/Krammer02.pdf`. 43, 260

[70] S.I. Parker, C.J. Kenney, and J. Segal. 3D - A proposed new architecture for solid-state radiation detectors. *Nucl. Instrum. & Meth. A*, 395(3):328 – 343, 1997. 45, 115

[71] Wikimedia Commons. Visualisation of a diamond cubic unit cell, 2016. URL `https://upload.wikimedia.org/wikipedia/commons/c/ce/Visualisation_diamond_cubic.svg`. File: Visualisation_diamond_cubic.svg. 47, 260

[72] K. S. Novoselov, A. K. Geim, S. V. Morozov, et al. Electric field effect in atomically thin carbon films. *Science*, 306(5696):666–669, 2004. doi: 10.1126/science.1102896. URL `http://www.sciencemag.org/content/306/5696/666.abstract`. 47

[73] M.P. Pujadó. *Carbon Nanotubes as Platforms for Biosensors with Electrochemical and Electronic Transduction*. Springer Theses. Springer, 2012. ISBN 9783642314216. 47

[74] H. W. Kroto, J. R. Heath, S. C. O'Brien, R. F. Curl, and R. E. Smalley. C60: Buckminsterfullerene. *Nature*, 318(6042):162–163, 11 1985. URL `http://dx.doi.org/10.1038/318162a0`. 47

[75] J M Zazula. On Graphite Transformations at High Temperature and Pressure Induced By Absorption of the LHC Beam. Technical Report LHC-Project-Note-78, CERN, Geneva, Jan 1997. URL `http://cds.cern.ch/record/691793`. 48, 260

[76] Wikimedia Commons. Carbon allotropes, 2016. URL `https://upload.wikimedia.org/wikipedia/commons/3/31/Carbon_allotropes.svg`. File: Carbon_alltripes.svg. 48, 260

[77] J.E. Field. *The Properties of Natural and Synthetic Diamond*. Academic Press, 1992. ISBN 9780122553523. URL `http://onlinelibrary.wiley.com/doi/10.1002/crat.2170280504/abstract`. 48

[78] P.G. Read. *Gemmology*. Butterworth-Heinemann, 1999. ISBN 9780750644112. 48

[79] M.H. Nazare and A.J. Neves. *Part A - Properties of Diamond*. Institution of Engineering and Technology, 2001. ISBN 978-0-85296-785-0. URL `http://app.knovel.com/hotlink/toc/id:kpPGAD0004/properties-growth-applications/properties-growth-applications`. 49

[80] David R. Evans. Microelectronic device fabrication - intrinsic defects in semiconductors. online, 2014. URL `http://web.pdx.edu/~davide/Lecture3.pdf`. 49

[81] M.H. Nazare and A.J. Neves. *Part B - Growth and Doping of Diamond*. Institution of Engineering and Technology, 2001. ISBN 978-0-85296-785-0. URL `http://app.knovel.com/hotlink/toc/id:kpPGAD0004/properties-growth-applications/properties-growth-applications`. 49

[82] L.S. Pan and D.R. Kania. *Diamond: Electronic Properties and Applications*. Electronic Materials: Science & Technology. Springer US, 2013. ISBN 9781461522577. 49, 51, 260

[83] Klaus-Werner Benz and Wolfgang Neumann. *Introduction to crystal growth and characterization*. Wiley, Hoboken, NJ, 2014. URL `http://cds.cern.ch/record/1748578`. 49

[84] Sergei M. Pimenov, Igor I. Vlasov, Andrey A. Khomich, et al. Picosecond-laser-induced structural modifications in the bulk of single-crystal diamond. *Applied Physics A*, 105 (3):673–677, 2011. doi: 10.1007/s00339-011-6645-0. URL `http://dx.doi.org/10.1007/s00339-011-6645-0`. 49

[85] Argonne National Laboratory. Lattice constants and crystal structures of some semiconductors and other materials. online, January 2016. URL `http://7id.xray.aps.anl.gov/calculators/crystal_lattice_parameters.html`. 50

[86] W.M. Haynes. *CRC Handbook of Chemistry and Physics, 93rd Edition*. CRC Handbook of Chemistry and Physics. Taylor & Francis, 2012. ISBN 9781439880494. URL `https://www.crcpress.com/CRC-Handbook-of-Chemistry-and-Physics-93rd-Edition/Haynes/p/book/9781439880494`. 50

[87] Ioffe Institute. New semiconductor materials - characteristics and properties. online, January 2016. URL `http://www.ioffe.ru/SVA/NSM/`. 50

[88] John Fontanella, Richard L. Johnston, Jack H. Colwell, and Carl Andeen. Temperature and pressure variation of the refractive index of diamond. *Appl. Opt.*, 16(11):2949–2951, Nov 1977. doi: 10.1364/AO.16.002949. URL `http://ao.osa.org/abstract.cfm?URI=ao-16-11-2949`. 50

[89] Joohee Kim, Jonghyun Cho, Joungho Kim, et al. High-frequency scalable modeling and analysis of a differential signal through-silicon via. *Components, Packaging and Manufacturing Technology, IEEE Transactions on*, 4(4):697–707, April 2014. ISSN 2156-3950. doi: 10.1109/TCPMT.2013.2239362. 50

[90] G. Eranna. *Crystal Growth and Evaluation of Silicon for VLSI and ULSI*. Taylor & Francis, 2014. ISBN 9781482232813. URL `https://books.google.ch/books?id=bo6ZBQAAQBAJ`. 50

[91] J.V Manca, M Nesladek, M Neelen, et al. High electrical resistivity of CVD-diamond. *Microelectronics Reliability*, 39(2):269 – 273, 1999. ISSN 0026-2714. doi: http://dx.doi.org/10.1016/S0026-2714(98)00225-X. URL `http://www.sciencedirect.com/science/article/pii/S002627149800225X`. 50

[92] Chris J.H. Wort and Richard S. Balmer. Diamond as an electronic material. *Materials Today*, 11(1–2):22 – 28, 2008. ISSN 1369-7021. doi: http://dx.doi.org/10.1016/S1369-7021(07)70349-8. URL `http://www.sciencedirect.com/science/article/pii/S1369702107703498`. 50

[93] H. Pernegger, S. Roe, P. Weilhammer, et al. Charge-carrier properties in synthetic single-crystal diamond measured with the transient-current technique. *Journal of Applied Physics*, 97(7):073704, 2005. 50, 87

[94] H. F. W. Sadrozinski. Applications of silicon detectors. *IEEE Trans. Nucl. Sci.*, 48:933–940, 2001. doi: 10.1109/23.958703. 50

[95] C. Canali, E. Gatti, S.F. Kozlov, et al. Electrical properties and performances of natural diamond nuclear radiation detectors. *Nuclear Instruments and Methods*, 160(1):73 – 77, 1979. ISSN 0029-554X. doi: http://dx.doi.org/10.1016/0029-554X(79)90167-8. URL `http://www.sciencedirect.com/science/article/pii/0029554X79901678`. 50, 54

[96] E. Berdermann and M. Ciobanu. *CVD-Diamond Detectors for Experiments with Hadrons, Nuclei, and Atoms*, pages 227–255. Wiley Series in Materials for Electronic & Opto-electronic Applications. John Wiley & Sons, Ltd, 2009. ISBN 9780470740392. doi: 10.1002/9780470740392.ch10. URL `http://dx.doi.org/10.1002/9780470740392.ch10`. 50

[97] Syed Naeem Ahmed. Solid-state detectors. In Syed Naeem Ahmed, editor, *Physics and Engineering of Radiation Detection (Second Edition)*, pages 259 – 329. Elsevier, second edition edition, 2015. ISBN 978-0-12-801363-2. doi: http://dx.doi.org/10.1016/B978-0-12-801363-2.00005-X. URL `http://www.sciencedirect.com/science/article/pii/B978012801363200005X`. 50

[98] J. Koike, D. M. Parkin, and T. E. Mitchell. Displacement threshold energy for type IIa diamond. *Applied Physics Letters*, 60(12):1450–1452, 1992. doi: http://dx.doi.org/10.1063/1.107267. URL `http://scitation.aip.org/content/aip/journal/apl/60/12/10.1063/1.107267`. 50

[99] A.S. Barnard. *The Diamond Formula: Diamond Synthesis–a Gemmological Perspective*. Butterworth-Heinemann, 2000. ISBN 9780750642446. URL `https://books.google.ch/books?id=kCc80Q4gzSgC`. 49

[100] Hendrik Jansen. *Chemical Vapour Deposition Diamond - Charge Carrier Movement at Low Temperatures and Use in Time-Critical Applications*. PhD thesis, CERN, 2013-09-03. URL `https://inspirehep.net/record/1339815/files/CERN-THESIS-2013-339.pdf`. 51, 260

[101] Freiburg Diamond Materials. CVD diamonds, 2016. URL `http://www.cvd-diamond.com/`. File: http://www.cvd-diamond.com/images/p6.jpg. 51, 260

[102] Jes Asmussen and TimothyA Grotjohn. *Microwave Plasma-Assisted Diamond Film DepositionDeposition*, chapter 7, page Figure 29. CRC Press, 2016/07/12 2002. ISBN 978-0-8247-9577-1. doi: doi:10.1201/9780203910603.ch7. URL `http://dx.doi.org/10.1201/9780203910603.ch7`. 52, 260

[103] University of Bristol. Modelling CVD diamond growth, 2016. URL `http://www.chm.bris.ac.uk/pt/diamond/growthmodel.htm`. 53, 260

[104] Michael Schwander and Knut Partes. A review of diamond synthesis by CVD processes. *Diamond and Related Materials*, 20(9):1287 – 1301, 2011. ISSN 0925-9635. doi: http://dx.doi.org/10.1016/j.diamond.2011.08.005. URL `http://www.sciencedirect.com/science/article/pii/S0925963511002913`. 52

[105] Paul W. May. Diamond thin films: a 21st-century material. *Philosophical Transactions of the Royal Society of London A: Mathematical, Physical and Engineering Sciences*, 358 (1766):473–495, 2000. ISSN 1364-503X. doi: 10.1098/rsta.2000.0542. URL `http://rsta.royalsocietypublishing.org/content/358/1766/473`. 52

[106] S. Koizumi, C. Nebel, and M. Nesladek. *Physics and Applications of CVD Diamond*. Wiley, 2008. ISBN 9783527408016. 54, 261

[107] H. Kagan. Update on diamond manufacturers. Talk at RD42 Collaboration Meeting, May 2016. URL `https://indico.cern.ch/event/505107/`. 55

[108] W. Adam, W. de Boer, E. Borchi, et al. Radiation hard diamond sensors for future tracking applications. *Nucl. Instrum. Meth.*, A565:278–283, 2006. doi: 10.1016/j.nima.2006.05.127. 55, 61

[109] Irena Dolenc Kittelmann, V Cindro, and M Mikuž. *Development of Beam Conditions Monitor for the ATLAS experiment.* PhD thesis, Ljubljana U., Ljubljana, 2008. URL `http://cds.cern.ch/record/1390440`. Presented 18 Sep 2008. 57

[110] Markus Friedl. Diamond detectors for ionizing radiation. Master's thesis, University of Technology, Vienna, 1999. 58, 261

[111] W. Adam, E. Berdermann, P. Bergonzo, et al. Pulse height distribution and radiation tolerance of CVD diamond detectors. *Nucl. Instrum. Meth.*, A447:244–250, 2000. doi: 10.1016/S0168-9002(00)00195-9. 58, 61

[112] M H Nazaré, B Foster, and R.S. Gilmore. Development of diamond tracking detectors for high luminosity experiments at the LHC. R&D proposal CERN-DRDC-94-21. DRDC-P-56, CERN, Geneva, 1994. 58

[113] Benedikt Roland Vormwald. CMS Tracker Upgrades: R&D Plans, Present Status and Perspectives. Technical Report CMS-CR-2015-240, CERN, Geneva, Oct 2015. 61

[114] C Bauer, I Baumann, C Colledani, et al. Pion irradiation studies of CVD diamond detectors. Technical Report CERN-PPE-95-173. OHSTPY-HEP-E-95-018. RUTGERS-ASTROPHYSICS-47, CERN, Geneva, Oct 1995. URL `http://cds.cern.ch/record/293403`. 61

[115] W Adam, C Bauer, E Berdermann, et al. Development of CVD diamond radiation detectors. Technical Report CERN-EP-98-080, CERN, Apr 1998. URL `http://cds.cern.ch/record/356683`.

[116] D Meier, W Adam, C Bauer, et al. Proton Irradiation of CVD Diamond Detectors for High Luminosity Experiments at the LHC. *Nucl. Instrum. Methods Phys. Res., A*, 426(CERN-EP-98-079. 1):173–80. 7 p, Apr 1998. URL `http://cds.cern.ch/record/356682`.

[117] D. Asner, M. Barbero, V. Bellini, et al. Diamond pixel modules. *Nucl. Instrum. Meth.*, A636:S125–S129, 2011. doi: 10.1016/j.nima.2010.04.096. 61

[118] Los Alamos Neutron Science Center. Neutron and nuclear science facility, 04 2016. URL `http://wnr.lanl.gov/`. 61, 89

[119] CERN. Short Introduction to the use of the H6 beam. online, May 2000. URL `http://sba.web.cern.ch/sba/BeamsAndAreas/h6/H6manual.pdf`. 62

[120] C. Colledani, W. Dulinski, R. Turchetta, et al. A submicron precision silicon telescope for beam test purposes. *Nucl. Instrum. & Meth.*, A372:379–384, 1996. doi: 10.1016/0168-9002(95)01414-4. 62

[121] C Amsler, K Bösiger, M Glättli, et al. A high resolution silicon beam telescope. *Nuclear Instruments and Methods in Physics Research Section A: Accelerators, Spectrometers, Detectors and Associated Equipment*, 480(2–3):501 – 507, 2002. ISSN 0168-9002. doi: http://dx.doi.org/10.1016/S0168-9002(01)01241-4. URL `http://www.sciencedirect.com/science/article/pii/S0168900201012414`. 62

[122] Integrated Detector and Electronics (IDE) AS. *The VA2 - Specifications*, Nov 2016. URL `https://webint.ts.infn.it/fileadmin/int/servizi/label/pubblico/VA2TA/VA_23_DATAVA2.PDF`. 63, 125

[123] W. Dulinski. Strip detectors read-out system user's guide, 2015. URL `http://www.iaea.org/inis/collection/NCLCollectionStore/_Public/28/059/28059773.pdf`. This sirocco is similar to CAEN's model V 550. 63, 125

[124] Analog Devices. *AD 1671 - Complete 12-Bit 1.25 MSPS Monolithic A/D Converter*, 2014. URL `http://www.analog.com/media/en/technical-documentation/data-sheets/AD1671.pdf`. 63

[125] D. Meier. CVD Diamond Sensors for Particle Detection and Tracking. *thesis at CERN*, 1999. 64, 68

[126] Rene Brun and Fons Rademakers. ROOT - An Object Oriented Data Analysis Framework. In *AIHENP'96 Workshop, Lausane*, volume 389, pages 81–86, 1996. 64

[127] Boris Grube, Rita De Masi, Jan Friedrich, et al. Architecture of the Common GEM and Silicon Readout for the Compass Experiment. In *Proceedings, 7th International Conference on Advanced Technology and Particle Physics (ICATPP-7)*, pages 264–268, 2002. doi: 10.1142/9789812776464_0040. 64

[128] Emlyn Peter Corrin. *Development of Digital Readout Electronics for the CMS Tracker*. PhD thesis, High Energy Physics Imperial College London, November 2002. 64

[129] Aysha Abdel-Aziz. Common mode corretions for the 'Strasbourg' telescope. Summer Student Work, 2011. 65

[130] E. Belau, R. Klanner, G. Lutz, et al. The Charge Collection in Silicon Strip Detectors. *Nucl. Instrum. Meth.*, 214:253, 1983. doi: 10.1016/0167-5087(83)90591-4. 70

[131] R. Turchetta. Spatial resolution of silicon microstrip detectors. *Nucl. Instrum. Meth.*, A335:44–58, 1993. doi: 10.1016/0168-9002(93)90255-G. 72

[132] P.J. Sellin, C.M. Buttar, C.N. Booth, et al. Spatial resolution measurements of gallium arsenide microstrip detectors. *Nucl. Instrum. Meth.*, A381:57–63, 1996. doi: 10.1016/0168-9002(96)00436-6. 75

[133] Thomas Valentin Eichhorn. *Development of Silicon Detectors for the High Luminosity LHC*. PhD thesis, U. Hamburg, Dept. Phys., 2015. URL `http://pubdb.desy.de/search?of=hd&p=id:DESY-THESIS-2015-024`.

[134] Joachim Erfle. *Irradiation study of different silicon materials for the CMS tracker upgrade*. PhD thesis, U. Hamburg, Dept. Phys., 2014. URL `http://www-library.desy.de/cgi-bin/showprep.pl?thesis14-010`. 75

[135] ORTEC. GEM Series Coaxial HPGe Detector, 04 2016. URL `http://www.ortec-online.com/download/gem.pdf`. 89

[136] ORTEC. Multichannel analyzers, 04 2016. URL `http://www.ortec-online.com/Solutions/multichannel-analyzers.aspx`. 89

[137] W Adam, E Berdermann, P Bergonzo, et al. Performance of irradiated CVD diamond micro-strip sensors. *Nucl. Instrum. & Meth. A*, 476(3):706 – 712, 2002. ISSN 0168-9002. doi: http://dx.doi.org/10.1016/S0168-9002(01)01671-0. Proc. of the 3rd Int. Conf. on Radiation Effects on Semiconductor Materials, Detectors and Devices. 107

[138] Peter Trüb. *CMS pixel module qualification and Monte-Carlo study of $H \rightarrow \tau^+\tau^- \rightarrow l^+l^- ET$*. PhD thesis, Zurich, U., 2008. URL `http://e-collection.library.ethz.ch/view/eth:31112`. 112

[139] A Miucci. The atlas insertable b-layer project. *Journal of Instrumentation*, 9(02):C02018, 2014. URL `http://stacks.iop.org/1748-0221/9/i=02/a=C02018`. 112

[140] T.V. Kononenko, M.S. Komlenok, V.P. Pashinin, et al. Femtosecond laser microstructuring in the bulk of diamond. *Diamond and Related Materials*, 18(2–3):196 – 199, 2009. ISSN 0925-9635. doi: http://dx.doi.org/10.1016/j.diamond.2008.07.014. URL `http://www.sciencedirect.com/science/article/pii/S0925963508003981`. {NDNC} 2008 Proceedings of the International Conference on New Diamond and Nano Carbons 2008. 115, 117

[141] T.V. Kononenko, M. Meier, M.S. Komlenok, et al. Microstructuring of diamond bulk by IR femtosecond laser pulses. *Applied Physics A*, 90(4):645–651, 2008. ISSN 0947-8396. doi: 10.1007/s00339-007-4350-9. URL `http://dx.doi.org/10.1007/s00339-007-4350-9`. 115, 117

[142] H.O. Jeschke, M.E. Garcia, and K.H. Bennemann. Theory for laser-induced ultrafast phase transitions in carbon. *Applied Physics A*, 69(1):S49–S53, 1999. ISSN 1432-0630. doi: 10.1007/s003399900340. URL `http://dx.doi.org/10.1007/s003399900340`. 115

[143] T. V. Kononenko, V. V. Kononenko, S. M. Pimenov, et al. Effects of pulse duration in laser processing of diamond-like carbon films. *Diamond and Related Materials*, 14(8): 1368 – 1376, 2005. ISSN 0925-9635. doi: http://dx.doi.org/10.1016/j.diamond.2005.02.009. SMAC '04 Conference Proceeding S.I. Proceedings of the 5th Specialist Meeting on Amorphous Carbon. 115

[144] F. Bachmair, L. Bäni, P. Bergonzo, et al. A 3D diamond detector for particle tracking. *Nucl. Instrum. & Meth. A*, 786:97 – 104, 2015. ISSN 0168-9002. 115

[145] Iain William Philip Haughton. *3D detectors for the High Luminosity LHC, with a feasibility study into the observation of ZZ production in the $Z \rightarrow ee/\mu\mu$, $Z \rightarrow \tau\tau$ channel with the ATLAS detector*. PhD thesis, School of Physics and Astronomy, University of Manchester, 2015. 116

[146] Coherent Inc. Libra series, December 2014. URL `http://www.coherent.com/downloads/LibraSeries_CoherentDataSheet_revC_May2013_4.pdf`. data sheet (22nd Dec 2014). 117

[147] Element Six Ltd. Properties of electronic grade CVD diamonds. online, 11 2014. URL `http://www.e6cvd.com/cvd/page.jsp`. 120, 202

[148] NDT Education Resource Center. Material properties tables. online, 2016. URL `https://www.nde-ed.org/GeneralResources/MaterialProperties/ET/Conductivity_Misc.pdf`. File: Conductivity_Misc.pdf. 122

[149] A. Grill. Electrical and optical properties of diamond-like carbon. *Thin Solid Films*, 355: 189–193, November 1999. doi: 10.1016/S0040-6090(99)00516-7. 122

[150] M. Shimizu, Y. Shimotsuma, M. Sakakura, et al. Periodic metallo-dielectric structure in diamond. *Opt. Express*, 17(1):46–54, Jan 2009. doi: 10.1364/OE.17.000046. URL `http://www.opticsexpress.org/abstract.cfm?URI=oe-17-1-46`. 122

[151] II-VI Incorporated. CVD Diamond Substrates, 10 2015. URL `http://www.iiviinfrared.com`. 375 Saxonburg Blvd., Saxonburg, PA 16056-9499, US. 123, 202, 204

[152] CERN. Secondary beam areas of the PS, SPS machines, December 2014. URL `http://sba.web.cern.ch/sba/`. 127

[153] Inc. Tektronix. Catalog model 237 high voltage source-measure unit, 2016. URL `http://www.tek.com/sites/tek.com/files/media/media/resources/237.pdf`. File: 237.pdf. 127

[154] CAEN S.p.A. N1471 - NIM High Voltage Power Supply, 2016. URL `http://www.caen.it/csite/CaenProd.jsp?parent=21&idmod=622`. 127

[155] K A Olive, K Agashe, C Amsler, et al. Review of Particle Physics (RPP). *Phys.Rev.*, D86: 010001, 2012. doi: 10.1103/PhysRevD.86.010001. 139

[156] Synopsis Inc. Sentaurus TCAD computational modeling, 2014. URL `http://www.synopsys.com/home.aspx`. 143, 159

[157] G. Forcolin. *TBD*. PhD thesis, University of Manchester, 2016. 143, 159, 160, 166, 266

[158] C. Da Via, M. Deile, J. Hasi, et al. 3D Active Edge Silicon Detector Tests With 120 GeV Muons. *IEEE Transactions on Nuclear Science*, 56(2):505–518, April 2009. ISSN 0018-9499. doi: 10.1109/TNS.2009.2013951. 143

[159] K Gabathuler. PSI46 pixel chip - external specification. Technical Report rev1, Paul Scherrer Institut, Villigen, 10 2005. URL `"http://cmspixel.phys.ethz.ch/docs/psi46-readout-chip/psi46v2.pdf"`. 174

[160] ORTEC. Modular Electronic Instruments, 11 2015. URL `http://www.ortec-online.com/Solutions/modular-electronic-instruments.aspx`. 174

[161] Michael Philipp Reichmann. COCPITT - the COmpaCt PIxel Tracking Telescope. Master's thesis, ETH Zürich, September 2015. 174, 177, 180

[162] Paul Scherrer Insitut. LHC/CMS Particle Tracking Upgrade (PSI46dig). online, 2016. URL `https://www.psi.ch/ltp/cdct-projects`. 175

[163] Danek Kotlinski. The CMS Phase1 Pixel Detector. Talk at ACES 2016, Mar 2016. URL `https://indico.cern.ch/event/468486/contributions/1144331/attachments/1240612/1824099/aces2016_kotlinski.pdf`. 175

[164] CERN CMS. Digital Testboard for CMS pixel ROC. online, 03 2016. URL `https://twiki.cern.ch/twiki/bin/view/CMS/PixelDTB`. 176

[165] P. Roloff. The EUDET high resolution pixel telescope. *Nuclear Instruments and Methods in Physics Research A*, 604:265–268, June 2009. doi: 10.1016/j.nima.2009.01.069. 177

[166] E. Corrin. EUDAQ software user manua. online, April 2010. 177

[167] Hamamatsu Photoniks K.K. *Photosensor Modules H10720/10721 Series*, Dec 2015. 179

[168] D. Cussans. *Description of the JRA1 Trigger Logic Unit (TLU), v0.2c*. University of Bristol, UK, v0.2c edition, September 2009. 179

[169] M. Seeli. Study of Signal Uniformity in CVD Diamond Particle Detectors. Master's thesis, ETH Zürich, University of Toronto, 2015. 180, 201

[170] S. Ritt. Best timing resolution of DRS4 evaluation board. personal communication, 2015. 185

[171] Jozef Stefan Institute. Reaktorskicenter - TRIGA Mark II research reactor. online, 05 2016. URL `http://www.rcp.ijs.si/en/index.html`. 204

[172] R. Hall-Wilton, R. Loos, V. Ryjov, et al. Results from a beam test of a prototype PLT diamond pixel telescope. *Nucl. Instrum. Meth.*, A636:S130–S136, 2011. doi: 10.1016/j.nima.2010.04.097. 225

[173] C. Dorfer. Upgrades to the PSI test beam setup. Technical report, ETH Zurich, 2016. 226

[174] H Kagan. Development of CVD diamond tracking detectors for experiments at high luminosity colliders. Talk at 126th LHCC Meeting, May 2016. URL `https://indico.cern.ch/event/527359/contributions/2158538/attachments/1278647/1898380/RD42-LHCC-Talk2016.pdf`. 228

[175] H Kagan. internal communication, May 2016. 228